Alma Mater Studiorum – Università di Bologna

DIPARTIMENTO DI FISICA E ASTRONOMIA
Corso di Dottorato di Ricerca in Astronomia
CICLO XXV

MULTIPLE STELLAR POPULATIONS IN GLOBULAR CLUSTERS WITH PHOTOMETRY AND LOW RESOLUTION SPECTROSCOPY

Dottorando
Carmela Lardo

Relatori
Chiar.mo Prof. B. Marano
Dott.ssa E. Pancino
Dott. M. Bellazzini

Coordinatore
Chiar.mo Prof. L. Moscardini

Esame finale anno 2013

SCUOLA DI DOTTORATO IN SCIENZE MATEMATICHE, FISICHE E ASTRONOMICHE
Settore Concorsuale: 02/C1 – Astronomia, Astrofisica, Fisica della Terra e dei Pianeti
Settore Scientifico-Disciplinare: FIS/05 – Astronomia e Astrofisica

"Dans la vie l'essentiel est de porter sur tout des jugements *a priori*. Il apparaît en effet que les masses ont tort, et les individus toujours raison. Il faut se garder d'en déduire des règles de onduite: elles ne doivent pas avoir besoin d' être formulées pour qu'on les suive. Il y a seulement deux choses: c'est l'amour, de toutes les façons, avec des jolies filles, et la musique de la Nouvelle-Orléans ou de Duke Ellington. Le reste devrait disparaître, car le reste est laid, et les quelques pages de démonstration qui suivent tirent toute leur force du fait que l'histoire est entièrement vraie, puisque je l'ai imaginée d'un bout à l'autre."

Boris Vian, *L'écume des jours*.

Acknowledgements

This research project would not have been possible without the help of many people. I wish to thank Alessio Mucciarelli, Antonino Milone, Angela Bragaglia, Eugenio Carretta, Emanuele Dalessandro, Ricardo Carrera, Fabiola Marino, Manuela Zoccali, Marina Rejkuba, Oscar Gonzalez, Giuseppe Altavilla, Silvia Marinoni and Gabriele Cocozza.

I would like to thank my family and friends for their love and encouragement.

Carmela

Abstract

Our view of Globular Clusters has fundamentally changed in the last decade. A large body of spectroscopic and photometric data have conclusively established that globulars are neither coeval nor monometallic, reopening the issue of the formation of such stellar systems. The formation of globular clusters is now schematized as a two-step process, during which the enriched material from the more massive stars of a first generation gives birth, in the cluster innermost regions, to a second generation of stars with the characteristic signature of fully CNO-processed matter. However, there are still several points regarding this *self-pollution* scenario that remain to be properly understood before we can claim a profound comprehension of the multiple population phenomenon

In this thesis I present my contribution to the study of multiple populations in Galactic globular clusters.

The first chapter gives a broad introduction to the topic, both from the observational and the theoretical point of view. The chapter ends with a description of presently open questions and the motivation for the various studies contained in this thesis.

In the second chapter we use the property of photometric indices including near ultraviolet passbands to trace spread in light-element abundances. I show how accurate photometry based on ultraviolet filters can be used as an efficient tool to trace the presence of multiple populations in globular clusters, as it can be obtained in a modest amount of observational time and also for distant clusters. To this end we use publicly available multi-band Sloan photometry for nine Northern Galactic globular clusters. We detect multiple populations in seven out of nine clusters and present radial distributions for the first-to-second generation number ratio for these seven objects. Our work more than doubles the number of clusters for which such studies exist and indicates that the younger generation stars are *always* more concentrated toward the cluster center with respect to the first generation of stars.

The third chapter contains a spectroscopic and photometric study of main sequence and subgiant branch stars in NGC 1851. This cluster belongs to the group of massive clusters, i.e., such as ω Centauri and M 22, which display a spread in iron abundance in addition to the spread in light element abundance found also in *normal* globular clusters. For this reason, they have been suggested that they may be the relics of more massive primeval dwarf galaxies that were disrupted by and merged with the Galaxy. We use Hubble space telescope and ground-based photometry to select two groups of faint- and bright-SGB stars from the visual and Strömgren color-magnitude diagrams. Significant variations in the carbon and nitrogen abundances are present among stars of each group, which indicates that each SGB hosts multiple sub-generations of stars. Coupling our results with literature photometric data and abundance determinations from high-resolution studies, we identify the fainter SGB with the red-RGB population, which also

should be richer on average in Ba and other s-process elements, as well as in Na and N, when compared to brighter SGB and the blue-RGB. I discuss the implications of our findings for the theoretical models on the formation and evolution of NGC 1851 in the last part of the chapter.

Similarly, in the fourth chapter, we use spectral synthesis to measure C and N abundances for a large sample of stars along the red giant branch of the globular cluster M 2. We found evidence of multiple populations also in this cluster. Our data allow us to investigate the mixing effects on carbon surface abundance during red giant branch evolution as well. We detect from UV photometry an additional, redder red giant branch sequence, amounting to a small fraction of the total giant population. This substructure could be connected to the faint sub giant branch component recently reported from space observations. Additionally, we identify two CH stars in our $V, U-V$ diagram. These stars, which are both cluster members, fall on this redder sequence, and exhibit both enhanced CH and CN bands. This evidence perfectly fits the suggestion that stars located onto the red red giant branch should have a peculiar chemical nature.

The fifth chapter investigates the behavior of nitrogen and carbon abundance variations at relatively high metallicities ([Fe/H] $\geqslant$ –0.5 dex). We consider unevolved stars in NGC 5927, NGC 6352, and NGC 6388. These main sequence stars show intrinsic (anticorrelated) abundance variations in both C and N that cannot be explained by mixing. More interesting, when the signal-to-noise was good enough, we could detect separated groups of stars in the C-N diagram. First generation stars are chemically homogeneous while the second population has an intrinsic spread that follows its own C-N anticorrelation, with a hint of bimodality. This result raises the question of whether all clusters should have always bimodal (or multimodal) distribution with respect to the C and N abundances, or whether high metallicity clusters are unusual in this regard.

In chapter sixth, I summarize the main results presented in previous chapters and the open problems addressed in this dissertation. The last part of this chapter presents a list of future steps that would be the natural outcome of my Thesis work.

Contents

CHAPTER

1 The multiple population phenomenon in globular cluster

Until few years ago, globular clusters (GCs) were thought to be stellar systems hosting a simple stellar population (SSP), i.e., an ensemble of stars with the same age and chemical composition (Renzini and Buzzoni, 1986). Omega Centauri, whose stars were known to span a significant range in metallicity since long time (Cannon and Stobie, 1973; Freeman and Rodgers, 1975; Dickens and Bell, 1976; Butler et al., 1978; Norris, 1980; Persson et al., 1980), was considered as an outstanding exception, since it is also the most massive GC of the whole Galaxy (3×10^6 $M_\odot$, Pryor and Meylan, 1993).

Today the situation appears more complex: the considerable progress made in the domains of high-resolution photometry and multi-object spectroscopy has produced precise data, that raise many challenging issues for the understanding of the formation process of GCs, and of the structure and evolution of their stars.

In particular, it is now well established that most (perhaps all) GCs have been sites of two or even more star-formation episodes, producing a peculiar chemical self-enrichment pattern. From a chemical perspective, GCs show a large variation in the abundances of light elements (Li, C, N, O, F, Na, Mg, and Al; i.e., Kraft, 1994, Gratton et al., 2004, Carretta et al., 2010c, Martell and Smith, 2009, Kayser et al., 2008, Pancino et al., 2010, Gratton et al., 2012a) both internally to a given cluster, and between clusters. Conversely, the abundances of heavier α (Si, Ca, Ti), iron-peak (Fe, Ni, Cu), and neutron-capture elements (Ba, La, Eu) do not, in general, show the same star-to-star variation.

Interestingly enough, these chemical inhomogeneities are not confined only to Galactic GCs, but signature of extreme chemical abundance anomalies has been found also in extragalactic stellar cluster (e.g., M 31, Large Magellanic Cloud, and Fornax; see Colucci et al., 2009; Mucciarelli et al., 2009; Johnson et al., 2006; Letarte et al., 2006).

Nowadays, the multiple population phenomenon cannot longer being considered a oddity, as it emerges naturally within massive cluster formation. Therefore, a clear comprehension of the mechanisms that lead to the formation and evolution of GCs and the relation existing between GCs and field stars is a basic requirement to understand how galaxies assembled.

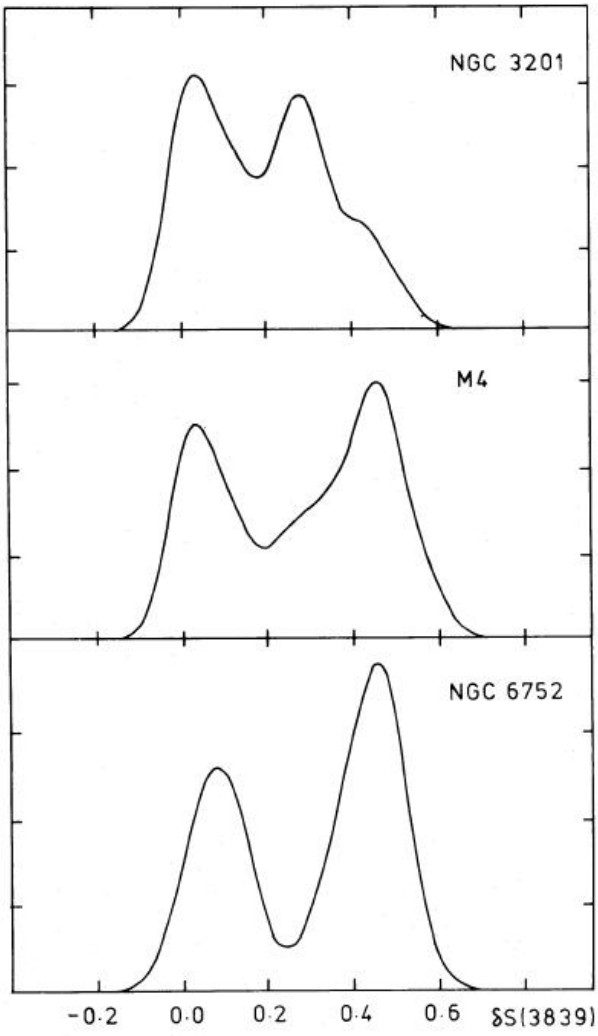

Figure 1.1: The cyanogen distribution for RGB stars in NGC 6752 (Norris et al., 1981), M 4 and NGC 3201 (Norris, 1981) is represented in this plot from Smith and Norris (1982). The scale on the ordinate is arbitrary.

1.1 Star-to-star abundance variations

1.1.1 Light element abundance variations: a historical overview

The first evidence of departure from chemical homogeneity among stars within individual GCs came from studies of the more accessible, bright red giant branch (RGB) stars since forty years ago (e. g., Osborn, 1971, Norris, 1981, Hesser et al., 1982, and Norris et al., 1984). The first of the unusual chemical patterns to be revealed were the anticorrelated variations in the CH and CN spectral features for stars at the same absolute magnitude on the RGB (i.e., at the same evolutionary phase), with most of the GCs analyzed presenting a bimodal distribution of

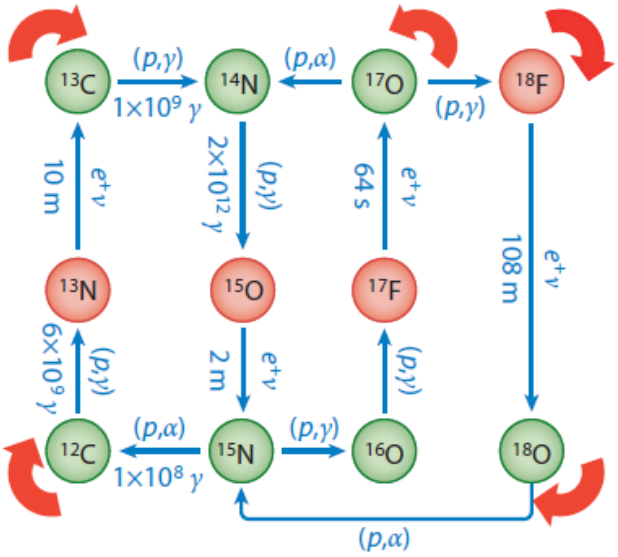

Figure 1.2: The nuclear reactions in the CNO cycle from Wiescher et al. (2010). This cycle processes ^{1}H into ^{4}He through a series of nuclear reactions involving the different species of carbon, nitrogen and oxygen.

CN strength (see Fig. 1.1). This was promptly recognized as a characteristic feature of stars in clusters, because typical field or open cluster stars show weak CN bands and strong CH bands, at odds with GC giants (Smith and Norris, 1984, Jacobson et al., 2008, Gratton et al., 2004, Martell and Smith, 2009[1]).

Because the CNO cycle, operating in equilibrium, tends to convert both carbon and oxygen into nitrogen (see Fig. 1.2), CN-strong giants were promptly interpreted as having some amount of CNO processed material in their atmospheres.

When a star evolves off the main sequence (MS), the envelope expands outward, and convection penetrates into a region that had already experienced partial CN processing, whose abundance of light elements had therefore been changed by proton-capture, *dredging up* material toward the stellar surface (see Fig. 1.3). As a result of the convective mixing, the outer atmosphere will display the spectral signature of hydrogen fusion: the ^{12}C/^{13}C and C/N ratios are lowered, and the surface abundances of lithium is strongly reduced (see Langer, 1985, Shetrone et al., 1993, Palacios et al., 2006, Gratton et al., 2000). Therefore, the CNO cycle and mixing capable of bringing processed material to the stellar surface were immediately proposed as a viable source to explain these chemical inhomogeneities. However, this *mixing* scenario was soon put into trouble by the observational evidence. In fact, the first dredge-up (FDU) depends only on mass and chemical composition of stars, and therefore cannot account *(a)* for the bimodal CN band strength distribution observed in intermediate metallicity clusters and *(b)* the presence of these chemical inhomogeneities in low metallicity stars, which convective envelopes will never

[1] Using moderate-resolution spectra of 561 field giants with typical halo metallicities, Martell et al. (2011) find that 3% of the sample shows the CN-CH band strength behavior typical of GC stars. They argue that these stars are genuine second-generation GC stars that have been lost to the halo field.

dig deep enough to come in contact the H-burning shell along the entire RGB evolution according to stellar models (Gratton et al., 2004). Additionally, the origin of CN-strong stars cannot be ascribed to mere surface pollution, because surface pollution on already-formed stars would result in abundance anomalies that are largely diminished after the FDU (Iben, 1965). The general impression at that time was that mixing-mechanism should obviously take a rôle, but this was not the entire story. They found that a clear anticorrelation between the O and Na abundances among evolved RGB stars exists for all studied GCs and variations in Al and Mg (anticorrelated with each other) were also discovered (see Fig. 1.5 and Fig. 1.6).

When higher-resolution spectra became available, it was found that stars depleted in carbon and enhanced in nitrogen were also depleted in oxygen and magnesium, and enhanced in sodium and aluminum (e.g., correlation between CN strength and Na, Al found by Cottrell and Da Costa, 1981, or anticorrelation between CN and O, coupled with correlation between CN and Na, found by Sneden et al., 1992, see Fig. 1.4).

In the late ninety eighties, a collaboration between the Lick Observatory and McDonald Observatory (Texas) led by R. P. Kraft started a spectroscopic survey of GCs in a large metallicity

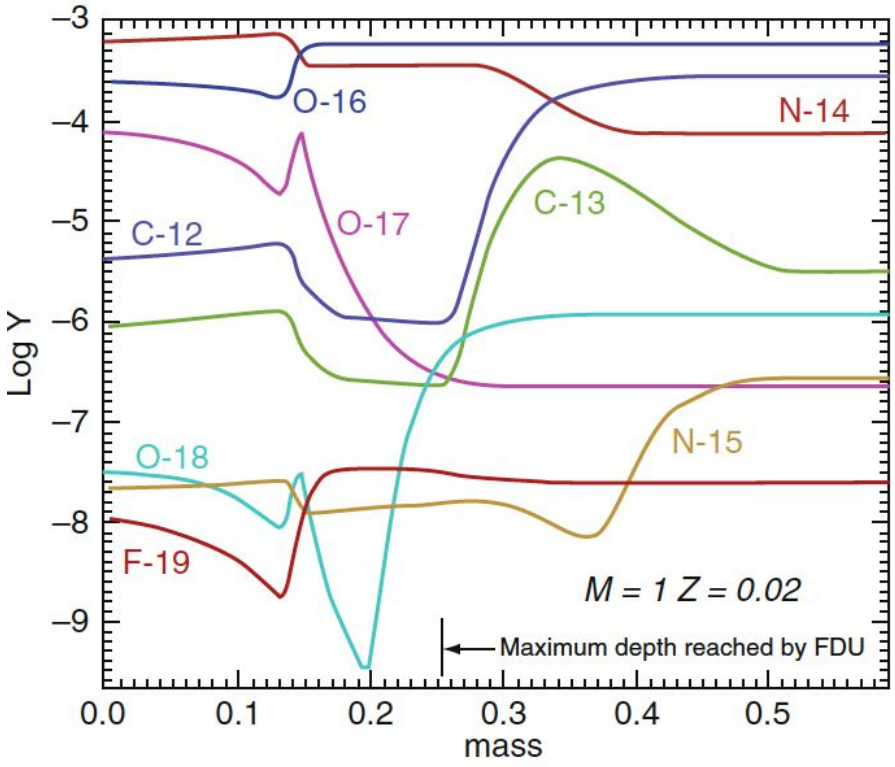

Figure 1.3: The composition profile for the C, N, and O isotopes as a function of the interior mass for the 1 $M_{\odot}$ and Z=0.02 models from Karakas (2010a). The unit of the *y*-axis is the logarithm of the number fraction, Y, where the mass fraction is given by X = Y A, and A is the atomic mass. By definition, the mass fraction of all species sums such that Σ X = 1. The composition profile is a *snap-shot* of the interior of the star at the end of core hydrogen exhaustion. The position of the maximum inward penetration of the convective envelope during the first dredge-up is reported.

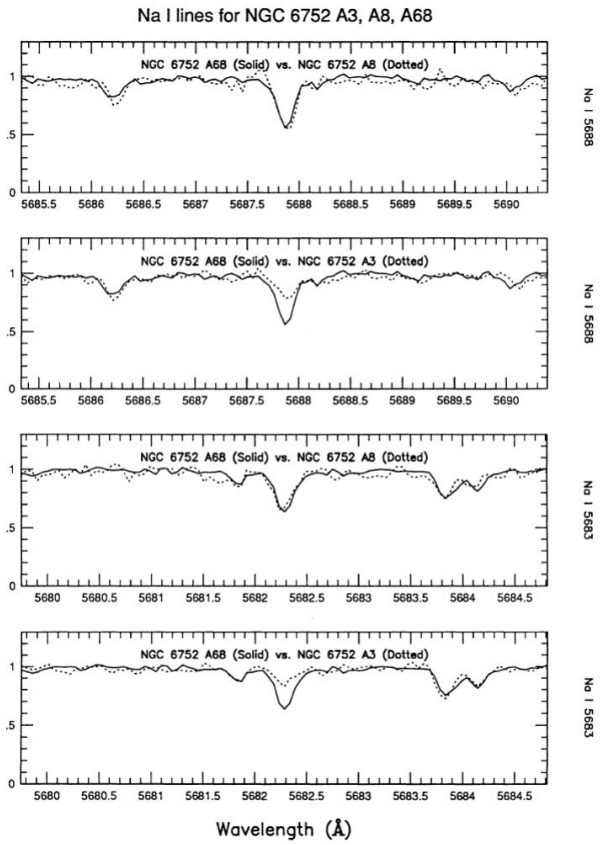

Figure 1.4: Spectra of the NGC 6752 giants A3, A8, and A68 around the 5683Å and 5688Å Na lines. The two CN-strong stars, A8 and A68, exhibit Na lines of comparable strength, much stronger than the Na line observed in the CN-weak giant A3 (from Smith and Wirth, 1991).

range. This extensive work delivered abundances of light elements (O, Na, Mg, Al), α-, and Fe-peak elements for stars typically within a magnitude from the RGB tip (a summary of some results of Lick-Texas group is shown in Fig. 1.5, taken from Ivans et al., 2001).

We refer to the reviews by Gratton et al. (2004) and Gratton et al. (2012a) for an exhaustive summary of earlier Na-O anticorrelation studies undertaken by others groups in the same years. The presence of Na-O and Mg-Al anticorrelations point towards the NeNa and MgAl chains (see Fig. 1.7) that take place at much higher temperatures than the hydrogen-burning through CNO cycle, which can not be reached in the MS or in RGB phases of GC stars. ^{23}Na could be produced at the expense of ^{22}Na in the same regions where O begins to be depleted in the ON cycle. At T $\geqslant 3 \times 10^7$ K in regions of O depletion, ^{20}Ne could produce ^{23}Na, and at higher temperatures (T $\geqslant 7 \times 10^7$ K) ^{27}Al could be processed by p-captures first on ^{25}Mg and ^{26}Mg, then on ^{24}Mg (see Denisenkov and Denisenkova, 1989, Langer et al., 1993, Salaris et al., 2002, Prantzos et al., 2007 and references therein).

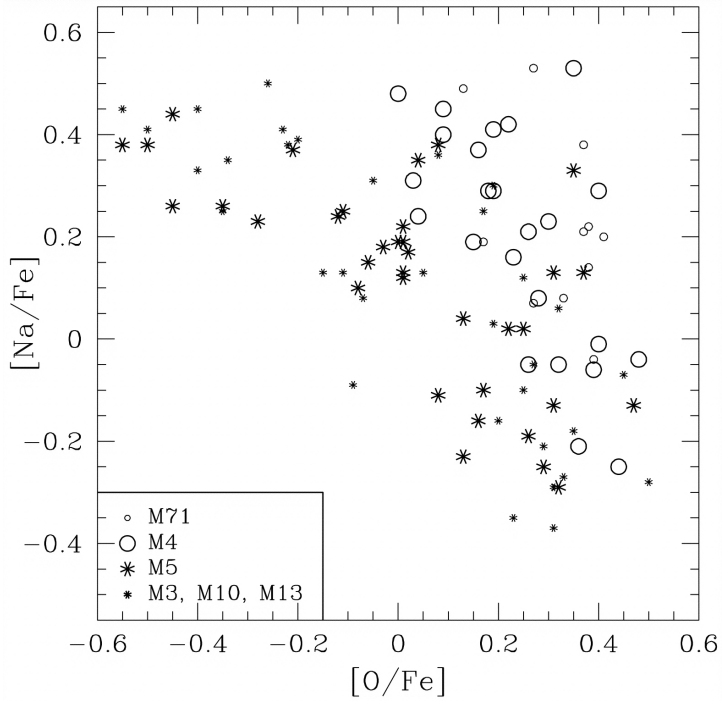

Figure 1.5: Na-O anticorrelations from Ivans et al. (2001) for clusters with intermediate metallicity.

Significant spreads in C and N abundances, as well as their anticorrelations, were lately found also among MS and turn-off (TO) stars (see Figures 1.8 and 1.9; e.g, Cannon et al., 1998, Harbeck et al., 2003, Suntzeff and Smith, 1991, Cohen et al., 2002, Ramírez and Cohen, 2003, and Cohen et al., 2005; among others).

From the high-resolution front, the Na-O anticorrelation was found in unevolved stars in M 13 (Cohen and Meléndez, 2005), NGC 6397 and NGC 6752 (Carretta et al., 2005 and Gratton et al., 2001), 47 Tuc (Carretta et al., 2004), and recently by D'Orazi et al. (2010), Lind et al. (2011) and Monaco et al. (2011) on large samples of stars in 47 Tuc, NGC 6397, and M 4; where Na, O and Li abundances were measured. The extension of the abundance anomalies to unevolved or scarcely evolved stars provided compelling evidence that this pattern cannot be due to *in situ* nuclear reactions but they were present in the material out of which the stars formed. In fact low mass MS stars are not hot enough for the required set of nuclear reaction to occur within their interiors. Moreover stellar models do not predict any physical mechanism able to bring processed material from the core to the surface of these stars.

Indeed, these stars were *born* with the observed CNONa abundance patterns. An evolutionary component to the abundance variations is still demanded by the variation of C (Suntzeff and Smith, 1991) and Li (Grundahl et al., 2002) with luminosity along the RGB sequence. Hence, some degree of *internal mixing* is required in any case.

The actual sources of the anomalous chemical enrichment observed in clusters have not been firmly identified yet. Intermediate-mass asymptotic giant branch (AGB) stars having un-

dergone hot bottom burning (HBB; Dantona et al., 1983; Ventura et al., 2001), fast rotating massive stars (FRMS; Decressin et al., 2007b), massive interacting binaries (de Mink et al., 2009), or novae (Smith and Kraft, 1996; Maccarone and Zurek, 2012) have been proposed as sources of the pollution of the intra-cluster medium (ICM) at the origin of second-generation stars (see Sects. 1.3 and 1.5 for a discussion).

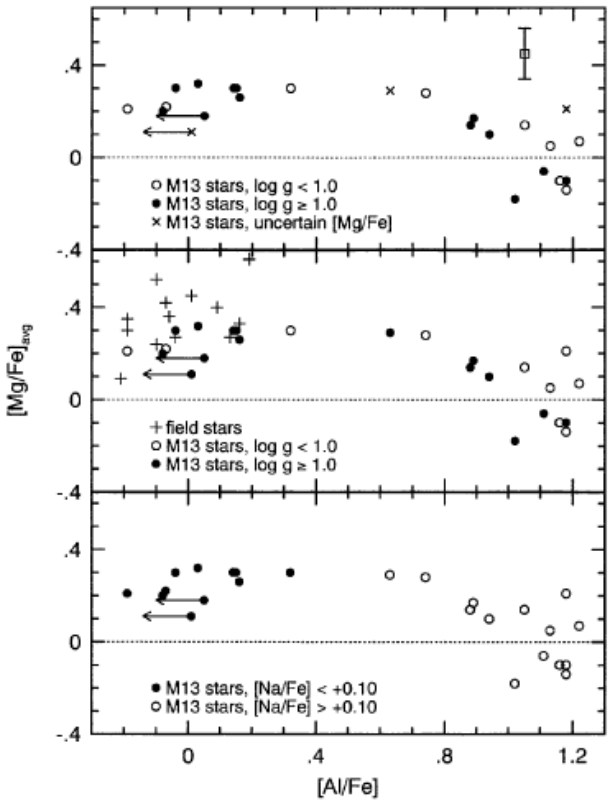

Figure 1.6: Relative Al and Mg abundances in ω Cen and M 13 giants (from Kraft et al., 1997)

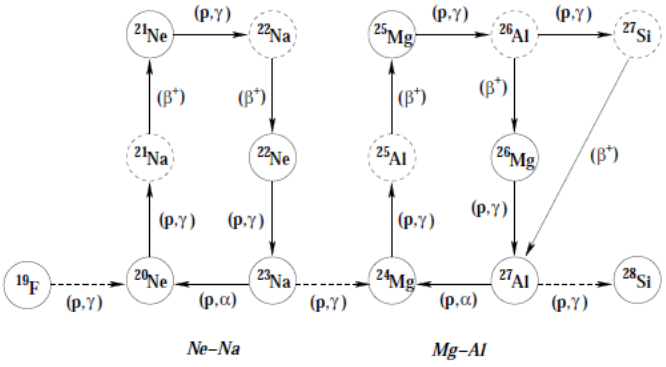

Figure 1.7: Reactions of the Ne-Na and Mg-Al chains. Unstable isotopes are denoted by dashed circles.

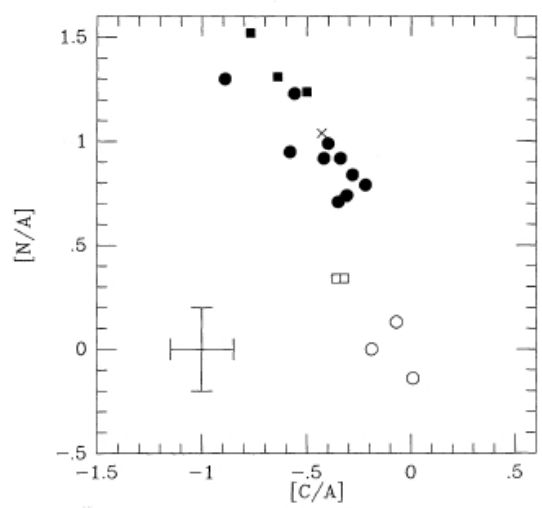

Figure 1.8: [C/A] vs [N/A] abundances for M 5 stars as derived from CH and CN band strengths from Briley et al. (1992). Square markers are used for RGB stars, circles for sub giant branch (SGB) stars, and filled/unfilled for CN-strong/CN-normal respectively. The typical observational uncertainties are shown in the bottom-left corner.

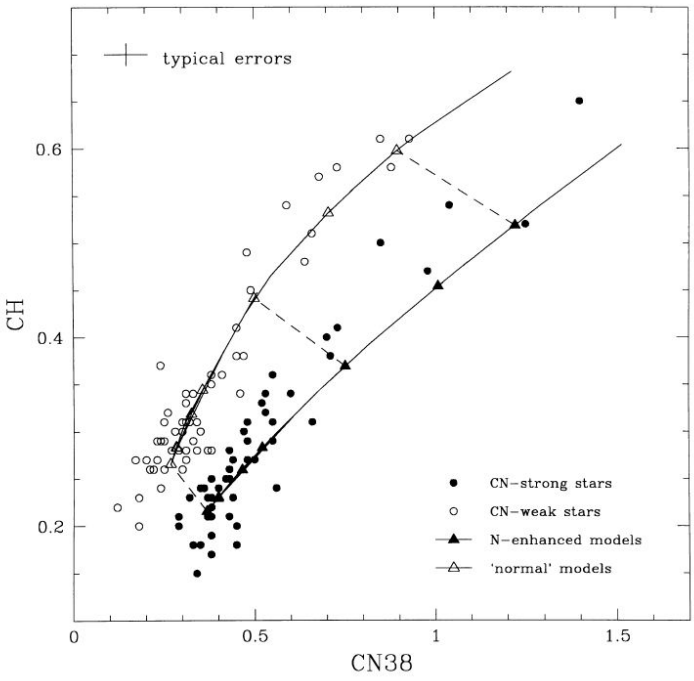

Figure 1.9: The division of the 47 Tuc MS stars into CN-strong and CN-weak stars from Cannon et al. (1998). The solid lines show the loci of synthetic spectra for two different C and N abundances, essentially the trend of the indices with temperature. Dashed lines join pairs of models with different abundances but the same temperature and gravity.

1.1.2 Present spectroscopic surveys

Nowadays, the *self-enrichment* scenario is largely accepted by the community (D'Ercole et al., 2008; D'Antona and Ventura, 2007; Ventura et al., 2001; Ventura and D'Antona, 2008a,b; Decressin et al., 2007b, 2008, 2010; Conroy and Spergel, 2011; Valcarce and Catelan, 2011), and observational efforts point toward the collection of a large amount of data, to shed light on the phenomenology of the multi populations in GCs through the study of possible trends of light element abundance with cluster parameters. Such kind of studies are allowed by the multiplex capabilities of the new generation of instruments (e.g. FLAMES for high resolution studies and FORS multi-object observations for low resolution works). Moreover, these large scale studies allow for the comparison of the cluster abundance behaviors within homogeneous observations, data reduction and analysis. The recent large scale studies by Kayser et al. (2008) and Pancino et al. (2010) measured CN and CH band strengths in stars from the MS to the RGB in a total of 14 Southern GCs (partly in common). Kayser et al. (2008) demonstrated that CN variations exist among unevolved stars in the clusters NGC 288, NGC 362, M 22 and M 55, which were not previously been observed to contain MS abundance variations.

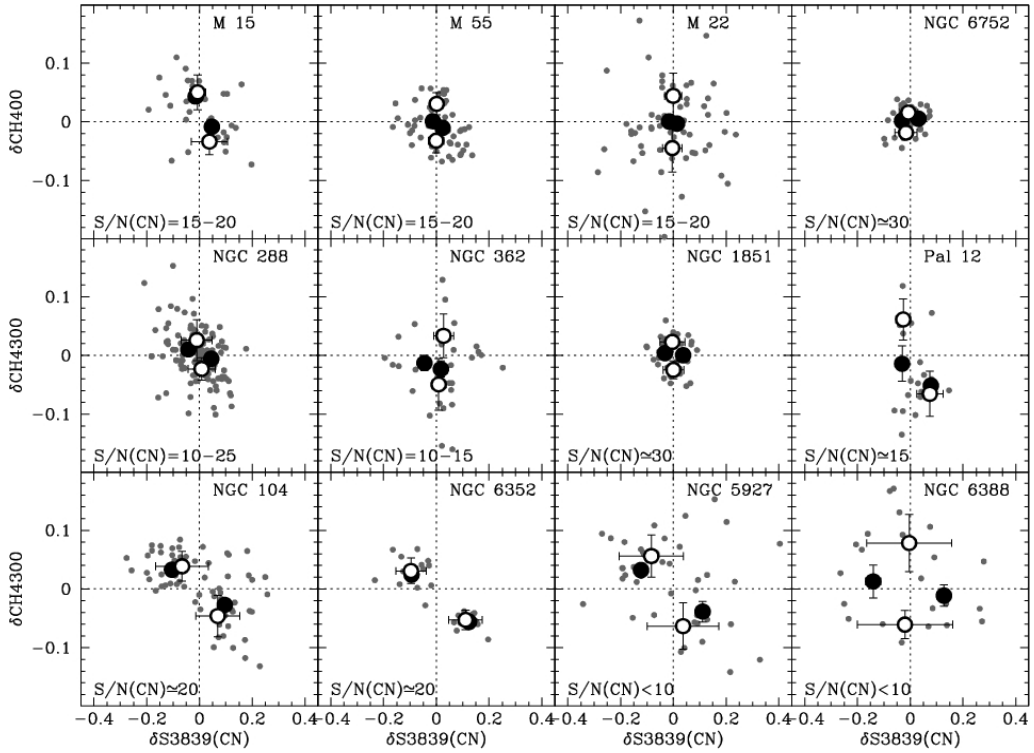

Figure 1.10: Anticorrelation plots for the CH and CN band strengths from Pancino et al. (2010). Each panel shows the measurements for stars (gray dots) in each cluster. CH strong and weak stars are separated by the horizontal dotted line, and their centroids are marked as large white dots, while CN strong and weak stars are separated by the vertical dotted line and their centroids are marked as large black dots. The S/N ratio in the CN band region is indicated in the lower left corners.

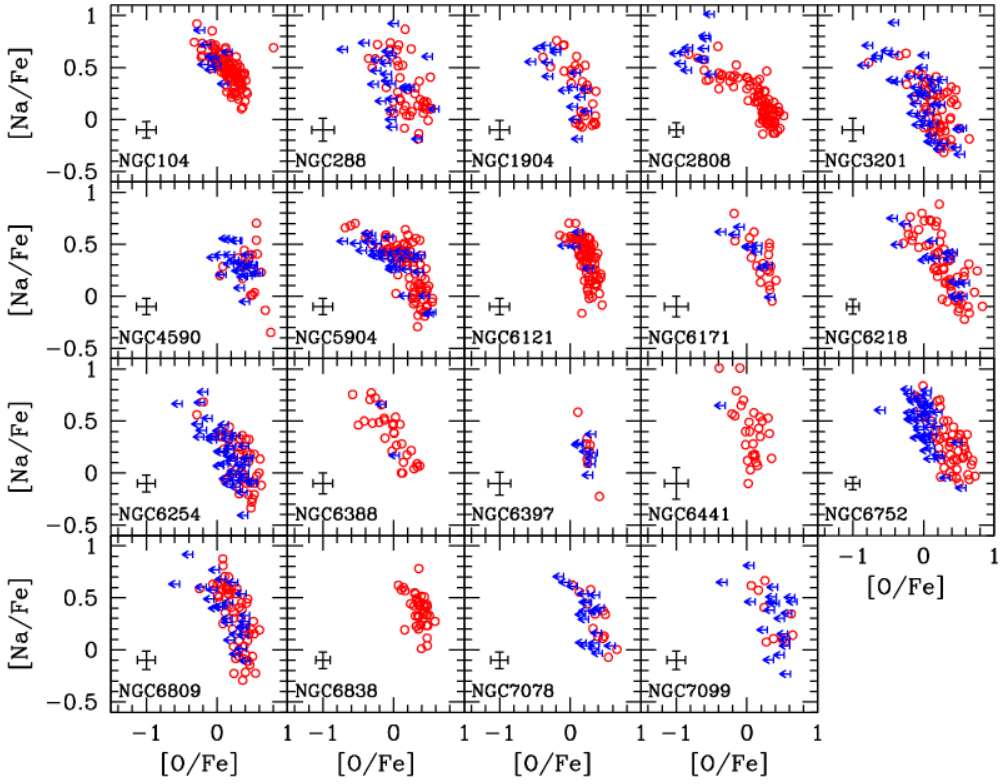

Figure 1.11: Na-O anticorrelations observed in 19 Galactic GCs from from Carretta et al. (2009c).

Pancino et al. (2010) detected a clear anticorrelation (and even a bimodality) between the CN and CH band strengths for MS stars in the metal-rich clusters in their sample (Pal 12, 47 Tuc, NGC 5927, NGC 6352), while they could not detect any clear anticorrelation or bimodality for the metal-poor clusters (but for M 15, see Fig. 1.10). Interestingly, they found that the ratio of CN-strong and CN-weak stars r_{CN} correlates with the cluster age, concentration c, total luminosity M_V, total present-day mass in units of log(M/M$_\odot$), orbital inclination, and orbital period P; albeit the statistical significance of the observed correlations is weak. These relationships fairly well agree with previous findings (e.g., correlation between r_{CN} and M_V; Kayser et al., 2008, Smith and Mateo, 1990, Carretta et al., 2010c), except for the correlation between r_{CN} and ellipticity ($\epsilon = 1 - (b/a)$; initially found by Norris, 1987, Smith and Mateo, 1990, and Smith, 2002 but not confirmed by Kayser et al., 2008).

In the framework of the *self -enrichment* scenario, this might mean that the relative number of the two stellar populations (or the efficiency of formation of the second generation stars) is only marginally influenced by the cluster total mass and orbital parameters, while the correlation with age might suggest that older clusters are more efficient in converting gas into the second generation of stars.

From the high resolution spectroscopy front, the study of Carretta et al. (2009c) reported homogeneous oxygen and sodium abundances for a sample of about 2000 RGB stars in 19 Southern GCs (see Fig. 1.11). The spectroscopic evidence is that *all* GCs surveyed so far (with the possible

exception of Terzan 7, Pal 12 and IC 4499) show the Na-O anticorrelation, although the slope and shape of the Na-O relationship and the lowest O abundance detected changes from cluster to cluster (Fig. 1.11). There are clusters with a well extended Na-O anticorrelation and clusters for which both Na and O abundances span very short ranges. In a few cases, Na-O distribution turns out to be bimodal (as for M 4, Marino et al., 2008). Moreover, Carretta et al. (2010c) found that there is a good correlation – that broadly agrees with past findings (Kayser et al., 2008; Pancino et al., 2010)– between the extension of the Na-O anticorrelation and the present-day total mass of the GCs (using the absolute magnitude M_V as a proxy for the mass). When placing abundance analysis results in a broader context, they suggest that the presence of a Na-O anticorrelation can be regarded as the operative definition of a *bona fide* GCs. On the other hand, the analysis of UVES spectra for $\simeq$200 stars by Carretta et al. (2009c) has shown that the Mg-Al anticorrelation is not present in all GCs. Both of these indications suggest that the typical polluter masses change from cluster to cluster: this variation is apparently driven by a combination of cluster luminosity and metallicity.

1.2 Photometric evidence of multiple populations

In recent years, thanks to the large capabilities of the Hubble space telescope (HST), the advent of 8-meter-class telescopes, and the massive use of U-based filter observations, accurate photometry has revealed unexpectedly complex CMDs in many GCs. Indeed, star-to-star variations in light- and alpha-element abundances, age, and metallicity can determine multimodal or broad sequences in the CMD observed within some galactic or extragalactic GCs (e.g., Pancino et al., 2000a; Bedin et al., 2004; Sollima et al., 2007; Piotto et al., 2007; Marino et al., 2008; Milone et al., 2009a; Lardo et al., 2011).

Omega Centauri is by far the most famous example and the first object for which photometric evidence of multiple populations was found. Its CMD (see Fig. 1.12) display multiple RGBs, multiple SGBs (Lee et al., 1999; Pancino et al., 2000a), and an extended horizontal branch (HB; Villanova et al., 2007; Cassisi et al., 2009; D'Antona et al., 2010; Bellini et al., 2010). As shown by Bedin et al. (2004), the MS is double with a third, less-populated MS probably associated with the most metal-rich population.

The blue MS is about 0.3 dex more metal-rich than the red one. This finding implies that the blue MS is highly enhanced in He (see Sect. 1.4.5). The complexity of the observational scenario indicates that ω Cen is so peculiar that it may not be a *genuine* GC: it has often been suggested (e.g., Bekki and Freeman, 2003 and references therein) that ω Cen may be the remnant of a tidally disrupted dwarf galaxy, once similar to the Sagittarius dwarf (with its central GC M54; e.g., Monaco et al., 2005; Bellazzini et al., 2008; Piotto, 2009; Carretta et al., 2010b). In this section we review the most interesting cases illustrative of various phenomenology of the multiple populations along the different evolutionary sequences in GCs.

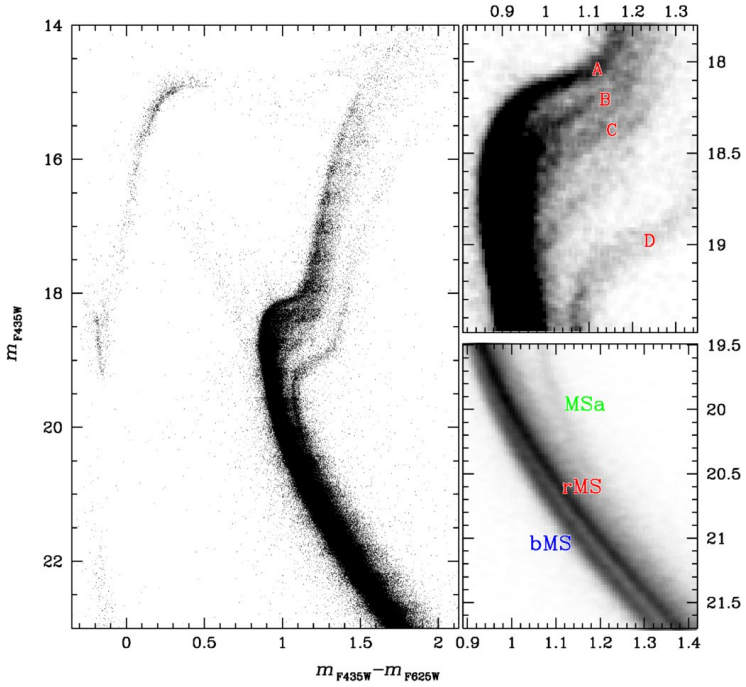

Figure 1.12: ω Cen CMD resulting from the 10 $\times$ 10 arcmin^2 mosaic of ACS images centered on the cluster center from Bellini et al. (2010). On the right-hand panel Hess diagrams are plotted to highlight the four main SGBs and the triple MS (following the notation from Villanova et al., 2007).

1.2.1 Main sequence

As showed by several recent studies, multimodal MSs could be quite common among GCs. In addition to the spectacular case of NGC 2808, which shows three distinct MSs[2] (Piotto et al., 2007, see Fig. 1.13), double and triple MSs have been observed in several GCs, including 47 Tuc, NGC 6752, and NGC 6397 (Anderson et al., 2009, Milone et al., 2012c,b, 2010) and have been associated to stellar generations with a different content of helium and light-elements (e. g. Norris, 2004; D'Antona et al., 2005; Piotto et al., 2005; Carretta et al., 2006; Bragaglia et al., 2010b; see also Sect. 1.4.5).

1.2.2 Sub giant branch

Apart from the case of extreme case of ω Cen (e.g., (Ferraro et al., 2004; Bedin et al., 2004; Sollima et al., 2005; Villanova et al., 2007; Pancino et al., 2011a,b), impressive evidence of multiple populations at the level of the SGB comes from the very precise photometry of an increasing number of lower-mass clusters: NGC 1851 (Milone et al., 2008; Zoccali et al., 2009; Han et al., 2009a; Lardo et al., 2012a; Piotto et al., 2012), NGC 6388 (Moretti et al., 2009; Piotto et al., 2012),

[2]Milone et al. (2012a) used infrared, space-based images to study the multiple MSs in this cluster. They found the three MSs detected by Piotto et al. (2007) from visual-band photometry to merge together at the level of the MS bend; at fainter magnitudes, the MS again splits into two components, with one component accounting only for the 35% of the entire population. This less-populated MS in the faint part of the near-IR CMD is helium-rich and poor in carbon and oxygen, and it can be associated with the middle and the blue MS of the optical CMD.

47 Tuc (Anderson et al., 2009; Milone et al., 2012c; Piotto et al., 2012), M 22 (Piotto, 2009; Marino et al., 2012b; Piotto et al., 2012), M 54 (Piotto, 2009), NGC 362 (Piotto et al., 2012), NGC 5286 (Piotto et al., 2012), NGC 6715 (Piotto et al., 2012), and M 2 (Piotto et al., 2012).

NGC 1851 and M 22 are the best studied of all these. We refer the reader to Chapter 3 for a complete review of the large literature on NGC 1851, here we focus only on M 22. As mentioned before, multiple stellar groups in M 22 are clearly manifest by a split in its SGB CMD domain and two distinct RGB sequences (see Fig. 1 of Marino et al., 2011). As in the case of NGC 1851, the split SGB appears to be related to chemical differences observed among its giant stars. Marino et al. (2009) and Marino et al. (2011) showed that this cluster hosts two metallicity groups, with mean [Fe/H] abundance which differs of about ∼0.15 dex. These two metallicity groups are characterized also by a different content of *s*-process elements: ⟨[Y, Zr, Ba, La, Nd/Fe] ⟩= –0.01 dex (σ= 0.06) in the lower metallicity group and +0.35 dex (σ = 0.06) in the high metallicity group; while the template *r*-process element Eu exhibits a constant abundance. Stellar models fail in reproducing the size of the SGB photometric split if only a metallicity spread between the two populations is assumed. Marino et al. (2009) suggest that the origin of the split could be more complex and also involves a difference in age and/or variations in the total CNO abundance, as

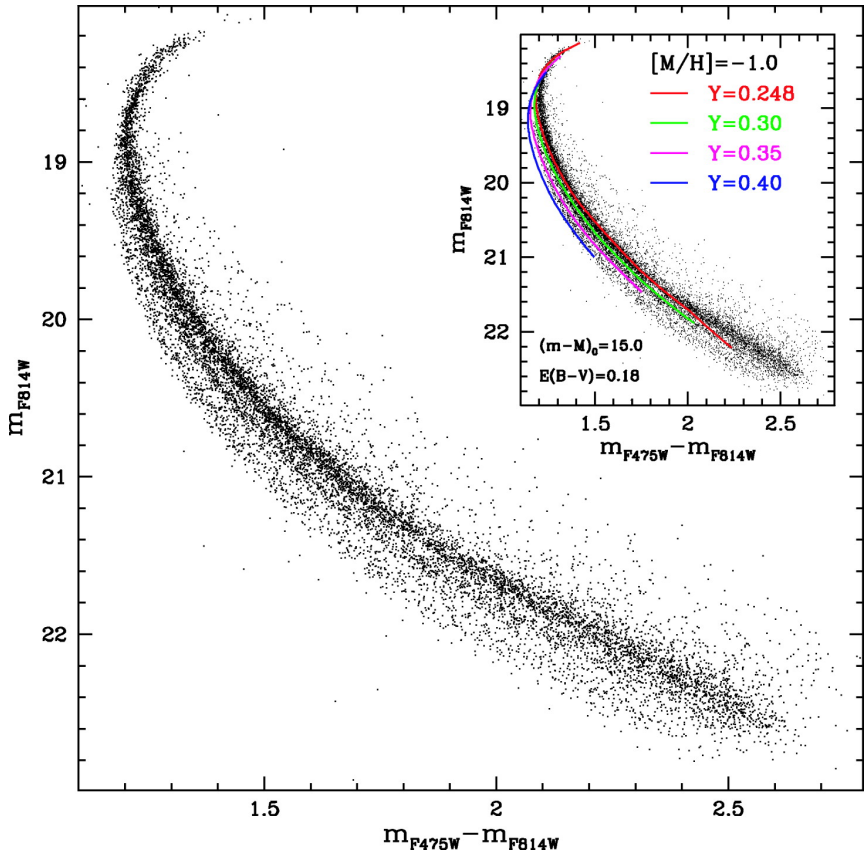

Figure 1.13: Proper-motion-selected, differential-reddening-corrected CMD of MS stars in NGC 2808 from Piotto et al. (2007). In the inset, the observed CMD is fitted with four 12.5 Gyr isochrones, with different He content.

proposed by Cassisi et al. (2008) and Ventura et al. (2009) for NGC 1851. Evidence supporting this scenario was found among its RGB stars (Marino et al., 2011). In a recent work, Marino et al. (2012b) demonstrates that the faint SGB is populated by *s*-rich (metal-rich) stars, and the bright SGB by *s*-poor (metal-poor) stars. This SGB*s*-RGBs connection is further confirmed by inspecting the $U,(U-V)$, in close analogy to what we discovered for NGC 1851 (Lardo et al., 2012a, see Chapter 3). As discussed above, Marino et al. (2011) found that *s*-rich giants are also enhanced in the total CNO with respect to the *s*-poor ones. The SGB*s*-RGBs connection allow the authors to extend this fundamental result to the SGB stars.

1.2.3 Red giant branch

To date, multiple or broad RGBs have been observed in nearly all the GCs that have been observed with good signal-to-noise in the appropriate photometric bands (e. g. Milone et al., 2012c; Yong et al., 2008a; Lee et al., 2009a, see Chapter 2).

As an example, Yong et al. (2008a) used Strömgren photometry from Grundahl and Andersen

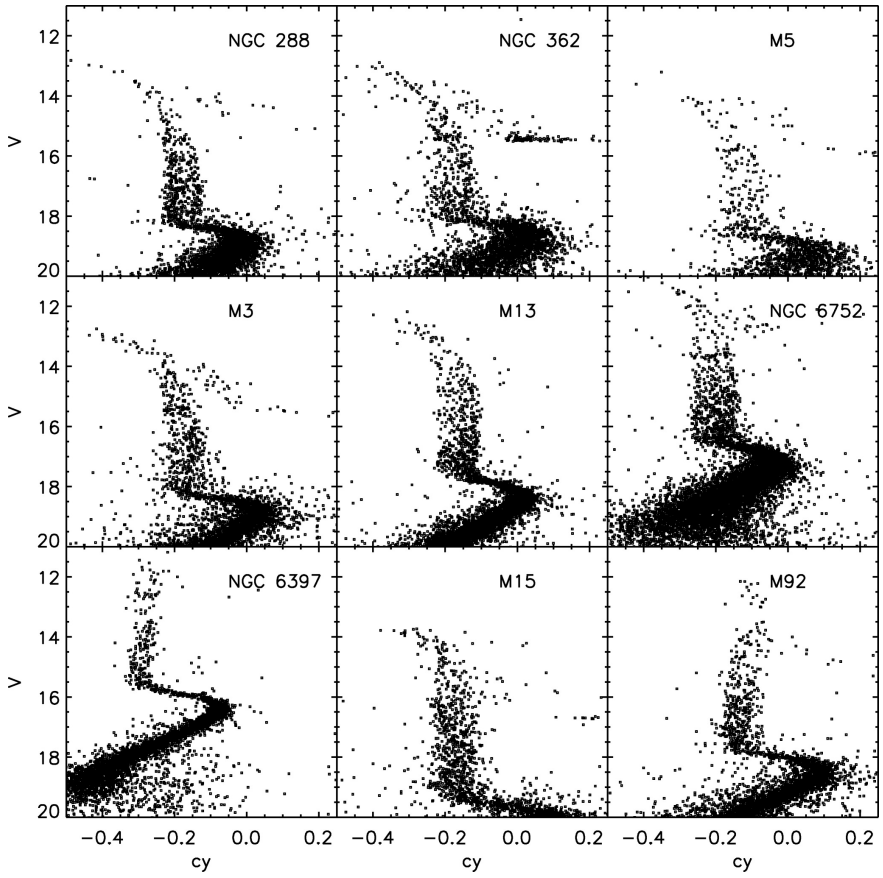

Figure 1.14: The V, c_y CMDs for a sample of clusters from Yong et al. (2008a) (photometry by Grundahl et al., 1999). All clusters exhibit a large range in c_y at all evolutionary stages.

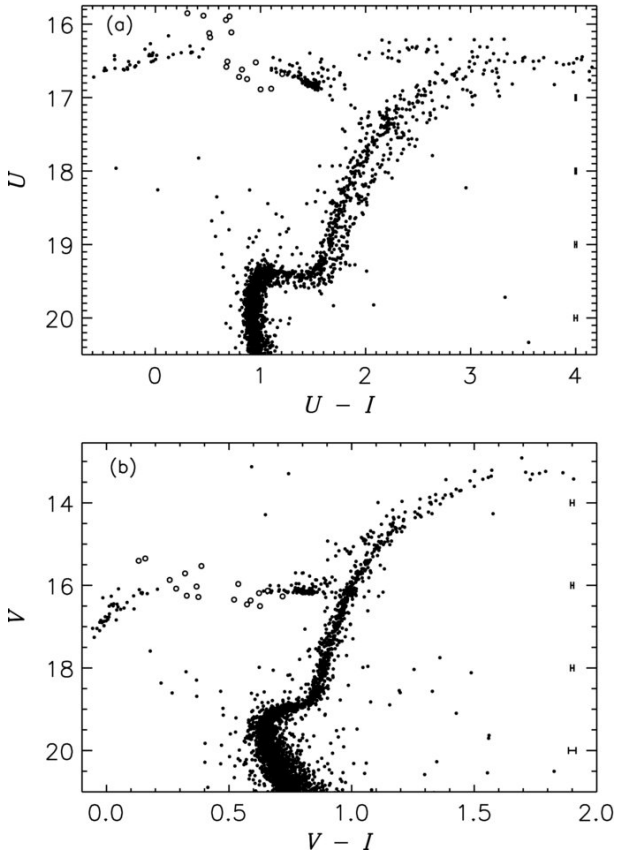

Figure 1.15: CMDs for NGC 1851 from Han et al. (2009a). Open circles denote RR Lyrae stars, and the photometric errors are shown.

(1999) to show remarkable spreads in c_y[3], at any magnitude along the RGB of NGC 288, NGC 362, M 5, M 3, M 13, NGC 6752, M 15, M 92, and NGC 6397 (Fig.1.14). Carretta et al. (2011a) and Alonso-García et al. (2012) also considered results from Strömgren photometry, extending the work by Grundahl and Andersen (1999) and Yong et al. (2008a). Kravtsov et al. (2010a,b) used U band photometry to identify multiple populations within the clusters NGC 3201 and NGC 1261. Similarly, Roh et al. (2011) found that the RGB of NGC 288 is clearly split into two in the $hk = [(Ca-b)-(b-y)]$ index, while the split is not shown in the $b-y$ color. Marino et al. (2008) were able to demonstrate for M 4 that a bimodal Na-O distribution, correlated with a bimodal distribution in CN strength, was also clearly associated with a bimodal spread in the color of RGB stars in the U vs. *(U-B)* CMD, not seen with other color indices.

The spread in *U-B* color among RGB stars of NGC 3201 was shown to correlate with Na abundance by Carretta et al. (2010c).

Finally, Han et al. (2009b) showed that the RGB of NGC 1851, which is narrow and well defined in optical CMDs not including U photometry, is clearly split into two parallel branches in the U vs. $(U-I)$ color (Fig. 1.15). Han et al. (2009b) suggest that the splitting is caused by a combination

[3] $c_y = c_1 - (b-y)$, where $c_1 = (u-v)-(v-b)$.

of effects due to variations in the abundances of not only of C,N,O but also of heavier elements (Ca, Si, Ti, and Fe) and helium.

1.2.4 Effects of different chemical compositions on photometry

There are several intriguing potential connections between the photometric multiplicity and the peculiar chemical pattern because is not surprising that the abundance variations should have large effects on photometry.

On the other hand, there is also a rich literature concerning the analysis of the effects on stellar evolution induced by a change of the heavy element abundances in the mixture (Salaris et al., 2006, Dotter et al., 2007, Pietrinferni et al., 2009, VandenBerg et al., 2012; to name the more recent works). Recently Sbordone et al. (2011) calculated synthetic spectra for typical chemical element mixtures (i.e., a standard α-enhanced distribution, and distributions displaying CN and O-Na anticorrelations) found in the various subpopulations hosted by individual GCs. From the theoretical spectra they determined bolometric corrections for standard Johnson-Cousins and Strömgren filters and predicted colors. They found that CNO abundance variations affect mainly the portion of the spectra short of about 4000Å (see Fig. 1.16) owing to the changes in molecular bands (such as NH, CN, and OH in the fainter MS stars).

As a result color and magnitude changes are largest in the blue filters (encompassing the wavelength range 3000 Å $\leqslant \lambda \leqslant$ 4000 Å), independently on the use of broad or intermediate bandpasses. Indeed, broadening or splits have been observed in the majority of cases when color indices including a near ultraviolet band (such as Johnson U or Strömgren u) are considered (Han et al., 2009a, Kravtsov et al., 2010a, Roh et al., 2011, Lardo et al., 2011, Marino et al., 2008, Carretta et al., 2009c, and Milone et al., 2010, Milone et al., 2012a, among others; see Fig. 1.14 and Fig. 1.15). We will discuss this in more details in the following Chapters.

We summarize the results presented by Sbordone et al. (2011) in Fig. 1.17. In general, when using BVI CMD, a splitting of sequences along the MS up to the TO can only be achieved by varying the helium content Y. A variation of the C+N+O-abundance (mixture CNONa1 in Fig. 1.17) leads to a split of the SGB (as in the case of NGC 1851; see Cassisi et al., 2008). When considering UBV and uy diagrams, CNONa abundances as well as Y differences may lead to multiple sequences from the MS to the RGB, where the effect tends to be larger and may reach 0.2–0.3 mag (see Fig. 1.17). We must note that this multiplicity is independent of the sum of C+N+O, as the individual element variations are decisive. For vy diagrams a splitting of the MS up to the TO can be achieved only by a variation in Y and a split of the SGB is the result of a change in C+N+O (as for the BVI colors). Additionally, a split along the RGB may result both from helium and from C+N+O variations; at variance with the BVI case. Finally, for the c_yV diagrams, all parts of a CMD show the influence of both element anticorrelations and of helium variations, and the strongest separation can be seen (see bottom left panel of Fig. 1.17).

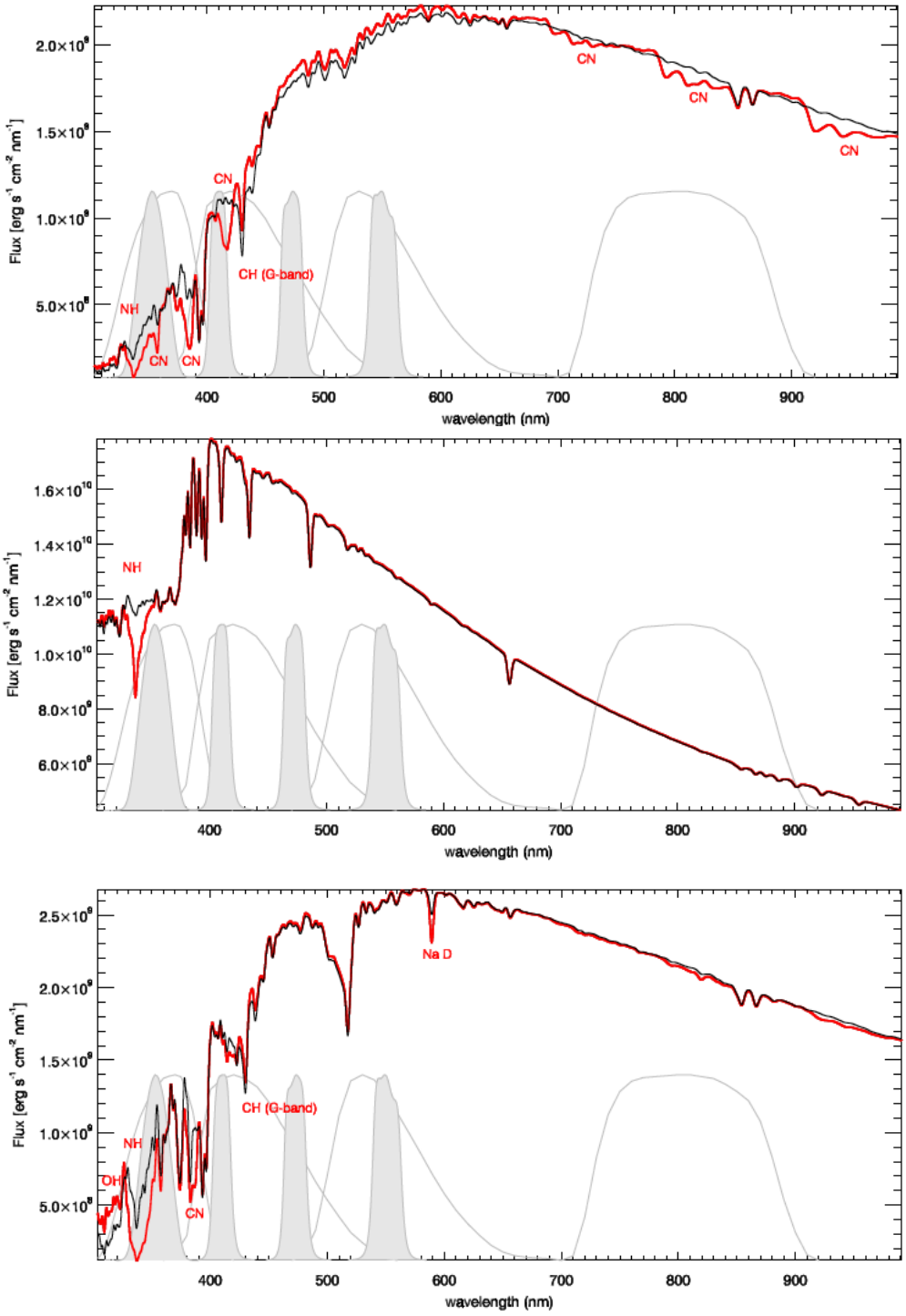

Figure 1.16: *From top to bottom:* flux distribution for the RGB (T_{eff} = 4476 K, log g = 1.2), SGB (T_{eff} = 6490 K, log g = 4.22), and MS (T_{eff} = 4621 K, log g = 4.47) model stars from Sbordone et al. (2011). The α-enhanced mixture employed in the BaSTI database (Pietrinferni et al., 2006), which corresponds to a typical first-generation star is plotted in black, while the mixture representative of a second-generation star is shown in red, and displays – compared to the black mixture, – enhancements of N and Na by 1.8 dex and 0.8 dex by mass, respectively, together with depletions of C and O by 0.6 dex and 0.8 dex, respectively. Both mixtures have [Fe/H]=–1.62 and Y= 0.246. Superimposed to the stellar spectra the transmission curves for the Johnson-Cousins U, B, V, and I filters (thin, gray lines; left to right) and for the Strömgren $uvby$ filters (grey-shaded regions). A number of molecular bands, which vary significantly between the two mixtures, are labelled.

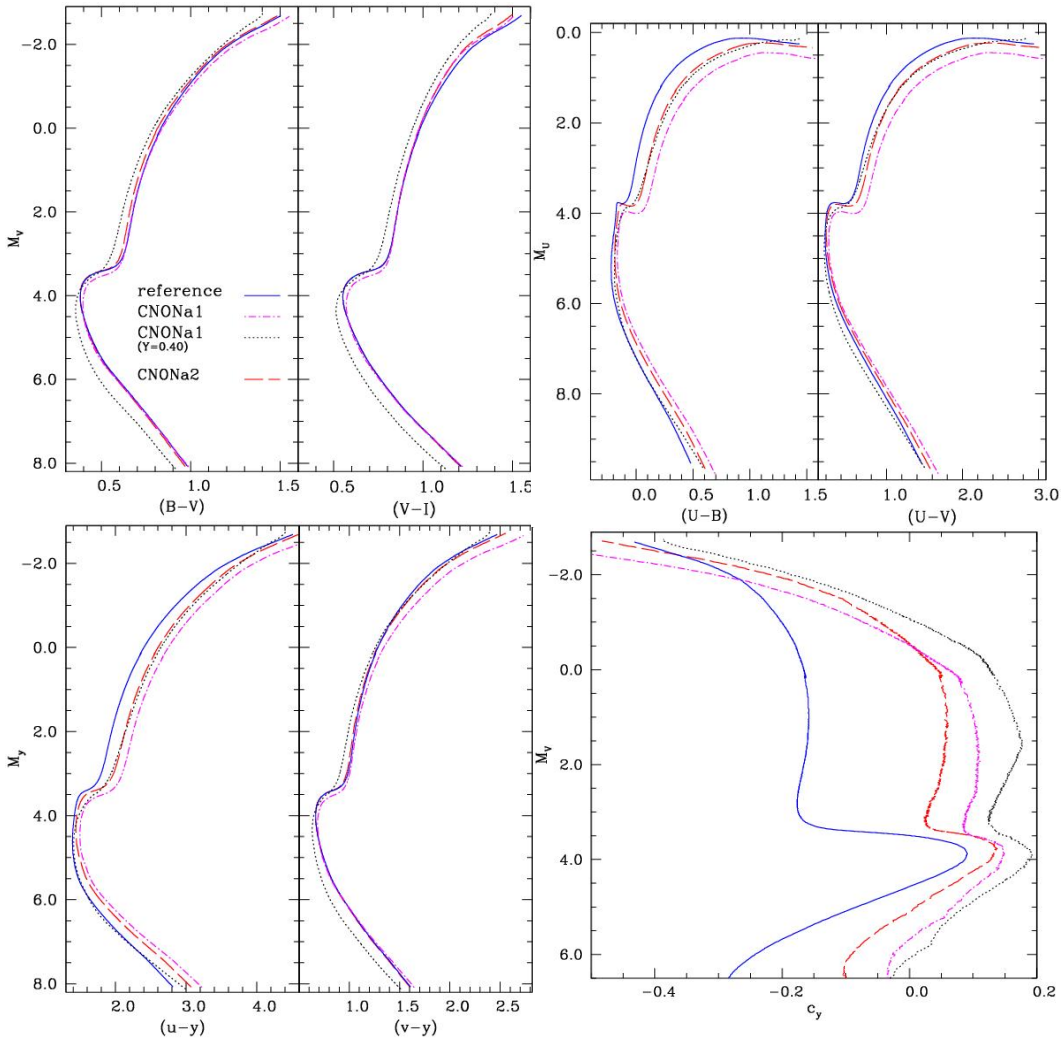

Figure 1.17: Several CMDs in Johnson-Cousins and Strömgren filters for three different metal mixtures are plotted (age 12 Gyr, [Fe/H] = –1.62 and Y = 0.246); from Sbordone et al. (2011). The reference mixture (solid blue line) refers to the α-enhanced mixture (first generation stars). The first mixture representative of second-generation stars is labelled CNONa1 (magenta dot-dashed line), and displays – compared to the reference α-enhanced mixture –enhancements of N and Na by 1.8 dex and 0.8 dex by mass, respectively, together with depletions of C and O by 0.6 dex and 0.8 dex, respectively. A CNONa1 mixture with Y=0.4 is also shown as black dotted line. An alternative composition for second-generation stars is labelled CNONa2 (dashed red line); it is the same as the CNONa1 mixture but for the enhancement of N that in this case is equal to 1.44 dex by mass. The important difference between CNONa1 and CNONa2 *second-generation* mixtures is that in the first case, at fixed Fe abundance, the C+N+O mass fraction is enhanced by a factor of 2 compared to the reference composition, whereas the CNONa2 mixture has the same CNO content (in both number and mass fractions) as the reference composition, within 0.5%. The CNONa pattern considered for the second generation stars is characterized by extreme values for the anticorrelation observed in Galactic GCs, the range of colors spanned by the isochrones should give a rough idea – considering also that the extension of the abundance anticorrelations varies from cluster to cluster (e.g. Carretta et al., 2010c)– of the maximum color spread to be expected in the CMD of a generic Galactic GC.

1.3 The nature of the polluters

The most natural explanation for chemical inhomogeneities in GCs is the *self-pollution* scenario, where a cluster experiences a relatively extended star formation period, with the younger population born from an ICM polluted by the ejecta from first generation stars that have processed material through hot H-burning. The older generation stars share the same chemical compositions of Population II field stars of similar metallicity, while the second generation is relatively enhanced in He, N, Na, and Al and depleted in C, O, Ne, and Mg. It may be useful to recall that the material that formed first generation stars is not pristine, but it was previously enriched by (at last a few) SNe, in most cases SNII, since we do not know any GC with [Fe/H] $\leqslant$ –2.5 dex and most of them have [α/Fe] $\geqslant$ +0.2 dex. This sets up the initial conditions for the subsequent self-enrichment and may have a strong impact on the observable effects of this process[4].

Critical for the understanding of the multiple population phenomenon in GCs is to identify the progenitor stars responsible for the excess of some element (like N, Na and Al) in the second generation of stars. Given the constraints imposed by the new observational evidence, valuable candidate polluters must:

(a) be able to modify only the light elements without contributing heavy elements like iron. The observed intrinsic spread in [Fe/H] is generally < 0.06 dex (e.g, Carretta et al., 2009b). Spreads in iron abundances have been found so far only in the most massive GCs: ω Cen (e.g., Pancino et al., 2000a, Sollima et al., 2007, Marino et al., 2012a, Johnson and Pilachowski, 2010), M 54 (Bellazzini et al., 2008; Carretta et al., 2010b), M 22 (Marino et al., 2009, 2011; Da Costa and Marino, 2011), Terzan 5 (Ferraro et al., 2009; Origlia et al., 2011); NGC 1851 (Yong and Grundahl, 2008, Carretta et al., 2010d, Gratton et al., 2012c; but see also Villanova et al., 2010), and perhaps NGC 5024 (Saviane et al., 2012).

(b) own a mechanism to bring the processed material from the core to the stellar surface,

(c) have a way to release this material to the ICM with a relatively low velocity to avoid the escaping from the cluster potential well.

1.3.1 Intermediate-mass AGB stars

In AGB stars more massive than about 3 – 4 $M_{\odot}$, the hydrogen burning shell with a temperature of 6 –10 $\times$ 10^7 K can extend into the convective envelope (HBB): in this way the envelope composition is directly affected by the various H-burning cycles (CNO, NeNa, MgAl; see Fig. 1.18). According to the AGB scenario, the CNONa anomalies arise within intermediate mass stars[5], because they experienced HBB process that even in presence of the TDU prevents the formation of carbon stars (Renzini and Voli, 1981). Moreover, $\simeq$ 3 – 8 $M_{\odot}$ stars experience the

[4] For example it is very different if AGB stars process and pollute a gas with initial [O/Fe]= +0.4 dex or [O/Fe]= –0.2 dex.

[5] In particular, intermediate-mass (4-11 $M_{\odot}$) AGB stars undergoing HBB (Cottrell and Da Costa, 1981; D'Antona and Ventura, 2007; Ventura et al., 2001; D'Antona and Caloi, 2004; Karakas et al., 2006), and/or super-AGB. Super-AGB stars are objects with initial masses in the range of 9 – 11 $M_{\odot}$ that undergo off-center carbon ignition in partially degenerate conditions, end end up as O – Ne white dwarfs.

second dredge-up (SDU) shortly before reaching the AGB, leading to a sizable He enrichment in the whole stellar envelope (Sect. 1.4.5). The mass lost via the slow winds of AGB stars could then be retained by the cluster from which CN-strong, Na-rich stars formed (Thoul et al., 2002; D'Ercole et al., 2008; Renzini, 2008). Star formation is eventually halted by SNe which sweep the remaining gas from the cluster, carrying with it the products of explosive nucleosynthesis. In this scenario, the mass of stars that first become SNe cannot significantly exceed the mass of the most massive stars that undergo thermal pulses. Moreover, the required fine-tuning of the dredge-up and HBB casts some doubt on the robustness of scenario. Additionally, AGB models cannot fully match the observed abundance trends (Denissenkov and VandenBerg, 2003; Fenner et al., 2004; Campbell et al., 2004)[6]. In particular, AGB stars fail in reproducing the notable O depletion observed in some GC stars ([O/Fe] < –0.5 dex; Ventura and D'Antona, 2009). Furthermore, AGB

[6]The abundance trends are also dependent on the number of TDU episodes and therefore on the adopted convection efficiency (Renzini and Voli, 1981), mass loss (Ventura and D'Antona, 2005), and nuclear reaction rates (Lugaro et al., 2004; Karakas et al., 2006).

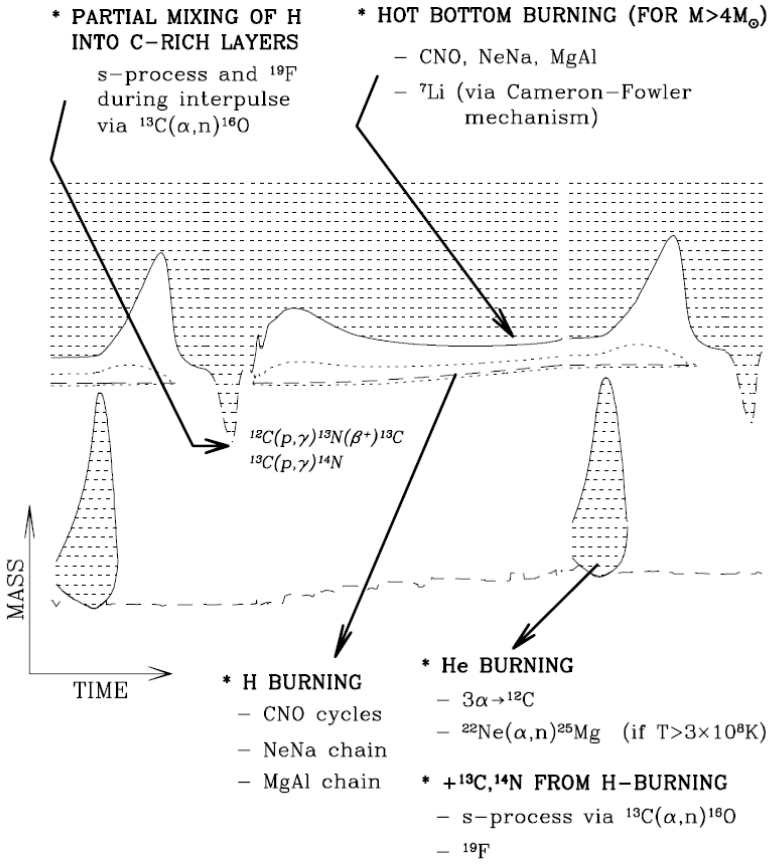

Figure 1.18: Overview of the nucleosynthesis occurring in 3 $M_\odot$ Z= 0.02 AGB stars. The figure displays a schematic representation of two successive pulses. The long-dashed lines locate the maximum energy production in the H-burning (*top*) and He-burning (*bottom*) layers. Short-dashed lines locate the extensions of the H-burning shell, defined by the region where the energy production exceeds 1 erg g^{-1} sec^{-1}. Dredge-ups following each pulse (identified by the dashed envelope border) are also displayed (from Mowlavi, 1998).

stars are expected to produce a substantial increase of the CNO sum as they enhance Na and Al and deplete Mg and O (e.g., Decressin et al., 2009). This is in stark contrast to observational requirements: whenever C, N, O abundances are available simultaneously, their sum is constant within the observational errors with few exceptions (see Yong et al., 2009 and Marino et al., 2012b for the case of NGC 1851 and M 22; respectively). The constant CNO sum, generally observed in GCs, is explained with more massive AGB progenitors for which the nucleosynthesis is not greatly affected by the third dredge-up, responsible for increasing the sum CNO and the slow neutron capture elements (Ventura and D'Antona, 2008a; Renzini, 2008; see also Sect. 1.4.1.1).

1.3.2 Fast rotating massive stars

Massive stars, more precisely, Wolf-Rayet stars, have been initially proposed by Brown and Wallerstein (1993) and Wallerstein et al. (1987) as possible sources of processed material from which second generation stars formed. More recently Prantzos and Charbonnel (2006) proposed a qualitative scenario for the role of massive stars, suggesting that their winds provide the metal-enriched material for the next stellar generation, and that the subsequent supernova explosions provide the trigger for star formation; the SN ejecta escape the GC environment along the cavities opened previously by the stellar winds.

This scenario was later developed and enlarged by the study of Decressin et al. (2007b). The key point of this scenario is the fast rotation of massive stars. Fast rotation is needed to remove material from the stellar surface and inject it with a low velocity in the interstellar medium. Furthermore, it triggers internal mixing which brings H-burning products (and hence matter with correct abundance signatures) from the convective core to the stellar surface. Massive stars have short lifetimes and can release H-synthesized material while low-mass stars are still forming in the nascent globular cluster. They can, through the wind and SN shocks or through the ionization front they produce, trigger star formation in their vicinity, being thus able to be at the same time the cause of new star formation and the provider of at least part of the material from which the stars form.

In Fig. 1.19 we report a simple sketch of the evolution of a FRMS from Decressin et al. (2010). In early stages, rotationally-induced mixing leads to strong internal mixing of H-burning products synthesized in the convective core. Providing initial rotation is high enough, the stars reach the break-up on the MS evolution and form an equatorial gas disk around them, similar to that of Be stars (e.g. Townsend et al., 2004). Unlike the normal winds of massive stars, which have velocities ranging from hundreds to a few thousand km s^{-1}, the equatorial disk loses mass with velocities lower than 50 km s^{-1}, that can then easily be retained by the potential wells of GCs. In this scenario, FRMS ejecta are mixed with pristine gas to form second generation stars near their massive progenitors. However, the latest version of the FRMS scenario predicts a gathering of polluted gas in the generic centre of the GC (Decressin et al., 2010). Even though this scenario may help us to explain the O-Na anticorrelation observed in all GCs, the multiple MSs observed in some GCs (see Sect. 1.4.5) cannot be explained without invoking discrete helium abundances,

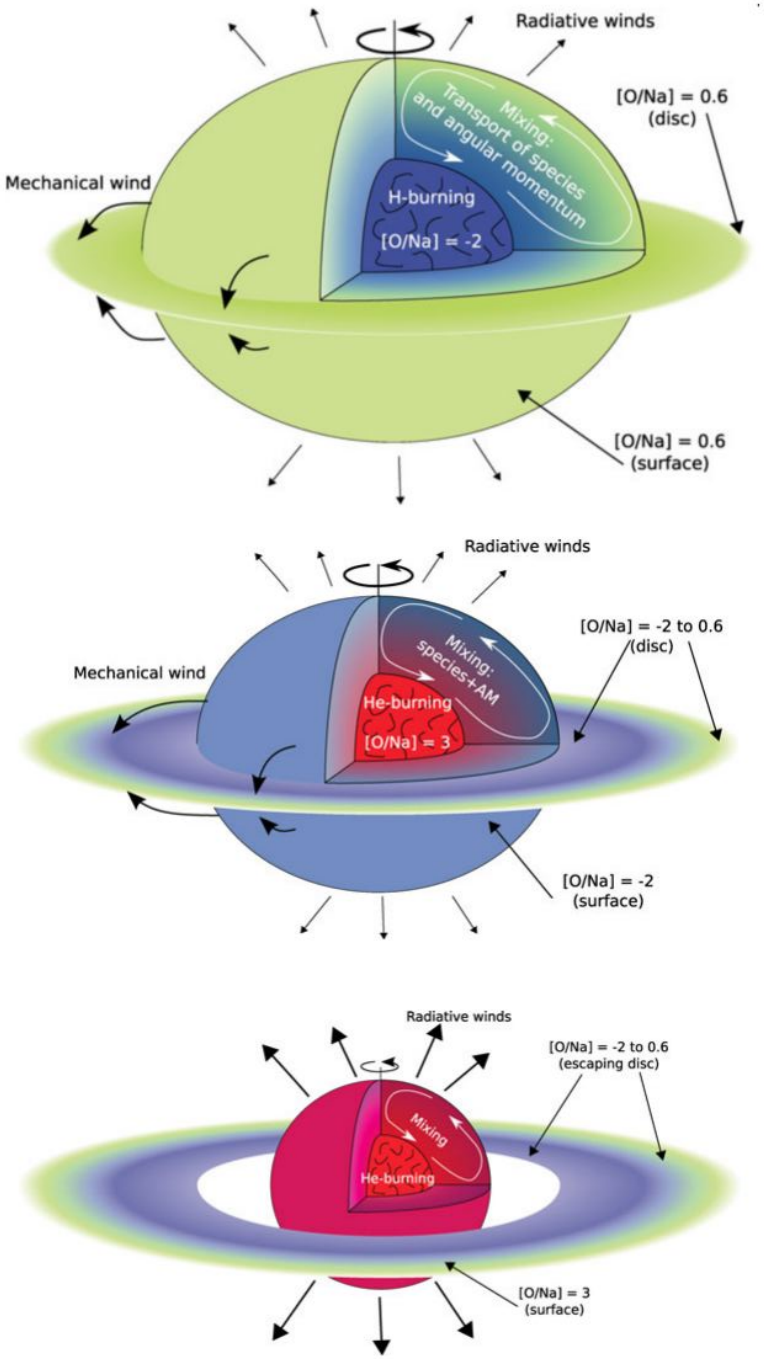

Figure 1.19: Schematic view of the evolution of FRMS from Decressin et al. (2010). The colors reflect the chemical composition of the various stellar regions and of the disc. *Top*: during the MS, a slow outflowing equatorial disc forms and dominates matter ejection with respect to radiative winds. *Middle*: at the beginning of central He-burning, the composition of the disc material spans the range in [O/Na] observed today in low-mass cluster stars. The star has already lost an important fraction of its initial mass. *Bottom*: due to heavy mass loss, the star moves away from critical velocity and does not supply its disc anymore; radiatively-driven fast wind takes over before the products of He-burning reach the stellar surface.

which is in conflict with the smooth spread in Y predicted by this scenario, as also pointed out by Renzini (2008).

Finally, we note that both scenarios are problematic, with issues relating to the initial mass function and the predicted nucleosynthesis yields (i. e., Fenner et al., 2004, Decressin et al., 2007b; see also Sect. 1.5).

1.3.3 Other candidate polluters

Although most of the active debate is centered on the two above mentioned main candidate polluters, also other channels have been proposed. While it may be observationally determined that one particular class of polluters could be dominant, it is highly probable that several mechanisms are active (Valcarce and Catelan, 2011). de Mink et al. (2009) proposed massive binaries as a source for the internal pollution of globular clusters. The majority of massive stars are expected to be members of interacting binary systems. These return most of the envelope of their primary star to the interstellar medium during non conservative mass transfer.

Maccarone and Zurek (2012) showed that the production of a substantial amount of helium from novae triggered by accretion of ICM by isolated white dwarfs is a necessary consequence of having a large amount of gas available in a globular cluster's core well after the white dwarfs have started forming.

1.4 Clues from less studied elements

Accurate measurements of specific element abundances could provide new insight in the multiple population phenomenon.

1.4.1 n-capture elements

For a few clusters, also dispersion in neutron-capture (n-capture) elements (Z > 30) has been found. Nuclear fusion of elements heavier than iron is endothermic. As a result, most heavy nuclei are formed by addition of neutrons onto Fe-peak elements, which act as *seeds*. These nuclei can then β decay if they are unstable, transforming neutrons into protons. This process is defined as slow (rapid) if the timescale for neutron capture is slower (faster) than the radioactive decay timescale, for unstable nuclei. Generally we refer to these as the s-processes or the r-processes.

1.4.1.1 s-process elements

The s-processes are the main channel for the production of elements such as Sr, Zr, Ba and La in the Solar System. At least two distinct components are needed to fit the solar abundance distribution of the s-process nuclei, there is the *weak* s-process component, which is confined to the atomic number 29 < Z < 40, and the *main* s-process component, which is responsible for the production of the heavier nuclei with 37 < Z < 84. These two components are associated with distinct stellar sites of s-element production: the *weak* component is mainly synthesized

in massive stars (M > 13 $M_{\odot}$), while the *main* component is produced during the AGB phase of low-mass stars ($\simeq$ 1.5 – 4 $M_{\odot}$). There is a third component to the *s*-processes called the *strong* component which produces the heaviest of the *s*-process elements (e.g. Pb). It is postulated to occur in low mass, low metallicity AGB stars (Travaglio et al., 2004).

Massive stars are hence too hot to have the required efficiency to produce heavier *s*-process elements (h_s; e.g., Ba, Nd, La)[7]. In this manner massive stars can pollute the surrounding material at most with only the lightest of these *s*-process elements. However, the yields of rapidly rotating massive stars from Frischknecht et al. (2012) showed that massive, rapidly rotating stars can produce significant amount of elements up to Ba over a wide range of metallicities. This strongly processed material can then be released to the ICM through binary interactions (de Mink et al., 2012)[8].

Only in a few clusters, interestingly those where a spread in iron is also found, variations in *s*-process elements, positively correlated with the iron abundance are detected. Several authors (e.g., Norris and Da Costa, 1995; Smith et al., 2000; Johnson and Pilachowski, 2010; Marino et al., 2012a) demonstrated that, as [Fe/H] increases in ω Cen, the *s*-process dominates the enrichment of the neutron-capture elements.

Marino et al. (2009, 2011, 2012b) showed that M 22 hosts two metallicity star groups separated by a difference in the iron content of $\simeq$ 0.15 dex, each with its own Na-O anticorrelation. These two metallicity groups are characterized principally by different relative contents of *s*-process elements.

Similarly to M 22, also NGC 1851 shows *s*-process element variations correlate with Al and Na abundances (Yong and Grundahl, 2008) and also a variable CNO abundance sum, positively correlated with Na, Al, Zr, and La variations, is found among four bright RGB stars (Yong et al., 2009) (see Fig. 1.20 and Chapter 3).

Indeed, a relation between the O-Na and *s*-process effects might be expected, since thermally pulsing AGB stars are the main source of *s*-process elements (Busso et al., 1999), and such stars, albeit of somewhat higher mass, are invoked to explain the O-Na anticorrelation (Ventura and D'Antona, 2009).

Moreover, in the case of M 22 and NGC 1851, also an overabundance in the total CNO sum is observed for the same stars (Marino et al., 2012b, Yong et al., 2009 but see Villanova et al., 2010 for the constancy of this sum for NGC 1851 stars), strongly supporting the AGB scenario.

However, there might be a significant timescale problem, since only the most massive AGBs (4-8 $M_{\odot}$) and the super-AGBs (Pumo et al., 2008; Ventura et al., 2009) contribute to the enrichment/depletion in light elements, on a timescale between 40 and 160 Myr (Schaller et al., 1992). On the other hand, the timescales involved in low-mass producers of *s*-process elements are of

[7] On the other hand, the light *s*-process element (l_s; e.g., Sr, Y, Zr) abundances can be attributed to either the *main* *s*-process from AGB stars or the *weak* *s*-process (Iliadis, 2007).

[8] A possible observational test to disentangle the contribution of AGB and spin stars to the *s*-process enhancement would be to look for the scatter in the [Pb/Fe] ratio in GC stars. Low-metallicity AGB mass-transfer models (Karakas, 2010b) have quite a robust prediction for the minimum expected [Pb/Eu] ratios, but *spin* star models predict a large scatter in the [Pb/Eu] ratios. Therefore, if Pb could also be measured for stars with known abundances of Sr, Y, Zr, Ba and La, it would be possible to distinguish between the two scenarios.

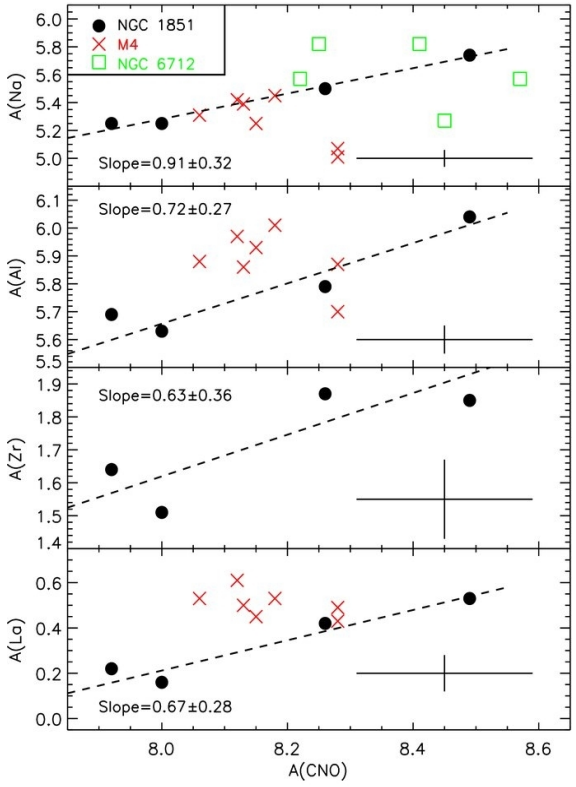

Figure 1.20: Abundances of Na, Al, Zr, and La vs. the abundance sum C+N+O. A representative error bar and a linear least-squares fit to the data (including formal slope and error) are shown (from Yong et al., 2009. Data for M 4 (Smith et al., 2005) and NGC 6712 (Yong et al., 2008b) are included for comparison.

340 Myr up to almost 2 Gyr. This implies a time delay of several 10^8 yr to be added in the phase of pollution from AGBs, which should instead run smoothly[9].

The high values of [Ba, La/Eu] at larger [Fe/H] in M 22, NGC 1851, and ω Cen contrast with the situation in the majority of other globular clusters, where the ratio typically reveals a dominant r-process contribution. Gratton et al. (2004) listed a mean [Ba, La/Eu] value of –0.23 $\pm$ 0.04 (σ = 0.21) dex for 28 clusters with [Fe/H] values between –2.4 and –0.7 dex. The one clear exception is M4, for which Ivans et al. (1999) give [Ba/Eu] = +0.25 dex, indicative of a more substantive s-process contribution to the gas from which the M4 stars formed. We note, however, that there is no evidence for any intrinsic spread in the barium abundances in M4 (Ivans et al., 1999; Marino et al., 2008).

1.4.1.2 r-process elements

In r-processes a very large number of neutrons are captured per second and element synthesis occurs far from stability in neutron-rich and very radioactive regions (see Sneden and Cowan,

[9] In this case, it is more likely that gas flows into and out of the star-forming systems are required as suggested by Bekki and Norris (2006).

2003, Cowan and Thielemann, 2004, and Arnould, 2008). Here typical r-process products are element such as Rh, Ag, Eu and Pt; although the clearest signature of stellar r-process richness is an anomalously large Eu abundance[10]. Despite more than two decades of intense study of field stars (see the review by Sneden et al., 2008), the specific astrophysical sites of r-process nucleosynthesis are unknown, though association with core-collapse supernovae (SNe) is likely based on the short timescales ($\simeq$1 s), high neutron densities ($N_n \simeq 10^{25}$ neutrons cm^{-3}) required, and appearance of r-process material in extremely metal-poor stars ([Fe/H] <–3 dex)[11]. The vast majority of Galactic globular clusters have [Eu/Fe] = +0.40 dex with relatively little cluster-to-cluster scatter (e.g., Armosky et al., 1994, James et al., 2004), a value consistent with halo field stars of comparable metallicity (Gratton et al., 2004). Generally, a lack of any variation of [Eu/Fe] with [Fe/H] is observed, that indicates that the r-process nucleosynthesis must be tightly coupled to that of iron. However, a notable exception exists: in the very metal poor GC M 15 a significant range in [Eu/Fe] abundances of the order of $\simeq$ 0.5 dex is seen at constant [Fe/H] (Sneden et al., 1997). However, the ratios of La and Eu show there are no (or insignificant) contributions from s-processes. Since chemical composition of stars in GCs are believed not to be affected by explosive events after their formation, there exists clear inhomogeneities in abundance of n-capture elements in the gases from which M 15 stars formed, while the lighter elements like Fe are essentially uniform.

1.4.2 Litium

Li abundances can provide constraints both on the nature of of polluters and the dilution between *processed* and *pristine* material (see also Sect. 1.8 for a discussion).

In all the scenarios proposed so far, the composition of stars is reproduced only by assuming dilution of the polluting material with pristine gas (see, e.g. D'Ercole et al., 2011). In the case of AGB stars, the current nucleosynthesis models indicate that the O and Na abundances are always correlated (e.g. Karakas and Lattanzio, 2007, Ventura and D'Antona, 2009, Siess, 2010). Thus, second generation stars forming from AGB ejecta would exhibit the same correlation, in evident contrast with what is observed. Also in the FRMS scenario some degree of dilution with pristine gas is needed to account for the presence of lithium in second generation stars because this fragile element is absent in the massive star ejecta (Decressin et al., 2007b; Lind et al., 2011).

As a matter of fact, some Li production is possible for AGB stars through the Cameron and Fowler (1971) mechanism at the beginning of the HBB (Ventura et al., 2002), so possibly the prediction of the two models differ.

Also for other scenarios lithium can be a sensitive discriminant: the polluting matter is Li-free also if it comes from runway collision between massive stars (Sills and Glebbeek, 2010), non-conservative evolution of massive binaries (de Mink et al., 2009), mass loss from first generation

[10] In the Solar System, $\simeq$ 97% of Eu was synthetised via the r-processes (Burris et al., 2000, and references therein).

[11] Other sites have also been proposed including colliding neutron stars (Argast et al., 2004) or black hole/neutron star mergers (Surman et al., 2008).

stars by winds (Gratton and Carretta, 2010a), and also if it is made up by the matter in non conservative evolution of interacting close binaries (Vanbeveren et al., 2012). In other words, the presence of very Li-rich stars among GC populations or the lack of correlation between Li and O (or a slope different from the unity), with the second generation stars also showing a rather high Li content, would be strongly consistent with the AGBs.

Some sets of observational data are already available. Decressin et al. (2007a) showed that the anticorrelation Li-Na in the data of NGC 6752 (Pasquini et al., 2005) is fully compatible with a simple dilution model, but Shen et al. (2010) presented new data Li-O, probably not compatible with dilution with Li-free matter. In other clusters, like NGC 6397 (Lind et al., 2011), M 4 (D'Orazi and Marino, 2010; Mucciarelli et al., 2011; Monaco et al., 2012), 47 Tuc (D'Orazi et al., 2010) the first generation and second generation stars have very similar Li content, and Li-depleted stars may be attributed to convective dilution. Generally, the similar Li abundances between the two subpopulations in these clusters seems in better agreement with the AGB scenario.

1.4.3 Fluorine

The F abundance, almost overlooked so far, may be regarded as an unique tool, because the F production is highly dependent on stellar mass.

Theoretical models of AGB stars (Jorissen et al., 1992) foresee fluorine production due to the activation of the chain of reactions ^{18}O(p,α)^{15}N(α,p)^{19}F in the He intershell during the thermal pulses associated with He burning. After the quenching of each thermal pulse the envelope may sink in mass deep in the He intershell and carry ^{19}F to the convective envelope via the TDU. The peak of F production in AGB stars is reached for stars of initial masses $\simeq$ 2 M$_\odot$ (Lugaro et al., 2004), i.e., stars that are also responsible for C+N+O and *s*-process variation. For stars with mass higher than roughly $\gtrsim$ 5 M$_\odot$ (depending on the metallicity), fluorine is destroyed both via α-captures in the He intershell, and via proton captures at the base of the convective envelope due to HBB.

As a result, we expect F abundances to be correlated with O (and Mg) and anticorrelated with those of Na (and Al). Indeed this was observationally confirmed by Smith et al. (2005) in M 4, by Yong et al. (2008b) in NGC 6712 and M 22 (D'Orazi et al., 2012)[12]. For M 22, Alves-Brito et al. (2012) did not find a significant correlation between F and other light elements. They attributed the absence of such correlations to the small sample size (7 stars) and/or the more complex chemical enrichment history of M 22. At a variance with the latter authors, D'Orazi et al. (2012) found large variations in the F abundances, which are correlated with O and anticorrelated with Na in the same cluster. Furthermore, the F-O-Na (anti) correlations can be marked separately within both *s*-process rich and *s*-process poor stars, with the *s*-process-rich group being, on average, also F-rich with respect to the *s*-poor one. The correlation between [F/H] and [La/H] suggests that the polluters responsible for the *s*-process production must account for a simultaneous F production.

[12] Cunha et al. (2003) presented F abundances for two giants in ω Cen. However, they provide a F measurement only for one star, giving an upper limit for the other.

By comparing these values with the model predictions by Lugaro et al. (2012) they found that AGB stars with masses of $\simeq$ 4-5 $M_{\odot}$ can well reproduce the observed chemical pattern.

For the sake of completeness, we recall that other sites have also been suggested for F production: the ν-process in core-collapse SNe (Woosley et al., 1990), and core He burning in Wolf-Rayet stars (Meynet and Arnould, 2000; Palacios et al., 2005). However, low-mass AGB stars are the only site observationally confirmed (Jorissen et al., 1992; Abia et al., 2010).

1.4.4 Magnesium-potassium anticorrelation

Mucciarelli et al. (2012) discovered the presence of two distinct, well-separated populations of stars in NGC 2419, differing in their magnesium and potassium contents, with the Mg-poor population significantly enriched in potassium by a factor $\simeq$10 (see also Cohen et al., 2011; Cohen and Kirby, 2012). The [Mg/Fe] distribution is also bimodal, with about 40% percent of the stars having sub-solar [Mg/Fe] abundance ratio (Mucciarelli et al., 2012).

NGC 2419 is characterized by an HB hosting a blue, faint population, clearly detached from the main component (Ripepi et al., 2007), which can be explained only by invoking a stellar component greatly enriched in helium (di Criscienzo et al., 2011, see also Sect. 1.4.5). Interestingly, the fraction of Mg-poor stars measured by Mucciarelli et al. (2012) is similar to that suggested by di Criscienzo et al. (2011) for the extreme population stars with initial helium abundance of Y $\simeq$ +0.4. According to the model by D'Ercole et al. (2008) (see also Sect. 1.5.1), these He-rich stars should be born directly from the ejecta of super-AGB and from the most massive AGB stars, with no dilution. Indeed, Ventura et al. (2012) compared the yields with observations and found that the low metallicity of the models allows a very strong HBB, especially for masses around 6 $M_{\odot}$, at the edge between the AGB and the super-AGB regime. Therefore, these ejecta are predicted to produce the most extreme contamination, with a strong depletion of oxygen, a significant reduction of the initial magnesium, and only a modest increase in sodium. The presence of a K-rich population of Mg-poor stars (Mucciarelli et al., 2012) is also a signature of extreme nucleosynthesis[13]. Magnesium depletion cannot be found in the ejecta of massive stars (Decressin et al., 2007b) or of massive binaries. On the other hand, super-AGB models with non-extreme mass loss rates (Siess, 2010) or massive AGB models with efficient convection (see Ventura et al., 2011) can predict it. If the Mg-poor stars will be found also extremely depleted in O and with normal Na, the Mg-K anticorrelation could indicate that AGB (and super-AGB) stars were at work.

1.4.5 Helium

Since He is the main product of H-burning, it is obvious that, whatever the polluters producing CN-strong and Na-rich stars are, they must provide matter that is enriched in He.

Recent photometric and spectroscopic studies have confirmed that such He variations exist (Bragaglia et al., 2010b,a; King et al., 2012; Norris, 2004; Piotto et al., 2005; Gratton et al., 2010;

[13] Potassium can be produced by proton capture on Argon nuclei if the relevant cross section is higher (by a factor of 100) than the standard rate (Ventura et al., 2012).

D'Antona et al., 2005; Dupree et al., 2011; Pasquini et al., 2011; among others), and that they might be indeed large (up to Y $\simeq$ 0.4) at least for the most extreme cases.

D'Antona et al. (2002) explained that variations in the abundance of He, which are expected to be correlated with the variations in Na and O and other elements, might result in large differences in the TO masses of stars of similar age: this is because He-rich stars evolve faster than He-poor ones and thus, at a given age, He-rich stars at TO are less massive. Therefore, similar mass losses along the RGB would lead to HB stars of very different masses, and hence colors. Similarly, Lee et al. (2005) suggested that the presence of a super-He rich population could account for the extreme HB stars observed in some GCs, which are hotter than normal HB stars.

The presence of a large enhancement in He in ω Cen can be inferred from the presence of a splitting MS in a high-precision HST- based CMD for the cluster (Norris, 2004; Bedin et al., 2004; Bellini et al., 2010; King et al., 2012). In this CMD the bluer sequence is less numerous and of higher iron abundance than the redder sequence (Piotto et al., 2005). The observations are best interpreted as indicating that the stars in the bluer sequence are enhanced in helium by ΔY $\simeq$ 0.10-0.15 relative to those in the redder sequence (Piotto et al., 2005; see also Sect 1.2). Very recently Dupree et al. (2011) have found direct evidence for an enhancement in He in ω Cen RGB stars. A perhaps more remarkable result is that multiple MS are also observed in other luminous, massive GCs without any significant heavy element abundance spread. The prime example is NGC 2808, whose CMD shows a triple main sequence (Piotto et al., 2007). Given the lack of heavy-element abundance variation in the cluster (e.g., Carretta et al., 2009c), the main sequence structure is best interpreted as indicating distinct He abundance groups, which are then likely also related to the multi-modal structure of the horizontal branch in the cluster CMD (D'Antona et al., 2005). Recently, a detailed photometric and spectroscopic study of RGB bump stars derived He abundance differences spanning a range of ΔY from 0.11 to 0.19 among the three sub-populations identified in NGC 2808 (Bragaglia et al., 2010a). A similar difference, ΔY $\simeq$ 0.15, was also proposed by D'Antona and Caloi (2008) to account for its HB morphology. This large He enhancement was actually found by Pasquini et al. (2011), who used used the He λ10830 line to estimate a helium value Y $\geqslant$0.39. Furthermore, Bragaglia et al. (2010b) found that, from X-shooter@VLT spectra of a two stars belonging to the red MS and to the blue one in NGC 2808, the first has the composition of a first generation star, while the latter show the typical chemical pattern of a second generation star (e. g., depleted in C and Mg, and enhanced in Na, N and Al).

Other clusters for which very deep and precise CMDs reveal the existence of split or broad CMDs (see Sect. 1.2.1) include 47 Tuc (Anderson et al., 2009), NGC 6752 (Milone et al., 2010), and NGC 6397 (Milone et al., 2012b). Recently, di Criscienzo et al. (2011) assembled accurate photometry from different telescopes and found that the observed F435W-F814W color spread along the RGB of NGC 2419 was significantly larger than what expected from observational errors. The observed RGB color distribution can be interpreted, together with the peculiar HB cluster morphology, by assuming that $\simeq$30% of the cluster stars belong to a second generation that is heavily enriched in He (Y $\simeq$ 0.42; di Criscienzo et al., 2011).

The He production occurs in the MS for both kinds of polluters. For FRMS the p-capture elements are also produced in the same phase, while their production is decoupled from that of He for AGB stars. In $\simeq$ 3-8 $M_{\odot}$ stars, He is brought to the convective envelope by the second dredge-up (Ventura et al., 2002; Renzini, 2008), while the light elements are produced in p-capture reactions in hot bottom burning (see Sect. 1.3.1) during the AGB phase. While FRMS are able to produce the extremely large He abundances (Y > 0.35) probably required to explain the blue MS of ω Cen and NGC 2808 (Norris, 2004; Piotto et al., 2005; D'Antona et al., 2005) it is difficult to produce Y > 0.35 with AGB stars, although values up to Y $\simeq$ 0.38 can be possibly produced by super-AGB stars (Ventura and D'Antona, 2011).

1.5 Formation scenarios for multiple populations

A quantitative investigation of the early stages of cluster formation and enrichment is necessary in order to go from a scenario to a model, which must rely as far as possible on computed models. From this point of view, very few are the models available in the literature, in spite of the large number of works recently published on this subject in the last years.

Essentially, any theoretical effort to understand the origin of these puzzling systems has to face three main issues:

(a) understand how gas from first generation of stars remains bound to the system for several 10^8 yrs despite the shallow potential well;

(b) identify the stars that process the material at $T > 10^7$ K (see previous section);

(c) explain why the observed number of first and second generation stars is approximately equal today.

1.5.1 D'Ercole et al. (2008) scenario

In the N-body hydrodynamical simulations performed by D'Ercole et al. (2008) and the first generation is 10-20 times more massive than at present. After the last core-collapse SN explosion, this polluted material collects in a cooling flow at the center of the cluster, where the second generation forms. The cooling flow is due to the low-velocity ($\simeq$10-20 km s^{-1}) stellar winds and planetary nebulae of super-AGB and massive AGB stars (Dantona et al., 1983; Thoul et al., 2002; Ventura and D'Antona, 2009; Pumo et al., 2008), and meets the physical conditions for a second epoch of star formation. Using N-body simulations, D'Ercole et al. (2008) studied the dynamical evolution of both populations, showing that if second generation stars are formed in the center of the GC, most of the stars that are lost belong to the first generation, which can result in a GC dominated by second generation stars. For their scenario, hydrodynamical simulations show that the star formation rate increases since 10 Myr (the time of the last core-collapse SN) until 40 Myr, when Type Ia SNe explosions end the star formation in the cluster. Moreover, they show that the three populations with different helium content, necessary to explain the presence of a triple main sequence in NGC 2808 (D'Antona et al., 2005; Piotto et al., 2007) can be reproduced

if the most helium rich population forms from the pure ejecta of super-AGB stars (Pumo et al., 2008), collecting in the cluster core devoid of pristine gas after the end of the SN II epoch. Afterwards, pristine gas is re-accreted and mixes with the massive AGB ejecta, giving origin to the Intermediate (following the classification by Carretta et al., 2009c,b) population having a helium content intermediate between that of the AGB and of the pristine gas.

However, D'Ercole et al. (2008) do not considered the effect of core-collapse SNe belonging to the younger population, which must stop the formation of the second generation stars after a few Myr. Valcarce and Catelan (2011) noted that every first generation star that does not explode as a core-collapse SN is a possible progenitor of a type Ia SN. The more massive the progenitor, the closest the remaining white dwarf will be to the Chandrasekhar mass (e.g., Salaris et al., 2009, Kalirai et al., 2009). Therefore, after the core-collapse SNe period, there must also be a period of type Ia SNe, which eventually halt the formation of stars with gas ejected by more massive intermediate-mass stars.

1.5.2 Bekki (2011) scenario

Bekki (2011) investigated whether and how AGB star ejecta from a fist generation of stars can be converted into new stars within originally more massive star clusters (MSCs). In this scenario MSC can be formed from high-mass, high-density giant molecular clouds (GMCs) in their host galactic building blocks embedded in dark matter haloes at high redshifts. Their 3D hydrodynamical simulations showed that nuclear MSC are found to retain much more effectively the AGB ejecta and convert more efficiently the gas into new stars (with efficiency in forming second generation stars of the order of $\simeq$0.3-0.9), only if their mass exceeds a threshold of $\simeq 10^6$ $M_{\odot}$, owing to the much deeper gravitational potential of their hosts. Additionally, capture and accretion of cold molecular gas (or small GMCs) by forming MSCs themselves can be mechanisms for mixing (i.e., dilution) of AGB ejecta with cold pristine gas. Bekki (2011) suggested that both the mass and the locations within their hosts can determine whether abundance spread can be seen only in light elements or even in heavy ones. Old, first generation stars are eventually lost, owing to tidal stripping by their host galactic building blocks.

1.5.3 Conroy and Spergel (2011) scenario

A particular model for the formation of two generations of stars within GCs was also proposed by Conroy and Spergel (2011), considering in detail the relative importance of (a) ram pressure, (b) Bondi accretion, and (c) the sweeping up of the ISM via geometric cross section, as a function of the GC total mass, relative velocity between GC and ambient ISM and density of the ambient medium. In this scenario, the cluster has an initial mass similar to the current one. The first generation stars are born in an ICM previously enriched in metals (i.e., characterized by the present-day GC metallicity), while after some Myr the remaining gas is completely expelled by core-collapse SN explosions. The GC starts then to accrete ejecta from intermediate-mass AGB stars for several $\simeq 10^8$ years. During this enrichment phase, the GC is also accreting pristine material from the ambient interstellar medium, which mixes with the AGB ejecta to form second

generation stars. The star formation process is then halted by second generation core-collapse SN and first generation type Ia SN explosions. Therefore an interesting feature of this model is that it predicts the presence or the absence of multiple populations within GCs as a function of the GC mass and its formation environment. To support their model, these authors used constraints from intermediate-age clusters in the LMC. They started from the recent analysis by Milone et al. (2009a), who analyzed – among other properties – internal age spreads for several clusters in the LMC, finding that only 5 GC out of 16 in their sample were consistent with being coeval. Conroy and Spergel (2011) found that there appears to be a critical mass below which the multiple stellar population phenomenon is suppressed: all clusters in the LMC with masses $< 10^4 M_{\odot}$ show no evidence for multiple populations, consistent with their predictions for the mass at which ram pressure stripping is capable of clearing gas from clusters in the LMC at the present epoch. As for other formation scenarios proposed so far, also this model suffers of some drawbacks. Even though the accretion of material from the ISM is plausible, it is unlikely that this accreted gas has a metallicity similar to that of the first generation. Moreover, if core-collapse SN explosions clean the ICM, they must also clean the surrounding ISM or/and increase its metallicity, implying that second generation stars will be formed with different metal abundances. As discussed by D'Ercole et al. (2011), Conroy and Spergel (2011) scenario can be easily ruled out for those few clusters with very high helium enrichment ($Y \simeq 0.38$, see Sect. 1.4.5), because such a large amount of helium cannot be released by a number of first generation stars as small as the present one (Renzini, 2008).

1.5.4 Carretta et al. (2010c) scenario

A qualitative scenario aimed to reproduce the trends of observable quantities with globular parameters was also proposed by Carretta et al. (2010c). In this scenario, GCs formed within a more massive precursor which was afterward disrupted by tidal interaction with the galaxy. First, a precursor population of stars is formed when the unborn GC (with typical size of $\simeq$100 pc, consisting of gas and dark matter) interacts strongly with other structures. Core-collapse SNe of this population enrich the remaining gas, and trigger the formation of the first generation of stars. The gas ejected by FRMS or super-AGB stars from this older population give rise to a gas in the center of the cluster, where the second generation of stars is born. Finally, second generation core-collapse SNe clean the remaining gas, thus ending star formation. During this time, the structure has lost all its dark matter content, almost all the precursor stars, and a large fraction of the primordial population. Therefore, according to this scenario, a large number of metal-poor, primordial stars must be present in the field. As stated by Valcarce and Catelan (2011), there are only 174 known stars with [Fe/H] $\leqslant$ –3 dex, and 659 stars with [Fe/H] $\leqslant$ –2 dex (SAGA database, Suda et al., 2008). Alternatively, the initial mass function (IMF) must be top-heavy at low metallicities (Skillman, 2008). In addition, the same authors noted that if the gas ejected by the precursor core-collapse SNe is retained in the initial structure, the ejecta of the primordial core-collapse SNe must also be retained, which would increase the metallicity of the second

generation stars unless the initial structure had already lost a large fraction of its mass in a short period of time.

1.5.5 Valcarce and Catelan (2011) scenario

Valcarce and Catelan (2011) proposed a toy model aimed to explain the different morphologies of GC CMDs, starting from the point that, while star-to-star abundance variations are now believed to be a universal characteristic of GC, not all of them display evidence of multiple populations in their CMDs. The main parameter at work would be the initial mass of the precursor (PS), that accounts for the different chemical pattern displayed by i) *extreme* PSs (like ω Cen, M 54, M 22 and Terzan 5), that were able to retain the gas ejected by massive stars, including the ejecta of core-collapse SNe (see Fig. 1.21); ii) *intermediate-mass* PSs can retain at least a fraction of the fast winds of massive stars, but none of the core-collapse SNe ejecta (NGC 2808,

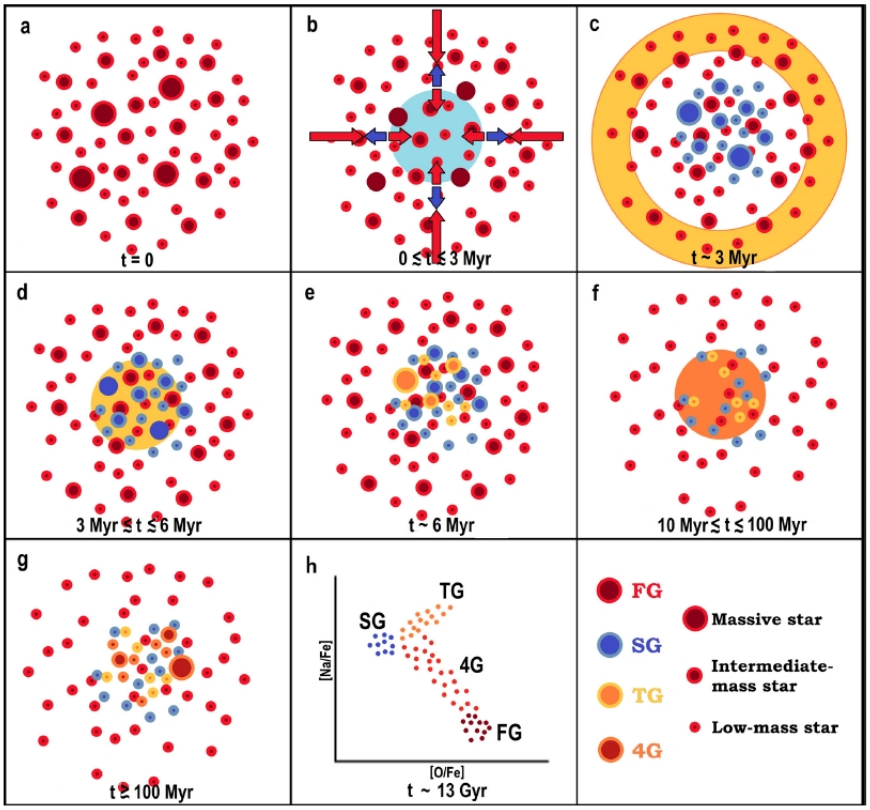

Figure 1.21: Schematic representation of the Valcarce and Catelan (2011) scenario for massive PSs. Stars of the first, second, third, and fourth generations (FG, SG, TG,and 4G; respectively) are represented as red, blue, yellow, and orange circles, respectively. Panels represent: a) formation of FG stars; b) gas accumulation, from a mix of winds of FG massive stars plus pristine gas; c) first core-collapse SN explosions, which trigger the formation of SG stars; d) gas accumulation, from a mix of FG SN ejecta, winds of FG and SG massive stars, and gas remaining from the formation of SG stars; e) formation of TG stars, when SN explosions end; f) gas accumulation, from winds of super-AGB and AGB stars from all generations; g) formation of 4G stars; h) present-day O-Na anticorrelation.

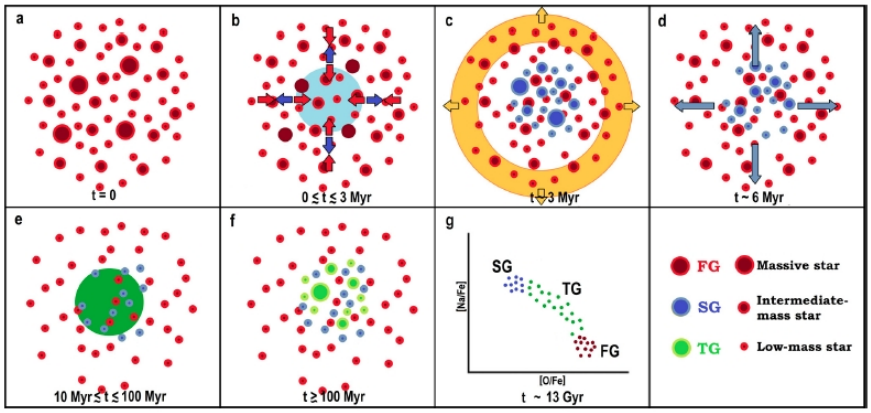

Figure 1.22: As in Fig. 1.21, but for intermediate-mass PSs (Valcarce and Catelan, 2011). Here the first, second, and third generation (FG, SG, and TG; respectively) of stars are represented in red, blue, and green, respectively. Panels represent: a) formation of FG stars; b) gas accumulation from winds of FG massive stars and pristine gas; c) first core-collapse SN explosions, which trigger the formation of SG stars and expel the gas that has not yet arrived at the core; d) FG and SG SN explosions; e) gas accumulation from winds of super-AGB and AGB stars of the FG and SG; f) formation of TG stars; g) present-day O-Na anticorrelation.

see Fig. 1.22); iii) *low-mass PSs* can only retain the slow winds of intermediate-mass stars (see Fig. 1.23).

To avoid the classical argument against the possibility of using the ejecta of massive stars because of the high velocity of their winds (from hundreds to some thousands of km s^{-1}), in their scenario they postulate that: i) GCs were (much) more massive in the past, hence had escape velocities of some hundreds of km s^{-1}, and a large percentage of first generation stars and the pristine gas were expelled by core-collapse SNe and/or SNe type Ia, and the interaction with their host galaxy; and ii) after the formation of the first generation of stars, the remaining pristine gas begins to fall to the center of the PS, interacting with massive stellar winds that try to escape the PS. An important aspect the Valcarce and Catelan (2011) scenario is that it can naturally explain the discrete nature of first generation and (especially) second generation stellar populations, as *photometrically* observed in GCs. Moreover, this scenario can also explain why the O-Na anticorrelation does not follow the same pattern for all GCs, where extreme high-Na/low-O stars are second generation stars formed with material processed by massive stars and a fraction of the pristine gas (massive and intermediate-mass PSs), while normal high-Na/low-O ones are second generation stars formed with material ejected by super-AGB or AGB stars (low-mass PSs). Subsequent generations are formed with a mixture of material from pre-existing generations, where the last stars to form are more chemically similar to first generation stars.

1.5.6 Decressin et al. (2010) scenario

Recently, N-body models whose main players are FRMS were presented (Decressin et al., 2010); taking into account the effect of primordial gas expulsion. In their model, they started from the hypothesis that primordial mass segregation holds, so that the massive stars are located

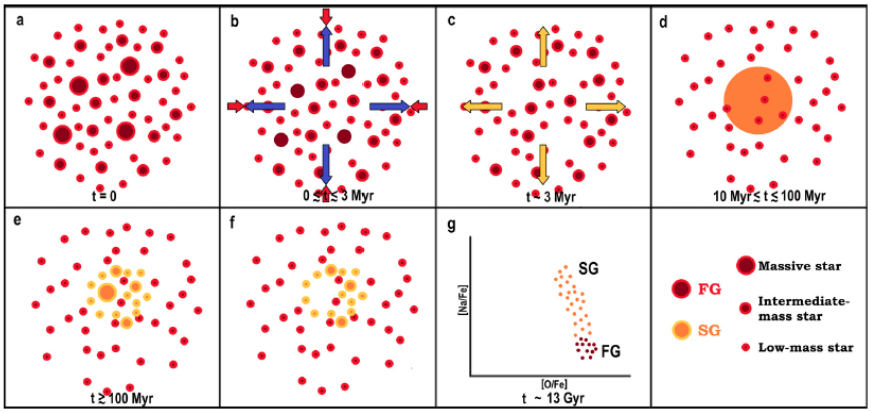

Figure 1.23: As in Fig. 1.21, but for low-mass PSs. Stars of the first and second (FG and SG; respectively) generations are represented as red and orange, respectively. Sizes indicate the different star masses, where large, medium, and small circles represent massive, intermediate-mass, and low-mass stars, respectively. Arrows show the gas flux, with the arrow color indicating the chemical composition following the same color scheme as for the stars of the different generations, and the arrow size being roughly proportional to the gas speed. Colored areas represent zones of gas accumulation. In each panel, an approximate time for these events is given. Panels represent: a) formation of FG stars; b) pristine gas expulsion due to winds of FG massive stars; c) core-collapse SN ejecta are not retained in low-mass PSs; d) gas accumulation from winds of FG super-AGB and AGB stars; e) formation of SG stars; f) SG core-collapse SNe period; g) present-day O-Na anticorrelation.

at their center. Since they expect that the formation of the second generation of low-mass stars happens locally around individual massive stars (Decressin et al., 2007b), the second generation of stars will also be initially more centrally concentrated than the first generation. As a result, (i) the loss of stars in the outer cluster parts will first reduce the number of bound first generation stars and (ii) the dynamical spread of the initially more concentrated second generation stars will stop this differential loss when the two populations are dynamically mixed. From their N-body models, presented in Decressin et al. (2008), they found that second generations stars can account for 25% of the low-mass stars present in the clusters. Compared to the observed ratios (50 to 80% in 19 globular clusters, e.g., Carretta et al., 2009b) the internal dynamical evolution and the dissolution due to the tidal forces of the host Galaxy are not efficient enough. An additional mechanism is thus needed to expel the first generation stars more effectively. Decressin et al. (2010) postulated that initial gas expulsion by SNe, operating a few million years after cluster formation at the latest, ensures a strong lowering of the potential well of the cluster so that the outer parts of the cluster can become unbound, accounting for the observed number ratio between the second to first generation stars.

1.6 Larsen et al. (2012) argument

Recently, Larsen et al. (2012) discussed the GC system in the dSph Fornax, in the context of the self-enrichment scenario. Detailed abundances suggest that Fornax GCs share the same

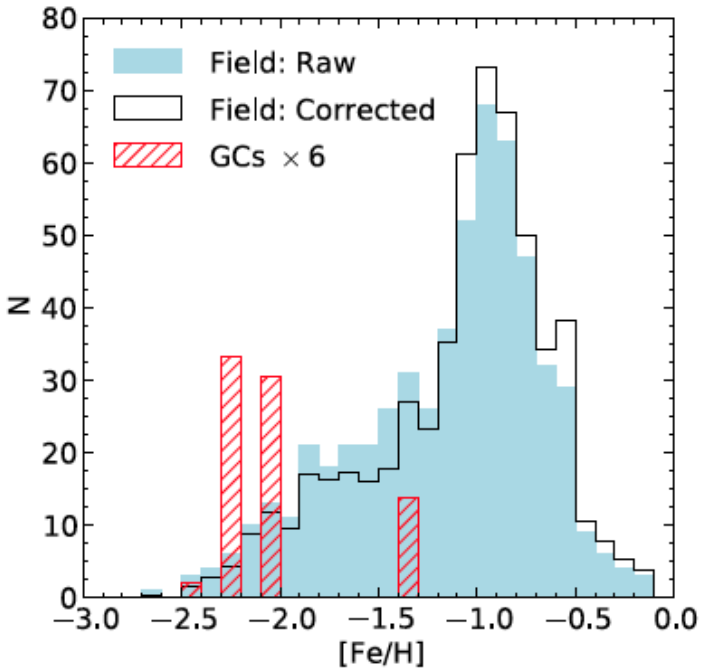

Figure 1.24: Metallicity distributions for field stars and globular clusters in the Fornax dSph from Larsen et al. (2012). The filled histogram shows the raw distribution of field star metallicities from Battaglia et al. (2006), while the outlined histogram is corrected for radial variations in the coverage (Larsen et al., 2012). The hashed histogram represents the GCs with weights scaled by their luminosities and exaggerated by a factor of 6 (note that Fornax 2 and Fornax 5 fall in the same bin).

abundance anomalies observed in Galactic GCs (Letarte et al., 2006). Four out of five clusters in Fornax are very metal-poor with [Fe/H] <–2 dex, the remaining cluster having [Fe/H] = –1.4 dex. This evidence is in clear contrast with the field star metallicity distribution which shows a broad peak around [Fe/H] $\simeq$ –1.0 dex, with only few percent of stars having [Fe/H] <–2 dex (see Fig. 1.24).

Given that, they found a very high GC specific frequency ($S_N \simeq 400$) when considering only stars and clusters with [Fe/H] <–2 dex. Larsen et al. (2012) estimated that a large fraction (1/5 – 1/4) of the most metal-poor stars ([Fe/H] <–2 dex) in Fornax belong to the four metal-poor GCs[14]. Therefore, Fornax GCs could at most have been a factor of 4-5 more massive in the past, and this is especially true for Fornax 3, the most massive cluster, whose very low metallicity places it even out in the tail of the field metallicity distribution.

The extreme ratio of metal-poor GC versus field stars in Fornax seriously challenges the self-enrichment scenario postulated for Galactic GCs, in which large fraction of first generation (up to 90-95%) stars were supposedly lost in the early stages of cluster life (D'Ercole et al., 2008; Decressin et al., 2010; Gratton et al., 2012a).

[14]For comparison with the Milky Way GC system, which has a combined mass of $\simeq 2.8 \times 10^7 M_\odot$ (Kruijssen and Portegies Zwart, 2009), or about 2% of the mass of the stellar halo if we assume for the halo a mass of $\sim 10^9 M_\odot$.

1.7 Mass budget problem

One of the main challenges for all the models proposed is to provide the large amount of ejecta needed to create a second population that is (at least) larger than the first population. The population of low-mass stars (0.1–0.8 $M_\odot$), which can still be observed today, represents 38% of the stellar mass initially present in the cluster assuming a standard Kroupa (2001) IMF between 0.1–120 $M_\odot$.

The ejecta of AGB stars with initial masses between 4 and 9 $M_\odot$ represent up to 8.9% of the initial stellar mass (assuming an initial-final mass relation by Ciotti, 1991). For spin stars this fraction is 3.4%, if one assumes that every massive star is single and born with a rotational velocity high enough to reach break-up rotation (using models by Decressin et al., 2007b). Obviously, there are not enough of these ejecta to create a second generation which is equally numerous as the first generation.

Let us consider that in a present-day GC, with a mass of $5 \times 10^5 M_\odot$, the ratio between first and second generation stars is 1:1. By assuming a reasonable value of 30% (note that typical values for AGB mass loss are $\leqslant 10\%$) for the star formation efficiency, it turns out that the generation of younger stars must have formed from $\simeq 8 \times 10^5 M_\odot$ of gas (see Martell, 2011). As a result, for a standard initial mass function (IMF), the ejecta produced by first-generation stars fall short by large factors compared to the actual mass of the second generation, even if a 100% efficiency in forming stars is postulated. Several solutions have been proposed to this *mass budget problem*:

(a) top-heavy first generation mass function (Decressin et al., 2007b),

(b) a second generation mass function truncated above 0.8 $M_\odot$ (e.g., D'Ercole et al., 2008),

(c) a fist generation with an initial mass 10 to 20 times its present mass (e.g., D'Ercole et al., 2010),

(d) infall of pristine gas (e.g., Carretta et al., 2010c; Conroy and Spergel, 2011).

1.8 Open issues

Throughout this Chapter, I tried to summarize the recent progress in the study of multiple population phenomenon. The current scenarios for GCs formation now include several populations of stars, that we may divide into a primordial, first generation and a second generation, although the second generation likely consists of several distinct sub-populations. Evidence for the presence of these different populations comes both from their chemical composition, in particular the abundances of the light elements involved in proton-capture processes (Sect. 1.1), as well as from the splitting of sequences in the CMDs (Sect 1.2). Nevertheless, it is clear, from this work and others, that we do not yet have a complete understanding of the multiple populations issue.

Here, I try to highlight a number of the largest remaining problems.

⋆ **The nature of polluters** While it has been conclusively established that the chemical anti-correlations are due to the fact that a fraction of stars in GCs formed from matter that has been polluted with the yields of a previous stellar generation, the debate about the kind of stars responsible for this pollution is still open (Sect. 1.3).

None of the current models for both AGB and FRMS are able to reproduce the exact pattern of abundances observed (Carretta et al., 2009c), and some fine tuning of the most relevant parameters (nuclear cross sections, efficiency of convection, etc.) is required (see e.g., Ventura and D'Antona, 2011 and Karakas, 2010a).

Identifying the stars responsible for the enrichment of the younger generation is needed to globally set the time scale of the whole phenomenon: the Na and O abundance variations allow us to resolve age differences of a few 10^8 yrs (in the case of AGB pollution) and as low as some 10^6 yrs (for FRMS). Hence, in the FRMS scenario there is a very narrow time gap between the end of the slow wind phase by most massive stars (about 6 Myr) and the explosion of the bulk of core-collapse supernovae (about 10 Myr after the star formation burst) when compared with the expected length of the star formation episodes. On the other hand, the age gap is often so short that AGBs do not have sufficient time to start polluting the new generation. Clearly more theoretical work and additional observations are required (see D'Orazi et al., 2012; Marino et al., 2012b; Karakas et al., 2006; Lugaro et al., 2004; Decressin et al., 2007b; Ventura and D'Antona, 2008a, 2011; D'Ercole et al., 2008, 2010; Carretta et al., 2010c; Gratton et al., 2012a, and references therein).

Insight may be reached by observing young massive clusters (see the review by Portegies Zwart et al., 2010) as proxy of early evolutionary phases in the formation of stellar clusters. A interesting starting point could be the detailed study of stellar systems that could become globular clusters in a few Gyr, such as the two young massive Galactic clusters RSGC1 (Bica et al., 2003) and RSGC2 (Stephenson, 1990). As mentioned above, we expect to resolve age differences of a few 10^8 yrs in the case of AGB and as low as some 10^6 yr for FRMS: if spreads in Na, O abundances are detected, only FRMSs can have enriched them, given their young ages (12 ± 2 and 17 ± 3 Myr, respectively, Davies et al., 2007, 2008).

⋆ **The need of dilution and the nature of diluting material.** The dilution of polluting gas with unprocessed material is necessary to reconcile the observation with theory, whatever the polluters are (Prantzos and Charbonnel, 2006; D'Ercole et al., 2011; Conroy and Spergel, 2011). Required for the FRMS scenario, the dilution is a mandatory ingredient for the AGB scenario, since the nucleosynthesis of AGB models actually predicts that Na and O correlate, at odds with all observed chemical patterns in globular clusters (see Sect. 1.4.2 for a complete discussion). Several mechanisms, neither of which devoid of drawbacks, have been proposed to gather the pristine matter required for dilution: gas left from early star formation, Bondi accretion and gas sweeping from the proto-cluster orbiting a gas-rich ancestral galaxy (Conroy and Spergel, 2011), self pollution by wind of first generation stars less massive than polluters (Gratton and Carretta, 2010b), and material collapsing back

from a torus left behind by a bi-conic, collimated gas sweeping generated by supernovae in the proto-cluster (D'Ercole et al., 2008).

⋆ **Fraction of first-to-second generation stars.** In the framework of the self-enrichment scenario, the ratio between first and second generation stars becomes a fundamental constraint to model the chemical evolution of a GC. Analysis of horizontal branch morphologies of several clusters also led to the first suggestion that the second stellar generation could account for a high fraction – from 30% to 100%– of the total number of stars (D'Antona and Caloi, 2008). The Carretta et al. (2009c,b) survey has shown evidence of multiple populations in all the clusters observed, and in all cases SG stars account for a significant fraction (50 – 80%) of the cluster mass. From their low resolution study, Pancino et al. (2010) found that the fraction of CN-strong (second-generation) stars was $\simeq$ 30-50%, distinctly lower than the 70% reported in Carretta et al. (2009c). This discrepancy is curious and future studies will need to measure the C-N and O-Na variations simultaneously in order to address the mismatch in frequency of second-generation stars found in low- versus high-resolution spectroscopic studies (see also Chapters 5 and 6).

⋆ **Globular clusters-Milky Way halo connection.** One of the main question is whether a part of the galactic field stars were formed in clusters and are now a main component of the halo. Since the composition of the second generation stars requires that they formed from the ejecta of only a fraction of the first generation stars, it may be concluded that most of their original population has been lost (see the **mass budget problem** in Sect. 1.7). In this light is even more interesting to determine the number of first-to-second generation stars (see also Chapter 6). According to a conservative estimate presented by Gratton et al. (2012a), the original proto-globular clusters should then have included > 50% of the halo mass. There is then a strong argument suggesting that the primordial stars of the current globular cluster were responsible for a large fraction, possibly the majority of the current field halo stars, although a contribution by dSph's, mainly to the outer halo, is certainly present (Helmi, 2008). Furthermore, if we consider that the total number of globular clusters per unit halo mass does not depend strongly on the magnitude or Hubble type of the host galaxy (Bekki et al., 2008) we can conclude that the massive star-formation episodes producing globular clusters played a very important role in the formation of stars in galaxies, and might have substantially contributed to the re-ionisation of the universe at $z \geqslant 6$ (Schaerer and Charbonnel, 2011).

However, the extreme ratio of metal-poor GC versus field stars in the Fornax dSph is difficult to reconcile with scenarios for self-enrichment and early evolution of GCs in which a large fraction (90%Ð95%) of the first-generation stars have been lost. It also suggests that the GCs may not have formed as part of a larger population of now disrupted clusters with an initial power-law mass distribution (see Sect. 1.6 for details on the **Larsen et al. argument**).

⋆ **Discreteness vs continuity.** The distinctly separated MSs observed for the more massive GCs (see Sect. 1.2) put serious constraints on dilution and polluters. The clear separation implies that within each sequence the matter is homogeneous within each group, both in He and in Fe. Generally, first and second generation stars are distributed smoothly in the Na-O anticorrelation (but see Marino et al., 2008 for a separation between the two stellar generations). This may indicate that the measurement errors on the abundances are not sufficiently small for this kind of analysis. On the other hand, such a bimodality in C and N enhancements has been found for a large number of clusters (see Sect. 1.1), while it is rarely found among red giants when the Na-O anticorrelations are considered. I present a critical discussion on this topic in Chapters 5 and 6.

⋆ **Construction of reliable 3-d hydrodynamical models.** Although a number of theoretical works based on the AGB scenario tried to explain the observational scenario in a self-consistent manner (e.g., Fenner et al., 2004, Bekki, 2011, D'Antona et al., 2005, Ventura and D'Antona, 2008a, D'Ercole et al., 2008, 2010, 2012, Vesperini et al., 2010, 2013), their models appear to have not yet explained all of the relevant observations on chemical abundances of the Galactic GCs in a fully self-consistent manner. Interestingly, earlier theoretical predictions stars were later confirmed by observations (i.e., systematic differences in the radial distributions of first and second generation stars, see Chapter 2).

Chemical evolution models based on the FRMS scenario have not yet been fully explored so that the validity of the FRMS scenario can not be currently assessed (but see Decressin et al., 2010). Therefore, the next step should be to investigate the secondary star formation processes within clusters by numerical simulations that can include various physical processes within clusters. Three-dimensional (3D) stellar and gas dynamical numerical simulations with a plausible model for star formation are ideal to investigate secondary star formation within clusters and can furthermore provide theoretical predictions that can be compared with the observed differences in 3D structures and kinematics between first and second generation stars (e.g., Sollima et al., 2005, Pancino et al., 2007, Bellini et al., 2009).

⋆ **Nucleosynthesis.** None of the candidate polluters can successfully reproduce the observed abundance patterns (Sect. 1.3). Additional measurements of the abundance pattern for those elements, such as He, Li, Al, and F, whose potential has not been fully exploited will be of great value (Sect. 1.4). All these will offer new insight into the light element abundance variations in globular clusters and potentially a new check on nuclear reaction rates.

1.9 Thesis layout

This thesis is structured as follows.

- ◇ First, in Chapter 2, I discuss the results derived from a photometric analysis in the context of multiple populations of a sample of nine galactic GCs from u, g, r Sloan Digital Sky Survey (SDSS) photometry.

- ◇ Chapter 3 presents the first analysis of the two populations hosted by NGC 1851 and clearly visible in its SGB split. We derived CH and CN index measurements and C and N abundances from IMACS@Magellan and FORS2@VLT spectra of faint, unevolved stars in this cluster. With these data we explored relationships between the observed SGB photometric split in this cluster and two stellar groups characterized by different contents of *s*-process elements (and perhaps iron), previously discovered by high-resolution spectroscopic studies.

- ◇ In Chapter 4 I present the results obtained applying the same method used for NGC 1851 to the poorly studied cluster M 2. We analyzed spectra of RGB stars and derived carbon and nitrogen abundances from CN and CH bands. We also studied evolutionary effects on the [C/Fe] abundance and the link between the derived abundances and the location of stars along the RGB in the $(U-V)$ color. From $U, U-V$ CMD we were able also to detect for the first time an additional RGB sequence, that can possibly be connected to the slit SGB discovered by Piotto et al. (2012). All these findings point toward a similarity of this cluster with the well studied cases of NGC 1851 and M 22 (see also Chapter 3).

- ◇ In Chapter 5, we derived C and N abundances for a moderately large sample of MS stars in three high-metallicity GCs (namely NGC 5927, NGC 6352, and NGC 6388). We obtained large (and anticorrelated) [C/Fe] and [N/Fe] variations in all clusters. However, the main result of this analysis is that the distribution of stars in the [C/Fe] vs. [N/Fe] plane appears to be bimodal, with second generation stars displaying a well extended anticorrelation. Finally, we explored the trends of this population ratio with some structural and orbital parameters of these three clusters plus two additional clusters from literature.

- ◇ in Chapter 6 I present a summary of my findings, I discuss the impact they had on the open issues discussed in Chapter 1, I present a list of future steps that would be the natural outcome of my Thesis work and I draw my conclusions.

CHAPTER

2 SDSS photometry to trace multiple populations in GCs

Nearly all GCs studied to date show evidence for multiple populations (Sect 1.1). Very recently a spectacular confirmation that the origin of the chemical anomalies must be primordial came also from properly constructed CMDs, at least for some GCs (Sect. 1.2). Variations in the light element abundances have been conclusively associated with the multiple sequences observed in the CMD, demonstrating that these two phenomena are intimately linked (Marino et al., 2008; Yong et al., 2008a; Carretta et al., 2011a; Sbordone et al., 2011; Milone et al., 2012c, among others). It is not surprising that the abundance variations should have large effects on photometry, particularly in the UV-blue bands where CN (band heads at 3883 and 4215Å), NH (around 3360Å), and CH (around 4300Å) molecular bands can be dominant (see Sect. 1.2.4 for a exhaustive discussion).

This property of medium/broad band UV photometry opens a new window to study multiple populations, as accurate U photometry for very large samples of GC stars can be obtained in a much easier way and for much more distant clusters than the mid-to-high-resolution spectroscopy needed to obtain direct chemical abundance determinations.

Wide-field photometry capable of discriminating between first and second generation stars would provide the large samples and the wide radial coverage that are needed to compare the radial distributions of the two groups, which might retain information about where they formed. According to some models of the early enrichment of GCs, at the end of the enrichment phase (supposedly lasting a few hundred Myr), stars from the first generation (P) should be significantly less concentrated toward the center of the cluster than stars of later generation(s) (I+E), born from material polluted by the ashes of P stars (e.g., D'Ercole et al., 2008; see Sect. 1.5.1). While it may be expected that this difference should have been largely erased long ago by the dynamical evolution of the cluster (D'Ercole et al., 2008; Decressin et al., 2008), the (sparse) available observational evidence about radial distributions of the two populations is in qualitative agreement with the prediction of the above quoted model. For example, Kravtsov et al. (2010b,a) found that the stars on the red side of of the broad $U-I$ distribution of the RGB of NGC 1261 and NGC 3201 are significantly more centrally concentrated than those on the blue side. In the case

of NGC 3201, Carretta et al. (2010a) used detailed Na, O abundances from high resolution spectroscopy to show that Na-rich RGB stars are redder (in $U-I$) and more centrally concentrated than Na-poor RGB stars.

Carretta et al. (2009c) merged the spectroscopic sample of RGB stars in 19 GCs, normalizing the distance of each star from the center of its cluster by the cluster r_h, and compared the radial distributions of P, I, and E stars. They found that I stars are significantly more centrally concentrated that P stars, while E stars appear slightly *less* concentrated than P stars. However, as discussed in detail by Carretta et al. (2009c), this result may be affected by serious selection biases, inherent to the process of efficient fiber allocation in multi-object spectroscopy of Galactic GC stars.

A difference in the radial distribution of the two sub giant branches of NGC 1851 (whose stars are presumed to differ in terms of CNO abundance; Cassisi et al., 2008) was detected by Zoccali et al. (2009), but the result was not fully confirmed by Milone et al. (2009b). However, Carretta et al. (2010d) find that the radial distribution of the RGB stars they analyzed depends on their iron abundance, more metal-poor stars being more centrally concentrated than their more metal-rich counterparts.

Different populations with different radial distributions are known to be present in ω Centauri (Pancino et al., 2003; Sollima et al., 2007; Villanova et al., 2007), but this system is more complex and may have a different origin with from classical GCs (see Carretta et al., 2010b, and references therein).

In this Chapter we used publicly available u[1] , g, r Sloan Digital Sky Survey photometry (SDSS; see Abazajian et al., 2009, and references therein) searching for anomalous u-g spread in the RGB of nine Galactic GCs. We confirmed the presence of multiple populations in seven of them. More interestingly, we recognized that, for these seven clusters, stars assigned to the second generation on the basis of their u-g color are more centrally concentrated than the first generation ones, as expected by theoretical models of GC formation that accounts for the presence of multiple populations (D'Ercole et al., 2008; Decressin et al., 2008).

Some preliminary results from this study were presented by M. Bellazzini at the meeting **The Giant Branches** held in Leiden in May 2009 [2].

The results presented in this Chapter have been published in Lardo et al. 2011, A&A, 525, A114.

2.1 Description of the photometric data set

An et al. (2008) reanalyzed SDSS images of the GCs and open clusters included in the survey using the DAOPHOT/ALLFRAME suite of programs (Stetson, 1987, 1994). These programs are

[1] The SDSS u filter has $\lambda_{eff} = 3521$ Å and $FWHM = 555$ Å. For details about the photometric filters quoted in this paper see the Asiago Database of Photometric Systems `http://ulisse.pd.astro.it/Astro/ADPS/` (Moro and Munari, 2000).

[2] `www.lorentzcenter.nl/lc/web/2009/324/Friday/Bellazini.ppt`

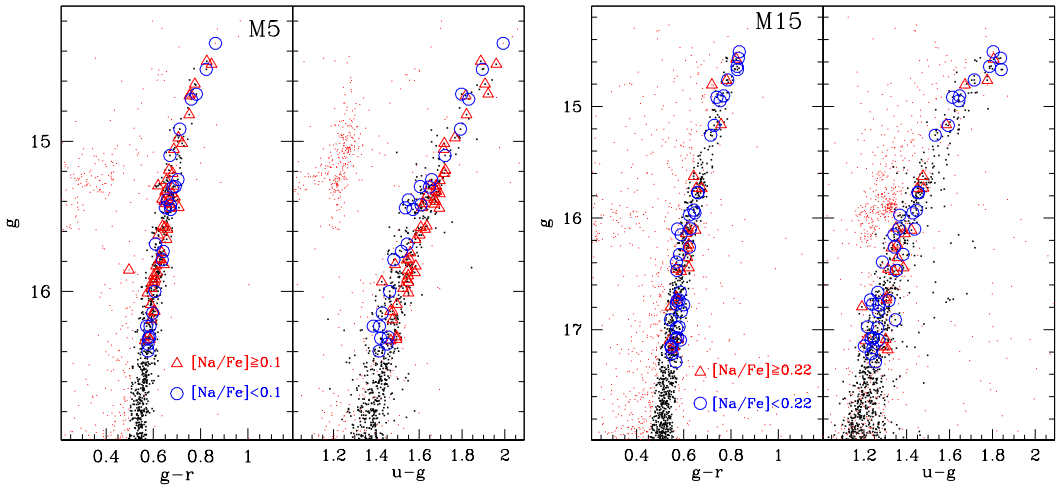

Figure 2.1: *g*,*g*-*r* and *g*,*u*-*g* CMDs for M 5 and M 15. The stars for which spectroscopic abundances are available from from Carretta et al. (2009b,c) are marked according to their Na abundances: Na-poor stars are marked as blue open circles, while Na-rich stars are marked with red open triangles. Stars plotted as heavy dark dots are those selected as candidate RGB stars from the *g*,*g*-*r* CMD.

known to perform more effectively than the survey photometric pipeline in the high-crowding conditions typical of dense star clusters.

We limited our analysis to the most favorable cases, excluding clusters with $|b| \leqslant 20°$– to avoid strong contamination from Galactic field stars – and/or with $E(B-V) \geqslant 0.15$ - i.e., clusters with relatively high extinction. Moreover, we decided to include in our sample only clusters with more than 100 candidate RGB stars between the HB and two magnitudes below this level, to ensure a solid statistic basis to our analysis. According to these criteria, among the seventeen clusters considered by An et al. (2008) we selected the nine GCs listed in Table 2.1.

Only stars with valid magnitude estimates in both g and r have been retained for subsequent analysis. When An et al. (2008) provided more that one catalog per cluster (i.e., in cases of clusters imaged in different overlapping SDSS "plates", see Abazajian et al., 2009, An et al., 2008, and references therein), we merged the catalogs into a single one including all the cluster stars listed by An et al. (2008) without duplications. The final catalogs cover fields including the vast majority of cluster stars but does not reach the tidal radius (except for NGC 2419, see below).

In some cases, the available photometry was highly incomplete and/or was characterized by large uncertainties in the innermost regions of the cluster, because of the high degree of crowding. In most cases the final catalog also covered a field of view including regions where the contamination from Galactic stars was not negligible. To avoid the inclusion of cluster stars with poor-quality photometry and contamination from fore/background Galactic stars, we limited the analysis to a radial corona between the r_{in} and r_{out} values specified in Table 2.1. In this table, r_{in} and r_{out} are also expressed in units of core, half-light, and tidal radii (r_c, r_h, and r_t,

Table 2.1: Globular cluster sample

NGC	Alt. Name	r_{in} arcmin	r_{out} arcmin	r_{in}/r_c	r_{in}/r_h	r_{out}/r_h	r_{out}/r_t	E(B–V)	[Fe/H]
2419		0.0	7.0	0.0	0.0	7.3	1.0	0.11	–2.12
5024	M 53	1.0	7.0	2.8	0.9	6.3	0.3	0.02	–1.99
5272	M 3	0.0	10.0	0.0	0.0	8.9	0.3	0.01	–1.57
5466		0.0	10.0	0.0	0.0	4.4	0.3	0.00	–2.22
5904	M 5	0.0	10.0	0.0	0.0	4.7	0.3	0.03	–1.34
6205	M 13	1.0	10.0	1.3	0.7	6.7	0.4	0.02	–1.54
6341	M 92	0.0	10.0	0.0	0.0	9.2	0.7	0.02	–2.28
7078	M 15	0.0	10.0	0.0	0.0	9.4	0.5	0.10	–2.32
7089	M 2	1.0	10.0	2.9	1.1	10.7	0.5	0.06	–1.62

Global parameters are from the Harris (1996) on-line database (year 2003), except for [Fe/H] for both M 5 and M 15, which are taken from Carretta et al. (2009b), and structural parameters for NGC 2419 that are taken from Bellazzini (2007).

respectively), to provide a more objective idea of the actual radial sampling and of the cluster-to-cluster differences in the radial sampling. We note that: (a) in all the considered cases we sample the clusters out to $> 4\ r_h$, and in most cases out to $6-10\ r_h$; (b) in the cases in which we excluded the innermost $1'$ from the analysis, the innermost regions between $\sim 1-3\ r_c$ were lost, the completeness in these inner parts possibly being remarkably low also in clusters for which we retained the central region[3]; and (c) the considered clusters span a wide range of central density (more than 4 orders of magnitude, see Harris, 1996), hence the different radial ranges also sample regions in widely different dynamical conditions, depending on the considered cluster.

The reddening for the GCs are taken from Harris (1996). The coefficients of the adopted extinction laws (A_λ/A_V) are taken from the computations by Girardi et al. (2004) for cool giants (T_{eff} = 4000, log g = 2.00 and [M/H]= –2), and assuming $A_V = 3.1\ E(B-V)$. In particular: $A_u = 4.84\ E(B-V)$, $A_g = 3.64\ E(B-V)$, and $A_r = 2.71\ E(B-V)$, and $E(u-g) = 1.20\ E(B-V)$ and $E(g-r) = 0.93\ E(B-V)$.

2.1.1 The correlation between Na abundances and *u-g* spreads along the RGB

For two of the selected clusters, M 5 and M 15, we found a significant sample of stars for which there are spectroscopic Na abundances over a remarkably wide luminosity range along the RGB, from Carretta et al. (2009b,c). Following the criteria used by these authors, we divide the RGB stars between a candidate first generation and a candidate second generation (P and I+E components, respectively, adopting their nomenclature[4]) by adopting a threshold in sodium abundance that depends on the cluster metallicity. In particular, stars having [Na/Fe]$_{min} \leqslant$ [Na/Fe]$<$ [Na/Fe]$_{min}$ +0.3 dex are assigned to the Na-poor P component, while stars having [Na/Fe] $\geqslant$ [Na/Fe]$_{min}$ +0.3 dex are assigned to the Na-rich I+E component (see Carretta et al., 2009c, for

[3] This should not affect the results presented below, as in all the cases we compare RGB stars having the same distribution in magnitude, see Sect. 2.2.1.

[4] P stands for the first - *Primordial* - generation (Na-poor stars), while Na-rich stars are divided into I (*Intermediate*) and E (*Extreme*) subsequent generations. For homogeneity, we follow the nomenclature by Carretta et al. but we always consider all Na-rich stars as a single class (I+E), for simplicity.

further details). The resulting thresholds are [Na/Fe]= +0.10 dex for M 5 and [Na/Fe]= +0.22 dex for M 15; we stress, however, that the results presented below are not particularly sensitive to the adopted threshold.

The left-hand panel of Fig. 2.1 shows that, in the case of M 5, *the Na-poor and Na-rich stars, that are tightly aligned along the narrow cluster RGB in the g, g-r CMD, are clearly separated into two parallel sequences in the much broader giant branch seen in the g, u-g diagram, the Na-rich stars appearing systematically redder than Na-poor ones* (at least below the HB level), a behavior strictly analogous to that observed by Marino et al. (2008) in M 4, by Milone et al. (2010) in NGC 6752, using *U* photometry, and by Carretta et al. (2009c), again in NGC 6752, but using Strömgren *u* photometry.

This result clearly indicates that SDSS *u* photometry can also be used to trace the UV color spread correlated with the light-element abundance spread described in Sect. 1.2.4. We note that most of the RGB stars displaying the color segregation as a function of Na abundance *are fainter than the RGB bump* (at $g \simeq 15.4$, see Fig. 2.2 and Fig. 2.3, below), as expected if the observed chemical anomalies are not due to extra-mixing phenomena known to occur in evolutionary phases brighter than this feature (Gratton et al., 2000; Smith and Martell, 2003).

However, the clear *u-g* color segregation between Na-poor and Na-rich stars observed in M 5 is not seen in M 15 (right-hand panel of Fig. 2.1). A likely explanation of this different behavior calls into play the difference in overall metal content between the two clusters. The iron abundance in M 5 is ten times higher than in M 15 and the average abundance of the light elements should scale similarly. Hence, the same degree of N abundance with respect to iron (as expressed by [N/Fe]) corresponds to very different absolute abundances of N ([N/H]). This, in turn, should correspond to significant differences in the strength of the absorption features that are supposed to drive the spreads observed in broad-band near-ultraviolet photometry (see also Martell et al., 2008). In particular, the strengths of spectral lines of diatomic molecules (such as CN, NH) depend quadratically on the overall metallicity and it has been noted that CN bands become very weak in the spectra of GC giants for [Fe/H] $\leqslant$ –1.8 (Smith, 2002). In this context, we note that the clusters for which the color spread in the RGB has been detected using the broad *U* (or *u*, in the present case) filter and correlated with spectroscopic light-element abundances, have intermediate metallicities, i.e. [Fe/H]= –1.34 for M 5, [Fe/H]= –1.17 for M 4, [Fe/H]= –1.51 for NGC 3201, [Fe/H]= –1.55 for NGC 6752 (metallicities from Carretta et al., 2009c), and [Fe/H]= –1.18 for NGC 1851, (metallicity from Carretta et al., 2010d).

On the other hand, we need also consider that the RGBs of M 5 and M 15 seem to display similar spreads in the (V, c_y) plane (Yong et al., 2008a), thus not supporting the above hypothesis. It is difficult to draw a firm conclusion at the present stage and this kind of investigation is clearly beyond the scope of the present work. However, we note that a stark discrepancy exists also when comparing the fraction of CN-strong and Na-rich stars (Pancino et al., 2010; Carretta et al., 2009c). This is quite curious, and Pancino et al. (2010) suggests that C and N abundance variations are contributed, at lest in part, by a different feedback source from the Na-O anticorrelation studied by Carretta et al. (2009c). For our present purposes, we take as the basis of the

further analysis of the clusters in our sample the clear evidence that, at least in some cases, star-to-star differences in light-element abundances in the RGB of GCs can be discerned with the $u-g$ color.

In particular, the sought-after anomaly should be distinguishable as a significant color spread in the RGB in the *g, u-g* CMD, not seen in the *g, g-r* CMD and unaccounted for by other effects, such as an increase in the photometric error and/or an increase in the amplitude of the effect of differential extinction (see Sect. 2.2). Independently of its true origin, we refer in the following section to the observational effect under consideration as a UV-spread and we will look for its presence in the clusters of our sample, trying to establish, in the various cases, whether it is (at least partially) due to intrinsic star-to-star physical differences or it can be fully accounted for by trivial effects.

2.2 Introducing a method to detect anomalous u-g spreads

In Fig. 2.2 and Fig. 2.3, we present the *g, g-r* CMDs, flanked by their *g, u-g* counterparts for all the clusters listed in Table 2.1. In all cases, two horizontal segments enclose the magnitude range to which we limit our analysis of the color spread: we tried to select similar portions of the RGB in all clusters, spanning a wide region below the horizontal branch. Given the different distances and reddenings of the various clusters, this was not always possible (in particular, for NGC 2419 which is far more distant than the other GCs in our sample). This gives rise to differences in the sensitivity of the adopted method as (a) the color spread corresponding to a given abundance spread is always observed to decrease with increasing luminosity along the RGB, virtually disappearing at the RGB tip (Yong et al., 2008a; Marino et al., 2008; Milone et al., 2010), and (b) the same portion of the RGB occurs at different apparent magnitudes in different clusters, which is indicative of different distance, and causes a different photometric accuracy.

The line located approximately at the red edge of the RGB, within the two horizontal segments, is a ridge line following the curvature of the observed RGB, and is taken as a reference to compute the color spreads, that is the difference between the color of a given star and the color of the ridge line at the same magnitude, Δ_{col}, where $col = g-r$ or $col = u-g$. Both Δ_{g-r} and Δ_{u-g} are computed only for stars selected as candidate RGB in the $g, g-r$ CMDs (heavier dots in Fig. 2.2 and Fig. 2.3). To limit the effects of possible spurious $u-g$ outliers, we considered only stars for which $-0.2 \leqslant \Delta_{u-g} \leqslant 0.05$; these limits were found to be appropriate for all clusters except NGC 2419 for which we adopted $-0.8 \leqslant \Delta_{u-g} \leqslant 0.05$.

There are several cases in Fig. 2.2 and Fig. 2.3 in which a conspicuous broadening of the RGB in *u-g* with respect to *g-r* is apparent. However, as anticipated above, a few factors unrelated to physical differences among cluster stars may also (in principle) produce this effect. These factors and the methods we adopted to keep their effect under control can be summarized as follows:

Field contamination. The degree of contamination by Galactic fore/background stars is very modest, because of the combination between the relatively high (absolute) Galactic latitude of the considered clusters (all have $|b| > 25°$and four $|b| > 70°$) and the relatively

small area of the considered annular fields. We used the Galactic model TRILEGAL (Girardi et al., 2005) to obtain a conservative estimate of the degree of contamination affecting the samples of candidate RGB stars considered in the present analysis (see Fig. 2.2 and Fig. 2.3). We found that the fraction of Galactic field stars in our samples is lower than 5% for seven of the nine clusters, reaching 8% for M 15 and 10% for M 92. Moreover, the effect of even this small degree of contamination should be minimized by the way in which we selected candidate RGB stars. In the following, we analyze the color spreads of candidate RGB stars selected in the *g*, *g–r* CMD as the most tightly clustered along the narrow RGB sequence

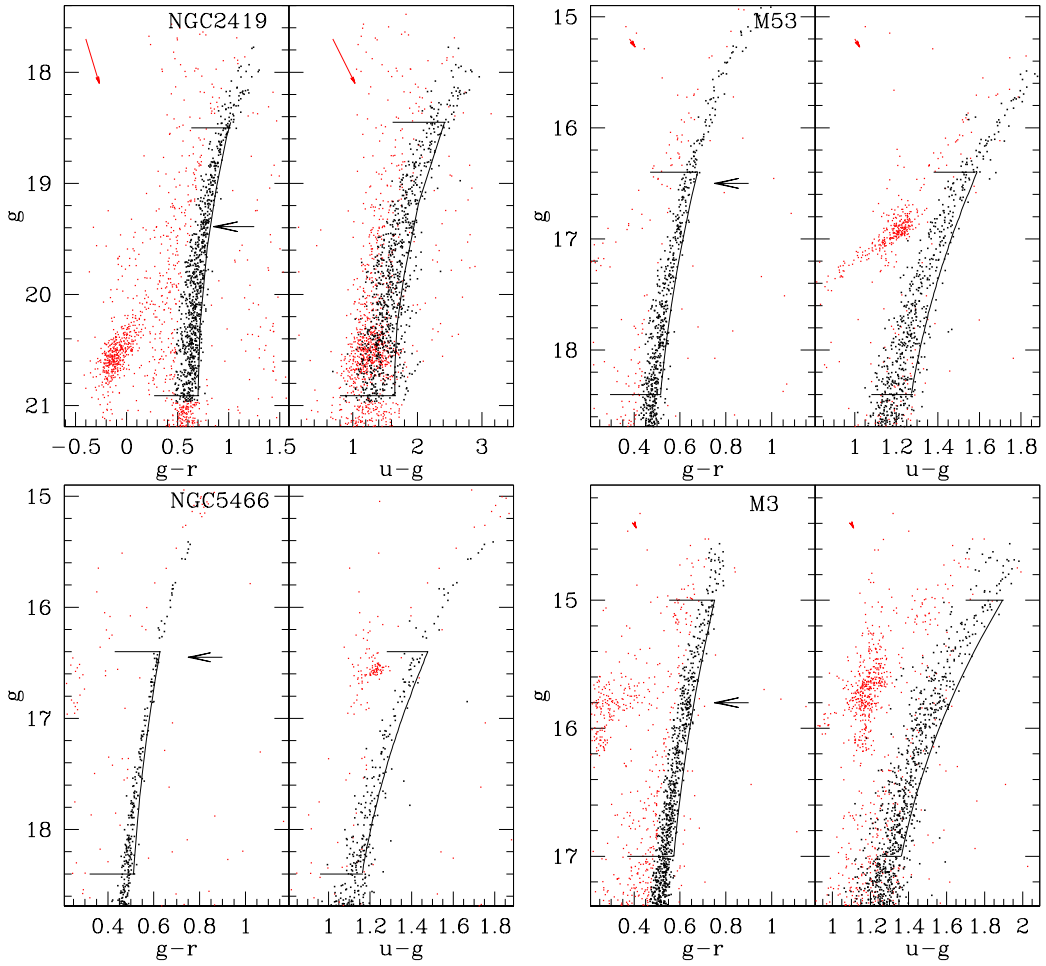

Figure 2.2: *g*, *g–r* and *g*, *u–g* CMDs for NGC 2419, M 53, NGC 5466 and M 3. In some cases, the RGB is truncated due to SDSS saturation. The red arrows in the upper right corner of each panel are the reddening vectors whose amplitudes correspond to the average $E(B-V)$ values reported in Table 2.1. Horizontal black arrows mark the position of the RGB bump. Stars selected as candidate RGB on the *g*, *g–r* CMDs are plotted as heavy dark dots, the remaining ones as lighter red dots. The curves approximately tracing the red edges of the RGBs are used as references to compute the color spread distributions shown in Fig. 2.4; the the two horizontal segments display the portion of the RGB that is used to compute those distributions. In most cases, note that the asymptotic giant branch starts above the bright end of the adopted selection box (NGC 2419 is an obvious exception).

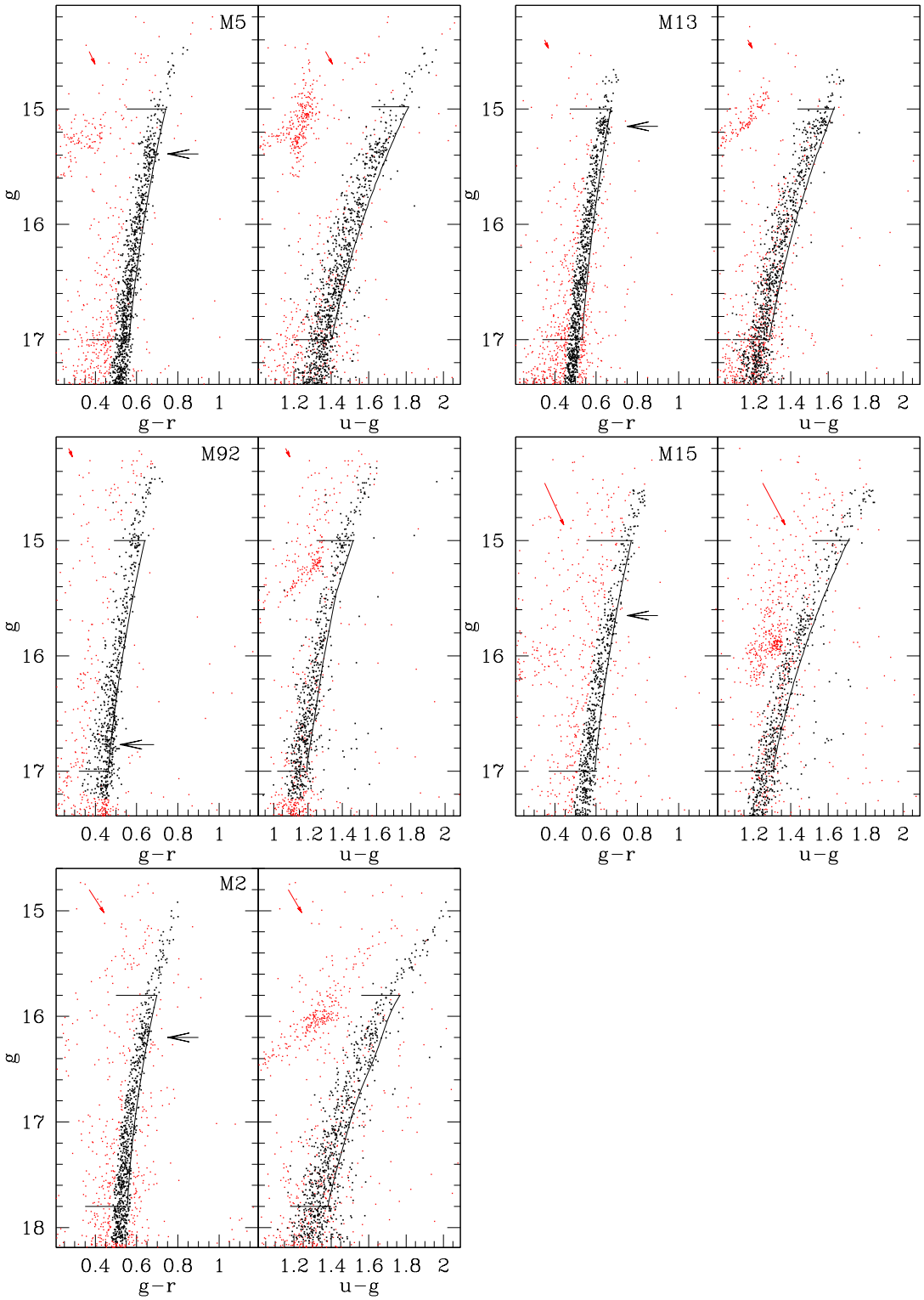

Figure 2.3: The same as in Fig. 2.2, but for M 5, M 13, M 92, M 15 and M 2.

in this plane (heavy dark dots in Fig. 2.2 and Fig. 2.3. This means that we compare the *g*–*r* and *u*–*g* color spreads produced by *exactly the same stars*. Hence, any field star artificially broadening the distribution of Δ_{col} in *u*–*g* should also have a similar effect on *g*–*r*.

Blendings and artifacts. Any photometry of crowded fields (especially ground-based seeing-limited ones) is expected to include some fraction of sources that are either blends of two (or more) fainter stars, or non-stellar sources, such as unresolved distant galaxies or flukes in the halo of bright stars, both misclassified as stars. While it is likely that our samples of RGB candidates include some of these sources, their effect is expected to broaden the distribution of Δ_{col} by a similar amount in both of the considered colors, given the adopted selection, as for the case of contamination described above.

Differential reddening. In principle, if there is a star-to-star difference in the degree of stellar extinction (due to spatial a variation in the reddening over the considered field of view) this will produce a larger color spread in *u*–*g* than in *g*–*r*, mimicking the effect we are looking for. However, the ratio of the expected spreads is quite small $\frac{\Delta E(u-g)}{\Delta E(g-r)} = 1.29$, meaning that a difference of 0.02 mag in $E(B-V)$ would correspond to 0.019 in $E(g-r)$ and 0.024 in $E(u-g)$, i.e. a mere difference of 5 millimag between *g*–*r* and *u*–*g*. The clusters considered here have, in general, low average reddening values (four having $E(B-V) \leqslant 0.02$, seven $E(B-V) \leqslant 0.06$, and all nine $E(B-V) \leqslant 0.11$) and, as far as we know, no indication of differential reddening has ever been reported in the literature. In the cases for which we report the detection of significant *u*–*g* spread, the full width at half maximum (FWHM) of the distribution spread in *u*–*g* is $\geqslant 2$ times larger than in *g*–*r*, more than the factor of 1.29 that can be attributable to differential reddening alone. Finally, the case of M 5 presented here as well as the previous cases reported in the literature (see Sect. 2.1.1) suggests that differential reddening does not play a major role in producing the UV-spread, in the cases where this has been revealed up to now. We conclude that the effects of differential reddening for the considered sample should be negligible.

Photometric errors. Since all the SDSS observations are performed at fixed exposure time and RGB stars emit much less light in the near-UV than in the visible range[5], any given star in our sample has larger photometric errors in *u* than in either *g* or *r*: as a consequence, the color spread due to photometric errors is larger in *u*–*g* than in *g*–*r*. We see below that this is the most serious problem in the present analysis, as there are cases in which a large observed UV-spread can be fully accounted for by (relatively) large photometric errors which hide any (possible) underlying signal associated to real differences among stars. To take this effect into due account, we divided the color spread of each star by the associated photometric uncertainty in each color $\Delta'_{col} = \frac{\Delta_{col}}{\sigma_{col}}$ (*normalized color spread*), which should

[5]There are other factors concurring to lower the signal-to-noise ratio of *u* observations with respect to *g* or *r* ones. For example: (1) CCDs are less sensitive in near-UV than in visible bands; (2) as in the SDSS the photometry of a given field is taken simultaneously in all the $ugriz$ passbands and the seeing worsens at shorter wavelengths, *u* images hence experiencing the worst seeing; (3) at fixed atmospheric transparency conditions and air mass, *u* light suffers from the highest amount of atmospheric extinction.

be (approximately) expressed in units of standard deviations. Comparing Δ'_{col} distributions in *g–r* and *u–g*, we can check whether there is any significant *UV*-spread in addition to that due to photometric errors; if the latter were the main contributor to the observed *u–g* spread, the two distributions should be indistinguishable.

In Fig. 2.4, we plot the distribution of Δ_{col} and Δ'_{col} for all the considered clusters. Histograms in *g–r* are plotted as dotted lines, and those in *u–g* as continuous lines. The Δ'_{col} distributions have been shifted by (small) arbitrary amounts to ensure that their maxima approximately coincide with $\Delta'_{col} = 0$, to allow for a more direct comparison between the distributions in the two color indices[6]. We shall see below that the significance of the detected differences is maintained independently of the adopted shifts.

It may be useful to start the discussion of Fig. 2.4 from the pair of panels in the lower right corner (NGC 2419). As readily visible in the CMD of Fig. 2.2 and Fig. 2.3 there is an impressive broadening of the RGB color spread passing from *g–r* to *u–g* in this case. The broadening in *u–g* color is so large that we had to adopt a different horizontal scale in this panel to accommodate the bulk of the Δ_{u-g} distribution. However, the distributions of Δ'_{col} are indistinguishable, with essentially all the stars lying within $\pm 3\sigma$ of the mean, as expected for (approximately) normal errors[7]. Hence, all the *UV*-spread observed in NGC 2419 can be accounted for by the effect of photometric errors. We note that *this does not mean that there is no underlying spread in light-element abundance, but that the photometric accuracy is not sufficient to reveal it, if it exists.* The same is true for NGC 5466, while the case of M 15 is discussed in more detail below.

On the other hand, in all the cases considered in the left raster of panels pairs of Fig. 2.4 (M 5, M 53, M 13, M 3, and M 2), plus M 92 in the right raster of panels, the differences in the Δ_{col} distributions correspond to significant differences in the distributions of Δ'_{col}, implying that the detected *UV*-spread cannot be entirely accounted for by observational effects, thus requiring the presence of some physical star-to-star difference. In particular, the Δ'_{u-g} distributions display extended tails toward the blue that are completely lacking in the remarkably symmetric $g-r$ distributions. In the case of M 5, we know from Sect. 2.1 that the observed *u–g* spread correlates with Na abundances (and it is likely to be caused by differences in N abundances, Yong et al., 2008a). It is interesting to note that the Δ_{u-g} distribution of this cluster appears to be bimodal (as in the case of M 4 Marino et al., 2008), even if it is not possible to firmly establish the statistical significance of this feature. Hints of multi-modality are indeed visible in all the Δ_{u-g} (and Δ'_{u-g}) distributions of these six clusters.

A Kolmogorov-Smirnov (KS) test would be the most straightforward non-parametric way to quantitatively establish the statistical significance of the detected differences between the *u-g* and *g-r* Δ'_{col} distributions. However, it is well known that this test is very sensitive to offsets between distributions and the shifts adopted in Fig. 2.4 are quite arbitrary. In principle, a given

[6] In particular, the *g–r* distribution has been shifted to ensure that its well defined maximum occurs at $\Delta'_{col} = 0$, while for the broader *u–g* distributions, with less clear peaks, we searched for a compromise between placing the peak at $\Delta'_{col} = 0$ and matching the right (red) edge of the two distributions, to make the comparison easier.

[7] We note that this is true for all the *g-r* distributions of Δ'_{col}.

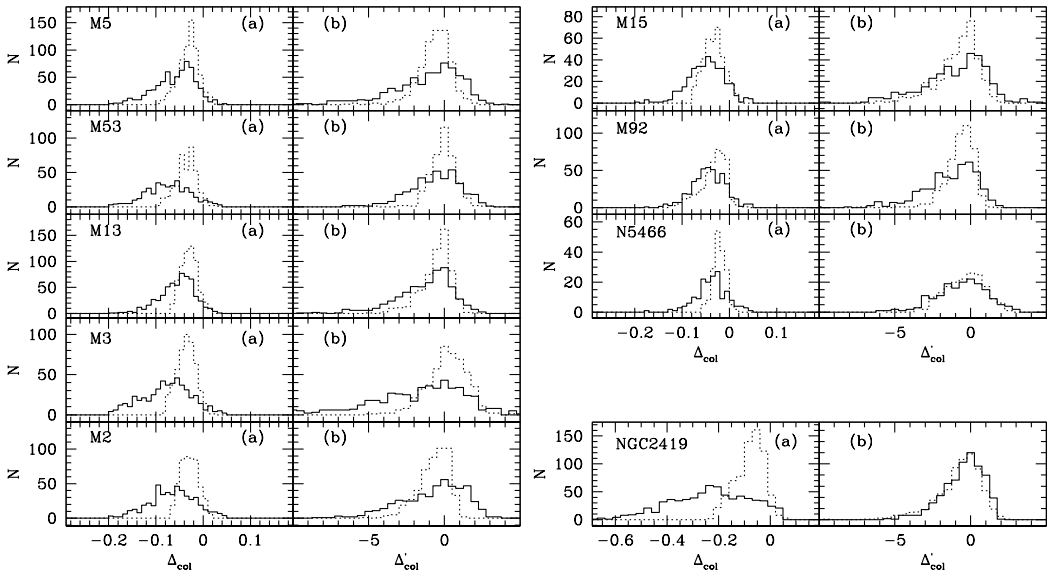

Figure 2.4: Distributions of $u-g$ (solid histograms) and $g-r$ (dashed histograms) color spreads (with respect to the RGB fiducials of Fig. 2.2 and Fig. 2.3) for the clusters in our sample. Panels marked with (a) show the distributions of absolute color spreads, while those marked with (b) show the *normalized* color spreads, in units of σ.

Table 2.2: Dimensions of the samples and results of KS tests.

NGC	N_{stars}	Shift	P_{KS}^{phot}	$N_{UV-blue}$	N_{UV-red}	P_{KS}^{rad}
M 5	652	0.2	1.1×10^{-11}	199	453	2.0×10^{-6}
M 2	492	–0.3	6.0×10^{-10}	132	360	$<1.0\times10^{-11}$
M 3	501	1.5	3.9×10^{-10}	206	295	3.8×10^{-10}
M 13	596	0.4	5.7×10^{-8}	185	411	1.3×10^{-4}
M 92	442	0.4	3.8×10^{-7}	139	303	$<1.0\times10^{-11}$
M 53	394	0.4	2.9×10^{-7}	75	319	5.7×10^{-11}
M 15	371	0	8.9×10^{-4}	110	261	7.8×10^{-11}
NGC 5466	172	0.2	0.60	37	135	0.15
NGC 2419	693	–0.2	0.79	94	599	0.24

N_{stars}: total number of candidate RGB stars selected for the analysis of color spread. "Shift" is the differential shift in Δ'_{col} that is found to maximize P_{KS}^{phot}. $N_{UV-blue}$ and N_{UV-red} are the number of stars having $\Delta'_{col}<2.0$ and $\Delta'_{col}\geqslant 2.0$, respectively. P_{KS}^{phot} and P_{KS}^{rad} are defined in the text. Clusters are listed in order of increasing P_{KS}^{phot}.

choice of the shift between the two distribution may add spurious significance to their mutual difference measured by the KS test. To circumvent this problem, we proceeded as follows:

(1) keeping the *g*–*r* distributions shown in Fig. 2.4 fixed, we moved the *u*–*g* distribution from −5 to +5 Δ'_{col} units in steps of 0.1;

(2) at each step, we performed the KS test computing the probability that the two samples are drawn from the same parent population, P_{KS}^{phot}; and,

(3) we adopted the value of the shift that *maximize* P_{KS}^{phot}, i.e. the shift that *minimize* the significance of the difference between the two distributions.

In this way, we are guaranteed that the residual differences considered by the KS test are genuine differences *in the shape of the distributions*, not due to unphysical shifts. The adopted differential shifts and the corresponding values of P_{KS}^{phot} are reported in Table 2.2. The significance of the difference in the *u*–*g* and *g*–*r* distributions of Δ'_{col} is very high for all the clusters whose distributions are plotted in the left hand panels of Fig. 2.4 plus M 92 ($P_{KS}^{phot} < 10^{-4}$). In particular, we note that the difference is also significant in the case of M 15: the probability that the *u*–*g* and *g*–*r* distributions of Δ'_{col} measured in this cluster are drawn from the same parent population is just 0.08%. A careful inspection of the Δ'_{col} distributions for this cluster in Fig. 2.4 reveals that while the wings virtually coincide, the core of the *g*-*r* distribution is far more peaked than its *u*-*g* counterpart, which exhibits hints of bimodality (compare with the cases of NGC 5466 and NGC 2419, where the distributions nearly coincide in both the wings *and* the core). Hence, while the amplitude of the effect is insufficient to provide an obvious color segregation in the CMD of this cluster (see Fig. 2.1), the underlying signal is there and can be revealed once the much larger photometric sample is considered and the observational effects are properly taken into account, in agreement with the results of Yong et al. (2008a). This conclusion is strongly supported by the behavior of the radial distributions of RGB stars as a function of their color spread in this cluster, as discussed in the following section.

We note that the four clusters displaying the most obvious and significant difference in their Δ'_{u-g} and Δ'_{g-r} distributions have metallicity around [Fe/H]= −1.5, while M 53, M 92, and M 15, which have larger P_{KS}^{phot}, are significantly more metal-poor ([Fe/H]$\leqslant -2.0$). This is likely due to the weakening of the intrinsic *UV*-spread effect at low metallicity, discussed in Sect. 2.1.1.

2.2.1 The radial distribution of UV-red and UV-blue stars

As anticipated above, it would be very interesting to verify whether RGB stars with different $u-g$ colors (at the same magnitude) may have different radial distributions. Indeed, one way to understand how the multiple populations may have originated is to study the spatial distributions of the different populations, which might retain information about where they formed. In particular, theoreticians have been finding that if the second generation of stars is formed from an interstellar medium polluted and shocked by the winds of the first generation, then we would

expect that the second generation would be more concentrated towards the center of the cluster than the first one (see D'Ercole et al., 2008, Decressin et al., 2008).

To follow up this line of investigation, we divided the selected RGB candidates in each of the considered clusters into two sub-samples, according to the value of their normalized u–g spread Δ'_{col}. For brevity, we dub UV-blue the stars having $\Delta'_{col} < -2.0$ and UV-red those having $\Delta'_{col} \geqslant -2.0$, in the scale of Fig. 2.4 (i.e. using the shifts adopted there). It is important to recall that any observational effect potentially affecting the radial distributions (notably, the radial variation in the degree of completeness, due to the increase in crowding toward the center) must affect the two sub-samples exactly in the same way, as they have the same distribution of magnitudes.

The comparison between the radial distributions of UV-blue and UV-red RGB stars for all the considered clusters is presented in Fig. 2.5; the probability that the two distributions are drawn from the same parent population according to a KS test (P^{rad}_{KS}) is reported in the last col-

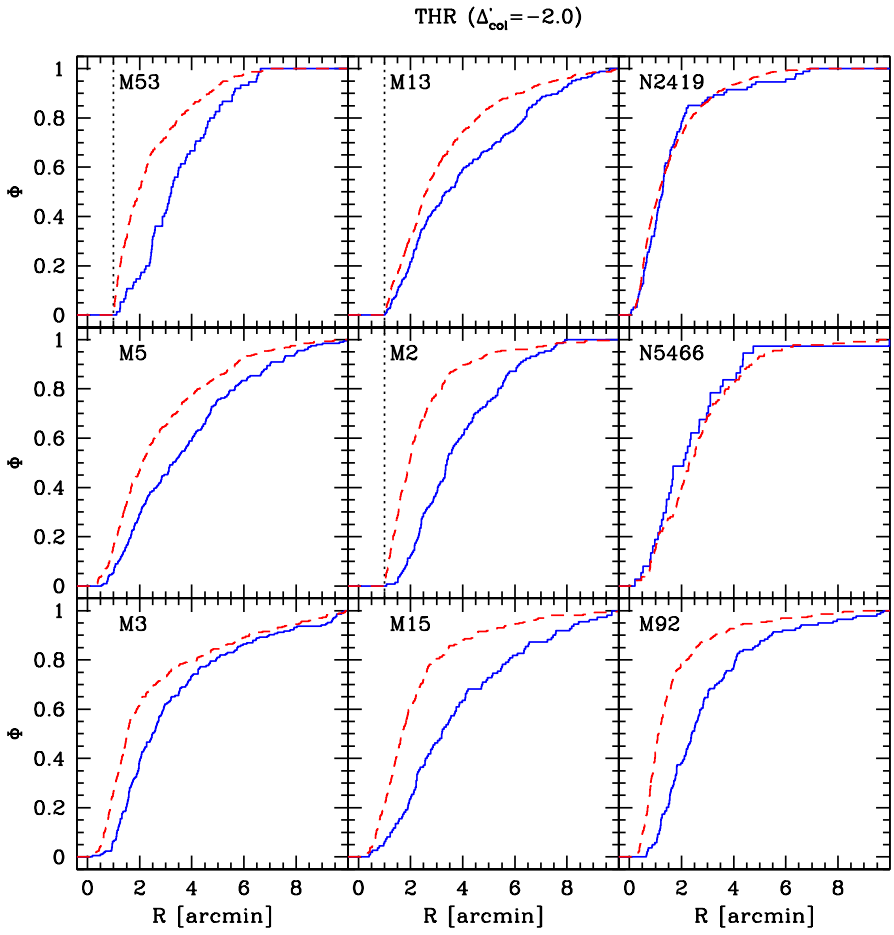

Figure 2.5: Comparison between the radial distribution of UV-blue (continuous blue line) and UV-red (dashed red line) for all the considered clusters (for a chosen threshold $\Delta'_{col} = -2.0$). The data within the radius marked by the dotted lines in the plots of the distributions for M 53, M 2, and M 13 were not included in the analysis (see Sects. 2.1 and 2.1.1). See Table 2.2 for the significance of the detected differences, as measured by the KS test.

Table 2.3: Dimensions of the samples and results of KS tests.

NGC	$N_{UV-blue}$	N_{UV-red}	P_{KS}^{rad}	$N_{UV-blue}$	N_{UV-red}	P_{KS}^{rad}
M 5	167	204	4.1×10^{-12}	131	521	3.5×10^{-7}
M 2	199	293	$< 1.0 \times 10^{-15}$	86	406	8.0×10^{-14}
M 3	267	234	5.3×10^{-11}	154	347	8.9×10^{-9}
M 13	292	304	9.0×10^{-4}	102	494	4.7×10^{-5}
M 92	231	211	1.5×10^{-15}	78	364	2.1×10^{-13}
M 53	145	249	2.0×10^{-11}	34	360	7.5×10^{-8}
M 15	167	204	4.1×10^{-10}	60	311	9.2×10^{-10}
NGC 5466	67	105	0.24	16	156	0.80
NGC 2419	224	469	0.09	36	657	0.09

umn of Table 2.2. In all clusters for which we detected a significant intrinsic *u*–*g* spread (including M 15), the UV-red population is obviously more centrally concentrated than the UV-blue one, with P_{KS}^{rad} always lower (and in most cases *much* lower) than 0.02%. We note that this result is very insensitive to the actual choice of the $\Delta_{col}^{'}$ threshold; the difference remains highly significant for a large range of adopted thresholds (in particular, for the whole range $-3.0 \leqslant \Delta_{col}^{'} \leqslant 0.0$).

This result clearly provides further support to the physical significance of the *u*–*g* spread: it is very hard to conceive how any spurious observational effect can be associated with such a strong difference in the radial distribution. Moreover, it suggests that the higher degree of central concentration of UV-red (putative I+E) stars with respect to UV-blue (putative P) stars may be a general characteristic of all GCs where intrinsic UV-spread can be detected, therefore any model intended to explain the origin of the spread in light-element abundances in GCs should also be able to reproduce this feature.

Fig. 2.5 aims to demonstrate the high level of statistical significance of the detected differences between the radial distributions of UV-red and UV-blue stars. To allow for a more direct comparison with the predictions of chemo-hydro-dynamical models (D'Ercole et al., 2008; Decressin et al., 2008, 2010), in Fig. 2.6 we present the radial profile of the ratio of the number of UV-red to UV-blue stars ($\frac{N_{UV-red}}{N_{UV-blue}}$), where the radial coordinate is expressed in units of the clusters core radii (r_c), and the distances of 1, 2, 3, 4, and 5 half-light radii (r_h) are also indicated (vertical dashed lines). This ratio should approximately scale as the ratio of second generation(s) (I+E) to first generation (P) stars, whose radial distribution is a typical outcome of the considered models. However, we stress that while the overall shape of the observed profiles does not change much when different thresholds between UV-blue and UV-red stars are adopted[8], the true values of $N_{UV-red}/N_{UV-blue}$ depends on the adopted threshold, hence they cannot be directly compared with second-to-first generation ratios computed elsewhere. The only safe conclusion that we can draw here is that UV-red stars are more abundant than UV-blue stars (in the innermost $\sim 3-4$ r_h) for any threshold $\Delta_{col}^{'} \leqslant -1.0$ (see also Fig. 2.7), albeit with cluster-to-cluster

[8]Over the range $-3.0 \leqslant \Delta_{col}^{'} \leqslant -1.0$. In particular, the slope of the inner rising branch of the profile changes with the adopted threshold (the relative height of the central peak grows by a factor of $\leqslant 3-4$ changing the threshold from –1 to –3) but the radius where the profile flattens remains unchanged. In Fig. 2.6, we have adopted $\Delta_{col}^{'} = -2$, as above.

differences of a factor of a few; this is in qualitative agreement with the predictions by D'Ercole et al. (2008) and Decressin et al. (2008), and with the observations by Carretta et al. (2010c).

The profiles shown in Fig. 2.6 cover the range given by $\simeq 0.5-1\ r_h$ and $>4\ r_h$. In nearly all cases, the profiles display a relatively steep decline from the innermost bin out to a radius of $\sim 3\ r_h$ where they flatten at a level $N_{UV-red}/N_{UV-blue} \leqslant 1$, remaining approximately flat out to the last observed point. Hints of another increase at $r_h \geqslant 10\ r_h$ are seen in the profiles of M 3 and M 2 but their significance seems only marginal, if any. A notable exception to this general trend is provided by M 13, whose profile is nearly flat out to $\sim 3\ r_h$, then declines into another flat branch at $r \sim 4\ r_h$.

It is interesting to compare the observed profiles with the model predictions shown in Fig. 18 of D'Ercole et al. (2008). In that specific model, after 25 half-light relaxation times of evolution, the profile of the second-to-first generation number ratio is nearly flat within $r \simeq 0.5\ r_h$ (a region always entirely enclosed in the innermost bin of our profiles, or not even included in the considered sample, in the cases of M 2 and M 53), then declines by a factor of a few by $\simeq 2\ r_h$, at the

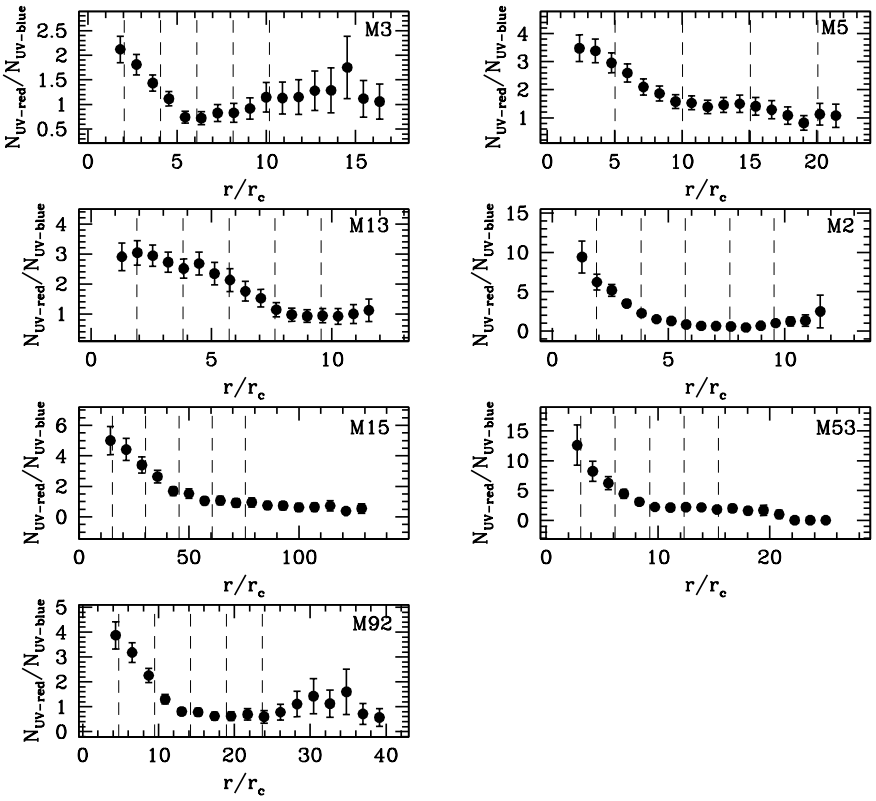

Figure 2.6: Ratio of the number of UV-red to UV-blue stars as a function of distance from the cluster center, for the seven clusters in which we detected a significant intrinsic UV-spread. The radial coordinate is expressed in units of cluster core radii, the dashed vertical lines marks the radial distances corresponding to 1, 2, 3, 4, 5 half-light radii (r_c and r_h from Harris, 1996). The ratio is computed in radial bins 2.5″ wide in steps of 0.5″. Note that the actual value of the ratio depends on the adopted threshold between UV-red and UV-blue stars: here we adopted $\Delta'_{col} = -2.0$ as in Table 2.2 and Fig. 2.5.

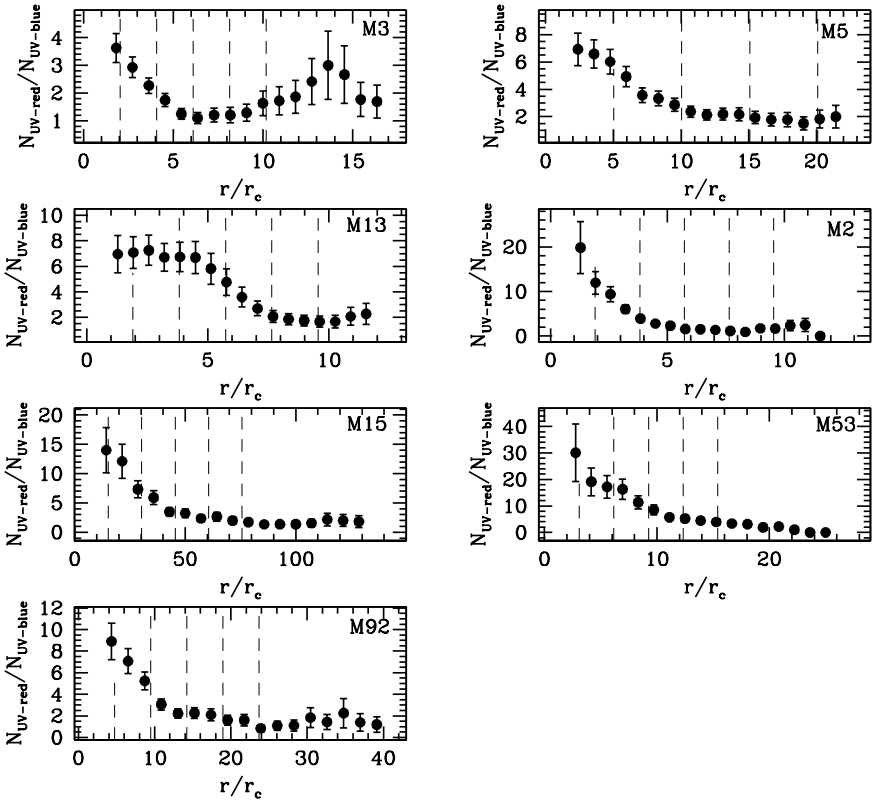

Figure 2.7: The same as in Fig. 2.6, but for an adopted threshold $\Delta'_{col} = -3.0$

limit of that figure. This is in fair agreement with the observed profiles[9]; a broad agreement is also found with some of the models presented in Decressin et al. (2010, see the middle bottom and right bottom panels of their Fig. 1). A detailed comparison with models is far beyond the scope of the present work. On the other hand, we feel that Fig. 2.6 provides a very useful set of observational constraints that must be reproduced by models of GC formation. Unfortunately, our data do not sufficiently probe the innermost regions ($r \leqslant 0.5\ r_h$) of the considered clusters; and complementary HST observations are probably needed to check this part of the profiles. Finally, a fully meaningful comparison with the profiles of Fig. 2.6 would require dedicated models for each cluster, taking into account its specific structural and dynamical properties, as well as accounting for its evolution for a Hubble time.

2.2.2 Comments on individual clusters considered in this work

In this section, we briefly report on previous results about abundance and/or UV color spreads in the clusters considered in this Chapter.

Five of our clusters were also considered in the study by Yong et al. (2008a), namely M 5, M 3, M 13, M 15, and M 92. These clusters display a significant spread at all evolutionary stages in

[9]However, it is expected that the inner flat region of the profile would progressively extend as dynamical evolution proceeds beyond the 25 t_{rh} time lapse considered in that simulation (Vesperini et al., 2013).

the V, c_y CMD (from photometry by Grundahl et al., 1999). According to Yong et al. (2008a), the observed spreads are comparable to what seen in NGC 6752, suggesting that all these clusters exhibit a $\simeq$2.0 dex dispersion in [N/Fe], i.e., the value found in NGC 6752.

Grundahl et al. (1998) provided evidence of stars from two different populations in the horizontal branch of M 13. In particular, they noted that at any given $(b-y)_0$ color, there is a large spread in the c_0 index (defined as $c_0 = c_1 - 0.2\ E(b-y)$) that they interpreted as being due to star-to-star-variations in CNO abundances.

Turning to spectroscopic analyses, Martell et al. (2008) showed that M 53 has a broad but not strongly bimodal distribution of CN band strength, with CN and CH band strengths that are anticorrelated for unevolved stars.

For the well-studied cluster M 5, Smith and Norris (1983) showed that the cyanogen distribution is strongly bimodal for a sample of 29 stars near the RGB tip. The classic Na/O anticorrelation has been found by Sneden et al. (1992) and confirmed by Ivans et al. (2001). This was further correlated with the CN strength index, δS(3839): stars with larger CN indices also have larger Na and Al abundances and lower O abundances than stars with lower CN indices. Finally, Briley et al. (1992) and Cohen et al. (2002) found strong (and anti-correlated) variations in the abundances of C and N of stars down to the base of the RGB of M 5.

An extended Na/O anticorrelation was found also in the extremely metal-poor cluster M 92 (Sneden et al., 1991), as well as strong (and anticorrelated) variations in the abundances of C and N (Carbon et al., 1982).

Spectroscopic observations revealed star-to-star variations in the abundances of the CNO group elements among the M 3 giants (Pilachowski and Sneden, 2001), with both oxygen-rich and oxygen-poor stars coexisting in the cluster (Kraft et al., 1992; Cohen et al., 2005). Lee (2000) claimed the existence of a C-N anticorrelation among stars on the lower RGB of M 15, although no bimodality is found (Cohen et al., 2005). Kayser et al. (2008) showed a weak indication of a bimodality in the CH-CN plane (two clumps separated at CN$\sim$–0.6), although the observational errors are large compared to the separation of the two clumps. Pancino et al. (2010) detected a clear and bimodal CN and CH anticorrelation among the unevolved stars measured by Kayser et al. (2008). Finally, Smith and Mateo (1990) found a CN-CH band strength anticorrelation and a possible bimodality in their sample of red giants in the cluster M 2. We will present a spectroscopic analysis of RGB stars in this cluster in Chapter 4.

We note that for all the clusters in which we detected a significant intrinsic *u*–*g* spread, there was previous evidence of inhomogeneity in their stellar population reported in literature, supporting our findings.

Previous detections of differences in radial distributions between different populations in GCs were limited to the cases of ω Cen, NGC 1851, NGC 1261, and NGC 3201, as discussed in Sect. 2.2.1. The results presented here more than double the number of GCs where these differences are detected at a very high degree of significance.

2.3 Summary & conclusions

We have used publicly available *u, g, r* photometry from An et al. (2008) to search for anomalous spread in near UV color (*u–g*) along the RGB of nine high-latitude, low-reddening, and well populated Galactic GCs. This anomalous spread was detected before in some clusters, using colors including other broad/intermediate band filters, such as Johnson's U or Strömgren u, and it was shown to be associated with the well known spread in the abundance of light elements (C, N, O, Na, etc.; see Carretta et al., 2009c, and references therein). The main results of our analysis can be summarized as follows:

- ◇ We revealed anomalous *u-g* spreads in seven of the nine clusters. The lack of detection of any significant intrinsic *u-g* spread in the two remaining clusters (NGC 2419 and NGC 5466) may be due to a real lack of chemical spread but it may also be associated with insufficient photometric accuracy and/or radial sampling. NGC 2419 is far more distant than any other cluster in the sample and its RGB is observed at much fainter apparent magnitudes, implying much larger photometric errors in the range of interest; for the same reason, the available photometry for this cluster samples mostly the portion of the RGB between the HB and the tip, where the amplitude of the UV-spread effect is known to decrease. The radial range explored here for NGC 5466 is the smallest of the whole sample, $r \leqslant 4.1\ r_h$. There are indications that the UV-spread effect may be weaker at very low metallicity and this may also hamper our ability to detect it in clusters with [Fe/H]$\leqslant -1.8$.

- ◇ In the case of M 5 ([Fe/H]= –1.34), we have demonstrated that the Na abundance correlates with the *u–g* color along the RGB, in the same way as in other clusters studied in the literature: The same effect is not seen in M 15 ([Fe/H]=–2.32): we attribute this to the weakening of the UV-spread with decreasing metallicity, which is probably associated with the extreme weakening of CN lines for [Fe/H]$\leqslant -1.8$ However, the case of M 5 illustrates that light-element abundance variations can be traced with the $u-g$ color as done before with $U-B$, $U-V$, $U-I$, and c_y indices (see, for example Yong et al., 2008a; Marino et al., 2008; Han et al., 2009b; Carretta et al., 2009c, 2010c).

- ◇ Dividing the RGB stars of each cluster into UV-blue and UV-red subsamples, according to their Δ'_{u-g}, we found that UV-red stars are more centrally concentrated than UV-blue stars in all the seven clusters in which we detected a significant intrinsic UV-spread. Kolmogorv-Smirnov tests have proven that the difference in the radial distributions of the two groups are highly significant in all cases: the probability that UV-blue and UV-red stars be drawn from the same radial distribution is always lower than 0.02%. This result does not depend critically on the choice of the the dividing line between UV-blue and UV-red.

- ◇ The radial profiles of the ratio of UV-red to UV-blue stars typically show an approximately linear decline from the first sampled point (at $\simeq 0.5-1\ r_h$) out to $3-4\ r_h$, where they flatten

and remain approximately flat out to the last sampled point (at $\simeq 4-8\ r_h$). This behavior is in qualitative agreement with the predictions of most recent models of formation and chemical evolution of globular clusters. It is interesting to note that in M 13 the profile is flat in the innermost $\sim 3\ r_h$, then declines at larger radii. The *shape* of the observed profile provides a quantitative basis to test these theoretical scenarios, once specific models reproducing the present-day status of the considered clusters become available.

The results presented here clearly suggest that the difference in the radial distribution of first and second generation stars is be a general characteristic of globular clusters. Moreover, it has been demonstrated that near UV photometry can be a very efficient tool to trace light element spreads in very large samples of RGB stars in clusters, and it is especially well suited to studying the radial distribution of the various cluster populations. It must be considered that the very encouraging results presented in this Chapter have been obtained with a relatively small (2.5 m aperture) ground-based telescope, under non-ideal seeing conditions ($\leqslant 1.6''$ FWHM, An et al., 2008). A survey performed with larger telescopes and/or under good seeing conditions (e.g., with service mode observations) and complemented with HST observations of the cluster cores would provide a completely new insight into the problem, and would surely contribute to shedding light on the mysterious earliest phases of the evolution of globular clusters.

CHAPTER

3 A spectroscopic and photometric investigation of the split SGB in NGC 1851

NGC 1851 is one of the most intriguing clusters with multiple stellar populations. It exhibits a double SGB, with the faint component accounting for 35% of the stars (Milone et al., 2008). If age is the sole cause, then the SGB split is consistent with two stellar groups with an age difference of ∼1 Gyr. As an alternative, the two SGBs could be nearly coeval but with a different C+N+O content (Cassisi et al., 2008; Ventura et al., 2009). The HB is also bimodal, with about ∼35% of HB stars on the blue side of the instability strip. Both the HB and the MS morphology leave no room for strong helium variations (Salaris et al., 2008; D'Antona et al., 2009). Nor is the RGB consistent with a simple stellar population (Grundahl et al., 1999; Calamida et al., 2007). Lee et al. (2009b) and Han et al. (2009a) pointed out two *distinct* RGB evolutionary sequences, using Strömgren Ca $uvby$ photometry, and proposed that the split might be attributed to differences in calcium abundance.

Many spectroscopic studies have been dedicated to RGB stars in NGC 1851. Almost 30 years ago, Hesser et al. (1982) noticed three out of eight bright-RGB stars with anomalously strong CN bands and with enhanced Sr and Ba lines. More recently, Yong and Grundahl (2008) analyzed UVES spectra of eight giants. Their analysis revealed that star-to-star abundance variations of O, Na, and Al with a clear anticorrelation of O and Na also exist in this cluster, and the amplitude of these variations is comparable with those found in clusters of the same metallicity. More interestingly, they argued for the presence of two different populations in this cluster, characterized by significant differences in the the light *s*-process element Zr and the heavy *s*-process element La. Yong et al. (2009) and Yong et al. (in preparation) found a wide spread in the abundance sum C+N+O (while a constant sum of C+N+O was derived by Villanova et al., 2010 from the abundance analysis of 15 RGB stars); with the CNO-rich stars being also enhanced in Zr and La. Yong and collaborators associated the group of CNO-rich *s*-rich stars to the progeny of the faint-SGB and suggested that intermediate-mass AGB stars might have contributed to the enrichment of the ICM before the formation of the second generation of stars. Interestingly, both the *s*-rich and the *s*-poor groups exhibit their own Na-O anticorrelation, which suggests that NGC 1851 has experienced a complex star-formation history. In these respects, Campbell et al. (2012) concluded

that the merger scenario suggested by Carretta et al. (2010d) leads to a natural expectation that the two bimodal CN populations in the original clusters would also be superimposed, giving the quadrimodality detected among both RGB and AGB stars in their sample.

Yong and Grundahl (2008) also suggested the presence of a slight metallicity spread ($\leqslant$0.1 dex) among NGC 1851 RGB stars. This result has been recently confirmed by Carretta et al. (2010d) on the basis of a larger sample of stars. Following a classification scheme based on Fe and Ba abundance, Carretta et al. (2010d) distinguished between a metal-rich, barium-rich (MR) and a metal-poor, barium-poor population (MP). They associated the MR and the MP components to the bright- and the faint-SGB respectively, which is at odds with what was suggested by Yong and Grundahl (2008). Very recently, Gratton et al. (2012b) studied the Na-O anticorrelation from moderately high resolution spectra for a large sample of stars on the bimodal HB of NGC 1851. They found that the red HB stars clearly separate into two groups: the vast majority are O-rich and Na-poor, while about 10-15% are Na-rich and moderately O-poor. Most (but not all) Na-rich red HB stars are also Ba-rich and there is an overall correlation between Na and Ba abundances within the red HB. The group of Ba-rich red HB stars resides on the warmer edge and includes 10% of the red HB stars. They proposed that they are the descendant of the stars on the RGB sequence with very red $v-y$ colour (Carretta et al., 2010d). Gratton et al. (2012b) also showed that a Na-O anticorrelation among blue HB stars exists, partially overlapping that found among red HB stars, though generally blue HB stars are more Na-rich and O-poor.

While the above listed spectroscopic studies targeted evolved stars in NGC 1851, before this work, only Pancino et al. (2010) analyzed a sample of unevolved stars in this clusters to provide index measurements, and we present for the first time an abundance analysis of MS, TO and SGB stars.

In particular, we observed stars located on the faint- and bright-SGB and derived for them C and N abundances; aiming to provide insights on the chemical signature differences between the two discrete sequences on the SGB. Soon after the publication of this study, Gratton et al. (2012c) presented abundances for Fe, C, Ca, Cr, Sr, and Ba for stars located onto the double SGB in this cluster. They found that the blue SGB is slightly more metal-poor than the faint SGB, with [Fe/H] = –1.227 $\pm$ 0.009 dex and [Fe/H] = –1.162 $\pm$ 0.012 dex, respectively. They confirmed that the abundances of the n-capture elements Sr and Ba have a bimodal distribution, reflecting the separation between faint SGB (Sr and Ba-rich) and bright SGB stars (Sr and Ba-poor).

The results presented in this Chapter have been published in Lardo et al. 2012, A&A, 541, A141.

3.1 Observations and data reduction

3.1.1 Source catalogs and sample selection

We selected our targets from literature photometry: FORS2 V and I photometry presented by Zoccali et al. (2009), in the southwest quadrant of the cluster, as well as $F606W$ and $F814W$

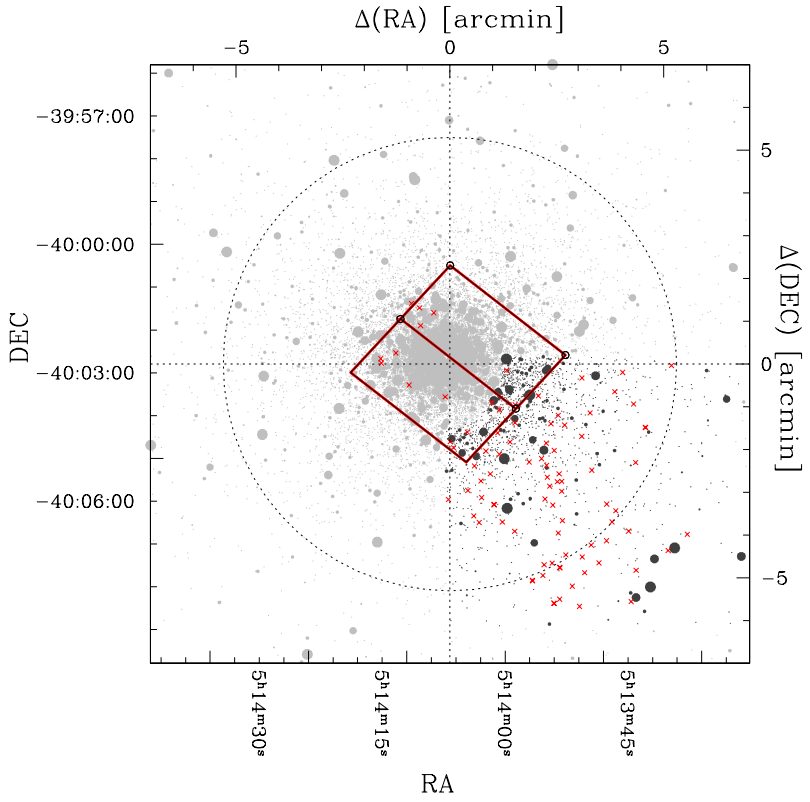

Figure 3.1: Area covered by the catalogs from which the spectroscopic selection was made: the FORS2 in the outer part (shown in black) and the ACS/HST field (continuous red line) in the inner region. The red crosses represent the IMACS+FORS2 sample. We also indicate the half tidal radius in this figure (dotted circle).

HST/ACS photometry from the GGC treasury program GO-10775 for the inner part of the cluster (Milone et al., 2008). The area covered by the catalogs and the selected spectroscopic targets is shown in Fig. 3.1. We transformed the coordinates using 2MASS as a reference astrometric catalog, so the final catalog is on the same relative astrometric system. Spectroscopic targets were selected as the most isolated stars located around the turn-off and the SGB, reaching the RGB base. The resulting photometry was calibrated using stars in common with the V, I Bellazzini et al. (2001) catalog, covering an $8' \times 8'$ field centered on the cluster. We also used publicly available Strömgren u, v, b, y photometry[1] of NGC 1851 from Grundahl et al. (1999) and Calamida et al. (2007). We refer the reader to those paper for details about observations and data reduction of Ströemgren photometry.

3.1.2 Observations and spectroscopic reductions

We acquired low-resolution (R$\simeq$1123 and R$\simeq$1246 at 3880 and 4305 Å, respectively) spectra of turnoff and SGB stars in the globular cluster NGC 1851 with the IMACS multi-object spectrograph at the Magellan 1 (Baade) telescope at the Las Campanas Observatory in Chile. The

[1] `http://www.mporzio.astro.it/spress/stroemgren.php`.

adopted instrumental setup with the grating GRAT 600-I covers the nominal spectral range between 3650–6750 Å with a dispersion of 0.38 Å /pix. This spectral range includes CN (3883 Å) and CH (4305 Å) molecular bands used to derive nitrogen and carbon abundances. However, the actual spectral coverage depends on the location of the slit on the mask with respect to the spectral dispersion. Because we observed faint stars, the total integration time was long, requiring ten exposures of 1800 seconds each. Therefore all observations were made with a single-mask setup with 48 slits. We were able to extract spectra for 46 targets from our initial target list. To these 46 spectra observed with Magellan, we added 47 other MS and SGB spectra from Pancino et al. (2010) observed with the FORS2 multi-object spectrograph on the ESO VLT at the Paranal Observatory in Chile[2]. We refer the reader to that paper for details of the FORS2 observations. We reduced our data following the procedure described in Pancino et al. (2010). For the data prereduction, we used the standard procedure for overscan correction and bias-subtraction with the routines available in the *noao.imred.ccdred* package in IRAF[3]. Cosmic rays were removed with the IRAF Laplacian edge-detection routine (van Dokkum, 2001). The frames were then flat-fielded and reduced to one dimension spectra with the task *apall*. Once we obtained ten

[2]Under programme ID 68.D-0510.

[3]IRAF is distributed by the National Optical Astronomy Observatory, which is operated by the Association of Universities for Research in Astronomy, Inc., under cooperative agreement with the National Science Foundation.

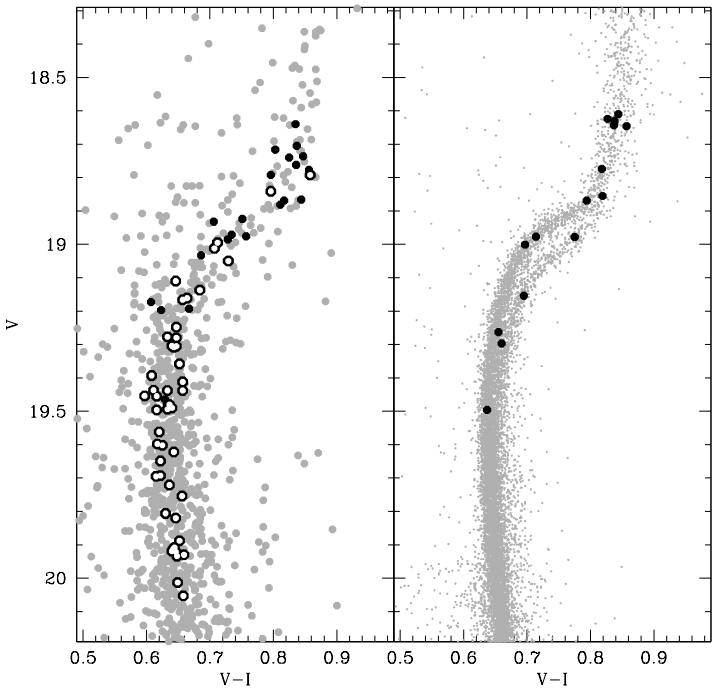

Figure 3.2: Color-magnitude diagrams for NGC 1851. Gray dots show $V-I$ photometry for the outer field (*left panel*) and inner field (*right panel*) from FORS2 and ACS, respectively. White dots mark spectroscopic targets presented in Pancino et al. (2010), while black dots show our newly observed stars.

wavelength-calibrated, one-dimensional spectra for each star, we co-added them on a star-by-star basis to reach a relevant S/N (typically between 20-30 per pixel at 3880 Å) even in the bluer part of the spectrum[4]. As a final step, we examined each spectrum and rejected those spectra with bad quality, following the recipes outlined in Pancino et al. (2010). We defined several criteria for this rejection:

1. S/N ratio < 10 (per pixel) in the CN 3883 Å band;
2. clear defects (like spikes or holes) from an individual inspection of the spectrum on the band or continuum windows;
3. discrepant Ca (H+K) and H_β index measurements.

Forty-three stars survived our criteria of selection. Moreover, 20 stars had spectral or continuum passbands falling in the gap between the CCDs because of the location of the slit on the mask with respect to the dispersion direction. We were not able to measure CH and CN band strengths for these stars, but in some cases we determined N and C abundances (Sect. 3.3). Therefore we decided to retain these spectra and consider them in the subsequent analysis.

3.1.3 Membership

NGC 1851 ($l, b = 244.51, -35.08$; Harris, 1996, 2010 edition) is projected at a far distance from the Galactic plane and consequently the contamination from field stars is almost negligible. In addition, the average radial velocity of cluster stars significantly differs with respect to the field (320.5 km/s; Harris, 1996, 2010 edition), hence cluster non members can be easily identified from their radial velocities. For the stars in the ACS/WFC field of view, member stars were furthermore selected on the basis of their proper motions (see Milone et al., 2008 for details).

For all the spectra, radial velocities were measured with the IRAF task *fxcor*, which performs the Fourier cross-correlation between the object spectrum and a template spectrum (the latter with known radial velocity). As a template we chose the spectrum of the star with the highest S/N: its radial velocity was computed using the laboratory positions of several strong lines (e. g. H_β, H_α, H_γ and Ca (H+K) among others) with the IRAF task *rvidlines*. To derive a robust determination for the radial velocities, we performed for a given star the cross-correlation against the template in four different spectral regions that span the entire spectral coverage, from the bluest part out to the reddest part of the spectrum. Then, the four values were averaged together, obtaining typically internal errors of $\simeq$ 25-30 km s^{-1}. We obtained an average V_{rad} of 317 km s^{-1} with a dispersion of 11 km s^{-1}, which fully agrees with the previous determination by Yong and Grundahl (2008), Villanova et al. (2010), and Carretta et al. (2010d).

[4] Before co-adding we checked that the shifts between spectra from different exposures were negligible compared to our wavelength calibration uncertainty (30 km s^{-1}) .

3.2 CH and CN index measurements of NGC 1851 stars

Spectral indices are defined as a window centered on the molecular band of interest and one or two windows around it to define the continuum level. For each spectrum, S(3839) and CH(4300) indices sensitive to the absorption by the 3883 Å CN band and the 4300 Å CH band were measured. Several spectral index definitions exist in literature, generally optimized to quantify the CN content of the atmospheres of red giant stars. In our case, to be consistent with the previous work of Pancino et al. (2010), we decided to adopt the indices as defined in Harbeck et al. (2003):

$$S(3839) = -2.5\log\frac{F_{3861-3884}}{F_{3894-3910}}$$

$$S(4142) = -2.5\log\frac{F_{4120-4216}}{0.5F_{4055-4080}+0.5F_{4240-4280}}$$

$$CH(4300) = -2.5\log\frac{F_{4285-4315}}{0.5F_{4240-4280}+0.5F_{4390-4460}}.$$

In particular, the S(3839) index we used differs from that of Norris (1981) or Norris and Freeman (1979), and it accounts for stronger hydrogen lines in the region of CN feature for stars cooler than red giants. As an additional check, we defined and measured two different CN band indices in the wavelength region covered by our spectra: the S(3839) for the CN band around 3880 Å and the S(4142) for the one around 4215 Å[5]. We obtained index measurement uncertainties with the expression derived by Vollmann and Eversberg (2006), assuming pure photon noise statistics in the flux measurements. In addition, we measured the two indices centered around the calcium H and K lines and the H_β line as defined again in Pancino et al. (2010) to reject outliers from our sample.

The final reduced spectra generally show a strong decline of the signal toward bluer wavelengths. This is largely expected and may be due to the different instrumental efficiency, higher absorption of the Earth's atmosphere in the blue and stellar flux wavelength dependency (see Cohen et al., 2002, for a complete discussion). The CH band at 4300 Å is not affected by the change in spectral slope from atmosphere or instrumental effects thanks to two continuum bandpasses. On the other hand, we had to rely only on a single continuum bandpass in the red part of the spectral feature for the 3883 Å CN band. Following Cohen et al. (2002, 2005), we decided to normalize the stellar continuum in the spectrum of each star, then found the absorption within the CN bandpass. Moreover, by fitting the continuum, we were able to directly compare the indices measured in this section and the abundances derived from spectral synthesis in Sect. 3.3. We fitted a third-order polynomial masking out the region of the CN band (see Cohen et al., 2005). The polynomial fitting used a 6σ high and 3σ low clipping, running over a five pixel average.

[5] As discussed by different previous authors, the S(3839) index is found to be by far much more sensitive to CN variations with respect to S(3839). For the S(4142) index, the spread is generally of the size of (or slightly wider) than the median error bar on the index measurements. Therefore, we decided to rely only on the S(3839) index measurements throughout the rest of this Chapter.

Then we computed S3839 indices from these continuum-normalized spectra and used the average (0.126±0.04 and 0.05±0.01 for IMACS and FORS2 spectra respectively) to set a zero point offset and thus delete the instrumental signature present in the raw S(3839) indices.

The measured indices are listed in Table 3.5 and plotted in Fig. 3.4.

3.2.1 Eliminating dependencies on temperature and gravity

CN and CH bands are stronger at a fixed overall abundance for stars with lower temperature and gravity. In particular, the formation efficiency of the CN molecule strongly depends on the temperature, therefore we expect the indices depend on the color of the single stars. These dependencies are usually eliminated (see Harbeck et al., 2003; Kayser et al., 2008, for example) by fitting the lower envelope of the distribution in the index-magnitude plane (or index-color plane). For our sample, we used the *median ridge line*, shown as dashed red lines in Fig. 3.4, to eliminate these dependencies (see Pancino et al., 2010). These rectified CN and CH indices are

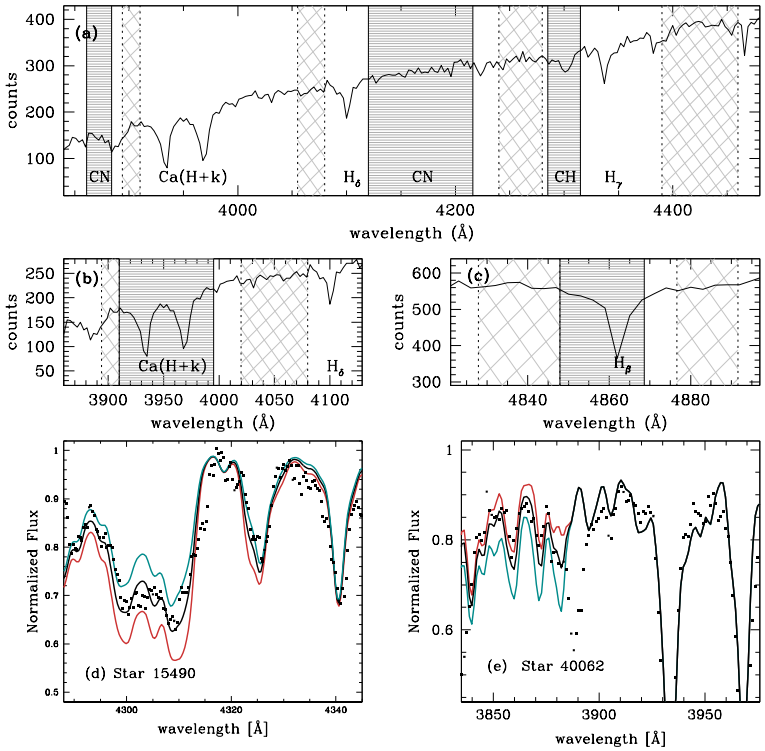

Figure 3.3: *Panel a*: example of the windows from which we measured the CN and CH indices (dark gray hatched regions) together with their respective continuum windows (light gray hatched regions). *Panels b* and *c* show the windows adopted for the H and K calcium index and the H_β index. The non-normalized superimposed spectrum (star 41213, S/N≃35 in the S3839 region) was smoothed for clarity. *Panel d*: Observed (small black dots) and synthetic (line) spectra around CH band for the star 15490. The black best fits, while the red and green lines are the syntheses computed with C abundance altered by ± 0.10 dex from the best value. *Panel e*: The same as in *panel d* but for the CN feature for the star 40062. The synthetic spectra show the best fit (thick black line) and the syntheses computed with N abundance altered by ± 0.20 (thick red and green lines).

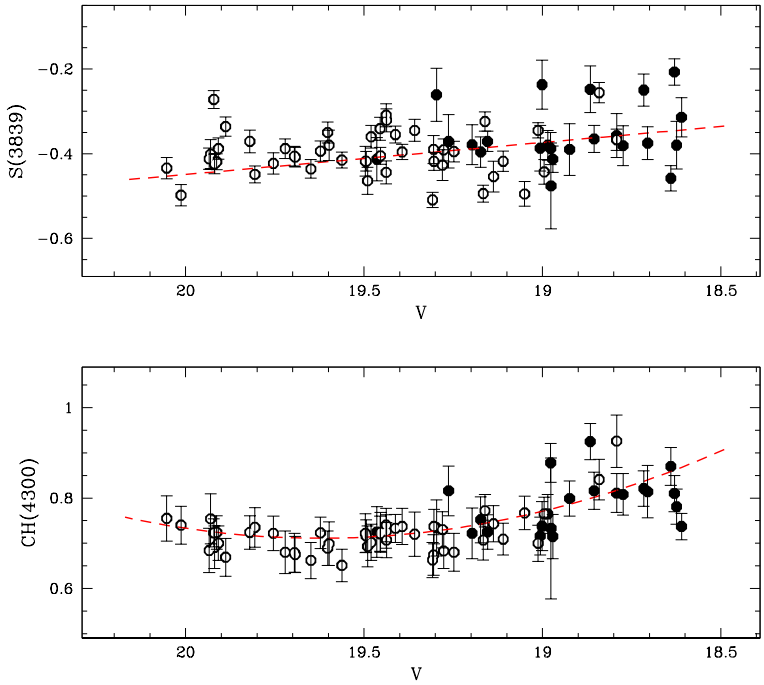

Figure 3.4: Measured S(3839) and CH(4300) indices for the program stars as a function of V. White dots are stars from Pancino et al. (2010), while black dots are from the IMACS sample. Dashed red lines in both panels are the *median ridge lines* used to eliminate temperature and gravity dependencies.

in the following indicated as δS(3839) and δCH(4300), respectively, and we refer to these new indices throughout the rest of this Chapter[6]. For the stars in common between this work and Pancino et al. (2010), the mean difference in the δS(3839) and δCH(4300) indices, derived by subtracting Pancino et al.'s values from ours, are 0.00 $\pm$ 0.02 mag and –0.01$\pm$0.01 mag, respectively. Because we adopted the same reduction procedures as in Pancino et al. (2010), we can only ascribe this small difference to the continuum normalization we performed.

3.2.2 CN and CH distribution

Variations of several light elements and anticorrelations between strengths of the CN and CH bands were detected for very many clusters. Because molecular abundance is controlled by the abundance of the minority species, the corrected CH index is a *proxy* for carbon abundance, while δS(3839) traces the nitrogen abundance. The visual inspection of the top panel of Fig. 3.4 reveals significant scatter in the CN index over the magnitude range with $V \gtrsim 19.5$ mag with some hints of bimodality toward the brightest tail of the distribution.

The range of CN becomes less evident at fainter luminosities as a consequence of the increasing temperature. In the bottom panel of the same figure, we plot the CH(4300) and S(3839)

[6]We obtained a rough estimate of the uncertainty in the placement of these median ridge lines by using the first interquartile of the rectified indices divided by the square root of the total points. The uncertainties (typically $\sim$ 0.01 for the CN index and $\sim$ 0.005 for the CH index) are largely negligible for the applications of this work.

versus the stellar V-band magnitudes. Here the variations among the measured index are very small and within the uncertainties.

Figure 3.5 shows the rectified index δS(3839) as a function of δCH(4300) for all stars. We found no evidence for a significant CH-CN anticorrelation, similarly to what was found by Pancino et al. (2010).

3.3 Spectral synthesis and abundance derivations

Indices are a fast tool to characterize chemical anomalies, but we can also rely on spectral synthesis to fully characterize our target stars. This becomes necessary when indices do not offer conclusive answers, as we saw in the previous sections.

3.3.1 Atmospheric parameters

We derived estimates of the atmospheric parameters from the calibrated ACS and FORS2 photometry presented in Sect. 3.1. Dereddened $(V-I)_0$ colors were obtained adopting $E(B-V)$ = 0.02 (Harris, 1996; 2010 edition). We obtained effective temperatures and bolometric corrections (hereafter T_{eff} and BC_V) with the Alonso et al. (1996, 1999, 2001) color-temperature relations, adopting [Fe/H]= –1.22 from Yong et al. (2009), and taking into account the uncertainties in the magnitudes and reddening estimates. Alonso et al. (1996, 1999) adopted Johnson's system

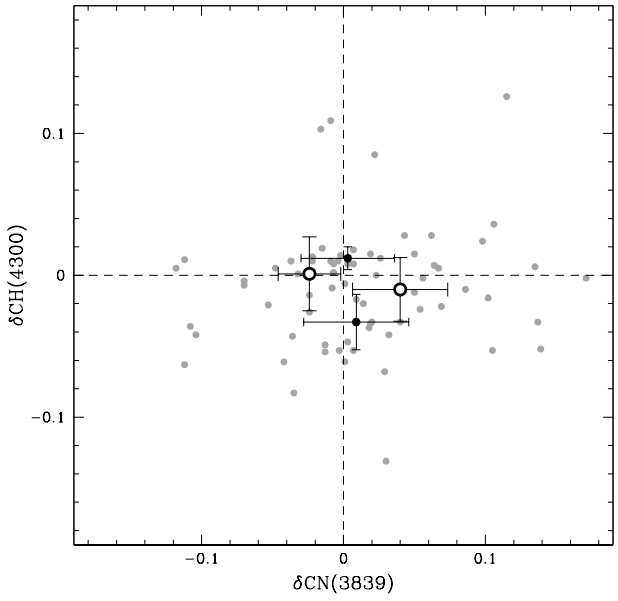

Figure 3.5: Plot for the distribution of CN and CH band strengths. Gray dots show measurements for stars. CH-weak and CH-strong stars are separated by the horizontal dashed line and their centroids with error bars (drawn at 1σ) are marked as black dots and large empty dots, respectively.

as a reference, therefore we converted $(V-I_C)$ into $(V-I_J)$ after dereddening using the prescriptions by Bessell (1979) to feed the Alonso et al. (1996, 1999, 2001) calibration. Gravities were then obtained by means of the fundamental relations

$$\log\frac{g}{g_\odot} = \log\frac{M}{M_\odot} + 2\log\frac{R_\odot}{R},$$

$$0.4\,(M_{bol} - M_{bol,\odot}) = -4\log\frac{T_{eff}}{T_{eff,\odot}} + 2\log\frac{R_\odot}{R},$$

where we assumed the solar values reported in Andersen (1999): $\log g_\odot$ = 4.437, $T_{eff,\odot}$ = 5770K and $M_{bol,\odot}$ = 4.75. For all our stars, we assumed a typical mass of 0.8 $M_\odot$ (Bergbusch and VandenBerg, 2001) and a distance modulus of $(m-M)_V$ = 15.47 (Harris, 1996; 2010 edition).

Finally, we obtained the microturbulent velocities (v_t) from the relation $\log g$ and v_t, i.e., $v_t = 1.5 - 0.03\log g$ as in Carretta et al. (2004). This method leads to an average microturbulent velocity estimate of $v_t = 1.0 \pm 0.1$ kms^{-1}, therefore we assumed v_t = 1.0 km s^{-1} for the entire sample. An additional check to test the reliability of our atmospheric parameter determination was performed using theoretical isochrones downloaded from the BaSTI[7] database (Pietrinferni et al., 2006). We chose an isochrone of 11 Gyr (12 Gyr for the faint-SGB) with standard α-enhanced composition, and metallicity Z = 0.002 and we projected our targets on the isochrone to obtain their parameters. We present the average difference between the two methods in Fig. 3.6. In the top panel we plot the difference in temperature obtained using the Alonso et al. (1999) calibration and the temperature obtained by projection of the stars on the BaSTI isochrones as a function of the temperature derived by means of the Alonso et al. (1999) empirical relations. The scatter for high temperatures is significant, as largely expected, because these empirical calibrations were obtained for giant stars and therefore are valid in a precise range of colors. On the other hand, the scatter is modest (and in many cases within the uncertainties) when comparing temperatures obtained by using theAlonso et al. (1999) and Alonso et al. (1996) relations (see bottom panel of Fig. 3.6), where the latter was derived for low main sequence stars. However, we preferred to avoid using temperatures derived by isochrone fitting mainly for these reasons: *(a)* we cannot assume *a priori* that the cluster is a single population (with the same [Fe/H] and CNO content, among others) and *(b)* the projection on the $(V, V-I)$ plane is always uncertain, and a rigorous treatment should include (asymmetrical) errors on the V magnitude and $V-I$ color, and finally, *(c)* different sets of isochrones (Padova, BaSTI, and DSEP for example) give different results.

As discussed in the following sections, even if the differences between the two temperatures scales appear non-negligible, the main results of this analysis appear totally unchanged if we adopt one or the other temperature scale. This is mainly because the abundances ranking among target stars is left unchanged. We therefore preferred to rely on the Alonso et al. (1999) parameter estimates and discuss the effect of the chosen temperature scale below.

[7] http://albione.oa-teramo.inaf.it/

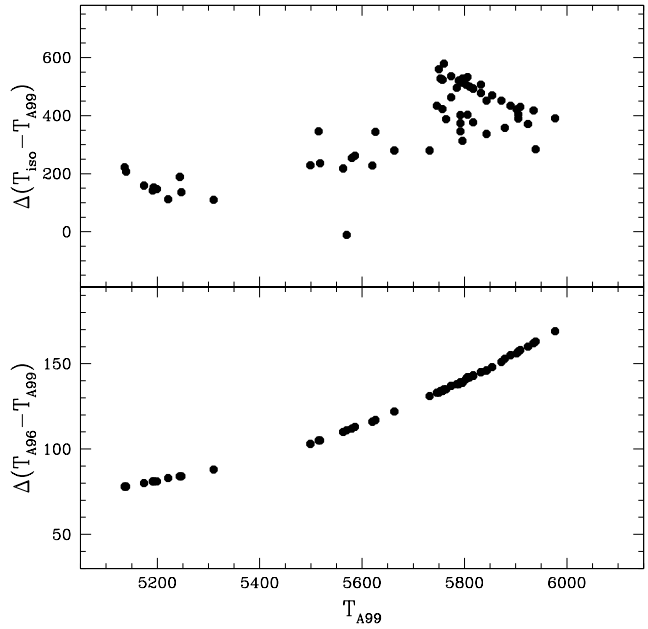

Figure 3.6: *Top panel*: Differences in the temperature estimates by means of isochrone projection procedure and using the Alonso et al. (1999) relation ($\Delta(T_{iso} - T_{A99})$) as a function of the Alonso et al. (1999) temperature (T_{A99}) for all our target stars. *Bottom panel*: The same, but for the Alonso et al. (1996) calibration (T_{A96}).

3.3.2 Abundances derivation

We used the local thermodynamic equilibrium (LTE) program MOOG (Sneden, 1973) combined with the ATLAS9 model atmospheres (Kurucz, 1993, 2005) to determine carbon and nitrogen abundances. The atomic and molecular line lists were taken from the latest Kurucz compilation and downloaded from F. Castelli's website[8].

Model atmospheres were calculated with the ATLAS9 code starting from the grid of models available in F. Castelli's website, using the values of T_{eff}, $\log g$, and v_t determined as explained in the previous section. The ATLAS9 models employed were computed with the new set of opacity distribution functions (Castelli and Kurucz, 2003) and excluding approximate overshooting in calculating the convective flux. For the CH transitions, the log g obtained from the Kurucz database were revised downward by 0.3 dex to better reproduce the solar-flux spectrum by Neckel and Labs (1984) with the C abundance by Caffau et al. (2011), as extensively discussed in Mucciarelli et al. (2011).

C and N abundances were estimated by spectral synthesis of the $^2\Sigma$–$^2\Pi$ band of CH (the G band) at ∼4310 Å and the *UV* CN band at 3883 Å (including a number of CN features in the wavelength range of 3876 – 3890 Å), respectively. Lower panels of Fig. 3.3 illustrate the fit of synthetic spectra to the observed ones in CH and CN spectral regions. Abundances for C and N were determined together in an iterative way, because for the temperature of our stars, carbon and

[8] http://wwwuser.oat.ts.astro.it/castelli/linelists.html

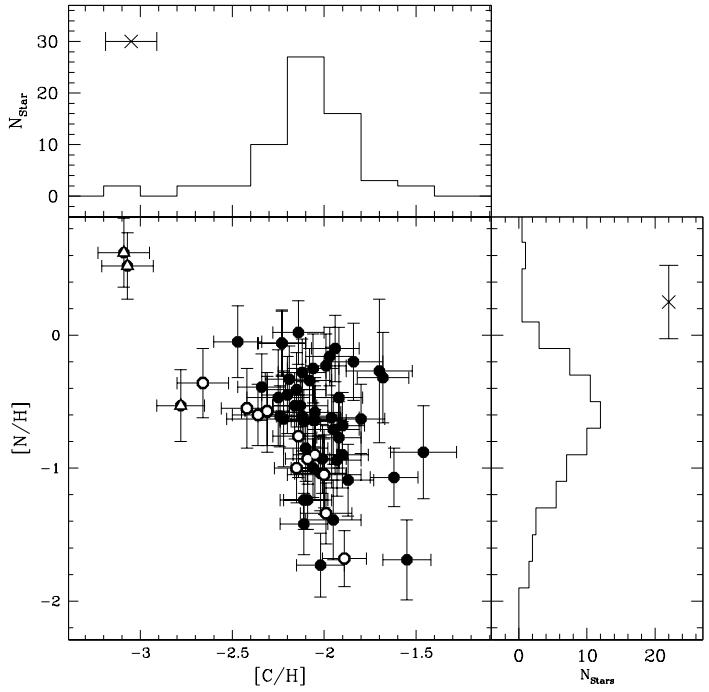

Figure 3.7: [C/H] and [N/H] abundances for the NGC 1851 SGB, TO and MS stars in Table 3.5 are plotted. A C versus N anticorrelation is evident. Stars that have already experienced some mixing episode are shown as large white dots, while three notable outliers are represented as large triangles (see text for comments). Histograms of [N/H] and [C/H] with typical median error bars are also plotted in this figure.

nitrogen form molecules and as a consequence their abundances are related to each other. The input model atmosphere was used within MOOG running the *synth* driver which computes a set of trial synthetic spectra at higher resolution (0.3 Å intervals) in the spectral region between 4150 – 4450 Å, varying the carbon abundance in steps of 0.1 dex typically in the range of –0.2 to –1.2 dex to fit a full band profile. After the synthesis computations, the generated spectra were convolved with Gaussians of appropriate FWHM to match the resolution of the observed spectra. In this way, the carbon abundances were derived by minimizing the observed-computed spectrum difference and were used to determine A(C). The carbon abundance was then used as input in the synthesis of the *UV* CN feature to derive nitrogen abundances. The procedure was repeated until we obtained convergence within a tolerance of 0.1 dex in the C and N abundances.

For the results presented here, a fit was determined by minimizing the observed-computed spectrum difference in a 60 Å window centered on 4300 Å for the CH *G*-band and 40 Å window for the *UV* CN feature at 3883 Å. Running *synth* on quite a broad spectral range (200 and 300 Å for the *G*-band and the CN feature, respectively) to produce synthetic spectra allowed us to set a reasonable continuum level also by visual inspection and thus to compute robust abundances.

We adopted a constant oxygen abundance ([O/Fe]=0.4 dex) throughout all computations. The derived C abundance is dependent on the O abundance and therefore so is the N abundance, and in molecular equilibrium an over-estimate in oxygen produces an over-estimate of

carbon (and vice versa), and an over-estimate of carbon from CN features is reflected in an under-estimate of nitrogen. We expect that the exact O values will affect the derived C abundances only negligibly, since the CO coupling is marginal for stars warmer than $\sim$ 4500 K. To test the sensitivity of the C abundance to the adopted O abundance we varied the oxygen abundances and repeated the spectrum synthesis to determine the exact dependence for a few representative stars in a wide range of T_{eff} (from 5200 to 5900 K). In these computations, we adopted [O/Fe]= –0.5, [O/Fe]= 0.0, and [O/Fe]= +0.5 dex. We found that strong variations in the oxygen abundance slightly affect ($\delta A(C)/\delta[O/Fe] \simeq 0.15$ dex) the derived C abundance in colder stars ($T_{eff} \leqslant 5400$ K), while they are completely negligible (on the order of 0.05 dex or less) for warmer stars. This is within the uncertainty assigned to our measurement.

The total error in the A(C) and A(N) abundance was computed by taking into account the two main sources of uncertainty: (i) the error in the adopted T_{eff}, typically δA(C)/$\delta T_{eff} \simeq$ 0.08–0.10 dex and δA(N)/$\delta T_{eff} \simeq$ 0.11–0.13 per 100 K for the warmest stars in our sample[9]; (ii) the error in the fitting procedure and errors in the abundances that are likely caused by noise in the spectra[10]. The errors due to uncertainties on gravity and microturbulent velocity are negligible (on the order of 0.02 dex or less). The sensitivity of the derived abundances to the adopted atmospheric parameters was obtained by repeating our abundance analysis and changing only one parameter at each iteration for several stars that are representative of the temperature and gravity range explored. Thus, we assigned the internal error to each star depending on its T_{eff} and $\log g$. The errors derived from the fitting procedure were then added in quadrature to the errors introduced by atmospheric parameters, resulting in an overall error of $\sim \pm$0.14 dex for the C abundances and $\sim \pm$0.28 dex for the N values.

Very recently Carretta et al. (2010d) found in NGC 1851 a small spread in metallicity for a large number of giants, which is compatible with the presence of two different groups of stars whose metallicity differs by 0.06-0.08 dex (but this result was not confirmed in Villanova et al., 2010) . This finding could affect our analysis in principle, because we adopted the same metallicity for all our stars in the synthesis ([Fe/H]=–1.22 dex). To test this effect we repeated the synthesis by altering the metallicity of stars belonging to the faintest SGB by 0.10 dex (well above the spread claimed by Carretta et al., 2010d). The resulting abundance variations are within the uncertainty assigned to our measurement (typically $\delta A(C)/\delta[Fe/H] \simeq 0.07$ dex and $\delta A(N)/\delta[Fe/H] \simeq 0.04$ dex) for our low-resolution spectra. Therefore this potential small [Fe/H] variation among our spectroscopic targets has no influence on our analysis and conclusions. We present the abundances derived as described above and the relative uncertainties in the abundance determination in Table 3.5. Additionally, this table lists the derived atmospheric parameters of all our targets.

[9] Cooler stars are slightly less sensitive to T_{eff} variations, typically at a level of δA(C)/$\delta T_{eff} \simeq$ 0.07–0.08 dex and δA(C)/$\delta T_{eff} \simeq$ 0.09-0.11 dex per 100 K.

[10] Additionally, in the treatment of internal error for nitrogen we varied the carbon abundance by $\pm$0.10 dex (that is the typical error associated to A(C)). We added these errors in quadrature with those introduced by the model atmosphere to estimate the internal uncertainty of the A(N) values.

3.3.3 C and N abundance results

Fig. 3.7 plots [C/H] versus [N/H] measured for our sample stars. We observe strong star-to-star variations in both elements, as already observed in all GCs studied to date. An anticorrelation, with considerable scatter, is apparent from Fig. 3.7. The scatter is consistent with the observational errors, but there are a few outliers. In a sample of 64 objects with Gaussian errors, two outliers at the 3 σ level are not expected. The deviation of stars 41350 (V = 19.3) and 40022 (V=19.9) with extremely depleted C, from the mean relation shown by the NGC 1851 sample in Fig. 3.7 is of higher statistical significance. We cannot provide a reliable explanation for this. Both stars are from the Pancino et al. (2010) sample and, judging from their radial velocities, are cluster members. Moreover, their V, I magnitudes do not have large errors. As a tentative hypothesis we suggest that these two stars could belong to the *extreme* population, using the scheme suggested by Carretta et al. (2009c).

All our stars are C-depleted, with moderately weak variations in carbon abundances (from [C/H]$\simeq$–2.7 to [C/H]$\simeq$–1.5 dex) anticorrelated with strong variations in N. The nitrogen abundance spans almost 2 dex, from [N/H]$\simeq$–1.9 up to [N/H]$\simeq$0.0 dex[11]. To check the dependence of the carbon and nitrogen abundances on the adopted temperature scale, we re-ran the synthesis using the atmospheric parameters derived by isochrone fitting (see Sect. 3.3.1). The result of this exercise is shown in Fig. 3.8. As can be seen from this figure, the carbon abundances would be higher considering these higher temperatures (ranging from $\simeq$ 0.2 dex for giants up to 0.4-0.5 dex for MS stars). This reflects on the nitrogen abundances, as demonstrated in the bottom panel of the same figure. This is only to show that the abundances ranking among target stars is left unchanged: while the zero point of our derived abundances would shift, the amplitude of the star-to-star variations for C and N would remain similar regardless of the adopted stellar parameter. Therefore, our conclusions do not depend on the adopted stellar parameters.

Evaluating the accuracy of our absolute abundance scale is very difficult because we found no literature data to compare with. Fig. 3.9 compares the C and N abundances derived here to the abundances derived for M 5 by Cohen et al. (2002), a cluster with a metallicity comparable ($\simeq$–1.29; Harris, 1996, 2010 edition) to that of NGC 1851. In panel *(a)* we present a comparison between C and N abundances derived by assuming the Alonso et al. (1999) temperature scale and abundances derived by Cohen et al. (2002) for stars at the base of the RGB in M 5, while panel *(b)* refers to isochrones-fitting temperatures. In both panel a clear C-N anticorrelation is apparent. According to theoretical computations and earlier investigations, the carbon abundance declines from MS to RGB. In panel *(a)* there is a mild disagreement with the Cohen et al. (2002) data; that is completely reconciled in panel *(b)*. This effect can be entirely explained because Cohen et al. (2002) used atmosphere parameters obtained from the isochrone. Still, although there is an offset, the two anticorrelations seem to follow a similar pattern. We conclude again

[11] If we exclude the outliers discussed above.

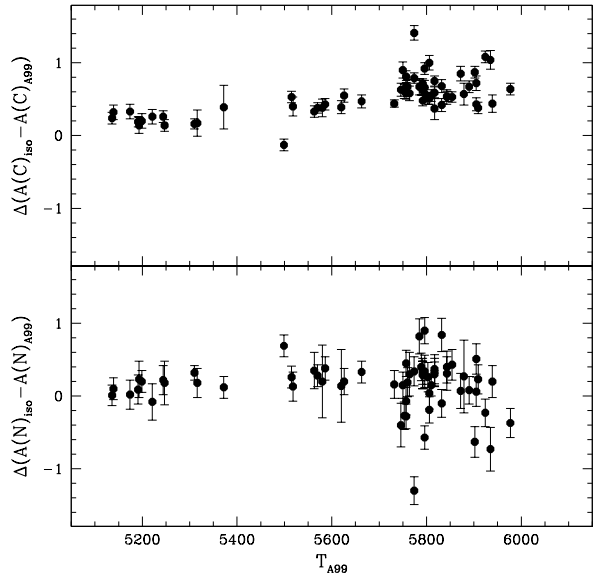

Figure 3.8: Comparison of carbon (top) and nitrogen (bottom panel) abundances derived by adopting different temperature scales ("A99" refers to the Alonso et al., 1999 calibration and "iso" to the isochrones fitting procedures) with their relative uncertainties.

from Fig. 3.9 that the anticorrelation we observe is totally untouched by the choice of the temperature scale, and shifts in the absolute abundance scale cannot account for the wide range in N abundances apparent in Fig. 3.7.

We therefore conclude that the C versus N anticorrelation among unevolved NGC 1851 stars in Fig. 3.7 is indeed real and from here on we will therefore only present results based on the Alonso et al. (1999) temperature scale.

We also plotted the derived abundances as a function of the V magnitude and $V-I$ color in Fig. 3.10 to evaluate possible systematic effects with luminosity and temperature.

While none of these effects are apparent, we can tentatively identify the occurrence of a mixing episode for NGC 1851 stars from this plot. The top panel of Fig. 3.10 shows a notable decline in the carbon abundances for stars with $V \lesssim 18.9$ and $(V-I) \gtrsim 0.8$ (stars marked as white dots in the same figure), which is expected for stars in the course of normal stellar evolution. This behavior of the C abundance allows us to identify stars that experienced a major mixing episode, which may alter the *primordial* abundances. Curiously enough, these stars, plotted again as large white dots, seem to define a pretty clear and narrow anticorrelation in Fig.3.7 (Spearman's rank correlation coefficient –0.92). The shape of this anticorrelation agrees with what we expect after the occurrence of a mixing episode: the high N enhancement found in unevolved or less-evolved stars is strongly softened by evolutionary effects and a large part of dwarfs and early subgiants have N abundances as high as those observed in slightly evolved RGB stars. We identify, again from Fig. 3.10, three outliers, coded as empty triangles as in Fig. 3.7. Two of these stars were found to deviate significantly from the main C-N relation if Fig. 3.7. We call these *anomalous*

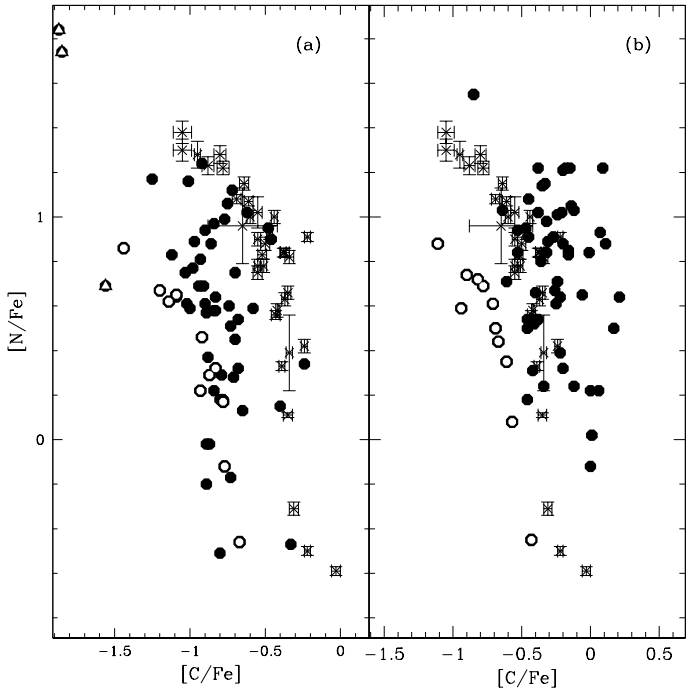

Figure 3.9: *Panel (a)*: [C/Fe] and [N/Fe] abundances for NGC 1851 stars. Stellar atmospheres and spectral syntheses were derived by assuming the Alonso et al. (1999) temperature scale. The symbols are the same as in Fig. 3.7. Abundances and relative uncertainties for stars in M 5 from Cohen et al. (2002) are also shown as crosses for comparison. *Panel (b)*: the same as in the left panel, but assuming temperatures and gravities obtained from the isochrones.

only by virtue of their positions in the upper panel of Fig. 3.10 and decided to not consider them further.

At this point we note that we cannot arbitrarily distinguish between two groups of stars with different [N/H] or [C/H] because we are unable to detect any clear bimodality. To be more quantitative, we ran the dip test on unimodality (Hartigan and Hartigan, 1985). We performed this simple statistical test only on stars with a magnitude $V < 18.9$ mag and can confirm that there is no bimodality in either the [C/H] or [N/H].

3.4 The chemical composition of the double RGB and SGB

As already discussed above, the discovery of multiple sequences in the CMD of NGC 1851 provided unambiguous proof of the presence of multiple populations and brought new interest and excitement about this GC. While it is now widely accepted that NGC 1851 hosts two or more stellar populations, the connection among its multiple SGBs, RGBs, and HBs is still controversial and the chemical composition of the two SGBs is also debated.

Several authors suggested that the groups of *s*-rich and *s*-poor stars detected from RGB-star spectroscopy are the progeny of the faint- and bright-SGB, respectively (e. g. Milone et al., 2008, Yong and Grundahl, 2008), in close analogy to what was observed in M 22 and ω Centauri (e.

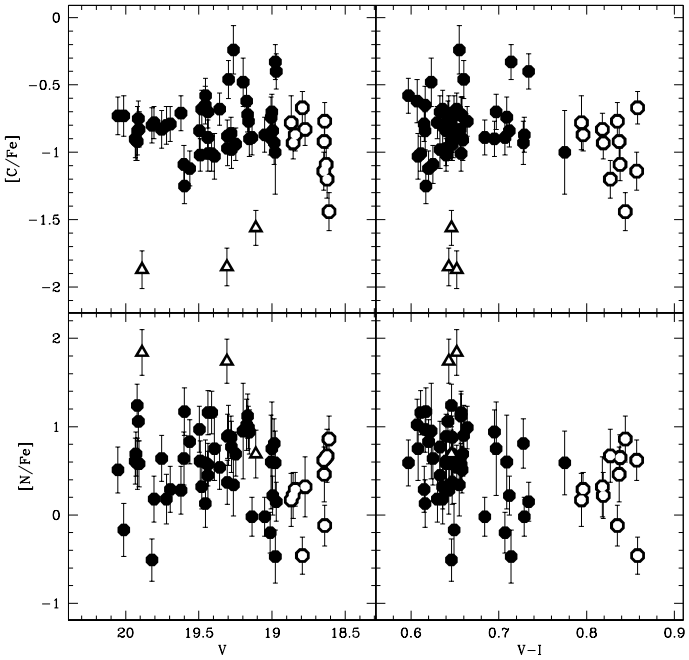

Figure 3.10: Derived C and N abundances are plotted against the photometry for NGC 1851 stars. No systematic trends with either luminosity or temperature are apparent in the abundances. We call stars marked as black empty triangles *anomalous*, while stars that supposedly underwent some mixing episodes are plotted as empty dots (see text).

g. Marino et al., 2009, 2011; Johnson and Pilachowski, 2010; Pancino et al., 2011a). In contrast, Carretta et al. (2011b) claimed that the faint-SGB consists of barium-poor metal-poor stars while bright-SGB stars have an enhanced barium and iron abundance.

3.4.1 Photometric connection between SGB and RGB

To investigate this question in more detail, we started analyzing literature photometry. We used the WFC/ACS *HST* CMD in $F606W$ and $F814W$ bands presented in Milone et al. (2008) (see Sarajedini et al., 2007; Anderson et al., 2008, for details) and the Strömgren u, b, v, y photometry from Grundahl et al. (1999) and Calamida et al. (2007). Here we are interested in high-quality photometry and included in the analysis only relatively isolated, unsaturated stars with good values of the PSF-quality fits and small rms errors in astrometry and photometry. A detailed description of the selection procedures is given in Milone et al. (2009b, Sect. 2.1). We corrected our photometry for remaining spatially dependent errors, caused by small inaccuracies of the PSF model (see Anderson et al., 2008). To account for the color differences of these variations we followed the recipes from Milone et al. (2012b, Sect. 3). Briefly, we defined a fiducial line for the MS by computing a spline through the median colors found in successive short intervals of magnitude, and we iterated this step with a sigma clipping; then we examined the color residuals relative to the fiducial and estimate for each star, how the observed stars in its vicinity may

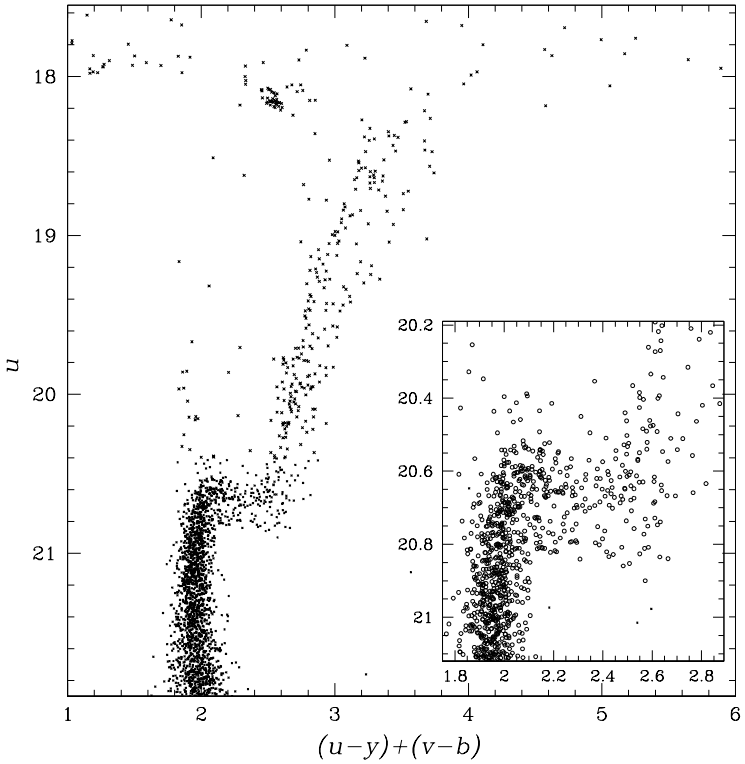

Figure 3.11: CMD for NGC 1851 from Strömgren photometry. The inset shows a zoom of the SGB region. Only stars with high-quality photometry were plotted (see Sect. 3.4.1 for details). Note the discrete double RGBs *connected* with the bimodal SGBs.

systematically lie to the red or the blue of the fiducial sequence. Finally we corrected the star's color by the difference between its color residuals.

To study multiple populations from the CMD analysis, we started searching for the combination of magnitude and colors that provides the best separation of the two RGBs and SGBs in NGC 1851. Results are illustrated in Fig. 3.11 where we plot u as a function of $(u-y)+(v-b)$. A visual inspection of this diagram leaves no doubts on the presence of a bimodal RGB and SGB and shows that the faint-SGB and the bright-SGB are clearly connected with the red- and the blue-RGB, respectively. A similar connection between the two SGBs and RGBs has already been observed for NGC 1851 by Han et al. (2009a) in the U versus $(U-I)$ CMD and was studied more recently by Sbordone et al. (2011) (see Sect. 1.2.4). These authors showed that while the double SGB is consistent with two groups of stars with either an age difference of about one Gyr or with different C+N+O overall abundance, the double RGB seems to rule out the possibility of a large age difference.

Fig. 3.11 revealed that the bimodality found in the SGB can also be seen in the RGB. To further confirm our association of the faint-SGB (bright-SGB) component with the red-RGB (blue-RGB), we focused on the relative number of stars of all evolutionary stages. To estimate the fraction of stars in the two RGBs we used only RGB stars between the two dashed lines in the magnitude

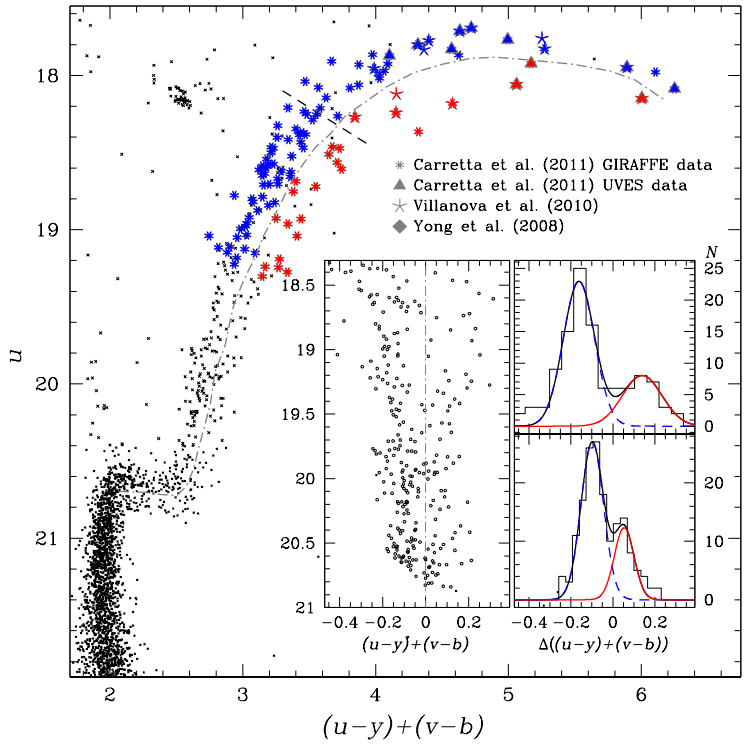

Figure 3.12: *Main panel*: Reproduction of the CMD of Fig. 3.11. We used red color codes for red-RGB and faint-SGB stars, while blue-RGB and bright-SGB stars are represented in blue. Symbols refer to stars from spectroscopic studies as indicated in the figure. The rectified CMD and the histogram color distribution of RGB stars between the two dashed lines is shown in the inset (see text for details).

interval where the split is more evident (main panel of Fig. 3.12). The procedure is illustrated in the inset of Fig. 3.12.

To obtain the straightened RGB of the right-hand panel, we subtracted from the color of each star the color of the fiducial sequence at the u magnitude of the star. The color distribution of the points in the middle panel were analyzed in two magnitude bins. The distributions have two clear peaks, which we fitted with two Gaussians (red for the red-RGB and blue for the blue-RGB). From the areas below the Gaussians, 70$\pm$3% of stars turn out to belong to the blue-RGB, and 30$\pm$3% to the red one. With the statistical uncertainties these fractions are the same in both magnitude intervals and roughly match the relative frequency on the fainter/brighter SGBs (35% versus 65%, Milone et al., 2008) and HB stars on the blue/red side of the instability strip (35% versus 65%).

3.4.2 Chemical composition of NGC 1851 subpopulations

Because the chemical abundance determinations presented so far do not define any clear bimodality, the clear separation of the sequences of Fig. 3.11 provides a unique opportunity to obtain information on the chemical differences between the two RGBs and SGBs in NGC 1851.

To do this, we used a $u,(u-y)+(v-b)$ diagram to isolate the samples of blue-RGB and bright-SGB stars, and red-RGB and faint-SGB stars. Then we plotted with red and blue symbols the red-RGB and blue-RGB stars for which abundance measurements are available from high-resolution spectroscopy.

Our analysis of the chemical abundance patterns of the two RGBs is summarized in Fig. 3.13. Lower panels show [Fe/H] versus the abundances of the *s*-process elements barium and lanthanum measured by Yong and Grundahl (2008), Villanova et al. (2010), and Carretta et al. (2011b) from GIRAFFE and UVES data. The histogram of the *s*-element distribution is illustrated in the middle panel, while upper panels plot [Na/Fe] versus [O/Fe].

The average iron, barium, lanthanum, sodium, and oxygen abundances are listed in Table 3.3 for the two groups of stars. In the light of our analysis of literature photometric and spectroscopic data we are now able to characterize the two RGBs and SGBs of NGC 1851 as follows:

— Faint-SGB and red-RGB stars are photometrically connected, therefore they represent the same subpopulation of NGC 1851; the same can be said about bright-SGB and blue-RGB (see also Marino et al., 2012b, for the case of M 22). This connection is supported by the relative (percentage) numbers of the sequences; therefore the data do not support the interpretation by Carretta et al. (2010d) that the red-RGB is associated to the bright-SGB. This

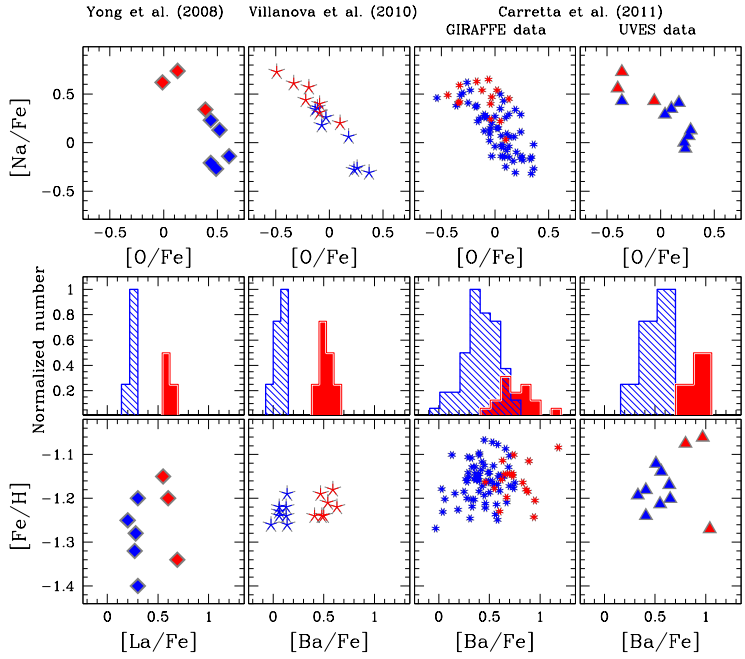

Figure 3.13: *Upper panel*: Na-O anticorrelation among NGC 1851 RGB stars from HR spectroscopy studies. Red color refers to stars photometrically selected to belong to the red-RGB in the Strömgren u, $(u-y)+(v-b)$ diagram, while stars located on the blue-RGB are shown in blue. Symbols and color code are consistent with those of Fig. 3.12. *Bottom panel*: The run of [La/Fe] versus [Fe/H] and the normalized number distribution for red and blue stars in this plane. The color code is consistent with the upper panel.

Table 3.3: Mean abundances for NGC 1851 stars from high-resolution studies.

Element	Abund (blue RGB)	N_{stars}	Abund (red RGB)	N_{stars}	Ref.
[La/Fe]	0.27±0.02	5	0.61±0.05	3	1
[Na/Fe]	–0.05±0.11	5	0.57±0.15	3	1
[O/Fe]	0.50±0.04	5	0.17±0.14	3	1
[Fe/H]	–1.29±0.04	5	–1.23±0.07	3	1
[Ba/Fe]	0.09±0.02	8	0.52±0.03	7	2
[Na/Fe]	0.04±0.11	8	0.47±0.07	7	2
[O/Fe]	0.09±0.07	8	–0.19±0.08	7	2
[Fe/H]	–1.23±0.01	8	–1.22±0.01	7	2
[Ba/Fe]	0.43±0.02	72	0.78±0.04	21	3^a
[Na/Fe]	0.13±0.03	81	0.47±0.04	24	3^a
[O/Fe]	0.04±0.02	66	–0.14±0.05	17	3^a
[Fe/H]	–1.16±0.01	82	–1.15±0.01	24	3^a
[Ba/Fe]	0.51±0.04	8	0.94±0.09	3	3^b
[Na/Fe]	0.20±0.07	8	0.57±0.11	3	3^b
[O/Fe]	0.12±0.08	8	–0.27±0.13	3	3^b
[Fe/H]	–1.18±0.01	8	–1.14±0.08	3	3^b

(1) Yong and Grundahl (2008); (2) Villanova et al. (2010); (3) Carretta et al. (2011b).
Red- and blue-RGB stars are defined according to their location with respect to the ridge line used to define color residuals in Fig. 3.12.
^{a} GIRAFFE data ^{b} UVES data

SGB - RGB connection was later confirmed also by Joo and Lee (2012) and Gratton et al. (2012c) [12].

– Literature data suggest that the red-RGB stars tend to be enriched on average in Na and *s*-process elements, and poor in oxygen, while blue-RGB stars appear to have their own, extended anticorrelation and to be solar in Ba and *s*-process elements. This is particularly evident in the Carretta et al. (2011b) dataset, which also has the highest statistical value.

– Red-RGB (and thus faint-SGB, according to our interpretation above) stars are enhanced in barium and lanthanum by ∼0.3-0.4 dex with respect to the blue-RGB (and consequently the bright-SGB).

– The literature data suggest that there is no significant iron difference between the two groups of stars. In this context we recall that Yong and Grundahl (2008) and Carretta et al. (2011b) detected a significant [Fe/H] variation among both *s*-rich and *s*-poor stars but these results strictly disagree with the narrow iron distribution observed by Villanova and collaborators. The presence of an intrinsic iron spread among NGC 1851 stars is still controversial.

[12] See also Gratton et al. (2012b) for the HB-RGB connection.

3.4.3 C and N abundances along the double SGB

In this section we present the chemical composition of stars on the two SGBs of NGC 1851. A bona fide sample of stars that belong unambiguously either to the faint-SGB or to the bright-SGB were selected using both the V, $V-I$ and u, $(u-y)+(v-b)$ diagrams (see Fig. 3.14).

The C and N abundances of these bona fide stars are plotted in Fig. 3.15, where it is immediately clear that stars belonging to the bright-SGB show a fully developed anticorrelation, while stars belonging to the faint-SGB appear to have a smaller scatter, and to have on average an excess of N (this remains still valid when considering temperatures derived by isochrone fitting as input of the synthesis, as anticipated in Sect. 3.3.3). This new result supports our previous identification of the faint-SGB as the parent population of the red-RGB, and of the bright-SGB as the parent of the blue-RGB, not only on the basis of photometry and population ratios, but also on the basis of chemical composition.

Cassisi et al. (2008) and Ventura et al. (2009) argued that the overall CNO abundance difference could account for the SGB split. Yong et al. (2009) found evidence for strong CNO variations in contradiction with the the results of Villanova et al. (2010). To further investigate this hypothesis, we computed the C+N sum for our bona fide faint-SGB and bright-SGB stars. We then derived the histograms of the distribution of the C+N sum. In the left panel of Fig. 3.16, we plot the histograms for the entire dataset (faint-SGB + bright-SGB bona fide stars) with the typical (median)

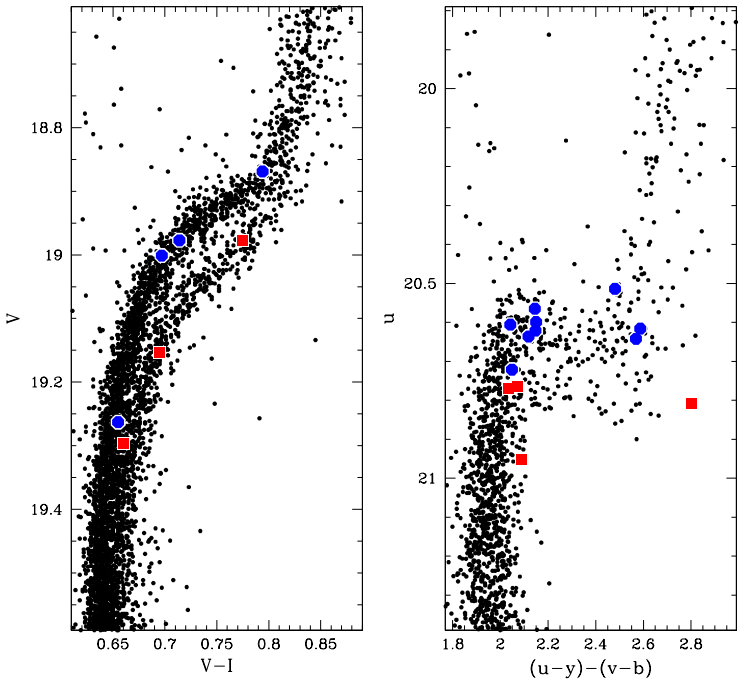

Figure 3.14: *Left panel:* selected bright-SGB (marked as blue dots) and faint-SGB (shown as red squares) stars are over plotted on the $V, V-I$ CMD presented by Milone et al. (2008). *Right panel:* selected bright- and faint-SGB stars are shown in the Strömgren u, $(u-y)+(v-b)$ diagram. The color code is consistent with the left panel.

error bar indicated. The histogram shows a high dispersion with a hint of bimodality (with two clumps separated at A(C+N)≃7.35). For this larger dataset, according to a KMM test (Ashman et al., 1994), a bimodal distribution is a statistically significant improvement over the single Gaussian at a confidence level of 89%. However, a much clearer result is obtained when histograms are built considering the bright- and the faint-SGBs *separately* (right panel of Fig. 3.16): they have a different (averaged) C+N content, the faint-SGB having A(C+N) $\simeq$ 7.64$\pm$0.24 and the bright-SGB A(C+N) $\simeq$ 7.23$\pm$0.3 (A(C+N) $\simeq$ 7.80$\pm$0.19 and A(C+N) $\simeq$ 7.47$\pm$0.26; using isochrone fitting temperatures, respectively, see Sect. 3.3.3). As an additional check, we performed a two-sample KS test computing the probability that these two samples are drawn from the same parent distribution and found a rather high (P_{KS} ~0.03) significance of the difference in the bright-SGB and faint-SGB distribution of A(C+N).

From Fig. 3.15 bright-SGB stars appear to be on average more N-poor than their faint-SGB stars; assuming an N-O anticorrelation, the bright-SGB stars are more O-rich than the faint-SGB stars. Even though we do not provide oxygen abundances for our SGB stars, we can speculate on the C+N+O sum for the two SGB components assuming [O/Fe] values from available measurements. Various oxygen abundance determinations of RGB stars can be found in the literature. From Fig. 3.13 we just note that large systematic differences exist between different

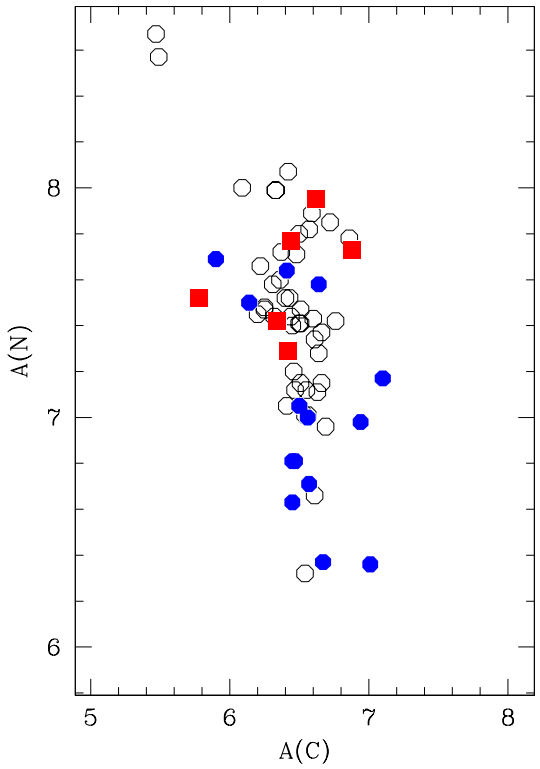

Figure 3.15: Photometrically selected bright-SGB (marked as blue dots) and faint-SGB (shown as red squares) stars are represented in the A(C) versus A(N) plane. Stars that we were unable to unambiguously associate with either of the two populations are shown with open circles.

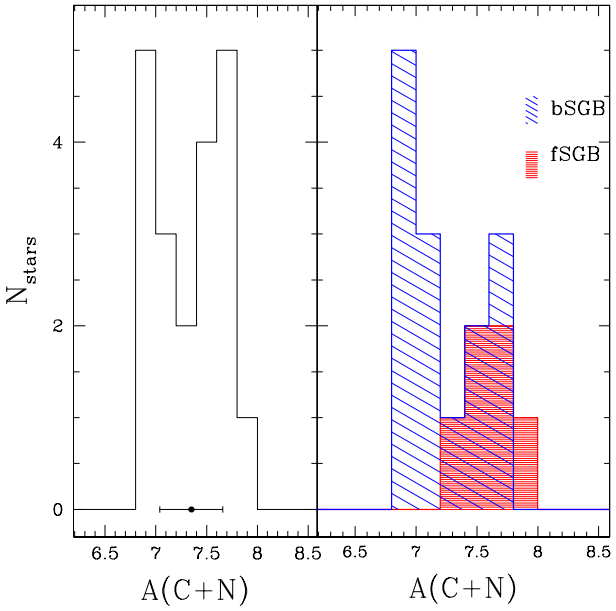

Figure 3.16: *Left panel:* Histogram of the C+N distribution for SGB stars selected as described in Sect. 3.4.3. The median error bar is plotted below the histogram for reference. *Right panel:* Histograms of the C+N sum for bright-SGB (dashed blue) stars and faint-SGB (hatched red) stars are shown.

determinations of the O content (see also Table 3.3) and we caution readers that assigning a reference [O/Fe] content to each SGB group could be naïve at this stage. If we assume for the bright and faint component [O/Fe]$\simeq$0.1 dex and [O/Fe]$\simeq$–0.2 dex, respectively[13], the separation one sees in C+N content virtually disappears when considering C+N+O. We found that the faint-SGB have A(C+N)$\simeq$7.89$\pm$0.14 and the bright-SGB A(C+N)$\simeq$7.93$\pm$0.07. The distributions even *swap* when considering O abundances suggested by Yong and Grundahl (2008) ([O/Fe]$\simeq$0.5 dex and [O/Fe]$\simeq$0.2 dex for the bright- and faint-SGB stars, respectively[14]. We conclude that the bimodality we observe in the C+N sum does not necessarily imply or exclude a bimodality in the C+N+O content and more observations are needed to settle the case of NGC 1851.

3.5 Summary & conclusions

We presented low-resolution spectroscopy for a large sample of MS and SGB stars in NGC 1851 with the goal of deriving C abundances (from the G band of CH) and N abundances (from the CN band at $\sim$ 3883 Å) and investigating the chemical differences between the two branches of the double SGB. We derived carbon and nitrogen abundances for 64 stars, whose spectra were obtained with FORS2 at VLT and IMACS at Magellan and analyzed in a uniform manner.

[13]We derived these averaged values from the works of Villanova et al. (2010) and Carretta et al. (2010d) reported in Table 3.3.

[14]Here we note that our N abundances are systematically lower than Yong et al. (2009), in some case as much as 0.6-0.7 dex. We can attribute this discrepancy to (a) the different spectral resolution, (b) the different evolutionary status of program stars (see Fig. 10 of Gratton et al., 2000) and (c) the fact that in Yong et al. (2009) N measurements come from the CN features at 8005 Å.

NGC 1851 is one of the most interesting GCs whose CMD displays a discrete structure at the level of the SGB and of the RGB. The photometric complexity is reflected in a peculiar chemical pattern that has only recently been investigated in detail. So far, the available abundance studies in NGC 1851 were limited to evolved stars that belong to the RGB (except for the study of Pancino et al., 2010). This is the first time that a precise chemical tagging of C and N content is made for stars directly located in the bright- and faint-SGB component. The main results of our analysis can be summarized as follows:

- ◇ We derived CH and CN band index measurements for 23 stars observed with IMACS, the spectrograph on the Magellan I telescope. We added to our sample spectra from Pancino et al. (2010). We were able to detect a large scatter and a hint of bimodality in the CN band strengths toward the brighter luminosities (refer to Fig. 3.4). We did not report any clear anticorrelation from these index measurements (Fig. 3.5).

- ◇ We performed spectral synthesis to separate the underlying C and N abundances from the CH and CN band strengths. Star-to-star strong variations with a significant range in A(C) and especially in A(N) were found at all luminosities from the MS ($V \simeq 20.1$ mag) up to the lower RGB ($V \simeq 18.6$ mag). C and N abundances are strongly anticorrelated, as would be expected from the presence of CN-cycle processing exposed material on the stellar surface (Fig. 3.7).

- ◇ We used literature photometry in u, b, v, and y Strömgren bands (Grundahl et al., 1999; Calamida et al., 2007) to define a new color index ($(u-y)+(v-b)$). We found that the u versus $(u-y)+(v-b)$ diagram is a powerful tool to identify the double RGB and SGB of NGC 1851 and showed that the faint-SGB is clearly connected with the red-RGB, while blue-RGB stars are linked to the bright-SGB (Fig. 3.11, see also Han et al., 2009a). Moreover, the relative frequency on the fainter/brighter SGBs (35% versus 65%) roughly matches the relative frequency of red-/blue-RGB stars selected in the $u,(u-y)+(v-b)$ diagram (30% versus 70%; see Fig. 3.12).

- ◇ We *photometrically* defined blue- and red-RGB stars according to their position on this bimodal RGB sequence. We used *s*-elements, Na, O, and iron abundance that are available from literature for some RGB stars of both populations to investigate their chemical content. The less populous red-RGB consists of Ba-rich La-rich stars and have, on average, a higher Na abundance, while the bulk of Ba-poor La-poor stars belong to the blue-RGB. However, since we have demonstrated that the two RGB and SGB are *photometrically* connected, we can confidently extend these results to the two SGB components for these *s*-process elements not studied in this work.

- ◇ Similarly, we isolated bona fide stars on the faint-SGB and bright-SGB using available photometry and analyzed their chemical composition. We noted a fully extended C-N anticorrelation for the bright-SGB stars, while faint-SGB stars tend to be richer in N, on average

(Fig. 3.15). The C-N pattern observed for SGB stars recalls the Na-O anticorrelation analyzed for RGB stars in previous papers. Specifically, the faint-SGB and bright-SGB samples are not completely superimposed on one another in the A(C), A(N) plane; but faint-SGB stars have, on average, a higher nitrogen abundance. This finding rules out the claims by Carretta et al. (2011b), who suggested that the faint-SGB is also nitrogen-poor.

- ◇ We analyzed the C+N sum for both bright-SGB and faint-SGB bona fide stars. Bright-SGB stars have A(C+N)$\simeq$7.23$\pm$0.31 dex, while for the faint component A(C+N)$\simeq$7.64.$\pm$0.24 dex. A difference in $\log_\epsilon$(C+N) of 0.4 dex as we find implies that the fainter SGB has about 2.5 times the C+N content of the brighter one. According to the Cassisi et al. (2008) scenario, the faint-SGB is anticipated to have the higher CNO content. The current findings of increased C+N content in the faint-SGB relative to the brighter one agree, in part, with the Cassisi et al. (2008) results. However, we caution that the separation one sees in C+N content could significantly decrease or disappear when considering the C+N+O sum (as discussed in Sect. 3.4.3).

The general picture demonstrates that NGC 1851 shows an impressive resemblance to M 22.

M 22 possesses a spread in s-process elements, iron content (although this is still debated for NGC 1851), and each of the two populations exhibits its own anticorrelation, with the *s*-rich having on average higher C, N, and Na abundances. The chemical anomalies point to a bimodal SGB and RGB both for M 22 and NGC 1851. Similarly to NGC 1851, also for M 22 the faint-SGB and the bright-SGB consist of *s*-rich and *s*-poor stars (see Marino et al., 2012b).

Since the Na-O and the C-N anticorrelations *alone* can be considered as the signature of multiple stellar populations, and both clusters are composed of two groups of stars with different *s*-element content (associated to the double SGB and RGB) possibly with their own Na-O, C-N anticorrelations, we conclude that each group in turn is the product of multiple stellar formation episodes. Very recently, Campbell et al. (2012) found that the CN band strengths in this cluster divide into four separate groups in both the RGB and AGB populations. This result fully support our conclusion for which in NGC 1851 each *s*-process group is the product of multiple star formation episodes.

NGC 1851 and M 22 do not harbor only two stellar populations (like *normal* GC) but have experienced a much more troubled star-formation history that resembles the case of ω Centauri (see e. g. discussions in Marino et al., 2009; Da Costa et al., 2009; Da Costa and Marino, 2011; Roederer et al., 2011; D'Antona et al., 2011),

D'Antona et al. (2011) suggested for ω Centauri a chemical evolutionary scenario where due to the large mass of the proto-cluster and its possible dark matter halo the material ejected by SNII may survive in a torus that collapses back onto the cluster after the SN II epoch (see also D'Ercole et al., 2008). The 3D-hydro simulations by Marcolini et al. (2006) show indeed that the collapse back includes the matter enriched by the SN II ejecta. This scenario could be easily extended to M 22 and NGC 1851 (see Marino et al., 2012a). For ω Centauri and M 22 it is tempting to speculate that enrichments in N and Na and depletion of C and O may have originated from

the ejecta, collected in a cooling flow, of AGB stars that evolve in the cluster when the gas has been entirely exhausted by previous star-formation events.

D'Antona et al. (2011) suggested that a poorly discussed site of *s*–nucleosynthesis that occurs in the carbon burning shells of the tail of lower mass progenitors of SNII (e.g. The et al., 2007), may become particularly apparent in the evolution of the progenitor systems of ω Cen, and similarly M 22 and NGC 1851 (see also Roederer et al., 2011).

As an alternative possibility, NGC 1851 has been recently suggested to be the merger-product of two independent stellar aggregates (van den Bergh, 1996). While this possibility seems unlikely for globular clusters in the Galactic halo, an origin as a merger product of two independent star clusters cannot be excluded in dwarf galaxies. In this case, numerical simulations (Bekki and Yong, 2011) showed that two clusters can merge and form the nuclear star cluster of a dwarf galaxy. After the parent dwarf galaxy is accreted by the Milky Way, its dark matter halo and stellar envelope can be stripped by the Galactic tidal field, leaving behind the nucleus (i.e., NGC 1851) and a diffuse stellar halo (as observed by Olszewski et al., 2009; see also Carballo-Bello et al., 2012 and Sollima et al., 2012). In these respects, it worths to recall the recent conclusions achieved by Joo and Lee (2012), for which the faint SGB can be explained mostly by the combined effects of the metallicity and helium enhancements[15], while the small variations in the total CNO abundance and age have only a little impact on the CMD. Their main result suggests that the metal-rich subpopulation is also enhanced in helium abundance. They concluded that, by assuming that NGC 1851 have formed by simple merging of two GCs having different heavy element abundances initially belonged to a proto-dwarf galaxy, would be difficult to understand why all stars in initially more metal-rich GC were selectively enhanced in helium abundance, while those in the metal-poor GC were not the merger scenario.

As already mentioned in the introduction, Carretta et al. (2011b) associated the *s*-rich and the *s*-poor populations to the bright-SGB and the faint-SGB, respectively, with the bright-SGB having also higher N and Na abundances. According to Carretta and collaborators, the possibility that the faint-SGB is CNO enhanced should be excluded, demonstrating that the split is caused by an age difference of $\sim$ 1 Gyr between the two populations. In this Chapter we have shown instead that the faint-SGB is made of N-rich and probably *s*-rich stars and bright-SGB stars are N-poor and probably *s*-poor.

While we added important pieces of information to the general picture, our results do not provide a conclusive answer on the occurrence of a merger in NGC 1851 and suggest that the measurement of the overall C+N+O abundance as well as a precise determination of the spatial distribution of the multiple SGBs and RGBs are still mandatory to shed light on the star-formation history of this GC.

[15] In their analysis, Joo and Lee (2012) adopted 0.1 dex for Δ [CNO/Fe] and Δ [Fe/H] = 0.13 dex between the two subpopulations

Table 3.4: Index measurements for NGC 1851 stars

ID	Ra (deg)	Dec (deg)	V	(V-I)	CN	err_{CN} (mag)	δ CN (mag)	CH (mag)	err_{CH} (mag)	δ CH (mag)
11219	78.5334822	-40.0274459	18.643	0.837	...	...	...	...	...	...
11755	78.5401486	-40.0328686	18.774	0.818	-0.381	0.047	-0.006	0.808	0.046	0.038
12485	78.5406833	-40.0253661	19.001	0.697	-0.237	0.058	0.134	0.738	0.054	-0.038
12925	78.5447857	-40.0234854	19.297	0.660	-0.261	0.063	0.106	0.734	0.062	-0.042
13062	78.5512037	-40.0301395	18.624	0.827	-0.380	0.056	-0.002	0.781	0.039	0.017
13872	78.5527462	-40.0445307	19.263	0.655	-0.371	0.063	-0.004	0.816	0.055	0.039
15182	78.5603478	-40.0469688	18.646	0.857	...	...	...	...	...	...
15490	78.5599836	-40.0488694	18.977	0.714	-0.388	0.038	-0.016	0.878	0.043	0.102
16047	78.5459885	-40.0581902	18.610	0.844	-0.314	0.046	0.064	0.737	0.029	-0.026
20295	78.5276335	-40.0632061	18.630	0.838	-0.207	0.031	0.171	0.810	0.040	0.046
40017	78.4595330	-40.1525297	19.695	0.615	-0.406	0.023	0.020	0.679	0.043	-0.033
40020	78.4724650	-40.1511010	18.841	0.796	-0.256	0.024	0.106	0.841	0.045	0.036
40022	78.4332081	-40.1504760	19.888	0.652	-0.336	0.023	0.105	0.669	0.042	-0.053
40028	78.4695406	-40.1494668	19.494	0.633	-0.418	0.023	-0.007	0.716	0.036	0.002
40051	78.4631667	-40.1439444	18.792	0.796	-0.357	0.052	0.018	0.811	0.043	0.040
40062	78.4834487	-40.1414047	19.161	0.664	-0.324	0.023	0.062	0.772	0.036	0.028
40072	78.4780543	-40.1393568	19.934	0.648	-0.412	0.025	0.032	0.684	0.049	-0.042
40078	78.4568778	-40.1381667	19.464	0.629	-0.413	0.051	-0.049	0.725	0.056	-0.048
40083	78.4307625	-40.1371584	19.305	0.647	-0.390	0.033	0.007	0.674	0.045	-0.053
40088	78.4695640	-40.1359246	19.248	0.647	-0.395	0.024	-0.003	0.680	0.042	-0.053
40094	78.4774387	-40.1347787	19.490	0.640	-0.464	0.032	-0.053	0.693	0.045	-0.021
40097	78.4733785	-40.1341169	20.053	0.658	-0.434	0.025	0.019	0.755	0.050	0.015
40100	78.4495611	-40.1340000	18.924	0.751	-0.390	0.061	-0.017	0.799	0.039	0.024
40117	78.4580365	-40.1314412	19.358	0.652	-0.345	0.026	0.056	0.720	0.049	-0.002
40123	78.4664750	-40.1306111	19.006	0.709	-0.387	0.054	-0.016	0.716	0.042	-0.060
40133	78.4144056	-40.1287500	19.193	0.667	...	...	...	...	...	...
40153	78.4534972	-40.1264167	19.479	0.632	...	...	...	...	...	...
40167	78.4457694	-40.1245556	18.932	0.706	...	...	...	...	...	...
40186	78.4047861	-40.1218056	18.869	0.817	...	...	...	...	...	...
40191	78.4702263	-40.1212996	19.598	0.617	-0.380	0.036	0.039	0.699	0.048	-0.012

Table 3.4: Index measurements for NGC 1851 stars (continued-I)

ID	Ra (deg)	Dec (deg)	V	(V-I)	CN	err_{CN} (mag)	δ CN (mag)	CH (mag)	err_{CH} (mag)	δ CH (mag)
40196	78.4923929	-40.1204995	19.649	0.622	-0.436	0.022	-0.013	0.662	0.040	-0.049
40197	78.4345480	-40.1204489	19.412	0.657	-0.355	0.020	0.050	0.733	0.031	0.015
40235	78.5103649	-40.1167899	19.921	0.646	-0.272	0.021	0.171	0.723	0.031	-0.002
40239	78.4986784	-40.1165524	19.562	0.620	-0.415	0.019	0.001	0.651	0.036	-0.061
40241	78.4430254	-40.1165272	19.693	0.622	-0.408	0.023	0.018	0.675	0.040	-0.037
40247	78.4682250	-40.1159722	18.705	0.837	-0.375	0.039	0.001	0.814	0.058	0.046
40271	78.5131639	-40.1140000	18.866	0.844	-0.248	0.055	0.126	0.925	0.040	0.152
40303	78.4411306	-40.1118056	19.033	0.686	...	...	...	...	...	...
40340	78.4730104	-40.1093919	19.913	0.642	-0.419	0.019	0.023	0.724	0.037	-0.000
40344	78.5028991	-40.1090554	19.438	0.633	-0.444	0.027	-0.037	0.726	0.037	0.010
40348	78.4456867	-40.1089487	19.820	0.646	-0.371	0.027	0.064	0.724	0.037	0.007
40376	78.4770704	-40.1067791	19.930	0.659	-0.401	0.034	0.043	0.754	0.055	0.028
40378	78.5259583	-40.1070000	18.740	0.825	...	...	...	...	...	...
40385	78.5091532	-40.1061629	19.806	0.630	-0.449	0.020	-0.015	0.735	0.044	0.019
40424	78.4685664	-40.1034580	19.438	0.657	-0.309	0.027	0.098	0.740	0.037	0.024
40431	78.5162111	-40.1031389	18.881	0.811	...	...	...	...	...	...
40465	78.4746278	-40.1013333	18.976	0.757	-0.476	0.101	-0.104	0.733	0.156	-0.043
40504	78.4685451	-40.0992400	19.454	0.597	-0.405	0.020	0.003	0.724	0.044	0.008
40507	78.4706722	-40.0993611	19.173	0.607	-0.396	0.036	-0.027	0.752	0.051	-0.025
40508	78.5094543	-40.0990863	19.602	0.625	-0.350	0.025	0.069	0.689	0.038	-0.022
40545	78.4757778	-40.0975278	18.985	0.728	-0.380	0.035	-0.008	0.765	0.043	-0.011
40571	78.5047352	-40.0960942	19.437	0.611	-0.321	0.027	0.086	0.707	0.039	-0.010
40575	78.4698407	-40.0960196	20.013	0.649	-0.498	0.025	-0.048	0.740	0.042	0.005
40620	78.4532694	-40.0945000	18.640	0.835	-0.458	0.030	-0.081	0.870	0.042	0.105
40665	78.5128445	-40.0926724	18.995	0.712	-0.443	0.029	-0.070	0.765	0.037	-0.007
40679	78.4762083	-40.0924444	18.716	0.803	-0.250	0.038	0.126	0.821	0.039	0.053
40709	78.4309537	-40.0912317	19.166	0.657	-0.494	0.020	-0.108	0.707	0.044	-0.036
40715	78.4849583	-40.0910365	19.908	0.644	-0.388	0.025	0.054	0.700	0.038	-0.024

Table 3.4: Index measurements for NGC 1851 stars (continued-II)

ID	Ra (deg)	Dec (deg)	V	(V-I)	CN	err_{CN} (mag)	δ CN (mag)	CH (mag)	err_{CH} (mag)	δ CH (mag)
40756	78.4788241	-40.0895444	19.280	0.647	-0.427	0.036	-0.032	0.730	0.040	0.001
40827	78.5001750	-40.0876944	18.762	0.836	...	...	...	...	...	...
40863	78.5070126	-40.0863515	19.393	0.608	-0.396	0.018	0.007	0.737	0.040	0.018
40874	78.4722925	-40.0860825	19.455	0.616	-0.341	0.027	0.067	0.721	0.039	0.005
40919	78.5234044	-40.0849874	19.496	0.637	...	...	...	...	...	...
40978	78.4762989	-40.0829703	19.919	0.640	-0.424	0.023	0.019	0.691	0.047	-0.034
41003	78.4946844	-40.0825071	19.050	0.729	-0.495	0.029	-0.118	0.767	0.037	0.005
41018	78.5251795	-40.0823269	18.855	0.819	-0.365	0.032	0.009	0.816	0.041	0.043
41108	78.4583652	-40.0800752	19.754	0.656	-0.423	0.025	0.007	0.722	0.038	0.008
41185	78.5009451	-40.0785878	19.110	0.646	-0.418	0.024	-0.036	0.709	0.035	-0.043
41213	78.5164942	-40.0782312	19.154	0.695	-0.371	0.024	-0.002	0.725	0.038	-0.052
41279	78.4260692	-40.0762239	19.277	0.633	-0.391	0.026	0.003	0.683	0.039	-0.047
41325	78.4670381	-40.0752654	19.480	0.636	-0.360	0.027	0.050	0.702	0.040	-0.012
41350	78.4739954	-40.0746754	19.308	0.643	-0.509	0.018	-0.112	0.663	0.039	-0.063
41372	78.4922083	-40.0743611	18.777	0.856	...	...	...	...	...	...
41558	78.4702879	-40.0710717	19.721	0.636	-0.388	0.023	0.040	0.680	0.047	-0.033
41610	78.4540666	-40.0700619	19.137	0.684	-0.454	0.036	-0.070	0.743	0.040	-0.004
41694	78.5000889	-40.0687222	18.736	0.847	...	...	...	...	...	...
41807	78.4921679	-40.0666366	18.792	0.858	-0.367	0.025	-0.009	0.926	0.058	0.109
41835	78.4320835	-40.0662831	19.012	0.707	-0.345	0.018	0.029	0.700	0.040	-0.068
41884	78.5039348	-40.0656429	18.978	0.775	...	...	...	...	...	...
42073	78.4802671	-40.0628473	19.304	0.640	-0.418	0.021	-0.022	0.737	0.038	0.010
42195	78.4415574	-40.0610284	19.622	0.643	-0.394	0.024	0.026	0.723	0.035	0.012
42623	78.4582694	-40.0551667	18.971	0.734	-0.413	0.031	-0.041	0.715	0.049	-0.060
42785	78.4376004	-40.0528185	19.496	0.616	-0.418	0.035	-0.007	0.722	0.043	0.008
42865	78.4964339	-40.0519295	18.869	0.794	...	...	...	...	...	...
43014	78.4127639	-40.0498611	19.197	0.623	-0.379	0.047	-0.011	0.722	0.056	-0.055

Table 3.5: Atmospheric parameters and carbon and nitrogen abundances for NGC 1851 stars.

ID	T_{eff} (K)	$\log g$	A(C)	eA(C)	A(N)	eA(N)
11219	5193 ± 90	3.4	6.42	0.14	7.29	0.31
11755	5247 ± 93	3.5	6.51	0.12	7.15	0.34
12485	5620 ± 116	3.8	6.64	0.13	7.58	0.53
12925	5746 ± 124	3.9	6.88	0.14	7.73	0.34
13062	5221 ± 92	3.4	6.14	0.14	7.50	0.30
13872	5764 ± 125	3.9	7.10	0.18	7.17	0.35
15182	5139 ± 87	3.4	6.20	0.14	7.45	0.23
15490	5563 ± 112	3.7	7.01	0.13	6.36	0.30
16047	5174 ± 90	3.4	5.90	0.14	7.69	0.26
20295	5191 ± 90	3.4	6.25	0.12	7.48	0.26
40017	5909 ± 135	4.1	6.55	0.13	7.12	0.26
40020	5310 ± 97	3.6	6.47	0.12	7.12	0.19
40022	5774 ± 126	4.2	5.47	0.14	8.67	0.26
40062	5732 ± 123	3.9	6.57	0.11	7.82	0.24
40072	5789 ± 128	4.2	6.44	0.14	7.44	0.26
40083	5792 ± 127	3.9	6.46	0.12	7.20	0.25
40088	5792 ± 127	3.9	6.40	0.12	7.52	0.25
40094	5817 ± 129	4.0	6.32	0.12	7.44	0.23
40097	5753 ± 125	4.2	6.61	0.14	7.34	0.26
40117	5774 ± 126	4.0	6.66	0.12	7.37	0.25
40123	5580 ± 102	3.7	6.60	0.15	7.43	0.53
40191	5902 ± 135	4.1	6.09	0.13	8.00	0.27
40197	5757 ± 125	4.0	6.33	0.13	7.99	0.24
40235	5796 ± 128	4.2	6.42	0.14	8.07	0.24
40239	5890 ± 135	4.1	6.22	0.13	7.66	0.25
40340	5810 ± 129	4.2	6.59	0.13	7.89	0.22
40344	5843 ± 130	4.0	6.64	0.12	7.28	0.27
40348	5796 ± 128	4.2	6.54	0.13	6.32	0.24
40376	5750 ± 124	4.2	6.43	0.15	7.52	0.25
40385	5854 ± 132	4.2	6.56	0.12	7.01	0.26
40424	5757 ± 125	4.0	6.45	0.13	7.40	0.24
40504	5977 ± 140	4.1	6.76	0.13	7.42	0.26
40507	5939 ± 117	3.9	6.72	0.16	7.85	0.29
40508	5872 ± 133	4.1	6.25	0.14	7.47	0.30
40545	5518 ± 100	3.7	6.41	0.16	7.64	0.28
40571	5924 ± 137	4.0	6.33	0.13	7.99	0.25
40575	5785 ± 127	4.2	6.61	0.15	6.66	0.30
40620	5199 ± 86	3.4	6.57	0.14	6.71	0.23
40665	5570 ± 113	3.7	6.50	0.12	7.05	0.22
40709	5757 ± 125	3.9	6.62	0.13	7.95	0.25
40715	5803 ± 129	4.2	6.51	0.13	7.41	0.26

Table 3.5: Atmospheric parameters and carbon and nitrogen abundances for NGC 1851 stars (continued).

ID	T_{eff} (K)	$\log g$	A(C)	eA(C)	A(N)	eA(N)
40756	5792 ± 127	3.9	6.48	0.12	7.71	0.24
40863	5935 ± 130	4.0	6.31	0.17	7.58	0.36
40874	5905 ± 135	4.0	6.69	0.14	6.96	0.27
40978	5817 ± 130	4.2	6.50	0.18	7.41	0.29
41003	5515 ± 109	3.7	6.47	0.13	6.81	0.22
41018	5244 ± 93	3.6	6.41	0.12	7.05	0.26
41108	5760 ± 125	4.1	6.51	0.14	7.47	0.26
41185	5796 ± 127	3.9	5.78	0.13	7.52	0.27
41213	5626 ± 116	3.8	6.44	0.13	7.77	0.25
41279	5843 ± 131	4.0	6.36	0.14	7.60	0.29
41325	5832 ± 130	4.0	6.66	0.14	7.15	0.25
41350	5806 ± 128	4.0	5.49	0.14	8.57	0.25
41558	5832 ± 130	4.1	6.54	0.14	7.01	0.28
41610	5663 ± 119	3.8	6.45	0.13	6.81	0.22
41807	5136 ± 87	3.5	6.67	0.12	6.37	0.21
41835	5586 ± 114	3.8	6.45	0.13	6.63	0.23
41884	5372 ± 97	3.7	6.34	0.31	7.42	0.36
42073	5817 ± 129	4.0	6.37	0.13	7.72	0.25
42195	5806 ± 128	4.1	6.63	0.13	7.11	0.27
42623	5499 ± 99	3.7	6.94	0.13	6.98	0.22
42785	5905 ± 130	4.1	6.50	0.14	7.80	0.26
42865	5316 ± 93	3.6	6.56	0.20	7.00	0.30
43014	5879 ± 115	3.9	6.86	0.18	7.78	0.54

CHAPTER

4 C and N abundances of stellar populations in M 2

In this Chapter we report the behavior of carbon and nitrogen along the RGB of M 2. This is an intermediate-metallicity ([Fe/H] =–1.65; Harris, 1996, 2010 edition) cluster, which is located 11.5 kpc from the galactic center, is relatively rich in stars, and lies in a sparse field.

M 2 is characterized by a bimodal CN distribution, with the majority of red giants found to be CN-strong stars (Smith and Mateo, 1990). Earlier works have already revealed a large number of stars with strong λ3883 CN bands (McClure and Hesser, 1981; Canterna et al., 1982). Furthermore, this cluster is found to contain CH stars (Smith and Mateo, 1990; Zinn, 1981). In a recent paper, Smolinski et al. (2011) detected signs of enhanced N enrichment well before the point of first dredge-up, besides the usual CN variations on the RGB.

On the photometric front, M 2 $g,(u-g)$ CMD from SDSS photometry (see Chapter 2) shows evidence of a spread in light-element abundances, which comes from the significant spread along the RGB (incompatible with measurements errors alone or with differential reddening effects).

As widely discussed in the previous Chapters, the broadening in the $U,(U-V)$ CMD (and/or usual visual colors) may be a different way to study in detail multiple stellar populations. In this Chapter, we used U-based photometry coupled with C and N abundances to tag multiple stellar populations in M 2.

The results presented in this Chapter have been published in Lardo et al. 2012, A&A, 548, A107.

4.1 Observational material

We selected M 2 spectroscopic targets from the An et al. (2008) publicly available photometry. An et al. (2008) reanalyzed SDSS images of the GCs (and open clusters) included in the survey using the DAOPHOT/ALLFRAME suite of programs (Stetson, 1987, 1994). In our previous work (Lardo et al., 2011), we used An et al. (2008) photometry to search for anomalous spread in near UV color (u-g) along the RGB of nine Galactic GCs and study the radial profile of

the first and second generation stars (see Sect. 2.1 for a detailed description of the photometric database employed to select spectroscopic targets). The initial sample of candidate stars consisted of those located more than $1'$ away from the center of M 2 (to facilitate sky subtraction) with $14.5 < V < 17.5$ mag. Spectroscopic targets were hence chosen as the most isolated stars (no neighbors within $2''$) as close as possible to the main locus of the RGB sequence in the $g,(u-g)$ and $g,(g-r)$ diagrams to reduce the incidence of blended images[1].

4.1.1 DOLORES U,V photometry

In addition, we also obtained images of the cluster in the standard Johnson U and V filters for a total of 540 seconds shifted in three single exposures in each filter with the DOLORES camera. DOLORES (Device Optimized for the LOw RESolution) is a low-resolution spectrograph and camera permanently installed at Telescopio Nazionale Galileo (TNG) located in La Palma, Canary Islands (Spain). The choice of passbands is due to the ability of separating photometric sequences at different evolutionary stages along the CMD (as discussed in Sects. 1.2 and 4.5). The DOLORES camera offers a field of view (FoV) of $8.6' \times 8.6'$ with a 0.252 arcsec/pix scale. The raw frames were processed (bias-subtracted and flat-fielded) using the standard tasks in IRAF. Point spread function (PSF) fitting photometry was thus carried out with the DAOPHOT II and ALLSTAR packages (Stetson, 1987, 1994) using a constant model PSF. The photometric calibration was done using stars in common with Stetson Photometric standard field (Stetson, 2000)[2]. Stars within $1'$ and outside of $4'$ from the cluster center are excluded from the CMD to reduce blending effects and the field star contamination, respectively. The rms in magnitude and the chi and sharp parameters are powerful indicators of the photometric quality[3]. To select a sample of well-measured stars we followed the procedure given in Lardo et al. (2012a), Sect. 5.1 and summarized in Sect. 3.4.1. The catalog of the selected sample is presented in Table 4.1. The resulting $V, U-V$ CMD, calibrated and corrected for differential reddening, and showing the position of the spectroscopic targets, is presented in Fig. 4.1.

4.1.2 Spectroscopic observations and reduction

Stellar spectra were obtained with DOLORES which allows for multi-slit spectroscopy. We defined three slit masks using the stand-alone version of the Interactive Mask Design Interface, provided by the DOLORES staff at the telescope[4]. The positions of the program stars were determined using M 2 catalogs by An et al. (2008), as discussed in Sect. 4.1. The slit width on the masks was fixed to $1.1''$, and the slit length was chosen to be at least $8''$ to allow for local sky subtraction. Typically, we succeeded to fit $\simeq$16 slits onto one mask (for a total of 48 target stars).

[1] Unfortunately, by using these selection criteria, we accidentally excluded stars belonging to a previously unknown additional RGB sequence (see Sect. 4.1.1) from our spectroscopic sample.

[2] available at `http://www3.cadc-ccda.hia-iha.nrc-cnrc.gc.ca/community/STETSON/standards/`

[3] On all stars we imposed the selection limits of CHI < 2.0 and -1 < SHARP < 1 on DAOPHOT II photometric parameters. The first of these parameters, CHI, is the ratio of the observed pixel-to-pixel scatter in the fitting residuals to the expected scatter, based on the values of readout noise and the photons per ADU specified in the DAOPHOT options file, while SHARP is a zeroth-order estimate of the square of the quantity $SHARP^2 \sim \sigma^2(observed) - \sigma^2(point-spread function)$; see the DAOPHOTII manual at `http://www.astro.wisc.edu/sirtf/daophot2.pdf`.

[4] see for reference `http://web.oapd.inaf.it/mos/`

Table 4.1: Photometry of M 2: selected sample.

ID	RA (deg)	Dec (deg)	V (mag)	ϵV (mag)	U–V (mag)	ϵU (mag)
164	323.3657998	-0.8890510	20.215	0.026	0.213	0.076
196	323.3800929	-0.8885692	19.943	0.019	0.311	0.072
234	323.3661658	-0.8882047	20.342	0.018	0.393	0.084
286	323.3795809	-0.8875061	19.015	0.012	0.220	0.028
303	323.3872881	-0.8872826	18.445	0.010	0.632	0.023
313	323.3674707	-0.8870783	19.661	0.024	0.202	0.050
330	323.3908254	-0.8869171	19.613	0.019	0.267	0.041
336	323.3657205	-0.8868386	19.325	0.012	0.305	0.037

A portion of the table is shown for guidance about its content, the complete table is available in electronic format through the CDS service via anonymous ftp to cdsarc.u-strasbg.fr (130.79.128.5) or via `http://cdsarc.u-strasbg.fr/viz-bin/qcat?J/A+A/548/A107` .

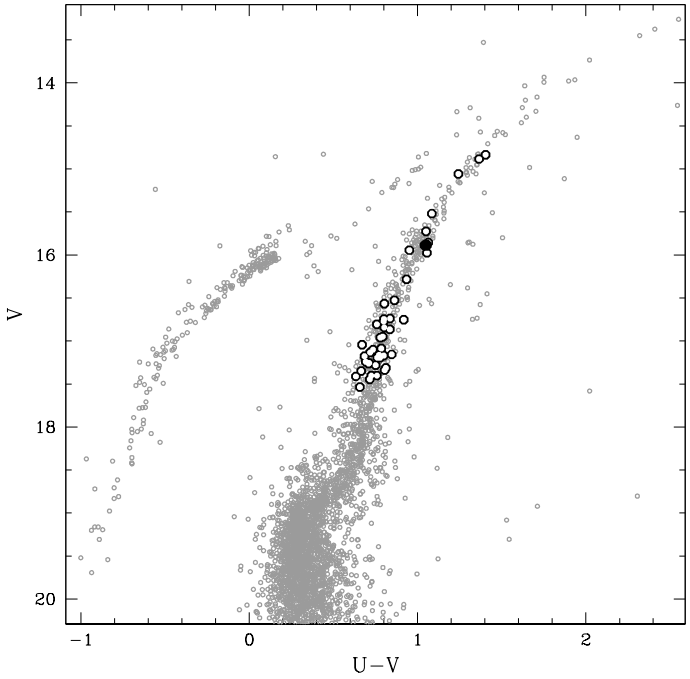

Figure 4.1: $V, U-V$ CMD for M 2 from DOLORES images. White dots mark spectroscopic targets, the black dot shows the probable field star (see Sect. 4.1.2).

.

Because the goal of our spectroscopic observations was to measure the strengths of the 3883 and 4300 Å CN and CH absorption bands, we used the LRB grism with a dispersion of 2.52 Å/pix. In combination with the chosen slit width this results in the spectral resolution of R(@3880Å) = 353 and R(@4305Å) = 391 in the wavelength region of interest. The grism's spectral region covers the nominal wavelength range between $3000-8430$ Å, while the actual spectral coverage depends on the location of the slit on the mask with respect to the dispersion direction. To reach a high S/N, each mask configuration was observed three times with exposure durations of 1800 sec-

onds each, leading to a total exposure time of 1.5 hours per mask and a typical S/N of $\simeq$ 20-30 in the CN region. Additionally, bias, flat field, and wavelength calibration observations were obtained in the afternoon.

For the data prereduction, we used the standard procedure for overscan correction and bias-subtraction with the routines available in the *noao.imred.ccdred* package in IRAF. First, we stacked the flat fields for each night and mask. Because each slit mask was observed three times and the alignment of the frames was quite good, we co-added the three frames for a given slit mask with cosmic-ray rejection enabled, providing resulting frames that were almost free of cosmic rays. For the following analysis we extracted the area around each slit with the optimal extraction and treated the resulting spectra as single-slit observations. The wavelength-calibration images and flat fields were treated in the same manner. TNG spectroscopic flats show a severe internal reflection problem in the blue regions of the spectra that could in principle heavily affect our further measurements. To minimize this effect, we fit the 2D large-scale structures in the normalized spectroscopic flat field by smoothing and dividing the original flat by the fit, keeping the small pixel-to-pixel variations, which are the ones we intend to correct for with flat fielding. The object spectra and arc images were flat-field-calibrated with these corrected flat fields. Standard IRAF routines were used to wavelength-calibrate, sky-subtract, and extract the stellar spectra. The wavelength solution from the HeNeHg arcs was fitted by a first-order spline. The typical rms of the wavelength calibration is on the order of 0.3 Å, which is largely expected at the given spectral resolution. The residual uncertainties in the wavelength calibration are then removed using the position of strong emission lines (in particular OI at 5577.7 Å and NaD at 5895 Å).

The shape of the final spectra is affected by the dependence of the instrumental response on the wavelength. Given the quite low instrument response in the blue part of the spectrum and the presence of many absorptions in this region, we avoided any attempt to remove this effect through flux calibration or continuum normalization (see Pancino et al., 2010, and references therein).

To derive the membership of candidate RGB stars, we first performed a cross-correlation of the object spectrum with the highest S/N star on each MOS mask as a template with the IRAF *fxcor* routine, as in Sect. 3.1.3. The template V_r were computed using the laboratory positions of the most prominent spectral features (e.g., H_α, H_β, H_γ, H_δ, and Ca (H+K), among others), yielding a mean radial velocity of -13 $\pm$ 30 km/s for the entire sample. This value, given the low resolution of our spectra, agrees quite well with the value tabulated (–5.0 km/s) in the Harris, 1996 (2010 edition) catalog. Then, we rejected individual stars with values deviating by more than 3σ from this average velocity, deeming them to be probable field stars. Only one star (ID:10427, see Fig. 4.1) was rejected based on its radial velocity. In a final step, we examined each spectrum individually and rejected spectra with defects (like spikes or holes) in the measurement windows.

4.2 CH and CN band strengths

A set of indices quantifying the strengths of the UV CN band, the G band of CH and the Ca_{II} H and K lines were measured for the spectra. We adopted the indices as defined in Sect. 3.2 and

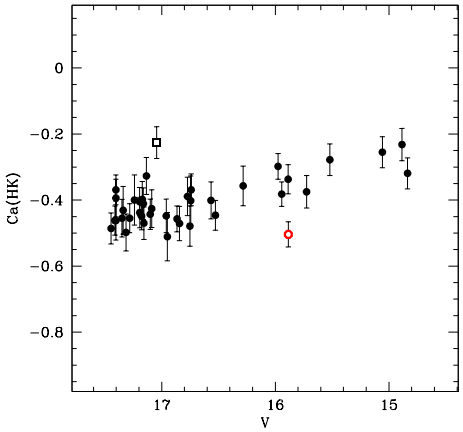

Figure 4.2: The Ca II H and K index plotted vs. V magnitude for the M 2 giants. A probable non-member star is shown as an open square. The small scatter, fully compatible with the formal measurement errors, in the Ca (H+K) values as a function of V provides additional evidence that all spectroscopic targets but the notable outlier are members of M 2. The open red symbol refers to star 10427, which is not a member of M 2, according to its radial velocity.

obtained uncertainties related to the index measurements as explained in the same section. To obtain additional membership information we employed the strength of the Ca_{II} H and K lines (see Sect. 4.2, as in Smith and Mateo, 1990) as a further discriminant between cluster and field stars, since the strength of these lines depends on the metal-abundance in this low to intermediate metallicity regime. By assuming that M 2 is chemically homogeneous with respect to the calcium abundance, we expect that stars belonging to the cluster show a tight sequence in the HK, V plane. We present the plot of HK index vs. the V magnitude in Fig. 4.2. A tight relation between HK index strength and the V magnitude is clearly present for all stars selected using radial velocity criteria. From this figure, we were able to pinpoint only one outlier (ID 21729), whose spectrum has a noticeably strong-lined appearance. We also measured indices for this star to allow for a direct comparison with respect to cluster members; however, we excluded this star from the abundance analysis. Again from Fig. 4.2, we note that the probable field star (rejected according to its radial velocity), does occupy an anomalous position in the the plot of HK index vs. the V magnitude. This evidence further confirms that this stars is not a cluster member. The measured indices, together with additional information on target stars, are listed in Table 4.3.

4.2.1 Index analysis

Figure 4.3 shows S(3839) and CH(4300) index measurements for our data set. Several low-resolution studies have demonstrated that the CN-band strength is a proxy for the nitrogen content of star atmospheres, whereas CH traces carbon (e.g., Smith et al., 1996). A visual inspection of the left hand panel of Fig. 4.3 reveals a clear bimodality in the CN index over the entire magnitude range, with a few mid-strength stars. The difference in S(3839) between CN-strong and CN-weak stars of comparable magnitude is $\sim$0.2-0.3 mag. Giants considered to have relatively strong CN bands and CN-poor giants are represented in Fig. 4.3. The right hand panel of Fig. 4.3

illustrates the relation between the CN and CH band strengths for all giants: it shows a plot of the CH(4300) index vs. the *V* magnitude with the CN-strong and CN-weak stars. In this case the spread among the measured index is very small and, in any case, within the uncertainties. There is a tendency, as expected, for CN-strong stars to also be CH-weak, even if exceptions exist.

Out of a sample of 38 stars, 16 have weak CN bands. The number ratio of CN-weak to CN-strong that we obtained ($\sim$0.73$\pm$0.2) is very different[5] from what is found by Smith and Mateo (1990) (0.33; 16 RGB stars[6]) and Smolinski et al. (2011) (0.35; 70 MS, SGB, and RGB stars.). Comparing these values directly is complicated by the fact that our study only uses RGB stars, while for example Smolinski et al. (2011) includes subgiants and dwarfs and Smith and Mateo (1990) focused on brighter stars. Dwarfs are significantly hotter than RGB stars and less likely to show

[5] We emphasize that the ratio derived here is based on relatively few stars and the criteria for defining CN-strong stars are different in each work.

[6] If we exclude the two CH stars.

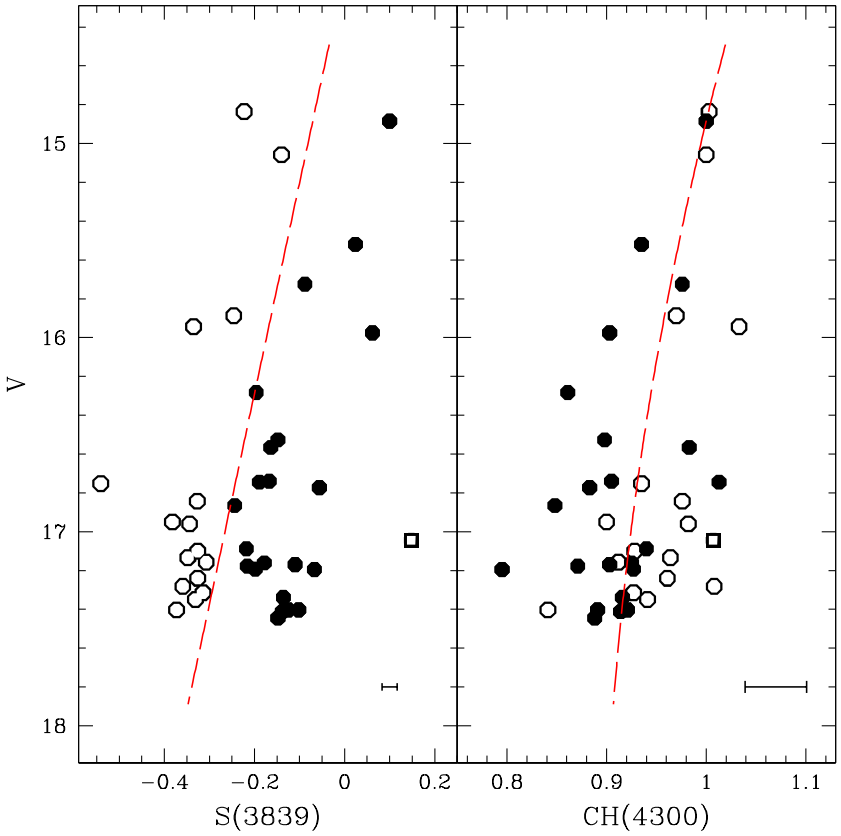

Figure 4.3: *Left panel*: Removal of gravity and temperature dependencies from CN index using median ridge line (shown as red dashed line). Stars considered to have mid-strength or strong CN bands are depicted by filled circles, while CN-weak giants are marked by open circles. A probable non-member star (see Sect. 4.2) is shown as an open square. The median error bar on the S(3839) and CH(4300) measurements is also shown in the lower-right corner of each panel. *Right panel*: The same as in the left panel but for the CH index. The color code is consistent with the left panel.

remarkable CN absorption, thus their inclusion may bias the CN-weak to CN-strong value downward.

To be consistent with our previous works (Sect. 3.2.1), we used *median ridge line* (Fig. 4.3) to minimize the effect of effective temperature and surface gravity in the CH and CN measurements. The baselines adopted for the M 2 red giants to correct S(3839) and CH(4300) indices are

$$S_0 = -0.09 \times V + 1.3$$

$$CH_0 = 0.005 \times V^2 - 0.21 \times V + 2.88,$$

The rectified CN and CH indices are indicated as δS3839 and δCH4300, respectively, and we refer to these new indices in the following[7].

[7]We obtained a rough estimate of the uncertainty in the placement of these median ridge lines by using the first interquartile of the rectified indices divided by the square root of the number of points. The resulting uncertainties (typically ~ 0.013 for the CN index and ~ 0.008 for the CH index) are largely negligible for the applications of this work.

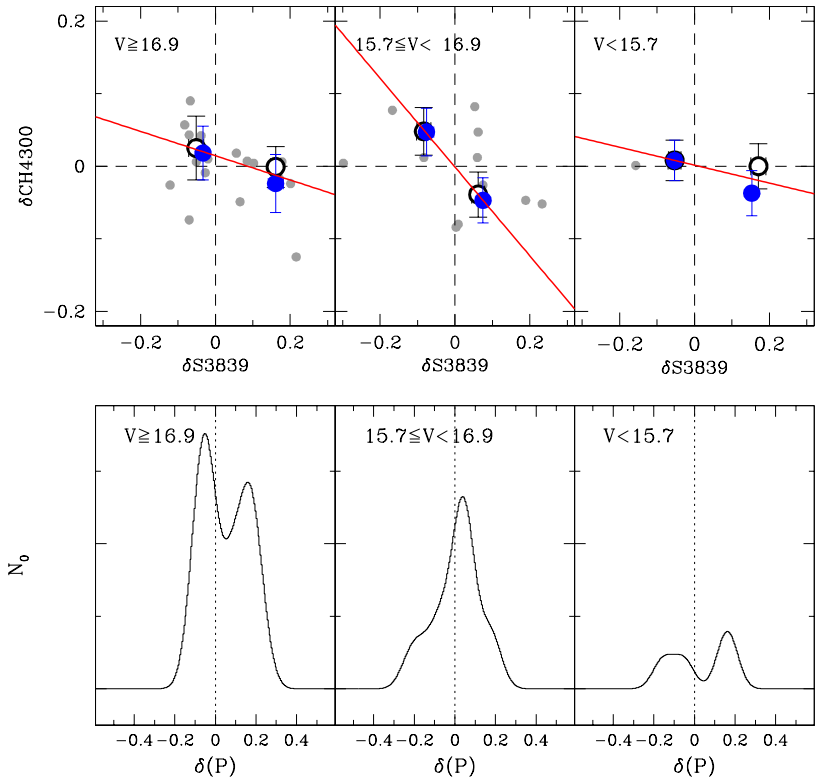

Figure 4.4: *Upper panel*: Anticorrelation plot for the CN and CH band strengths in three magnitude bins (V$\geqslant$16.9 mag, $15.7 \leqslant V < 16.9$ mag and $V < 15.7$ mag). Gray dots show measurements for stars. CH weak and CH strong stars are separated by the horizontal dashed line, and their centroids with 1σ are marked as large white dots. CN strong and weak stars are separated by the vertical dashed line, and their centroids with their 1σ are shown as large blue dots. The red continuous line connects the locus equidistant from CH-strong/CN-weak centroids and CH-weak/CN-strong ones.The generalized histograms in the bottom panels represent the distribution of distances of projected points from the origin P (see text for details).

Figure 4.4 shows the rectified index δS(3839) as a function of δCH(4300) for all the stars studied in this paper. Abundance analysis in Sect. 4.4 confirmed that carbon abundance depends on the evolutionary state and decreases towards brighter luminosities. Therefore, we separately considered stars in three different magnitude bins: $V \geqslant 16.9$, $15.7 \leqslant V < 16.9$, and $V < 15.7$ mag, to minimize the impact of evolutionary effects on our index analysis. To better visualize the hidden substructure in the δS(3839) vs. δCH(4300) plane we adopted the method described below.

- A median is used to compute the centroids of the CH-strong (δCH(4300) > 0) and CH-weak (δCH(4300) < 0) in the CH-CN plane. The resulting centroids with their 1σ errors are reported in Fig. 4.4 along with the measurements for each star. We also divided also the stars into CN-strong (δS(3839) > 0) and CH-weak (δS(3839) < 0) groups and their centroids with relative error bars are plotted in the same figure;

- A line passing through the midpoint connecting CH-strong/CN-weak and CH-weak/CN-strong centroids is traced;

- Each observed point in the CN-CH plane is projected onto this line;

- We take as origin (P) the intersection between this line and the perpendicular line passing through the point (δS(3839), δCH(4300))=(0,0);

- A generalized histogram of the distribution of distances of projected points from the origin P is constructed.

The histograms are shown in the bottom panels of Fig. 4.4, where different panels show different subsamples of RGB stars. Each data point in this histogram has been replaced by a Gaussian of unit area and standard deviation σ=0.04 [8]. We distinguish between CN-strong (CH-weak) stars and CN-weak (CH-strong) stars by cutting at zero the histogram of distances distribution. The dimension of the subsamples, and the number of CN-strong stars in each bin is listed in the second and third columns, respectively, in Table 4.2. Figure 4.4 shows that stars fainter than V$\simeq$16.9

Table 4.2: Dimension of the samples and results of KS test.

MAG BIN	N_{Stars}	CN-s(CH-w)	P_{KS}
$V \geqslant 16.9$ mag	21	11	$1.14e^{-0.5}$
$15.7 < V \leqslant 16.9$ mag	13	9	0.002
$V < 15.7$ mag	4	2	0.1

display clear bimodality, with both CN-strong (CH-weak) and CN-weak (CH-strong) stars, as is common among GCs of intermediate metallicity. For brighter giants, the distribution of the projected points is still not described well by a single symmetric Gaussian curve: indeed, a two-sided Kolgomorov-Smirnov returns a probability of $P_{KS} = 0.002$ ($P_{KS} = 1.14 \times 10^{-5}$ for stars in the first magnitude bin, see the last column in Table 4.2) that the CN-strong (CH-weak) and CN-weak

[8] The 0.04 magnitudes used as the Gaussian width in the generalized histograms of Fig. 4.4 is the same as the measurement error on δS(3839).

(CH-strong) are drawn from the same parent population. When analyzing all data sets, the underlying bimodality can be confused by evolutionary effects (mixing), but a wide spread with three notable peaks is still present. Again from Fig. 4.4 (top panel), for all magnitude bins we report a clear CH-CN anticorrelation for all magnitude bins.

4.3 Abundance analysis

4.3.1 Atmospheric parameters

We derived stellar parameters from photometry. The effective temperature T_{eff} was calculated using Alonso et al. (1999) T_{eff}-color calibrations for giant stars. We used the $U-V$ color from DOLORES photometry (once calibrated on the Stetson standard field), using $E(B-V)$ =0.06 and [Fe/H] = –1.65 from the Harris (1996) catalog (2010 edition). In addition, we used – when available – $B-V$, $V-J$, $V-H$, and $V-K$ colors from Lee and Carney (1999) and the 2MASS (Skrutskie et al., 2006) photometry. The final T_{eff} was the mean of the individual T_{eff} values from each color weighted by the uncertainties for each color calibration. The surface gravity was determined using T_{eff} , a distance modulus of $(m-M)_V$=16.05 (Harris, 1996), bolometric corrections BC(V) from Alonso et al. (1999), and an assumed mass of 0.8 $M_{\odot}$ (Bergbusch and VandenBerg, 2001). The microturbulent velocity was determined using the relation, $v_t = -8.6 \times 10^{-4} T_{eff} + 5.6$, adopted from the analysis by Pilachowski et al. (1996) of metal-poor subgiant and giant stars with comparable stellar parameters. This method leads to an average microturbulent velocity estimate of $v_t = 1.1 \pm 0.13$ km s^{-1}, therefore we chose to assign a reference microturbulent velocity of $v_t = 1.0$ km s^{-1} to all our program stars.

An additional check to test the reliability of our chosen atmospheric parameters was performed using theoretical isochrones downloaded from the Dartmouth Stellar Evolution Database (Dotter et al., 2008)[9]. We chose an isochrone of 12 Gyr with standard α-enhanced composition, and we projected our targets on the isochrone (following a criterion of minimum distance from the isochrone points) in the $U,(U-V)$ diagram to obtain their parameters. The *median* difference in temperature between the two methods is approximately 20$\pm$4 K, while the difference in gravity is negligible (on the order of 0.013$\pm$0.002). By projecting our targets on the isochrone in the *intrinsically* broad $U,U-V$ RGB, we could possibly erase differences in color (and thus in temperature) between spectroscopic targets; therefore, we preferred to rely on the Alonso et al. (1999) parameter estimates.

The residual external uncertainties, which could result only in a shift of the zero point, do not affect the amplitude of star-to-star variation in C and N, because we want to measure the internal intrinsic spread of our sample of stars. Table 4.4 reports the T_{eff}, $\log g$ values, and their uncertainties used to derive C and N abundances.

[9] `http://stellar.dartmouth.edu/models/isolf.html`

4.3.2 Abundances derivation

Abundances for a given element were derived by comparing synthetic spectra with observed spectra, as explained in Sect. 3.3.2. Briefly, the C and N abundances were estimated by spectral synthesis of the $^2\Sigma$–$^2\Pi$ band of CH (the G band) at ∼4310 Å and the UV CN band at 3883 Å , respectively. The synthetic spectra were generated using the local thermodynamic equilibrium (LTE) program MOOG (Sneden, 1973). The atomic and molecular line lists were taken from the latest Kurucz compilation (Castelli and Hubrig, 2004) and downloaded from the F. Castelli website[10].

Model atmospheres were calculated with the ATLAS9 code, starting from the grid of models available on the F. Castelli website (Castelli and Kurucz, 2003), using the values of T_{eff}, $\log g$,

[10] http://wwwuser.oat.ts.astro.it/castelli/linelists.html

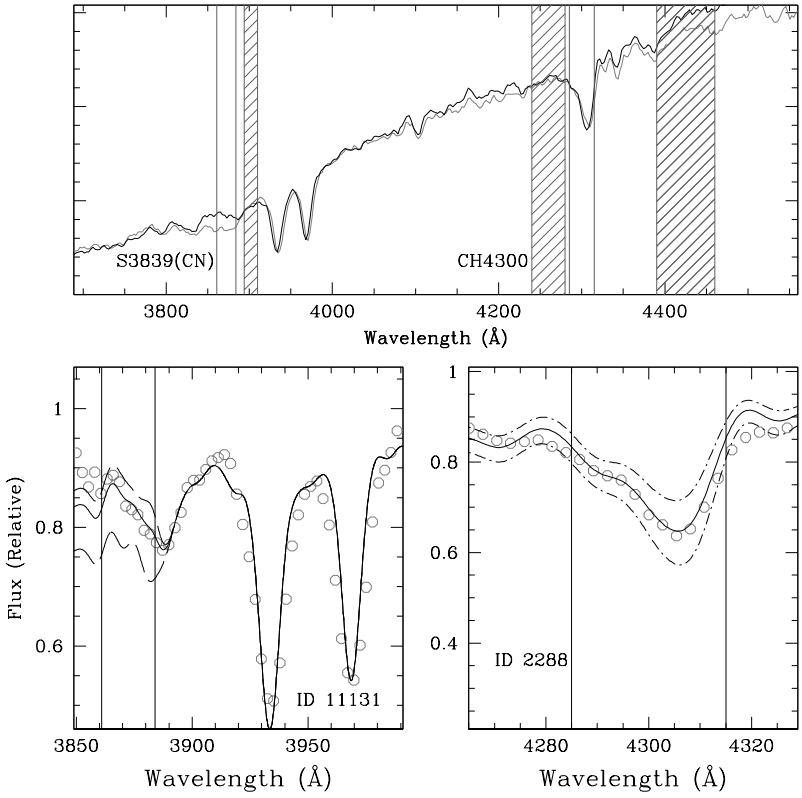

Figure 4.5: *Top panel*: DOLORES-LRB spectra of the stars 17116 (gray) and 18369 (black) in the region of the CN UV feature and CH band. The stars are essentially identical in V magnitude (V=15.86, 15.94 mag, respectively), $U-V$ color ($U-V$ = 1.06 and 0.95, respectively), and C abundance (see Table 4.4). The gray shaded regions show the continuum regions, while the solid gray lines show the window from which we measured the CN and CH indices. *Bottom panels:* observed (gray empty circles) and synthetic (line) spectra around the CN and CH band for the stars 11131 and 2288 stars, respectively. The solid line represents the best fit, while the dashed-dotted lines are the synthetic spectra computed with the derived C abundance altered by ±0.2 dex and N abundance altered by ± 0.5 dex from the best value. Vertical lines show the location of the CN (3861 – 3884 Å) and CH (4285 – 4315 Å) absorption bandpass.

and v_t determined as explained in the previous section. For all the models we adopted [A/H]= –1.5, according to the metallicity of the cluster. The ATLAS9 models we employed were computed with the new set of opacity distribution functions (Castelli and Kurucz, 2003) and excluded approximate overshooting in calculating the convective flux. For the CH transitions, the $\log g_f$ obtained from the Kurucz database were revised downward by 0.3 dex to better reproduce the solar-flux spectrum by Neckel and Labs (1984) with the C abundance by Caffau et al. (2011), as extensively discussed in Mucciarelli et al. (2012). Figure 4.5 illustrates the fit of synthetic spectra to the observed ones in CH and CN spectral regions. These stars have essentially the same stellar parameters ($T_{eff} \simeq 5000$ K log g =2.2 dex), lying at about the same place in the cluster CMD, yet their CN bands differ strongly. Because the abundances of C and N are coupled, we iterated until self-consistent abundances were obtained.

We assumed that all stars had the same oxygen abundance ([O/Fe] = +0.4 dex) regardless of luminosity (constant oxygen abundance as the star evolves along the RGB). The derived C abundance is dependent on the O abundance and therefore so is the N abundance. In molecular equilibrium an overestimate of oxygen produces an overestimate of carbon (and vice versa), and an overestimate of carbon from CN features is reflected in an underestimate of nitrogen. We expect that the exact O values will affect the derived C abundances only negligibly, since the CO coupling is marginal in cool stellar atmospheres ($T \leqslant 4500$ K). To quantify the sensitivity of the C abundance on the adopted O abundance, we varied the oxygen abundances and repeated the spectrum synthesis to determine the exact dependence for a few representative stars (4900 K $\leqslant T_{eff} \leqslant$ 5400 K). In these computations, we adopted [O/Fe]= -0.2 dex, [O/Fe]= 0.0 dex, and [O/Fe]= +0.4 dex. We found that strong variations in the oxygen abundance markedly affect the derived C abundance only for the brighter stars in our sample, for which [C/Fe] can change by as much as 0.17-0.20 dex for a 0.6 dex change in assumed [O/Fe]. This is within the uncertainty assigned to our measurement. See also a discussion of the effects of considering different O abundance on carbon abundance derivation in Martell et al. (2008).

The total error in the derived C and N abundances was computed by taking the internal errors associated to the chemical abundances into account. Two sources of errors can contribute to this internal error: (i) the uncertainty introduced by errors in the atmospheric parameters used to compute chemical abundances, and (ii) the error in the fitting procedure and errors in the abundances that are likely caused by noise in the spectra. To estimate the sensitivity of the derived abundances to the adopted atmospheric parameters, we therefore repeated our abundance analysis and changed only one parameter at each iteration for several stars that are representative of the temperature and gravity range explored.

Typically, we found δA(C)/δ $T_{eff} \simeq 0.09 - 0.13$ and δA(N)/δ $T_{eff} \simeq 0.14 - 0.18$ for the temperature. The errors due to uncertainties on gravity and microturbulent velocity are negligible (on the order of 0.03 dex or less). The contribution of continuum placement errors was estimated by determining the change in the abundances as the synthetic/observed continuum normalization

was varied[11]: generally, this uncertainty added 0.11 dex to the abundances. The errors derived from the fitting procedure were then added in quadrature to the errors introduced by atmospheric parameters, resulting in an overall error of approximately 0.20 dex for the C abundances and 0.22 dex for the N values.

We present the abundances derived as described above and the relative uncertainties in the abundance determination in Table 4.4. Additionally, this table lists the derived atmospheric parameters of all our targets.

4.4 C and N abundance results

Variations in light-element abundances were already observed in all GCs studied to date, and are also present in M 2. Carbon and nitrogen exhibit the typical anticorrelation, as shown in Fig.4.6, where the [C/Fe] values are plotted as a function of [N/Fe] with their uncertainties. For three stars out of 38, we were not able to derive C and N abundances because of the low S/N in the CN band spectral region. We observe modest variations in carbon abundances (from [C/Fe]$\sim$ –1.4 to [C/Fe]$\sim$ –0.4 dex) mildly anticorrelated (Spearman's rank correlation coefficient $r_S^{M\,2}$ = –0.35) with strong variations in N, which span almost 2 dex, from [N/Fe]$\simeq$ –0.3 up to [N/Fe]$\simeq$ 1.4

[11] We continuum-normalized our spectra using the same function (cubic spline) in the task IRAF *continuum* but with an order slightly higher with respect to that chosen for the first normalization.

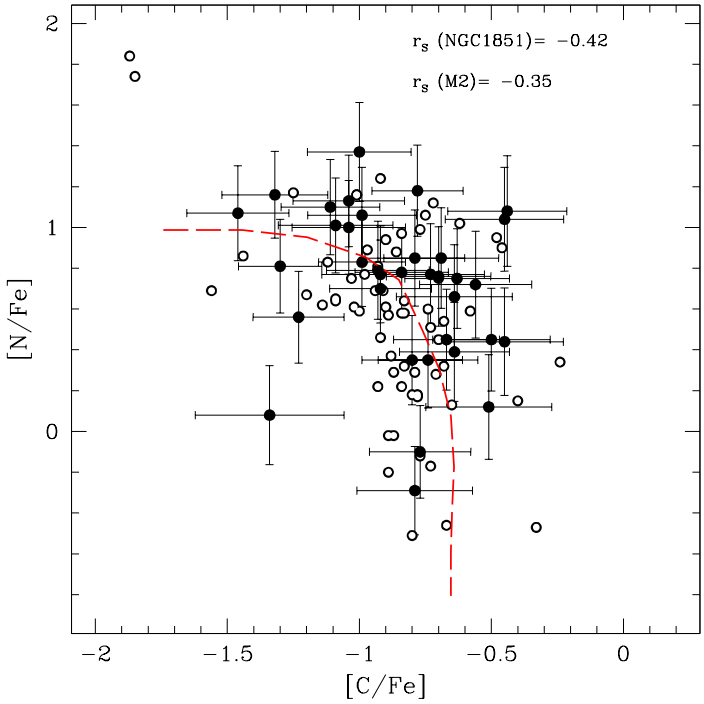

Figure 4.6: Derived [N/Fe] abundances for M 2 stars in Table 4.4 as a function of the [C/Fe] abundances from our sample (filled circles). A C vs. N anticorrelation is apparent. For comparison we also plotted our previous results on a sample of MS and SGB stars in the cluster NGC 1851 (white dots). The red dashed line indicates the relationship, shown over its full range, that prevails in NGC 1851 from our earlier work.

dex. In the same figure we also plot C and N abundances derived for NGC 1851 in our previous work (Lardo et al., 2012a) (see Chapter 3) with the [C/Fe]-[N/Fe] relationship that prevails for these stars ($r_S^{NGC\ 1851}$ = –0.42). The range of the spread in both C and N is about the same for M 2 and NGC 1851[12] (and fully agrees with the C and N abundances presented by Cohen et al., 2005, for M 71, 47 Tuc, M 5, M 13, and M 15). The two anticorrelations clearly follow a similar overall pattern in the [C/Fe] vs [N/Fe] plane.

4.4.1 Evolutionary effects along the RGB

Following the classical prediction, during the H-burning phase via the CNO cycle, N is enriched at the cost of C and O. When a star evolves off the main sequence, the convective envelope starts to move inward, *dredging up* material that has been processed through partial hydrogen burning by the CNO cycle and pp chains. Canonically, light-element abundances should be untouched by subsequent evolution along the RGB, but the observational evidence has shown that both various light-element abundances (particularly [C/Fe] and $\log\epsilon$(Li)) and isotopic ratios (^{12}C/^{13}C) vary as the stars evolve along the RGB, and this cannot be accounted by a single first dredge-up alone (see Sect. 1.1 for a complete discussion).

Some further nonconvective *deep mixing* should take place in the advanced phases of RGB evolution: after the end of the dredge-up phase is reached, the star's convective envelope begins to move outward, leaving behind a sharp discontinuity in mean molecular weight (the μ-barrier) at the point of deepest inward progress (Iben, 1968). The corresponding change in molecular weight can potentially hinder further mixing. However, during the evolution along the RGB, the hydrogen-burning shell advances outward and eventually encounters the μ-barrier. The influx of fresh hydrogen-rich material to the hydrogen-burning shell causes a temporary slowdown of the star's evolution, which manifests itself in a bump in the differential luminosity function (LF) of the cluster. Thereafter, since the molecular gradient is effectively canceled out, some further mixing episodes are allowed. Briefly, possible sources of extramixing could be rotation-induced mixing (Charbonnel, 1995) or thermohaline mixing associated with the reaction 3He(3He,2p)4He (Angelou et al., 2012). Extramixing is a universal mechanism that occurs in $\geqslant$ 96% of these RGB bump stars (Charbonnel and Do Nascimento, 1998) in the field, in open and globular clusters and also in stars in external galaxies. Therefore, surface abundance changes due to deep mixing are not expected to occur in stars fainter than the RGB bump.

We plotted the derived abundances as a function of the V magnitude and $U-V$ color in Fig. 4.7 to evaluate possible systematic effects with luminosity and temperature. While none of these effects is apparent, the top panel of Fig. 4.7 again illustrates the notable depletion in the carbon abundances with luminosity (Shetrone et al., 1993; Smith and Martell, 2003; Gratton et al., 2000, and references therein). The surface carbon abundance depletion along the RGB of M 2 can be straightforwardly interpreted within a deep-mixing framework. This implies that

[12] For comparison, the median value of carbon abundance is [C/Fe]=–0.79 dex (σ=0.2) for M 2 and [C/Fe]=–0.84 dex (σ=0.12 dex); respectively. Median nitrogen abundances are [N/Fe]=0.77 (σ =0.31 dex) for M 2 and [N/Fe]=0.61 for NGC 1851 (σ =0.30).

some form of deep mixing (i. e., meridional circulation currents, turbolent diffusion or some similar processes), which extends below the base of the conventional convective zone, must circulate material from the base of the convective envelope down into the CN(O)-burning region near the hydrogen-burning shell. The onset of the decline in the carbon abundance appears from Fig. 4.7 to occur at magnitude V$\simeq$15.7 mag: the strong C decline for stars brighter than V$\lesssim$15.7 mag can be interpreted as the signature of the extra mixing common among metal-poor cluster giants as they cross the RGB bump. Restricting our sample to those giants fainter than the RGB bump, we found an average C abundance of A(C)=6.11 $\pm$ 0.23. A significant decrease in C abundance occurs at about V$\lesssim$ 15.7, which is essentially the location of the RGB bump in this cluster (V_{BUMP} $\sim$15.82$\pm$0.05, Di Cecco et al., 2010): the average value for this group of upper RGB stars is A(C)=5.61 $\pm$ 0.05. Naturally, the extent of the carbon (nitrogen) depletion (enhancement) depends on the value of [O/Fe] used in the analysis. For comparison, in metal-poor field giants (Gratton et al., 2000), a drop in the surface ^{12}C abundance by about a factor 2.5, is seen after this second mixing episode. To connect CN index measurements with carbon and nitrogen

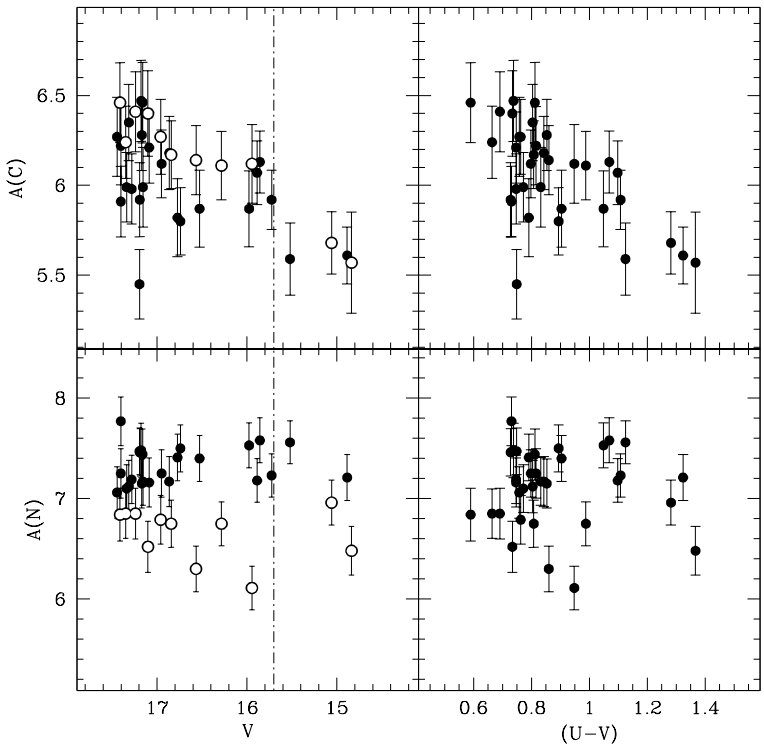

Figure 4.7: Derived C and N abundances plotted against the V magnitude and $U-V$ color for M 2 giants. The dot-dashed lines indicate the luminosity at which the RGB bump occurs (V $\sim$15.7 mag). Relatively N-rich and N-poor stars are shown in the left panels as filled and open symbols, respectively.

abundances derived by spectral synthesis, we labeled CN-strong and CN-weak stars in Fig. 4.8 as defined in Sect. 4.2 in the A(C) and A(N) vs. V mag and A(C) vs. A(N) planes. From Fig. 4.8, we note good agreement between the underlying [N/Fe] abundance and the measured CN band

strength: as expected CN-strong and CN-weak stars tend to occupy two separate regions in the A(C)-A(N) diagram.

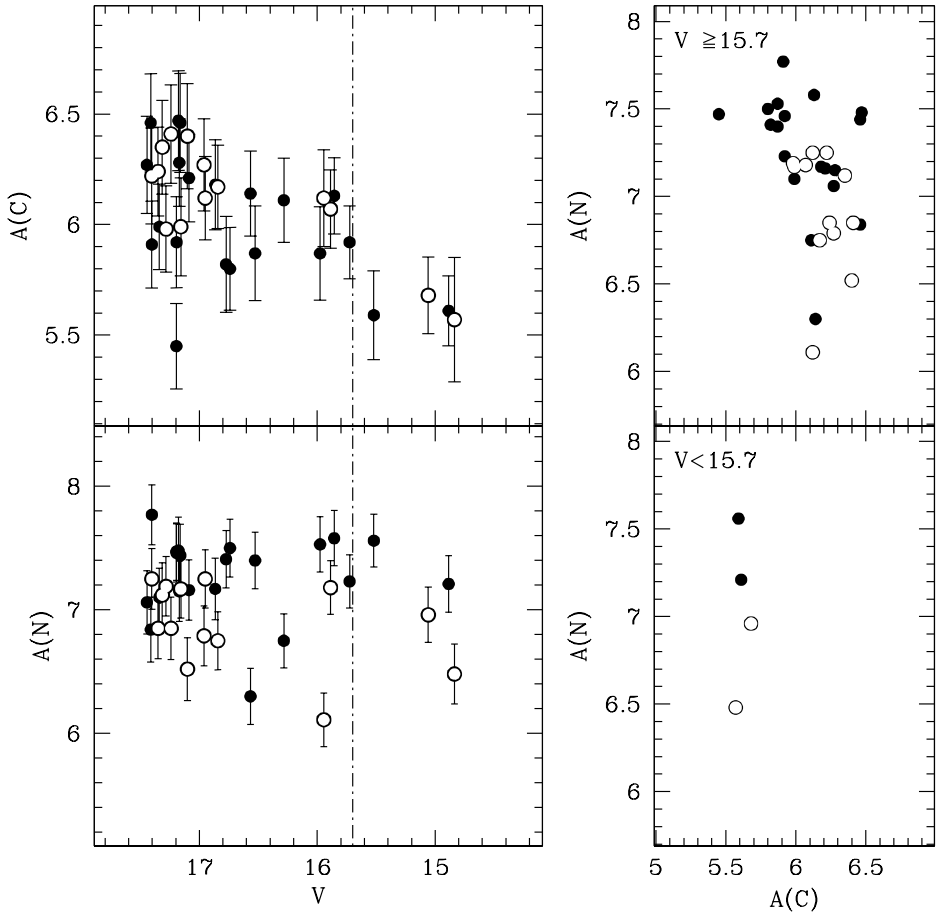

Figure 4.8: *Left panels*: derived C and N abundances are plotted against the V magnitude for M 2 RGB stars. The dot-dashed vertical lines indicate the luminosity at which the RGB bump occurs ($V \sim$15.7 mag). CN-strong and CN-weak stars, as defined in Sect. 4.2, are shown as filled and open symbols, respectively. *Right panel*: CN-strong and CN-weak stars (see Sect. 4.2) are plotted in the A(C)vs A(N) plane for stars with luminosities fainter (*top*) and brighter (*bottom*) than the RGB bump. The color code is consistent with the left panel.

Any difference of [C/Fe] at a given magnitude is difficult to interpret since it can arise from systematic differences between the analysis techniques. As discussed in Smith and Martell (2003), a reasonable estimate of the dependence of the carbon abundance on luminosity can be obtained by deriving d[C/Fe]/dM_V. To compare the behavior of [C/Fe] among from field giants with M 2 giants, we fit a linear least-squares regression of [C/Fe] against M_V for stars with –0.8 $\leqslant M_V \leqslant$ 1.6. We restricted our attention to stars selected by Smith and Martell (2003)[13] from the Gratton et al. (2000) survey. In close analogy with Smith and Martell (2003), we limited our fit to stars with $M_V \leqslant$1.6, because there is only a slight variation below this luminosity level (see Fig. 10

[13]We consider the the restricted sample with the exclusion of stars HD97 and HD218857.

of Gratton et al., 2000). The upper limit in luminosity was chosen to compare only the overlapping region between the two data sets. As far as can be ascertained from the carbon abundances, the rate of mixing in this cluster is comparable to the one for halo field stars and many cluster giants. We found a dependence of $d[C/Fe]/dM_V$=0.21$\pm$0.16 that is very similar within the observational errors to that found among halo field giants (d[C/Fe]/dM$_V$=0.20$\pm$0.03 dex) and other GCs (e.g., M 3, NGC 6397, and M 13; Smith and Martell, 2003).

From the bottom left hand panel of Fig. 4.7, we see no significant trend in the N abundance with either luminosity or color: the average nitrogen abundance we found for stars fainter than the RGB bump (A(N)=7.1 $\pm$ 0.4) agrees within the quite large error bar with the one obtained for the more luminous stars after the LF bump (A(N)=6.9 $\pm$ 0.6). We tentatively divided the target stars between candidate first-generation and candidate second-generation (N-poor and N-rich component, respectively) stars by adopting a threshold in nitrogen abundance A(N)=7.0. In Fig. 4.7, N-poor and N-rich stars are plotted, where we note that N-rich stars are systematically C-poor and vice versa, to further support the presence of C-N anticorrelation. Finally, Gratton et al. (2000) show an abrupt increase in N abundance of about $\sim$ 4 at $\sim V_{BUMP}$ for field giants. Here we could not detect such a trend as the effect of the poor statistics (4 stars) towards higher luminosities.

4.4.2 C-N anticorrelation

We have seen in Sect. 4.4.1 how deep mixing affects nitrogen and (strongly) carbon abundances, because it introduces carbon-depleted material into the stellar convective envelopes. All our target stars have luminosities well above the first dredge-up onset, so we expect that their atmospheres are already depleted in carbon abundance[14]. A matter we plan to investigate now is how to disentangle the *intrinsic* star-to-star differences in surface carbon and nitrogen abundances from the changes resulting from normal stellar evolution. First, we note that we cannot arbitrarily distinguish between two groups of stars with different A(C) or A(N) for stars fainter than the LF peak, because we are unable to detect any clear bimodality. To make more quantitative statements about bimodality, a KMM test (Ashman et al., 1994) was applied to the data[15]. Under the assumption that the two Gaussians have the same dispersion (homoscedastic test), we can confirm that there is no bimodality in either A(C) or A(N) for stars with $V \geqslant 15.7$. At this point we proceed to analyze the C-N anticorrelation as follows:

- computed the median abundance of carbon and nitrogen for stars with V magnitude < 15.7 and $\geqslant$ 15.7 mag (traced in red in Fig. 4.9);

- for each measured point in the A(C)-A(N) vs. V magnitude plane, and calculated the difference between A(C), A(N) and the *median* carbon and nitrogen abundance ($\delta A(C)$ and $\delta A(N)$, respectively);

[14] Among the field stars, Gratton et al. (2000) data support the occurrence of a small ($\approx$ 0.1 dex) drop in the region of the first dredge-up.

[15] The star 22047 with an anomalously low carbon abundance (A(C) $\simeq$ 5.6) is excluded from the fit.

– constructed a plot of the $\delta A(C)$ vs. $\delta A(N)$.

The *corrected* $\delta A(C)$ vs. $\delta A(N)$ anticorrelation is shown in the bottom right hand panel of Fig. 4.9. In this case, having corrected for the carbon decline due to normal stellar evolution, the anticorrelation appears tighter ($r_S^{M\,2\,corrected} = -0.43$).

To better visualize the distribution of *corrected* C and N abundance in the two magnitude bins, we constructed histograms of the $\delta A(C)$ and $\delta A(N)$ distribution in Fig. 4.10. For stars below the RGB bump we note hints of bimodality in $\delta A(C)$. Despite the low statistics, the *corrected* C-N anticorrelation shows evidence for bimodality in the distribution of N abundances, with at least two (or three) groups of stars populating the extremes of high N or low N (see the lower right panel of Fig. 4.9). To consider stars in the same evolutionary stage as much as possible,

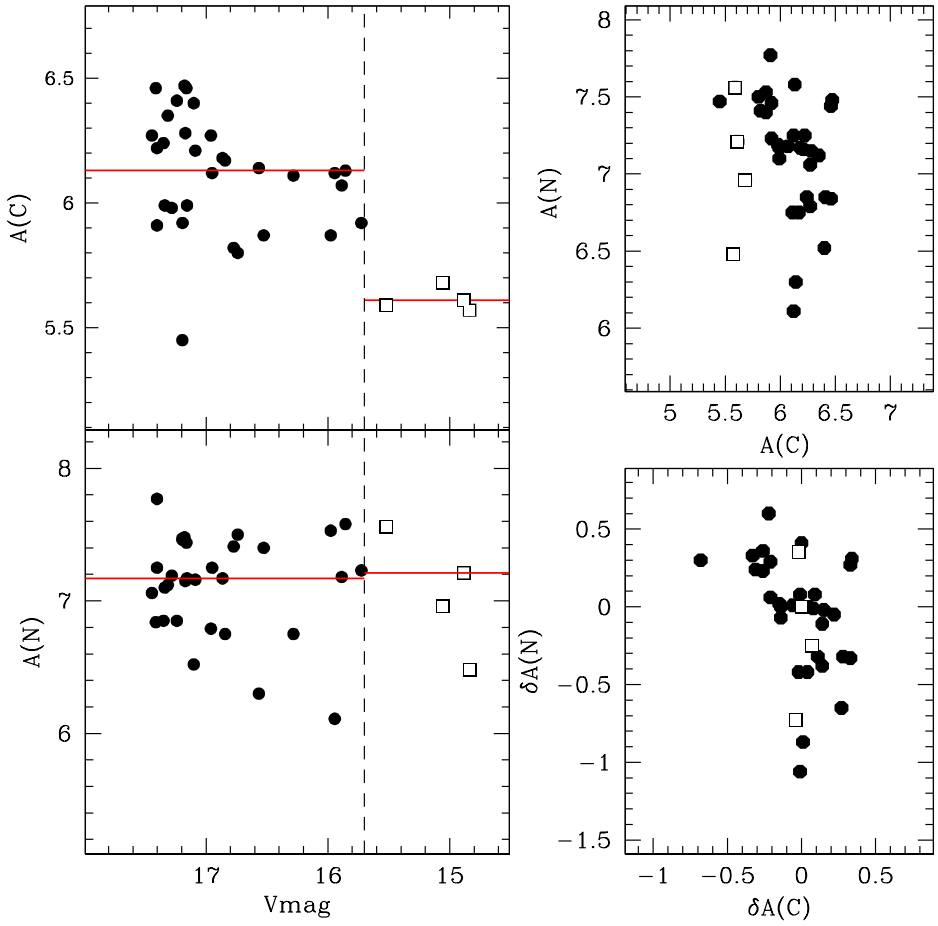

Figure 4.9: Correction of the C-N anticorrelation for evolutionary effect. The left panels show the runs of A(C) and A(N) vs. V magnitude for spectroscopic targets. The vertical dashed line marks the RGB bump position. The red continuous red line indicates *median* value of the carbon and nitrogen abundance for stars in two bins of magnitude ($V < 15.7$ and $V \geqslant 15.7$ mag). The top right panel shows the derived C-N anticorrelation uncorrected for carbon decline (and nitrogen enhancement) due to evolution of the stars along the RGB. The bottom right panel shows the *corrected* C-N anticorrelation. In this case we plotted the difference of A(C) and A(N) from the *median* abundance value shown in the left panels (see text for further details).

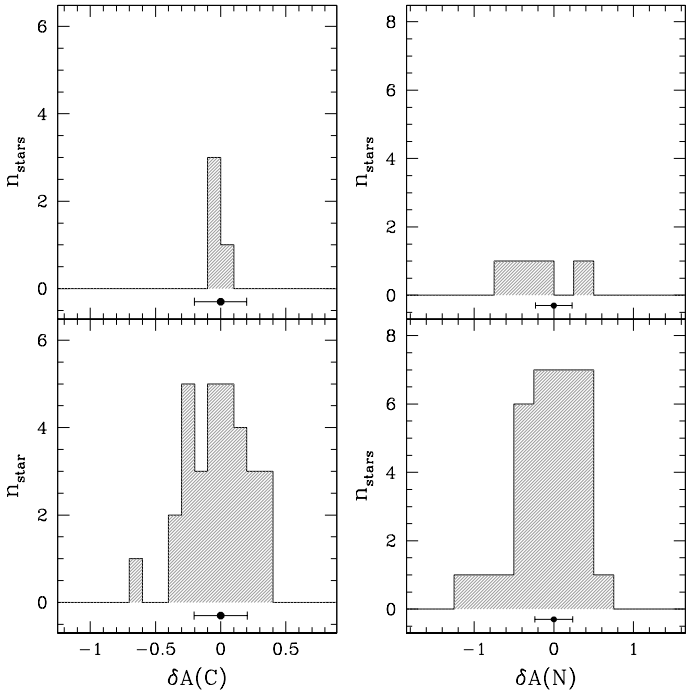

Figure 4.10: Histograms of the δA(C) and $\delta(N)$ (see text) distributions. The two vertical panels correspond to two bins of V mag ($V \geqslant 15.7$ and $V < 15.7$ mag; from bottom to up).The bin size is set to 0.1 and 0.25 for the δA(C) and $\delta(N)$, respectively. Typical median error bars are plotted below each histogram.

we first focused on the the *corrected* C-N anticorrelation for the faintest stars in our sample with magnitudes below the RGB bump ($V \geqslant 15.7$ mag). To confirm this suggestion, we analyzed the *corrected* distribution of stars along the C-N anticorrelation using a procedure similar to the one described in Marino et al. (2008). In brief, we first draw a fiducial (shown in the top right panel of Fig. 4.11) by putting a best-fit spline through the median abundance found in successive short intervals of δ A(N). Then we projected each program star in the δA(C)-δA(N) anticorrelation on this fiducial and plotted the histogram of the distribution of vertical distances (D) of the projected points from the line δA(N)=0. The histogram is shown in the left panel of Fig. 4.11. In this case (at least) two substructures are apparent, peaked at $\simeq$ –0.4 and 0.2. We tentatively divided RGB stars between a candidate first generation and a candidate second generation by setting an arbitrary separation at $D = -0.2$. To allow a direct comparison between CN-strong (as derived in Sect. 4.4) and these second-generation stars, we plotted CN-strong stars in the δA(C)-δA(N) plane in the same figure. We note that the smearing of CN-strong and CN-weak stars that happens in the A(C)-A(N) plane (see Fig. 4.7) is still present in the δA(C) vs. δA(N) plot.

A visual inspection of Fig. 4.11 suggests that the extent of the C-N anticorrelation in the *projected* plane for second-generation (Na-N/rich) stars is greater than the errors associated with abundance measurements. This evidence possibly suggests the presence of a third group of stars[16]; unfortunately, because of uncertainties on abundance measurements and low statistics,

[16]Stars with E (Extreme) composition, by adopting the nomenclature first introduced by Carretta et al. (2009b).

we cannot provide conclusive evidence.

In general, when stars with available Na and O abundances have been identified in the $U, U-B$ CMD (or in a different color combination that includes the blue filters), it was found that the group of Na-poor stars are systematically spread on the blue side of the RGB, while the Na-rich population define a narrow sequence on the red RGB (Grundahl and Briley, 2001; Marino et al., 2008; Han et al., 2009a; Milone et al., 2010). Several authors have demonstrated that a clear correlation exists between N abundances (and so λ3883 CN band strength) and Na, O and Al abundances (see for example Marino et al., 2008, and references therein). N-rich (CN-strong) stars clearly show significantly enhanced Na abundance. In contrast, N-poor (CN-weak) stars have a higher O content than the N-rich ones (see also Chapter 2).

In the bottom right hand panel of Fig. 4.11, N-rich and N-poor stars are superimposed on

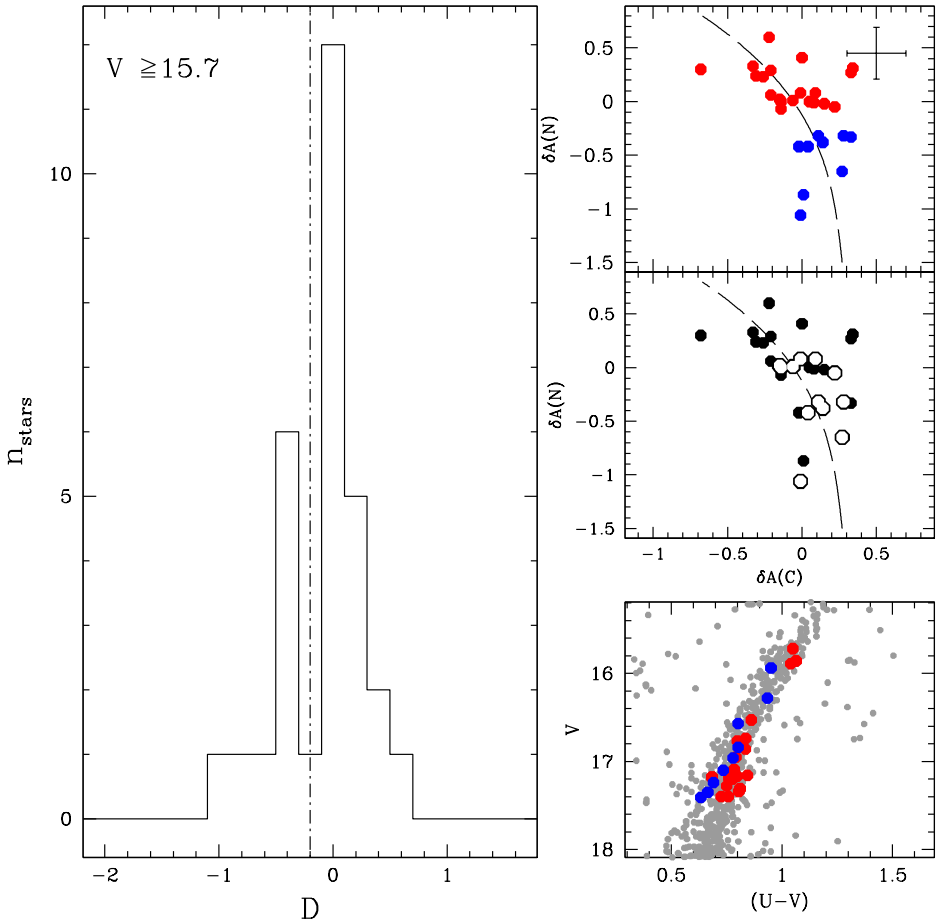

Figure 4.11: *Left panel*: distribution of the projected distance D of stars with V$\geqslant$ 16.9 on the fiducial plotted in the top right panel. The dotted-dashed line separates stars belonging to the two different N groups. *Top right*: *corrected* C-N anticorrelation for stars with $V \geqslant 15.7$. We *tentatively* discriminated between first (blue) and second (red) populations. The error bar represents the typical errors on A(C) and A(N). *Middle right:* CN-strong and CN-weak stars are plotted in the δA(C)-δA(N) plane. *Bottom right:* first- and second-generation stars are superimposed to $V, U-V$ CMD of M 2. The color code is used consistently in each panel.

M 2 $V, U-V$ DOLORES CMD. N-poor and N-rich stars are clearly separated into two parallel sequences in the broader giant branch seen in the $V, U-V$ diagram, with the N-rich stars systematically appearing redder than N-poor ones, a behavior strictly analogous to what is observed Marino et al. (2008) in M 4. It is clear that the strength of the CN and NH bands strongly influences the $U-V$ color, the NH band around 3360 Å, and the CN bands around 3590, 3883, and 4215 Å, located in the U being the main contributors to the effect (see Sect. 1.2.4).

4.5 The discovery of an anomalous RGB in M 2

As discussed in Sect. 1.1, GCs are essentially monometallic, e.g., all the stars in a cluster show the same [Fe/H] abundance. Besides the remarkable exception of ω Centauri (see Marino et al., 2012a, and references therein), variations in the heavy element content have been detected only for a few clusters: M 22 (Marino et al., 2012b), Terzan 5 (Ferraro et al., 2009; Origlia et al., 2011), M 54 (Carretta et al., 2010b), and NGC 1851 (Yong and Grundahl, 2008; Carretta et al., 2010d; Gratton et al., 2012c). In particular, among the clusters that displayed this anomalous behavior, NGC 1851 and M 22 appear rather peculiar. For these clusters, a bimodal distribution of *s*-process elements abundance has been identified (Yong and Grundahl, 2008; Marino et al., 2012b). The chemical inhomogeneity reflects itself in a complex CMD: multiple stellar groups in M 22 and NGC 1851 are also clearly manifested by a split in the SGB region (Piotto, 2009; Milone et al., 2008) which appears to be related to chemical variations observed among RGB stars (Marino et al., 2012b; Lardo et al., 2012a). Indeed, carefully constructed CMDs —based on colors that include a blue filter (Han et al., 2009a; Lardo et al., 2012a; Marino et al., 2012b)— clearly reveal that the bright SGB is connected to the blue RGB, while red RGB stars are linked to the faint SGB. The split of the RGB discovered in the U–I and U–V colors for NGC 1851 and M 22, respectively, would not be detected in the usual optical colors.

M 2 DOLORES photometry (see Fig. 4.1) displays an *anomalous* branch beyond the red edge of the main body of the RGB. The difference in color between stars belonging to this structure and *normal* RGB stars is quite large (on the order of 0.2–0.3 mags, well above the typical measurement errors) and extends down to the SGB region. There may be a second group of stars that are 0.3 mags redder with respect to this sequence and can possibly be more, the anomalous RGB stars. Unfortunately, because of low statistics, we cannot provide a conclusive evidence and radial velocity and proper motion measurements should be made to see whether these stars are members of the cluster.

As a high-latitude system, M 2 is not affected by high interstellar absorption ($E(B-V)$=0.06; Harris, 1996, 2010 edition), and it is very unlikely that the differential reddening has caused the double RGBs. The color difference between the two RGBs in the $U-V$ color, at the given V magnitude of the HB level, is $\sim$0.3 mag, which is about three times more than the maximum color difference expected in the extreme situation where one group of stars is all reddened by $E(B-V)$ = 0.06, while the other group has $E(B-V)$ = 0.00. Because the additional RGB sequence only amounts to a small fraction of the total giant population, we cannot exclude field contamination

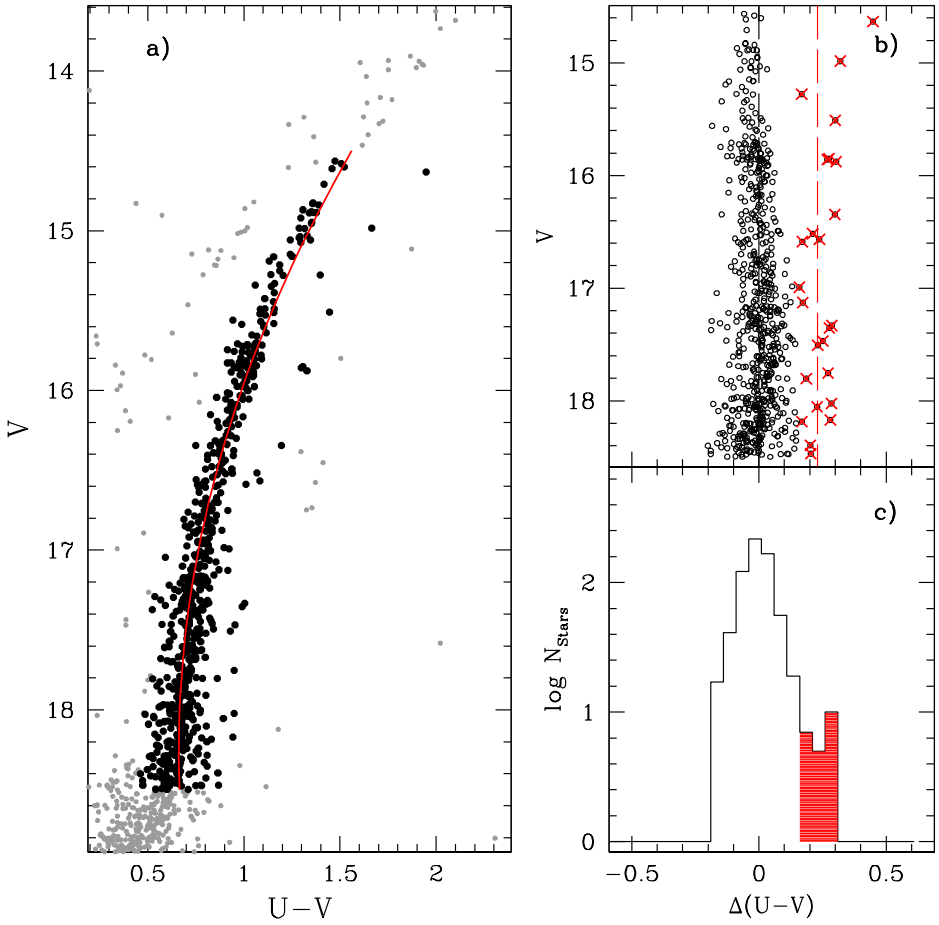

Figure 4.12: (a) U,V CMD from DOLORES images is shown in gray. Selected RGB stars are plotted as black dots, while the red continuous line is the fiducial obtained in the way described in the text. Panels (b) and (c) show the rectified RGB in function of the color difference and the histogram color distribution, respectively (see the text for details).

as the cause of the observed additional RGB branch. We expect a very modest degree of contamination by Galactic fore/background stars, because of the combination between the relatively high (absolute) Galactic latitude of the cluster (b=−36°) and the small area of the considered annular field ($1' < R < 4'$). We used the Galactic model TRILEGAL (Girardi et al., 2005)[17] to obtain a conservative estimate of the degree of contamination affecting the samples of candidate RGB stars with $0.4 \leqslant (U-V) \leqslant 2$ and $18.5 \leqslant V \leqslant 14.5$ mag in the present analysis (Fig. 4.12). We found that the fraction of Galactic field stars in our samples is lower than 1% in the considered annular field.

To take photometric errors into due account, we follow the method described in Anderson et al. (2009) to distinguish intrinsic color broadening from unphysical photometric error effects. We considered the two independent CMDs obtained from DOLORES and An et al. (2008) photometry. In Fig. 4.12 we selected the portion of the RGB sequence with magnitudes between

[17] http://stev.oapd.inaf.it/cgi-bin/trilegal

$14.5 \leqslant V \leqslant 18.5$ mag. In addition, we defined *bona fide* RGB members as the stars closer to the main RGB locus in the corrected DOLORES CMD (panel (a) of Fig 4.12). We obtained the RGB fiducial as described in Milone et al. (2008). In brief, we drew a ridge line (fiducial) by putting a best-fit spline through the average color computed in successive short (0.2 mag) magnitude intervals. In panel (b) we have subtracted from the color of each star the color of the fiducial at the same magnitude and plotted the V magnitude in function of this color difference; $\Delta(U-V)$. The histogram color distribution on a logarithmic scale in panel (c) presents a clear substructure at the red end of the RGB, and we arbitrarily isolated RGB stars with $\Delta(U-V)$ >0.15. These stars are plotted in panel (b). If the red branch we see is due to photometric errors, then a star redder than the RGB ridge line in the $V, U-V$ diagram has the same probability of being bluer or redder in a different CMD obtained with different data. To this purpose, we identified the selected stars in *u, g* photometry (An et al., 2008) in Fig. 4.13. The (a) panel shows a zoom around the RGB, and again the red line is the fiducial defined as discussed above. In the following analysis, we considered only those stars in common with the DOLORES photometry and, for the sake of homogeneity, we kept only stars between $1' < R < 4'$ from the cluster center. That the histogram distributions of the selected RGB stars systematically have red colors demonstrated that we are seeing a *real* feature: no random or systematic errors can explain that the two distribution remain confined in the CMDs obtained from independent data sets. Similar spatial distributions of stars on the bluer and redder RGBs (panel (a) of Fig. 4.13) also indicate that the differential reddening, if any, is not likely the cause of the double RGBs (see panel (c) in the same figure). Having demonstrated that the split RGB shown by the $U, U-V$ DOLORES photometry is *intrinsic*, we named giant stars belonging to the main body of the RGB sequence *blue*, while *red* are the stars located on the anomalous red substructure. We found that the average color difference for the *blue* stars is $\Delta(U-V)_{blue} = -0.005 \pm 0.016$, significantly different from the average color difference for *red* stars ($\Delta(U-V)_{red} = -0.251 \pm 0.017$), which account for only $\sim 4\%$ of the RGB population in this range of magnitude ($14.5 \leqslant V \leqslant 18.5$ mag). For comparison, $\sim 30\%$ of stars turn out to belong to the blue-RGB in NGC 1851 (Lardo et al., 2012a; see Sect. 3.4.1).

A visual inspection at the CMD of Fig. 3 from Dalessandro et al. (2009) indeed reinforces our finding and suggests that the anomalous RGB is also present in the cluster center. Moreover, Piotto et al. (2012) claim the presence of a split SGB for this cluster, with a fainter component remarkably less populous than the brighter one. We tentatively speculate that, also for M 2, this newly discovered double RGB might be photometrically connected to the split SGB, in close analogy to the case of NGC 1851 and M 22.

4.5.1 CH stars along the anomalous RGB

M 2 contains two CH stars, as discovered by Zinn (1981) and Smith and Mateo (1990). These stars show abnormally high CH absorption, together with deep CN bands, compared to other cluster giants. They are seen in dSph galaxies, and in the Galactic halo, but they are relatively rare within GCs. At present, a handful of stars having enhanced C and *s*-process elements have been reported in each of ω Cen (e.g., Harding, 1962; Bond, 1975), M 22 (McClure and Norris,

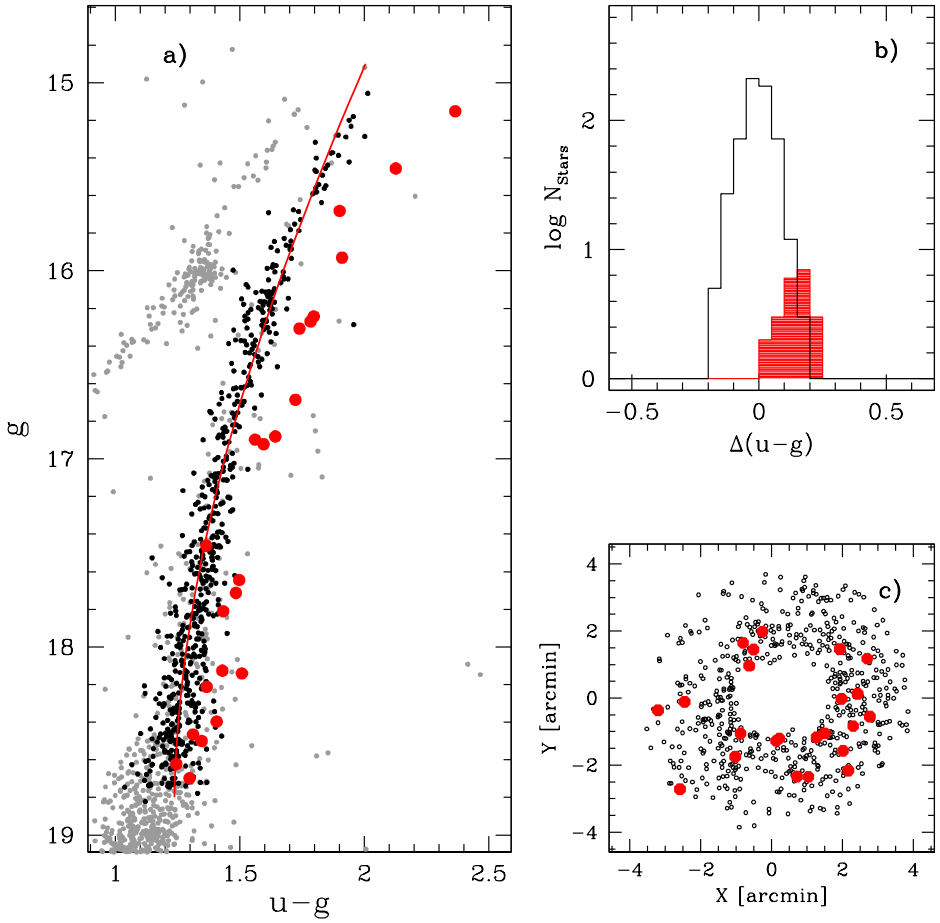

Figure 4.13: (a) $u, u-g$ CMD from An et al. (2008) *corrected* photometry zoomed in around the RGB. Stars selected as red in Fig. 4.12 are plotted as red circles, while the red continuous line is the fiducial obtained in the way described in the text. Panels (b) show the color distribution in the $u-g$ color, while panel (c) shows spatial distribution of the selected red stars.

1977), NGC 1851 (Hesser et al., 1982), M 55 (Smith and Norris, 1982), M 14 (Cote et al., 1997), and NGC 6426 (Sharina et al., 2012). Their spectra usually do not show strong Swan bands of C_2, which dominate optical spectral features of *classical* CH stars, suggesting that their anomalous carbon abundances probably arise through a different mechanism, such as incomplete CN processing (Vanture and Wallerstein, 1992). Indeed, among this sample of CH-enhanced stars in GCs, only two are likely to be genuine CH stars. Both of these stars, RGO 55 (Harding, 1962) and RGO 70 (Dickens, 1972), are found in ω Cen. The surface carbon enhancement of such stars has been attributed to a dredge-up of processed material via mixing or to the mass transfer of such material between members of a binary system (McClure, 1984). Moreover, that both ω Cen and M 22 display heavy element abundance variations suggests that in these clusters CH stars could owe their peculiar chemical pattern to initial enrichment.

Prompted by these considerations, in Fig. 4.14 we identified the two CH stars discovered by Zinn (1981) (ID: I-240) and Smith and Mateo (1990) (ID: I-451) in our $V, U-V$ photometry. Inter-

estingly enough, both stars belong to the additional RGB, pointing out the anomalous chemical nature of this redder branch. Regardless of the exact classification of I-240 and I-451, it is apparent that the anomalous RGB contains a population of giants that exhibit both a strong CN and strong G band. These stars may be the analogous to other CN and CH-strong RGB stars found in ω Cen, M 22, and NGC 1851 (Hesser et al., 1982). Given the peculiarity of other clusters that contain CH stars, it is of extreme interest to investigate the chemical pattern of stars in this red substructure. High-resolution spectroscopy of stars in the two distinct groups could be one of the next steps in deriving the chemical pattern in this cluster, with particular emphasis on the measure of heavy element abundances.

4.6 Summary & conclusions

We have presented low-resolution spectroscopy (R≃350) of RGB stars in M 2, with the goal of deriving C abundances (from the G band of CH) and N abundances (from the CN band at ∼ 3883 Å). We were able to measure CH and CN band strengths for 38 giants and derive carbon and nitrogen abundances for 35 stars, whose spectra were obtained with DOLORES at TNG. The main results of our analysis can be summarized as follows.

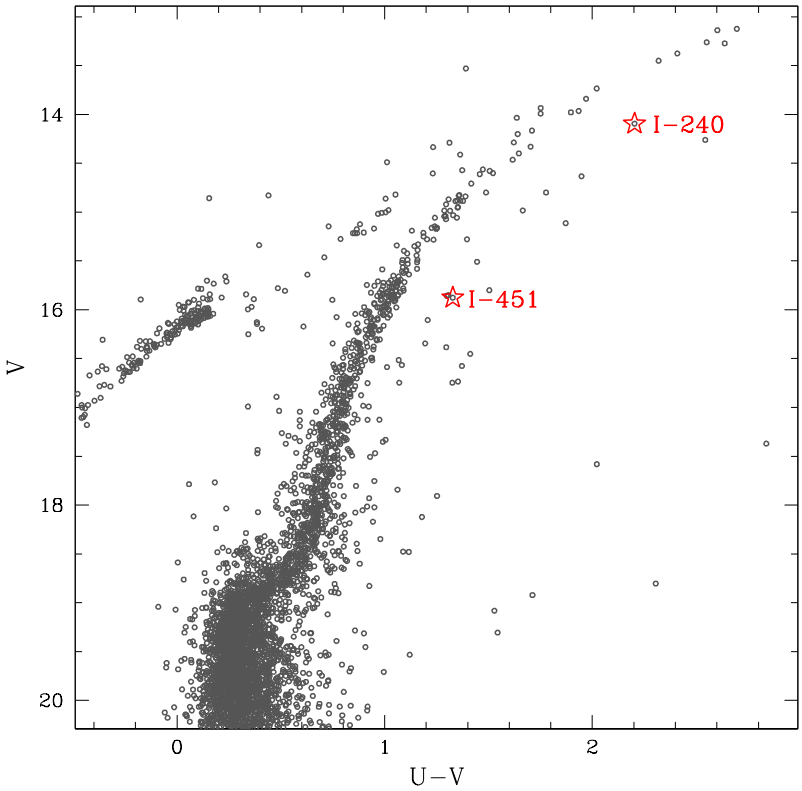

Figure 4.14: CMD for M2. The location of the carbon stars in the CMD is indicated by the open stars.

- ◇ We measured the CH and CN band strengths and found large variations ($\simeq$ 0.2-0.3 mag) and a bimodal distribution of CN index strengths (Fig. 4.3). We did report the presence of a clear CH-CN anticorrelation over the whole magnitude range (see Fig. 4.4).

- ◇ We used spectral synthesis to measure C and N abundances, and found variations of $\simeq$ 1 dex and $\simeq$ 2 dex, respectively, at all luminosities. C and N abundances appear to be anticorrelated, as would be expected from the presence of CN-cycle processing exposed material on the stellar surface (Fig. 4.6).

- ◇ Our derived C abundances show a decline with increasing luminosity. As far as can be derived from the carbon abundances, the rate of mixing in this cluster is comparable to that of halo field stars and many cluster giants. We found $d[C/Fe]/dM_V$=0.21$\pm$0.16, which is very similar within the observational errors to what is found among halo field giants and other globulars (e.g., M 3, NGC 6397, and M 13; Smith and Martell, 2003).

- ◇ We distinguished between first and second subpopulations and found that N-poor and N-rich stars are clearly separated into two parallel sequences in the broader giant branch seen in the $V,(U-V)$ diagram, the N-rich stars appearing systematically redder than N-poor ones, a result that is strictly analogous to the one of Marino et al. (2008) for M 4.

- ◇ In addition to these results, we detected an *anomalous* substructure beyond the red edge of the main body of the RGB (see Fig. 4.1) from DOLORES U,V photometry. When plotting CH stars from the studies of Zinn (1981) and Smith and Mateo (1990) onto the $V,U-V$ CMD (see Fig. 4.14), we found that both stars belong to this additional red RGB. These are giants that exhibit both enhanced CH and CN bands, and this evidence perfectly fits the suggestion that stars located on the red RGB should have a peculiar chemical nature. Moreover, this additional RGB could be connected to the less populated faint SGB detected by Piotto et al. (2012) in this cluster.

Among the GCs with photometric evidence of multiple populations, only NGC 1851 and M 22 display a bimodal SGB that is photometrically connected to the split RGB (see Chapter 3). Both M 22 and NGC 1851 host not only two subpopulations, but they have experienced a complex formation history that resembles the extreme case of ω Centauri (see Marino et al., 2012b; Da Costa and Marino, 2011; Roederer et al., 2011; D'Antona et al., 2011, for a discussion). The apparent similarity of M 2 to NGC 1851 and M 22 calls for a deeper and complete spectroscopic characterization of stars in this poorly studied cluster.

Table 4.3: Index measurements, magnitudes, colors, and radial velocities for the sample stars

ID	ID_{SDSS}	RA (deg)	Dec (deg)	V	U–V	V_r kms^{-1}	CN (mag)	dCN (mag)	δCN (mag)	CH (mag)	dCH (mag)	δCN (mag)
1047	205468	323.35400060	-0.87919450	16.740	0.8360	-30 ± 23	-0.167	0.010	0.075	0.905	0.032	-0.026
1221	204057	323.34119890	-0.87748070	16.283	0.9340	-9 ± 43	-0.196	0.015	0.003	0.861	0.022	-0.084
1249	205374	323.35306530	-0.87727650	16.566	0.8020	11 ± 37	-0.164	0.025	0.062	0.983	0.039	0.047
1921	204613	323.34594560	-0.87168230	15.725	1.0500	-9 ± 25	-0.088	0.017	0.060	0.976	0.024	0.012
1927	206299	323.36152960	-0.87163050	17.403	0.7582	17 ± 62	-0.373	0.025	-0.070	0.841	0.041	-0.074
2288	205760	323.35679530	-0.86887270	15.887	1.0400	-33 ± 21	-0.246	0.019	-0.083	0.970	0.025	0.012
3190	206918	323.36713180	-0.86275460	17.177	0.6840	-1 ± 22	-0.216	0.012	0.066	0.871	0.022	-0.049
3285	204469	323.34467810	-0.86211390	16.745	0.7995	11 ± 28	-0.189	0.035	0.053	1.013	0.041	0.082
3397	206350	323.36209610	-0.86148000	17.170	0.7990	-32 ± 36	-0.110	0.009	0.171	0.903	0.031	-0.017
3760	205848	323.35765450	-0.85923620	17.161	0.7712	-3 ± 25	-0.178	0.012	0.102	0.925	0.028	0.004
4144	206472	323.36324840	-0.85704770	16.527	0.8623	-33 ± 30	-0.148	0.013	0 .074	0.898	0.033	-0.039
5010	206002	323.35884820	-0.85232980	15.058	1.2417	-37 ± 30	-0.140	0.015	-0.053	1.000	0.028	0.008
5149	204376	323.34376850	-0.85158800	15.520	1.0842	11 ± 38	0.024	0.010	0.153	0.935	0.031	-0.037
5185	205505	323.35424850	-0.85143600	17.445	0.7163	-8 ± 29	-0.148	0.023	0.159	0.888	0.031	-0.027
6609	112780	323.36574622	-0.84405523	16.752	0.9172	-5 ± 27	-0.541	0.012	-0.298	0.935	0.023	0.004
9229	106190	323.33041650	-0.83108230	15.976	1.0558	-30 ± 36	0.062	0.012	0.233	0.903	0.021	-0.052
10803	105859	323.32844101	-0.82363565	17.314	0.8108	8 ± 68	-0.314	0.009	-0.020	0.927	0.050	0.010
11131	105112	323.32387272	-0.82204937	16.865	0.8347	-12 ± 27	-0.244	0.024	0.009	0.848	0.031	-0.080
11796	104710	323.32131086	-0.81884683	17.403	0.7250	-37 ± 34	-0.125	0.014	0.178	0.921	0.024	0.006
14343	103672	323.31346832	-0.80667018	16.950	0.7926	5 ± 61	-0.382	0.020	-0.121	0.900	0.049	-0.026
15217	105961	323.32904057	-0.80229140	17.349	0.6652	10 ± 64	-0.331	0.023	-0.033	0.941	0.041	0.025
16614	102869	323.30469421	-0.79511601	16.843	0.8018	-32 ± 24	-0.327	0.033	-0.076	0.976	0.037	0.048
17116	104710	323.30401959	-0.79241062	15.856	0.7250	-14 ± 21	-0.102	0.010	0.058	0.891	0.024	-0.068
17978	109421	323.34565833	-0.78756009	17.282	0.7500	-28 ± 24	-0.359	0.016	-0.067	1.008	0.037	0.090
18076	110938	323.35382365	-0.78697660	17.157	0.8453	15 ± 60	-0.307	0.020	-0.027	0.912	0.044	-0.009
18369	108550	323.34180935	-0.78528604	15.944	0.9510	-7 ± 25	-0.335	0.015	-0.167	1.033	0.033	0.077
18682	108795	323.34281919	-0.78336333	17.101	0.7351	15 ± 36	-0.326	0.015	-0.051	0.928	0.033	0.006

ID_{SDSS} is the DAOPHOT ID number from An et al. (2008) photometric catalog.

Table 4.3: Index measurements, magnitudes, colors, and radial velocities for the sample stars (continued).

ID	ID_{SDSS}	RA (deg)	Dec (deg)	V	U–V	V_r kms^{-1}	CN (mag)	dCN (mag)	δCN (mag)	CH (mag)	dCH (mag)	δCN (mag)
19348	105097	323.32380781	-0.77915460	17.240	0.6913	-36 ± 29	-0.326	0.015	-0.038	0.961	0.034	0.042
19928	110282	323.35007852	-0.77513187	16.773	0.7985	-5 ± 25	-0.056	0.018	0.189	0.883	0.028	-0.047
20163	112239	323.36202881	-0.77336422	17.339	0.8046	15 ± 44	-0.136	0.022	0.161	0.916	0.045	-0.001
20473	112049	323.36081815	-0.77080365	17.193	0.7606	-33 ± 22	-0.198	0.011	0.085	0.927	0.028	0.007
20654	113091	323.36801961	-0.76926014	17.412	0.6326	-1 ± 25	-0.138	0.026	0.165	0.914	0.040	-0.001
20871	107606	323.33741787	-0.76723645	16.960	0.7788	19 ± 39	-0.344	0.021	-0.082	0.982	0.053	0.057
20885	110521	323.35133131	-0.76713157	17.195	0.7770	-28 ± 24	-0.067	0.015	0.216	0.795	0.027	-0.125
21053	113761	323.37197589	-0.76537623	14.885	1.3645	-7 ± 48	0.100	0.020	0.171	1.000	0.031	0.000
21729	104749	323.32152639	-0.75746580	17.044	0.6698	-30 ± 42	0.148	0.018	0.418	1.007	0.027	0.084
22047	113079	323.36788890	-0.75307288	14.836	1.4040	-33 ± 28	-0.223	0.017	-0.157	1.003	0.026	0.001
22092	113393	323.36985251	-0.75241609	17.134	0.7180	-9 ± 20	-0.348	0.019	-0.070	0.964	0.050	0.043
22170	113230	323.36891078	-0.75140570	17.088	0.7840	14 ± 54	-0.218	0.042	0.056	0.940	0.052	0.018

Table 4.4: Atmospheric parameters and carbon and nitrogen abundances for sample stars.

ID	T_{eff} (K)	dT_{eff} (K)	$\log g$ (cgs)	A(C) (dex)	A(N) (dex)
1047	5184	60	2.7 ± 0.03	5.80 ± 0.19	7.50 ± 0.23
1221	5041	56	2.4 ± 0.03	6.11 ± 0.19	6.75 ± 0.22
1249	5111	59	2.6 ± 0.03	6.14 ± 0.19	6.30 ± 0.23
1921	4955	54	2.2 ± 0.03	5.92 ± 0.16	7.23 ± 0.22
1927	5304	85	3.0 ± 0.03	6.22 ± 0.22	7.25 ± 0.25
2288	4959	54	2.2 ± 0.03	6.07 ± 0.18	7.18 ± 0.22
3190	5581	71	3.0 ± 0.03	6.47 ± 0.23	7.48 ± 0.27
3397	5301	84	2.9 ± 0.03	6.28 ± 0.20	7.15 ± 0.24
3760	5421	86	2.9 ± 0.03	6.46 ± 0.22	7.44 ± 0.25
4144	5142	107	2.6 ± 0.05	5.87 ± 0.21	7.40 ± 0.23
5010	4732	65	1.8 ± 0.03	5.68 ± 0.17	6.96 ± 0.22
5149	4904	53	2.0 ± 0.03	5.59 ± 0.20	7.56 ± 0.21
5185	5413	67	3.0 ± 0.03	6.27 ± 0.22	7.06 ± 0.25
9229	5022	75	2.3 ± 0.03	5.87 ± 0.21	7.53 ± 0.22
10803	5458	88	3.0 ± 0.03	6.35 ± 0.21	7.12 ± 0.26
11131	5326	85	2.8 ± 0.03	6.18 ± 0.20	7.17 ± 0.25
11796	5282	87	3.0 ± 0.04	5.91 ± 0.20	7.77 ± 0.24
14343	5229	83	2.8 ± 0.03	6.12 ± 0.20	7.25 ± 0.24
15217	5328	88	3.0 ± 0.04	6.24 ± 0.20	6.85 ± 0.25
16614	5224	83	2.7 ± 0.02	6.17 ± 0.19	6.75 ± 0.24
17116	5006	73	2.2 ± 0.03	6.13 ± 0.17	7.58 ± 0.22
17978	5263	85	2.9 ± 0.03	5.98 ± 0.19	7.19 ± 0.24
18076	5232	82	2.8 ± 0.03	5.99 ± 0.22	7.17 ± 0.24
18369	4956	73	2.2 ± 0.03	6.12 ± 0.22	6.11 ± 0.22
18682	5397	87	2.9 ± 0.03	6.40 ± 0.24	6.52 ± 0.26
19348	5383	87	2.9 ± 0.03	6.41 ± 0.22	6.85 ± 0.25
19928	5146	81	2.7 ± 0.03	5.82 ± 0.22	7.41 ± 0.23
20163	5179	82	2.9 ± 0.04	5.99 ± 0.19	7.10 ± 0.24
20473	5200	82	2.8 ± 0.03	5.92 ± 0.21	7.46 ± 0.23
20654	5488	125	3.0 ± 0.04	6.46 ± 0.22	6.84 ± 0.26
20871	5263	83	2.8 ± 0.03	6.27 ± 0.21	6.79 ± 0.24
20885	5076	80	2.8 ± 0.04	5.45 ± 0.19	7.47 ± 0.23
21053	4661	62	1.7 ± 0.03	5.61 ± 0.16	7.21 ± 0.23
22047	4630	61	1.6 ± 0.03	5.57 ± 0.28	6.48 ± 0.24
22170	5271	83	2.8 ± 0.03	6.21 ± 0.20	7.16 ± 0.24

CHAPTER

5 On the CN bimodality of metal-rich clusters

Star-to-star variations of the strength of the CN band are nearly universal in moderate metallicity ([Fe/H] $\geqslant$ –1.6 dex) globular clusters of the Milky Way (see Sect. 1.1).

Most of the relatively metal-rich GCs surveyed present a bimodality (or in general a multimodality) of CN distribution on the RGB, HB, and AGB (e.g. Suntzeff, 1981, Smith and Norris, 1993, Smolinski et al., 2011, Kayser et al., 2008, Campbell et al., 2012, see Fig. 5.1). Significant variations in CN band strengths have been reported for stars prior to their undergoing first dredge-up (e.g. Briley and Cohen, 2001, Cohen et al., 2002, Ramírez and Cohen, 2002, Cohen et al., 2005), even down to the MS in 47 Tuc (Cannon et al., 1998; Harbeck et al., 2003).

However, searches within other cluster MS stars have produced mixed results. Cohen (1999a) reported no significant CN variation for MS and TO stars belonging to M 13, most probably because the CN feature in their spectra are too weak (Briley and Cohen, 2001). This interpretation is supported by the detection of a bimodality in CN index among MS stars in M 71 at a level larger than the measurement uncertainty, as well as an anticorrelation between CN and CH (Cohen, 1999b)[1]. In their sample of eight Southern globulars, Kayser et al. (2008) found no statistically significant variation in CN abundance for stars on the MS and SGB, and they attributed that to low S/N spectra producing relatively large measurement uncertainties. Some evidence for individual CN groups on the SGB of M 92, M 2, and M 13 was found by Smolinski et al. (2011). Finally, Pancino et al. (2010) reported CN bimodality for MS stars in four of their most metal-rich clusters among a sample of 12 clusters.

Clearly, as already said, the detection of CN variation for these unevolved stars demands that GC stars are initially formed with different chemical signatures, because the first mixing episode is expected to happen later on the star evolution. Therefore these stars are free from *evolutionary* effects that, superposed to the CH and CN *extrinsic* variations, could confuse the picture.

The fact that generally multiple CN behaviors at the level of the MSs are not observed for relatively metal-poor clusters could well be due to the large uncertainties associated to measure-

[1] Follow-up analysis of these data further showed that the variation is at the same level as that observed for RGB stars in that cluster, leading the authors to claim that no significant mixing is occurring on the RGB and that the abundance variations were in place at the time the stars formed (Briley and Cohen, 2001).

ments: the bands of bi-metallic molecules like CN become vanishingly weak at low metallicity, owing to their quadratic dependence on the metal abundance, therefore, CN band is particularly easy to observe at *relatively* high metallicities even at low signal-to-noise (S/N) ratio and for the fainter MS stars. In this case, the errors associated with the C and N abundances derived from spectral synthesis could be sufficiently small to reveal discrete components in the [C/Fe] vs. [N/Fe] plane.

In this Chapter we perform spectral synthesis on FORS2 data by Pancino et al. (2010) in order to investigate the extent of the [C/Fe] and [N/Fe] variations in three metal-rich clusters (namely NGC 6352, NGC 5927, NGC 6388, see Table 5.1). In the case of NGC 6352 and NGC 5927 we aim to confirm the presence of a bimodal [N/Fe] distribution as indicated by the bimodal CN strengths (Pancino et al., 2010). We also attempted an analysis of the peculiar cluster NGC 6388, for which Pancino et al. (2010) could detect neither a CN-CH anticorrelation nor a CN bimodality because

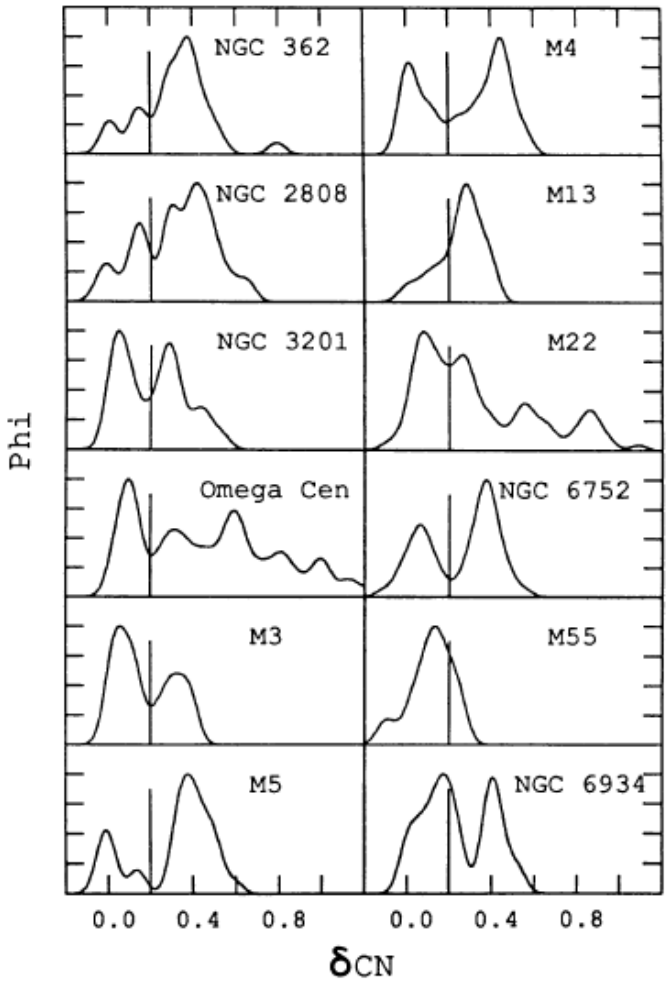

Figure 5.1: Generalized histograms of the cyanogen excess parameter δCN for 12 GCs from Norris (1987). A Gaussian kernel has been adopted with σ = 0.04 and all the distributions have been normalized to have the same peak value. The vertical line correspond to δCN = 0.20.

Table 5.1: Globular cluster sample

Name	[Fe/H] (dex)	$(m$-M$)_V$ (mag)	E(B-V) (mag)	M$_V$	$n_{star}(P10)$	N_{star} (this work)
NGC 5927	–0.49	15.82	0.45	–7.81	46	36
NGC 6352	–0.64	14.43	0.22	–6.47	24	24
NGC 6388	–0.55	16.13	0.37	–9.41	22	13

Global parameters are from the most recent version of the Harris (1996) on-line database (year 2010). The sixth and the seventh columns indicate the original dimension of Pancino et al. (2010) (P10) sample and the number of stars for which we were able to derive carbon and nitrogen abundances, respectively.

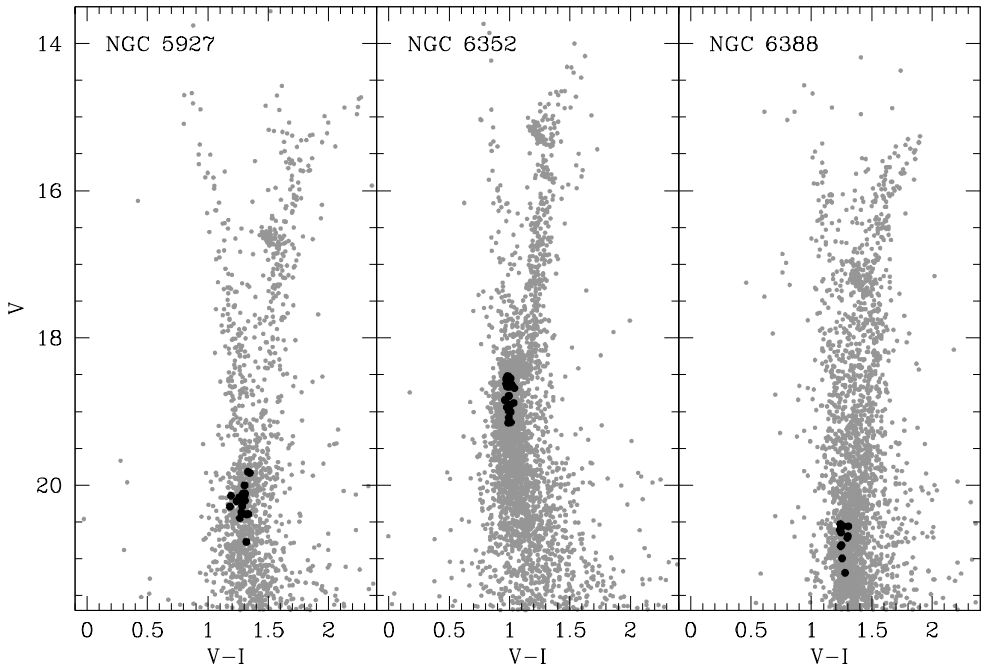

Figure 5.2: CMDs for the three GCs considered in this study. Grey dots show pre-imaging, $V, V-I$ photometry from Pancino et al. (2010). Black dots mark only the stars for which we we were able to measure [C/Fe] and [N/Fe] abundances.

of the low S/N ratio of the spectra, in an attempt to derive at least upper limits or to analyze combined spectra.

5.1 Observations and data reduction

For the pourpose of this Chapter it is only important to recall that target stars were selected from V, I pre-imaging (see Sect. 2.2 in Pancino et al., 2010) and the photometric calibration was done using stars in common with the HST photometry by Sarajedini et al. (2007). The original observational data set consists of $\simeq$ 100 MS stars acquired with FORS2 under the ESO program ID 69.D-0056 and presented by Pancino et al. (2010). We refer the reader to that paper for details of the FORS2 observations and data reduction.

5.2 CN and CH index results

As mentioned before, Pancino et al. (2010) were able to detect an anticorrelated CH and CN variation, with a clear bimodality in both the CN and CH content for NGC 6352 and NGC 5927. For NGC 5927 that study was the first one dedicated to light element anticorrelations, while in the case of NGC 6352 a correlated trend in Al and Na abundances was already suggested by Feltzing et al. (2009), based on nine HB stars. Although NGC 6388 was already found to show the Na-O and Mg-Al anticorrelations (Carretta et al., 2007), the insufficient S/N of their data prevented Pancino et al. (2010) from reaching any conclusion about the CH and CN anticorrelation for NGC 6388.

We corrected our CH and CN indices for temperature and gravity effects as described in Sect. 3.2.1. In Fig. 5.3 the clusters are arranged in order of increasing metallicity, from left to right, and the δS(3839) and δCH(4300) distributions on the MS are represented for each cluster.

To better visualize the hidden substructure in the δS(3839) vs. δCH(4300) plane we used the same method introduced in Sect. 4.2.1:

- A median is used to compute the centroids of the CH-strong[2] and CH-weak[3] in the CH-CN plane. The resulting centroids with their 1σ errors are reported in Fig. 5.3 along with the measurements for each star. We also divided also the stars into CN-strong[4] and CH-weak [5] groups and their centroids with relative error bars are plotted in the same figure;
- A line passing through the midpoint connecting CH-strong/CN-weak and CH-weak/CN-strong centroids is traced;
- Each observed point in the CN-CH plane is projected onto this line;
- We arbitrarily take as origin (P) the intersection between this line and the perpendicular line passing through the point (δS(3839), δCH(4300))=(0.0, 0.0);
- A generalized histogram (with σ = 0.10, 0.04, and 0.06, from left to right) of the distribution of distances of projected points from the origin P is constructed. Smoothing the histogram, in fact, could help eliminate any artificial substructure in the distribution created by small number statistics and additionally accounting for unidentified sources of uncertainty.

According to Pancino et al. (2010) (see also Sects. 3.2 and 4.2.1) we consider a distribution to be bimodal when the centroids of the CN-strong (CH-weak) and CN-weak (CH-strong) stars are clearly separated in the δCH-δCN plane. First, we see clear anticorrelations (upper panel in fig. 5.3) for all cluster. Moreover, for NGC 6352 and NGC 6388 these anticorrelation are also clearly bimodal: in both cases the generalized histograms of Fig. 5.3 appear bimodal.

[2] δCH(4300) > 0.0.
[3] δCH(4300) < 0.0.
[4] δS(3839) > 0.0.
[5] δS(3839) < 0.0.

For NGC 5927, the generalized histograms do not show signs of bimodality, but rather a deviation from the Gaussian shape, with asymmetric residuals. To get more insights in this issue, we studied the statistical significance of this spread using a KMM test (Ashman et al., 1994). The KMM test can reject the null hypothesis that a single population well describes the observed data in the case of NGC 5927 at a significance of 92%, possibly indicating a non-Gaussian distribution. In these respects, the determination of [C/Fe] and [N/Fe] via spectral synthesis could help in clarifying the picture.

5.2.1 On the CN-CH bimodality

It is important to stress that the measured bimodal CN distribution does not necessarily reflect a bimodal abundance spread: the distribution of CN absorption strengths measures the

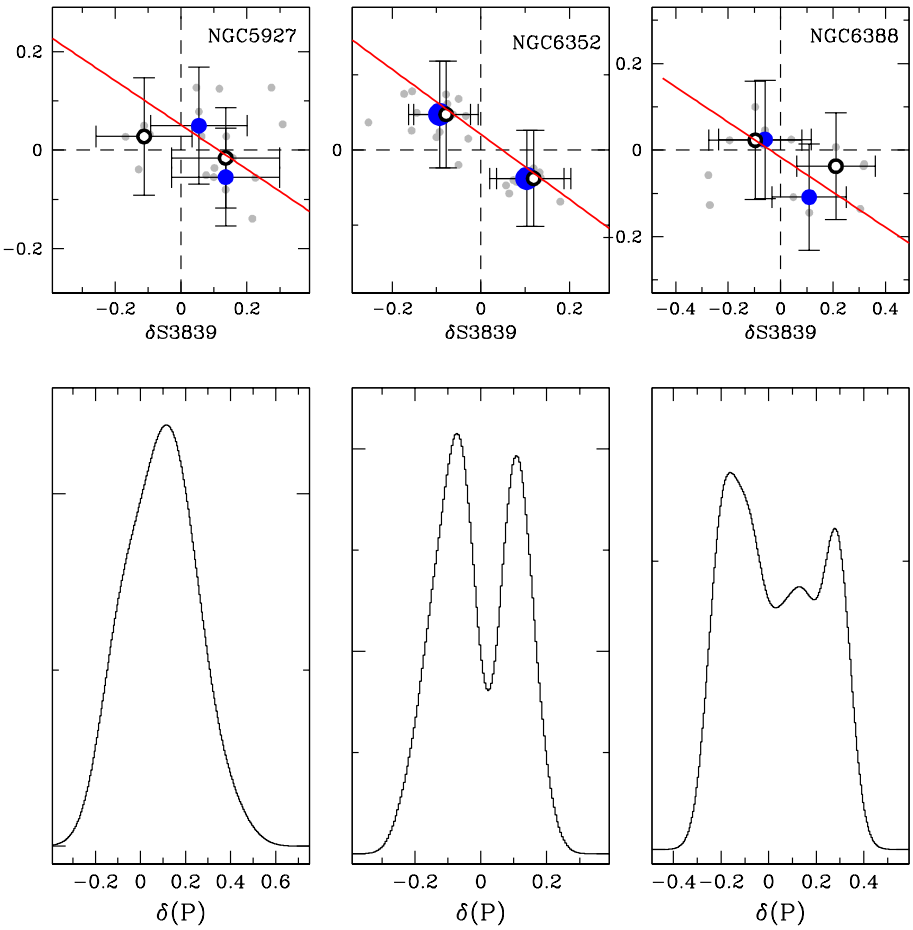

Figure 5.3: CH weak and CH strong stars are separated by the horizontal dashed line, and their centroids with 1σ are marked as large white dots. CN strong and weak stars are separated by the vertical dashed line, and their centroids with their 1σ are shown as large blue dots. The red continuous line connects the locus equidistant from CH-strong/CN-weak centroids and CH-weak/CN-strong ones. The generalized histograms in the bottom panels represent the distribution of distances of projected points from the origin P (see text for details).

true distribution of atomic abundances folded with the curve of growth (COG). As a matter of fact, a continuum of atomic carbon and nitrogen abundances could lead to more or less the same CN absorption strength at a given effective temperature if all the CN-enhanced stars are polluted, but they fall on the flat part of the COG. Such a *saturation* of the CN S(3839) band was proposed by Suntzeff (1981) and Langer (1985) to explain the bimodality of CN absorption in GC RGB stars. The similarity of CN absorption strength for the CN-rich stars might be explained by this saturation scenario, but the homogeneity of CN strength of the CN-weak stars remains unsolved. As discussed by Harbeck et al. (2003), these CN-weak stars represent the unpolluted, chemically homogeneous fraction of the cluster whose CN abundance falls on the rising part of the COG and one would expect a continuum of CN absorption strength until the flat part of the COG is reached.

5.3 Model atmospheres, synthetic spectra, and resulting abundances

The approach we have taken is identical to that of Lardo et al. (2012a) (see Sect. 3.3). Briefly, we derived estimates of the atmospheric parameters from the calibrated FORS2 photometry (Sect. 5.1), taking into account the errors on photometric parameters. For each cluster, we obtained effective temperatures (T_{eff}) with the Alonso et al. (1996) color-temperature relations, adopting metallicities and foreground reddenings listed in Table 5.1. Gravities were then obtained by means of theoretical isochrones downloaded from the Dartmouth Stellar Evolution Database[6] (Dotter et al., 2008), with the appropriate age and metallicity. Finally, we assumed a microturbulent velocity $v_t = 1.0$ km s^{-1} for the entire sample.

C and N abundances were determined via spectral synthesis, using the local thermodynamic equilibrium (LTE) program MOOG (Sneden, 1973) combined with the ATLAS9 model atmospheres (Kurucz, 1993, 2005). The atomic and molecular line lists were taken from the latest Kurucz compilation and downloaded from F. Castelli's website[7]. Abundances were computed as explained in Sect. 3.3.2 and Sect. 4.3.2. To investigate the effect of erroneous stellar parameters on the derived elemental abundances we have for two representative stars in each cluster varied the stellar parameters and re-derived the elemental abundances. The error in the adopted T_{eff} is typically δA(C)/$\delta T_{eff} \simeq 0.11 - 0.12$ dex and δA(N)/$\delta T_{eff} \simeq 0.12$–$0.16$ dex in the case of NGC 6352. For the more distant and high-reddened NGC 6388 and NGC 5927, the errors in the derived T_{eff} are larger, i.e.; δA(C)/$\delta T_{eff} \simeq 0.17 - 0.19$ dex and δA(N)/$\delta T_{eff} \simeq 0.20$–$0.22$ dex. In every case, the errors due to uncertainties on gravity is negligible (on the order of 0.03 or less). We expect that, in the case of MS stars, the exact O values will affect slightly the derived C abundances. Indeed, we found that strong variations ($\pm$ 0.5 dex) in the oxygen abundance are completely negligible (on the order of 0.07 dex or less) for these warmer stars.

The errors derived from the fitting procedure (see Sect.3.3 for further details) were then added in quadrature to the errors introduced by atmospheric parameters, resulting in an overall error of eA(C)$\simeq$0.18 dex and eA(N)$\simeq$0.24 dex for NGC 6352, eA(C)$\simeq$0.23 dex and eA(N)$\simeq$0.28 dex for

[6] http://stellar.dartmouth.edu/models/

[7] http://wwwuser.oat.ts.astro.it/castelli/linelists.html

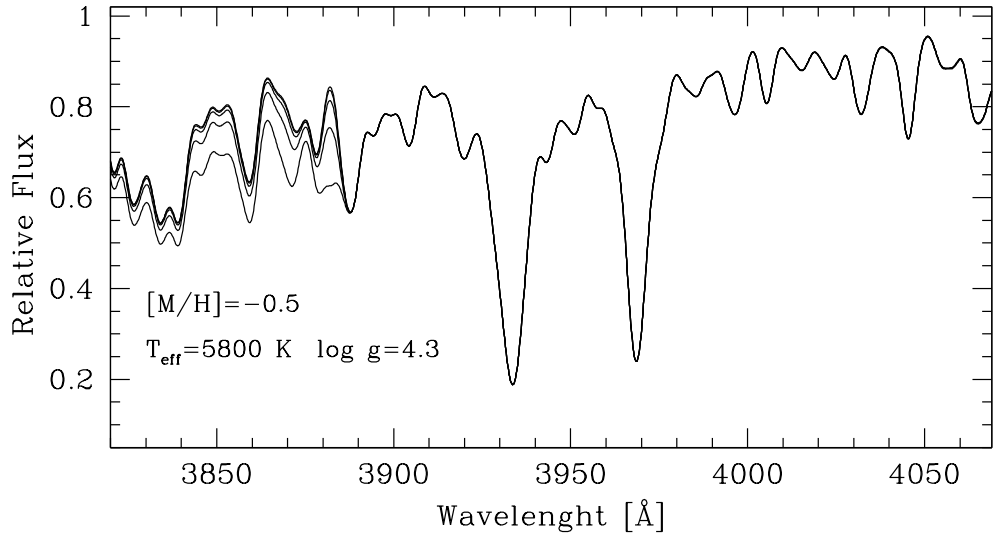

Figure 5.4: Synthetic spectra in the region of the 3883 Å CN band. Parameters are [N/Fe] = (-1.5,-1.0,-0.5,0.0,0.5) (from upper to bottom), [C/Fe] = -0.6, T_{eff}=5800 K, and log g=4.3. It is clear from this figure that, for this kind of stars and spectra quality, the CN feature becomes clearly insensitive to nitrogen abundance variations for [N/Fe] $\leqslant$ –0.5 dex.

NGC 5927, and eA(C)$\simeq$0.23 dex and eA(N)$\simeq$0.26 dex for NGC 6388. We adopted a constant oxygen abundance ([O/Fe]=0.4 dex) throughout all computations.

5.3.1 Stacked spectra to characterize N-poor population

While we were able to derive carbon and nitrogen abundances for the majority of the stars in our sample, the CN feature at 3876 - 3890 Å appears to be so weak for a group of stars, that only upper limits on the nitrogen abundances can be inferred. *As a matter of fact, we can reasonably distinguish between two groups of stars: (1) stars with both [C/Fe] and [N/Fe] measurements available (N-rich) and (2) stars for which we are able only to measure upper limits for the nitrogen abundances (N-poor).*

If the C/N ratio is solar, carbon atoms outnumber nitrogen atoms and the product of C and N is *small.* If nitrogen is initially under abundant in metal-poor stars ([N/C] < 0.0), the product of C and N will be still *smaller* and the CN bands still weaker. Figure 5.4 shows the dependence of the 3883 Å CN band on nitrogen abundance (for a fixed [C/Fe] = – 0.6 dex) for a representative star with atmospheric parameters similar to those derived for our target stars. This Figure shows that the CN feature become clearly insensitive to nitrogen abundance variations for [N/Fe] $\leqslant$ –0.5 dex.

Therefore, to provide a sound measure the difference in nitrogen the CN-normal and CN-enriched populations we proceeded by combining the spectra within each nitrogen group to produce summed spectra with much higher S/N as in Cannon et al. (1998).

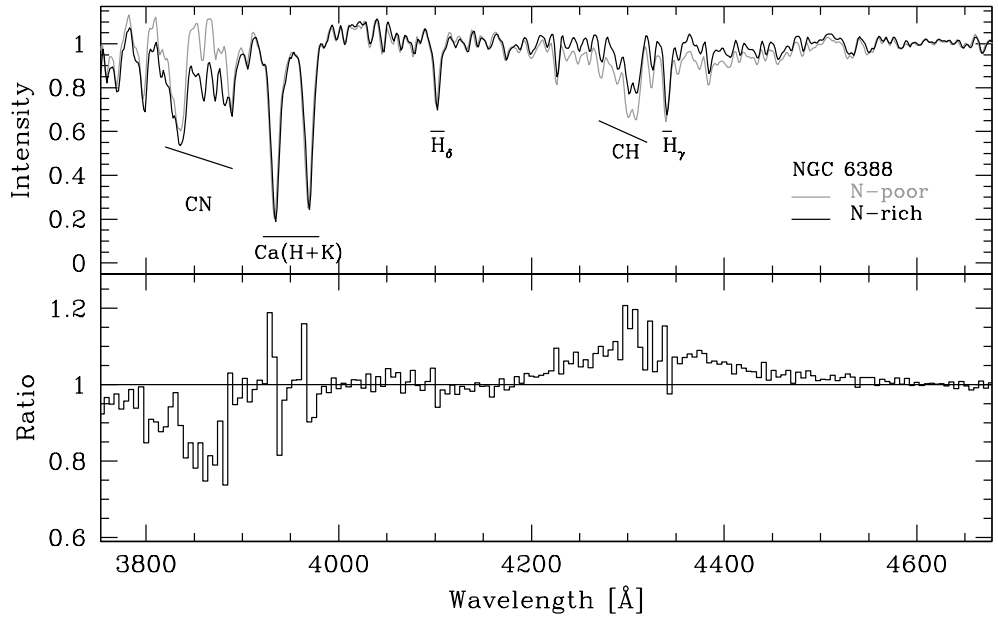

Figure 5.5: *Upper panel:* combined spectra for samples of N-rich (12 stars, black solid line) and N-poor (12 stars, grey solid line) groups on the MS of NGC 6352. *Lower panel*: the ratio of N-rich and N-poor spectra, after some binning (see text).

This technique assumes that the spectra of the stars are virtually identical apart from the molecular features, which appears to be our case, since we found that other major features in the spectra (e.g.; Ca (H+K) lines, H_β) do not correlate with CN or CH[8].

We show the combined spectrum for N-poor and N-rich stars for NGC 6352 in Fig. 5.5, which also illustrates the locations of the CN and CH bands and various lines. For this cluster, the spectra of twelve N-rich stars were added together to yield one spectrum, and twelve N-poor stars were combined to form another spectrum. The intensity scale in Fig. 5.5 gives flux per unit wavelength, scaled so that unity represents the continuum in the synthetic spectra. The two summed observed spectra in the upper panel of Fig. 5.5 are very similar everywhere (particularly near the region of the very strong Ca II lines and the Balmer H lines), demonstrates that the two samples of main-sequence stars do not differ in any important respect, except for the CN and CH molecular features. To verify that the difference in the *UV* CN band is real, we show in the bottom panel of Fig 5.5 the result of dividing the N-rich spectrum by the N-poor spectrum. For the purposes of this comparison, the observed and synthetic spectra were binned in steps of 3.5 Å to show the presence of broad features, before the division was performed bin-by-bin. The most striking feature of Fig.5.5 is that a deep S(3839) band corresponds to a strong CH G band, but the latter lies on the opposite side of unity; in other words, the CN and CH bands are anticorrelated (Sect. 5.2). The same could be said for NGC 5927 and NGC 6388 (see Fig. 5.6)

[8]We note that all our target stars lie in a small range of V magnitudes and $V-I$ colors (Fig. 5.2), therefore all our stars have very similar temperatures and gravities (see also Table 5.3).

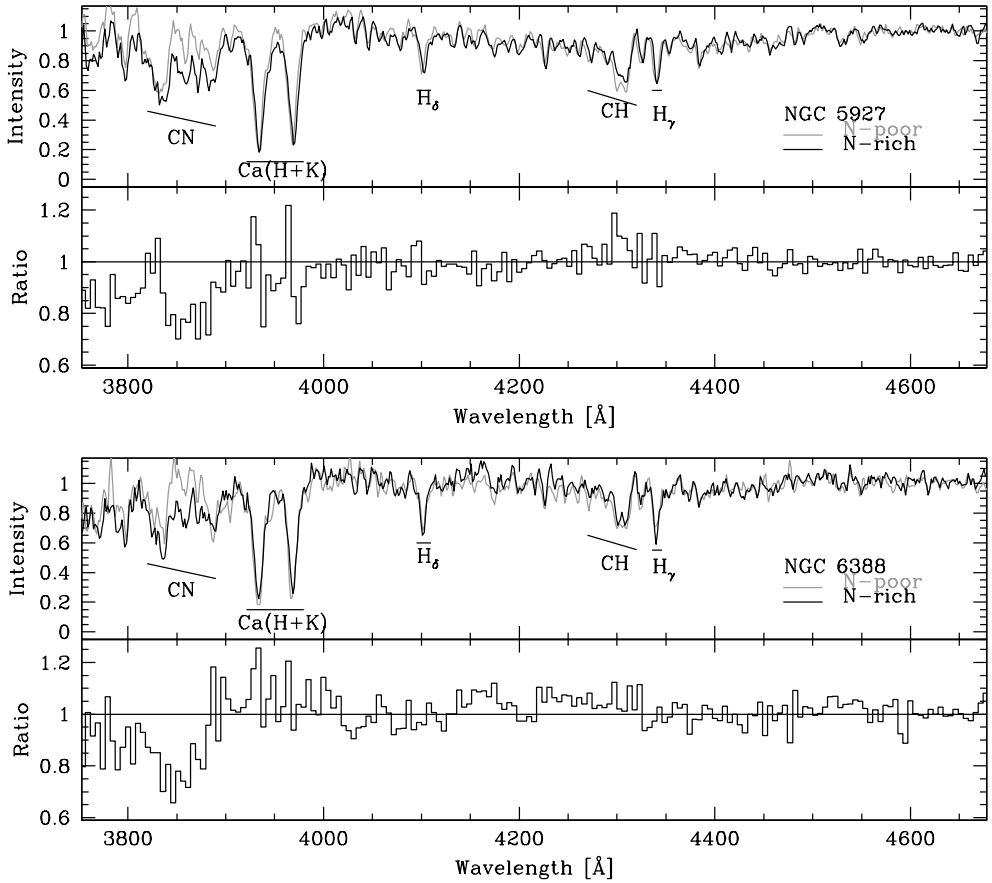

Figure 5.6: The same as in Figure. 5.5, but for NGC 5927 and NGC 6388. In this case we combine the spectra of 21 and 4 N-poor stars and 15 and 9 N-rich stars for NGC 5927 and NGC 6388, respectively.

As a final step, we used these combined spectra to derive upper limits for the N abundances of N-poor stars. The comparison with synthetic spectra in the CN region shows that a reasonable fit might be achieved at (upper limits) [N/Fe] $\leqslant$ – 0.64 $\pm$ 0.35, –0.61 $\pm$ 0.30, –0.5 $\pm$ 0.35 dex for NGC 5927, NGC 6352, and NGC 6388 respectively.

The abundances derived as described above and the relative uncertainties in the abundance determination are listed in Table 5.3 and plotted in Fig. 5.7. Additionally, Table 5.3 lists the derived atmospheric parameters of all our targets.

5.4 C and N abundance results

Carbon and nitrogen show the typical anticorrelation found in many other GCs (see Chapters 3 and 4), as shown in Fig. 5.7, where the [N/Fe] values are plotted as a function of [C/Fe]. The open white circles represent the 37 stars for which upper limits for the nitrogen abundance were derived from the stacked spectra (Sect. 5.3.1).

Although we were able to measure only upper limits for the N-poor group, in the case of NGC 6352 a sharp bimodality is present (see Fig. 5.7). Even taking into account the small number statistics and the large errors associated to the measurements, it does not seem premature to conclude that in NGC 6352 there there are two well separated groups of MS stars, with a gap of at least $\simeq$0.5 dex in between, and a number ratio of 1:1 approximately. Therefore, we can safely assume that all the stars for which we derived upper limits on [N/Fe] are first generation stars, while the remaining ones belong to a second generation. Concerning the carbon of the N-poor population, we found a median value of [C/Fe] = –0.57 dex (σ = 0.05), virtually consistent with a population with a single carbon abundance. At odds with the N-poor population, carbon is relatively depleted among N-rich stars [C/Fe] = –0.93 dex (σ = 0.19), while the nitrogen abundance

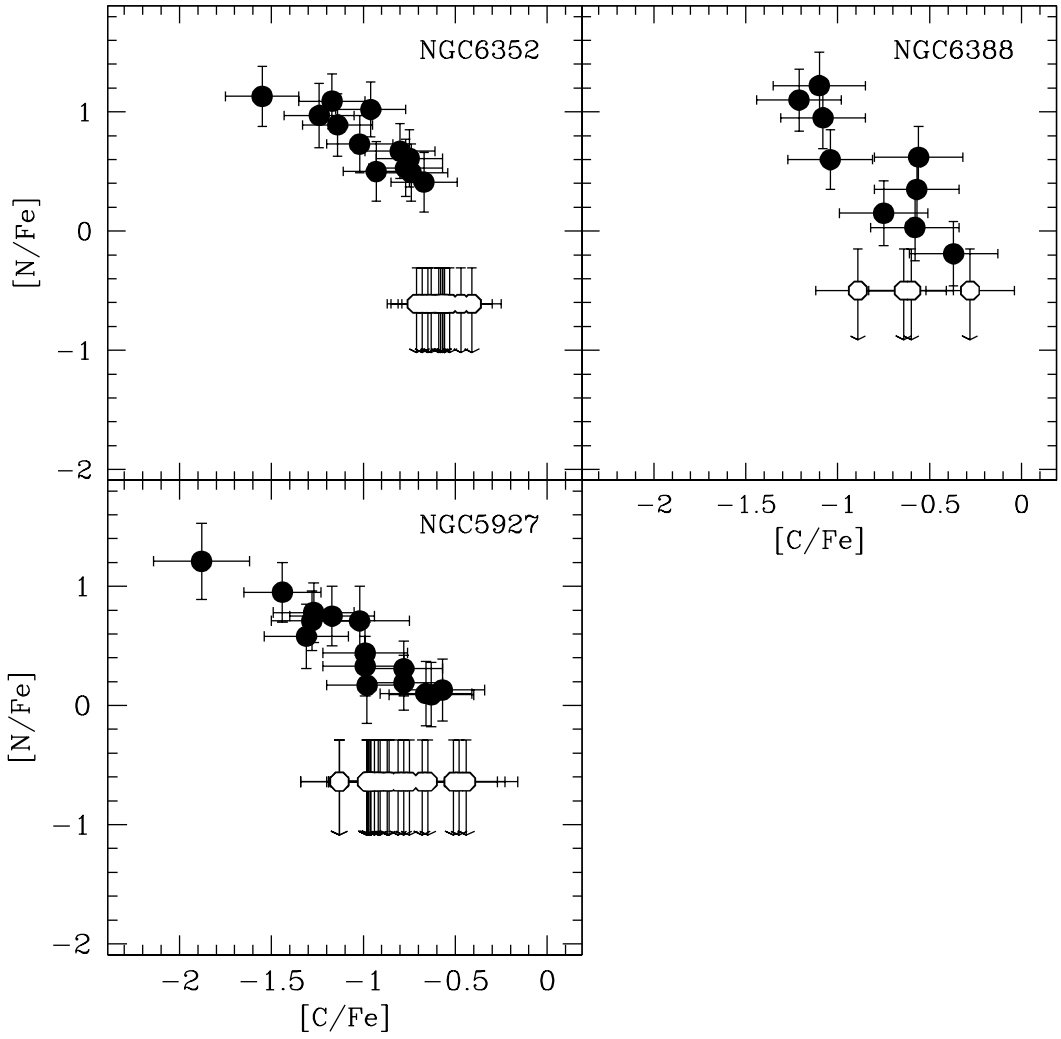

Figure 5.7: The C and N abundances, along with their measurement errors, are plotted each against the other for the three target clusters as black circles. The white circles refer to stars for which we were able to measure only upper limits for the nitrogen abundances from the combined spectra (see text).

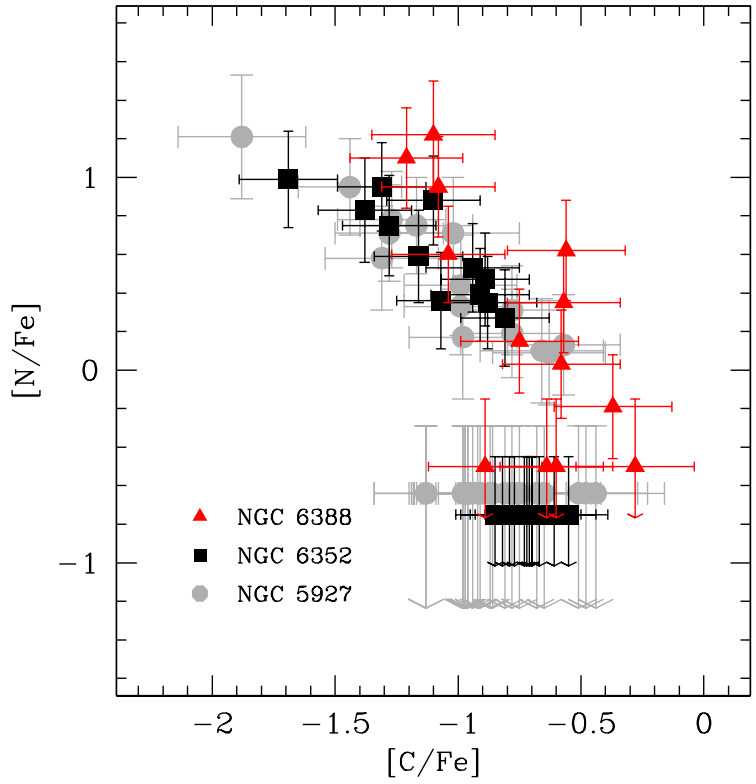

Figure 5.8: [C/Fe] vs. [N/Fe] abundances for all the three metal-rich GCs.

is highly enhanced [N/Fe] = 0.73 dex, with a large spread (σ = 0.24). NGC 5927 MS stars seem to share the same pattern in the [C/Fe] vs. [N/Fe] plane. However, here the separation of the N-poor and N-rich group is not so large: second generation stars are enhanced in nitrogen with respect to first generation stars by [N/Fe] $\simeq$ 1.0 dex (at least). Although the carbon depletion among N-poor stars in NGC 5927 might appear more extreme than in NGC 6352, this impression relies on one star only (possibly belonging to the extreme generation mentioned by Carretta et al., 2009c); the median value: [C/Fe] = –0.99 dex (σ = 0.25) is fully comparable to what obtained for NGC 6352, while the nitrogen excess appears lower when compared to NGC 6352 (with a median value [N/Fe] = 0.44 dex (σ = 0.29)).

The same cannot be said about the C-N anticorrelation in NGC 6388. Here the separation between first and second generation stars is not so clear, most probably because of the low S/N of the spectra. If we consider once again first generation stars, stars for which we could not infer reliable N abundances, we found also in this case a large enhancement of N among second generation stars [N/Fe] = 0.60 dex (σ = 0.40), similar to the N enhancement found for N-rich stars in NGC 6352.

These results resemble what was found by Marino et al. (2008) for M 4 in the [Na/O]-[O/Fe] plane, with two separated groups of stars [9] that corresponds to the two generations.

[9] With a number ratio of 1:1 approximately.

From these values we note what is immediately apparent in Fig. 5.8 for second generation stars: while the spread in [N/Fe] is well above 1 dex, in each cluster there is a smaller variation in C abundances. Figure 5.8 further highlights two issues in regard to the detected C-N anticorrelation. First, the pattern of C and N abundances among N-rich stars is similar for the three clusters. Certainly this is expected, as NGC 5927, NGC 6352, and NGC 6388 have nearly identical metallicities ([Fe/H] $\simeq$ –0.5 dex). Yet the abundances found among NGC 5927 and NGC 6388 show greater nitrogen abundance variations, with similar C depletions. This could resemble the correlation Carretta et al. (2010c) found between the extension of the O-Na anticorrelation and the present-day total mass of the GCs (using the absolute magnitude M_V as a proxy for the mass, see Table 5.1 and Fig. 5.8). Also in the case of the C-N anticorrelation, a large mass seems to be a requisite for an extended anticorrelation.

5.4.1 The C-N anticorrelation

The most interesting result of our investigation is that we can show that the N distribution for NGC 6352 and NGC 5927 is bimodal (Fig. 5.7). Moreover, a visual inspection of Fig. 5.7 suggests that the extent of the C-N anticorrelation for second-generation (Na-N/rich) stars is greater than the errors associated with abundance measurements for both clusters. This evidence possibly suggests the presence of a third group of stars[10]. To confirm this suggestion, we analyzed the distribution of stars along the C-N anticorrelation using the same procedure used in Sect. 4.4.2. In brief, we first draw a fiducial by putting a best-fit spline through the median abundance found in successive intervals of [N/Fe] = 0.5 dex (shown as red lines in the insets of Fig. 5.9). Then we projected each program star in the [C/Fe]-[N/Fe] anticorrelation on this fiducial and plotted the histogram of the distribution of vertical distances (D) of the projected points from the line [N/Fe]=0. The resulting histograms for the three clusters are shown in Fig. 5.9. The red overimposed curve is the normalized kernel density distribution:

$$K = \sum_{i=1}^{N} e^{\frac{-(x-x(i))^2}{2\sigma^2}}$$

where x = [N/Fe] and σ is the observational error associated to [N/Fe]. We used for each star σ = 0.26, 0.24, and 0.28 dex that has been taken equal to the dispersion of the group of stars with available N measurements for NGC 5927, NGC 6352, and NGC 6388 respectively.

For NGC 5927 and NGC 6352 at least two substructures are apparent, peaked at D $\simeq$ 0.4 and 0.7 for NGC 5927 and D $\simeq$ 0.5 and 1 for NGC 6352. We tentatively divided RGB stars between intermediate and extreme second generation stars by setting an arbitrary separation at [N/H] $\simeq$ 0.5 and 0.7 for NGC 5927 and NGC 6352, respectively.

For NGC 6388, the situation is less clear, because of the large errors associated to the abundance measurements and the poor statistics. Nevertheless, if we tentatively assume that stars with upper limits on N abundances are first generation stars, we can detect a hint of bimodality

[10] Stars with E (Extreme) composition, by adopting the nomenclature first introduced by Carretta et al. (2009b).

for N-rich stars also in this case. Similarly, Carretta et al. (2012a,b) demonstrated the the existence of three distinct stellar populations in NGC 6752 and 47 Tuc. In this case, the distribution of RGB stars is clearly clustered around three distinct Al values, low, intermediate, and high. Our data suggest the presence of three discrete sub-populations for all clusters, unfortunately, we cannot provide conclusive answers because the low number statistics in our data, rather than data quality, at least for the N-rich stars.

5.4.2 Comparison with index measurements

To directly compare results from index measurements and abundance analysis, we identified N-rich and N-poor (i.e., stars for which we were able to measure only an upper limit for the nitrogen abundance) stars in the plot showing the distribution of CN and CH indices against the stellar V magnitude in Fig. 5.10. Figure 5.10 shows that CN-strong stars are also N-rich and C-poor, as expected. This indicates that [N/Fe] abundances *linearly* correlate with the S(3839) band strengths for all the three clusters.

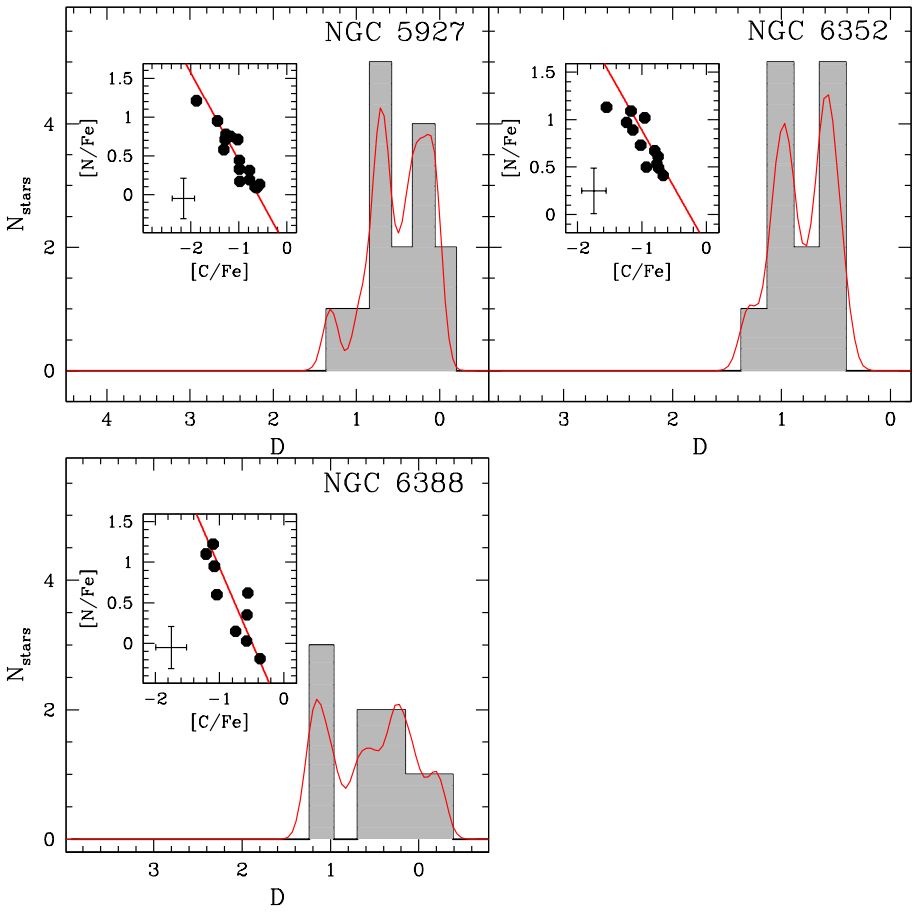

Figure 5.9: Distribution of the projected distance D of stars on the fiducial plotted in the the insets in the top-right corner. For NGC 5927 and NGC 6352 we considered only N-rich stars. The error bars in the inset represent the typical errors on [C/Fe] and [N/Fe].

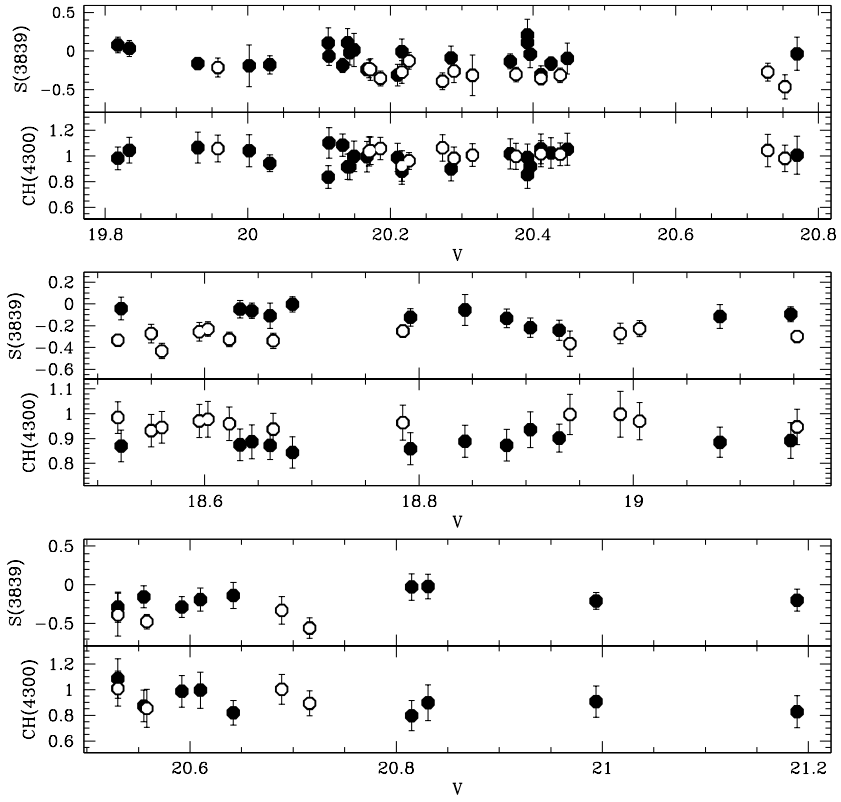

Figure 5.10: S(3839) and CH(4300) indices are plotted for all the sample stars in the three clusters NGC 5927, NGC 6352, and NGC 6388 (from up to bottom). N-poor stars are plotted as white circles, while N-rich stars are shown as black circles.

5.5 Comments on individual clusters

5.5.1 NGC 5927

According to Zinn and West (1984), NGC 5927 is one of the most metal-rich GCs ([Fe/H]=–0.3 dex). Cohen (1983) found that this cluster is +0.59 dex more metal rich than 47 Tuc. Other [Fe/H] estimates exist in literature (e.g., [Fe/H]= –0.5 dex; Francois, 1991), while Pancino et al. (2010) were the first to study light element anticorrelations in NGC 5927. As already mentioned throughout this Chapter, these authors found a clear anticorrelation of the CH and CN band strength, in spite of the low S/N ratio of the spectra and of the relatively high reddening in the cluster field. We confirm the presence of an extended C-N anticorrelation, with a bimodality in the nitrogen variations. While first generation stars share homogeneous carbon and nitrogen content, the second generation group displays an extended C-N anticorrelation. N-rich stars also show a hint of bimodality, with a third group of stars with extreme chemical composition.

The source of errors that most affects [C/Fe] and [N/Fe] determinations in our case is the large errors on the temperature of stars. Using differential reddening corrected photometry to derive atmospheric parameters in NGC 5927 stars could help in obtaining smaller errors on the

photometrically derived temperature. This will be the next step in the study of this particularly interesting cluster.

5.5.2 NGG 6352

NGC 6352 is a sparsely populated cluster with disk kinematics. Following Mackey and Gilmore (2004) classification, it is a bulge/disk GC, while Pritzl et al. (2006) placed it in the group of thin disk clusters. Its CMD (Pulone et al., 2003) is very similar to that of 47 Tuc and M 71 with a stubby red HB and a break at the RGB at the level of the HB. So far only few high-resolution spectroscopic studies exist for its bright giants. Cohen (1983) found that it is +0.38 dex more metal-rich than 47 Tuc, while Carretta and Gratton (1997) found an average [Fe/H] = – 0.64 $\pm$ 0.06 dex from their small sample (3 stars). This value was later adjusted to [Fe/H] = – 0.62 $\pm$ 0.05 dex by Carretta et al. (2009a). A possible Al-Na correlation was detected among HB stars by Feltzing et al. (2009). The presence of two distinct sub-population in this cluster was confirmed by the study of Pancino et al. (2010), who detected a bimodal CH-CN anticorrelation among MS stars from low resolution, blue spectra. Here, we confirm that two *discrete* sub-population exist in this cluster, with a remarkable difference in the N content. Moreover, N-rich stars display a clear C-N anticorrelation which possibly is also bimodal.

5.5.3 NGC 6388

NGC 6388 is a very peculiar cluster: in contrast to expectations for its high metallicity (e.g., [Fe/H] = –0.44 $\pm$ 0.01 dex; Carretta et al., 2007) the cluster displays an extended blue horizontal branch (Rich et al., 1997). In addition, the HB presents a slope, so that in the V band its blue tail lies about 0.5 mag brighter than the red HB clump (Raimondo et al., 2002). Recently, Moretti et al. (2009) detected a split at the level of the SGB region, indicative of two distinct stellar populations. Although the statistics is very poor, we were able to detect a clear anticorrelation also for this cluster. Moreover, the behavior of MS stars in the [C/Fe] vs. [N/Fe] plane appears to be bimodal in nature[11]. This is the first time that a C-N anticorrelation is detected for this cluster.

5.6 Trends with cluster parameters

When trying to connect the GC properties with the extension of the anticorrelations, two parameters are usually defined: (i) the *low-resolution community*, studying the strength of molecular indices, usually builds the ratio of CN-strong to CN-weak stars r_{CN} (e.g., Norris, 1987, Smith and Mateo, 1990, Smith, 2002, citealplayser08, Pancino et al., 2010, Smolinski et al., 2011); (ii) the *high-resolution community* (namely Carretta et al., 2010c) measures the extension of the Na-O and Mg-Al anticorrelations with interquartile ranges.

The two parameters measure two different physical quantities, and both give clues to the understanding of the anticorrelation phenomenon. Clearly, in the framework of the self-enrichment

[11] Unfortunately, because of uncertainties on abundance measurements and low statistics, we cannot provide conclusive evidence.

scenario, the ratio between N-rich and N-poor star is a fundamental constraint to model the chemical evolution of a GC, as this number tells us the relative importance of stellar groups with different chemical composition (Sect. 1.8). Because we observed discrete groups in the C-N plane, we have the opportunity to *directly* discriminate between first and second generation stars (at least for two clusters in our sample). This give us the opportunity to count the number of stars in the two groups. To this end we define the number ratio between first and second generation stars ($n_{(Nrich)}/n_{(Npoor)}$).

Similarly, we note that the C-N anticorrelation is clearly bimodal also in the case of 47 Tuc (Briley and Cohen, 2001) and M 71 (Cohen et al., 2002), therefore we decided to include these two cluster to our sample.

Although the sample is presently small, the use of low-resolution spectra to derive C and N abundances in GC stars appears very promising, as it requires less telescope time and data analysis efforts with respect to high resolution spectroscopy.

5.6.1 Ratio of first-to-second generation stars

We classified as first generation stars for which we have only upper limits for the nitrogen abundance. While this classification is supported by the C-N bimodality observed for NGC 5927 and NGC 6352, this is only a tentative classification for NGC 6388, where the errors are too large to discriminate between discrete groups[12]. The final errors on this ratio were propagated by assuming Poissonian errors on the [N/Fe] and [C/Fe] abundances. We obtained the following values or the number ratio between the second and first generation stars (r): r = 0.71 $\pm$ 0.50, 1.00 $\pm$ 0.40, and 2.25 $\pm$ 0.38 for NGC 5927, NGC 6352, and NGC 6388 respectively; with an average value of $<r>$ = 1.32 $\pm$ 0.81 ($<r>$ = 0.85 $\pm$ 0.20 if we exclude NGC 6388). The study by Pancino et al. (2010) (12 Galactic GCs), reported an average of r = 0.82 $\pm$ 0.29, while the average of the r values reported by Kayser et al. (2008) for RGB stars in their sample is 0.61. Our results appear consistent within the uncertainties with the values found by Kayser et al. (2008), Pancino et al. (2010), and the value derived for RGB stars in M 2 (Chapter 4). Together, these results indicate that for the studied clusters, generally CN-strong stars can account roughly for half of their respective cluster populations (or less). However, studies of Na and O abundances in cluster giants Carretta et al. (2009c) suggest that the ratio is much higher, with enriched stars comprising from 50 up to 70% of the total (r > 1). This discrepancy is curious, and Pancino et al. (2010) suggested that it may indicate that C-N abundance variations are contributed, at least in part, by a different feedback source from the O-Na abundance variations studied by Carretta et al. (2009c). In fact, the C, N, O, and Na are not directly comparable, because they are not produced exactly at the same temperature: C and N are altered within the CN bi-cycle, O is depleted in the complete CNO cycle and Na is produced in the NeNa cycle, each dominating at progressively higher temperatures. The observed mismatch could also depend on the way stars are assigned to different populations by the Padua group. Indeed, in the few cases where the Na-O anticorrelation is found to be bimodal

[12] However this classification seems to be reasonable if we compare the behavior of NGC 6388 in the [C/Fe] vs [N/Fe] plane with respect to the other two clusters for which the bimodality was found (see Figure 5.8).

Table 5.2: Global parameters of globular clusters of our sample. All sources for the parameters are listed in the footnotes.

Name	[Fe/H][a]	M_V[a]	R_{GC}[1a]	Age[b]	ϵ[2a]	σ_0[3c,d]	c[4a]	r_t[5a]	log(M/M$_\odot$)[e,f]
	(dex)	(mag)	(kpc)	(Gyr)		kms s^{-1}	(pc)	(dex)	
NGC 104	–0.72	–9.42	7.4	13.06	0.09	11.5	2.07	42.86	6.05
NGC 5927	–0.49	–7.81	4.6	12.67	0.04	4.3	1.75	16.68	5.32
NGC 6352	–0.64	–6.47	3.3	12.67	0.07	5.4	1.15	10.51	4.57
NGC 6388	–0.55	–9.41	3.1	12.03	0.01	18.9	1.60	6.21	6.02
M 71	–0.78	–5.61	6.7	12.54	0.00	2.3	1.10	8.96	4.98

[1] distance from Galactic center, [2] ellipticity, [3] central velocity dispersion, [4] concentration, [5] tidal radius. [a] Harris, 1996 (2010 edition); [b] relative ages Marín-Franch et al. (2009)converted to absolute ages multiplying by 12.8 Gyr; [c] Pryor and Meylan (1993); [d] Gnedin et al. (2002); [e] Mandushev et al. (1991); [f] McLaughlin and van der Marel (2005).

(i.e. with stars divided in two well separated groups having different light-element content, see Marino et al., 2008 for M 4 and Fig. 8 in Carretta et al., 2012b for 47 Tuc), we can assigning about half of stars to each group.

5.6.2 Comparison with cluster parameters

The possibility that the various physical parameters of the cluster and the environment could be linked in some way with the multiple population phenomenon has been examined extensively in several studies. For example, a possible correlation between CN band strength and the apparent ellipticity of the cluster was initially found by Norris (1987). This suggested correlation was also confirmed by Smith and Mateo (1990) and Smith (2002), but this trend is not confirmed by Kayser et al., 2008. Smith and Mateo (1990), Kayser et al. (2008), and Pancino et al. (2010) found that clusters with a higher fraction of CN-strong stars are also more luminous and therefore more massive. This finding is supported also by the trend found by Smith and Mateo (1990) with the central velocity dispersion σ_0.

In order to explore possible correlations of the ratio of first-to-second generation stars with global parameters of the GCs we combine our observations to quantities available in the literature. As mentioned above, we added to our sample also 47 Tuc and M 71 from the studies by Briley and Cohen (2001) and Cohen et al. (2002). The cluster quantities were selected from the 2010 version of the Harris (1996) and Pryor and Meylan (1993) globular cluster catalogs. The age estimates were adopted from Marín-Franch et al. (2009). Table 5.2 gives an overview of the extracted parameters. In order to quantify the statistical significance of possible correlations between the number ratio of CN-strong stars with various structural parameters we computed for each parameter the Pearson coefficient of rank correlation, r_P.

Figure 5.11 shows the number ratio of N-rich/N-poor stars (r-parameter, hereafter) for the clusters in our sample plotted against various cluster parameters. We plotted NGC 6388 in red, as in this case we were not able to detect a nitrogen bimodality. For the same reason, we decided

to calculate the correlation coefficients by neglecting this cluster[13]. We detected a correlation between the r-parameter and the central velocity dispersion (as found also in Smith and Mateo, 1990). There is also a trend of an increased percentage of CN-strong stars with increasing cluster tidal radius[14]. We observe a correlation between N enrichment and cluster ellipticity[15], cluster luminosity, mass and concentration that well agree with past findings (Norris, 1987; Smith and Mateo, 1990; Kayser et al., 2008; Pancino et al., 2010), albeit the statistical significance of the observed correlations is weak.

This result is consistent with expectations from the self-enrichment scenario –the most massive clusters possess the deepest gravitational potentials, allowing them to retain the largest amount of chemically enriched gas expelled from evolving stars. We caution, however, that the range of cluster metallicities, r_t, concentration, age and R_{GC} is not very broad to allow for firm

[13]However, we reported in the top right of each panel the value of the Pearson correlation coefficient computed when NGC 6388 is included in the sample.

[14]But note that when considering NGC 6388, the same test gives a much lower probability that a correlation is present.

[15]As pointed out by Smith, the CN-strong/ellipticity correlation may be a selection effect; i.e., the higher ellipticity clusters in the sample tend also to have higher masses.

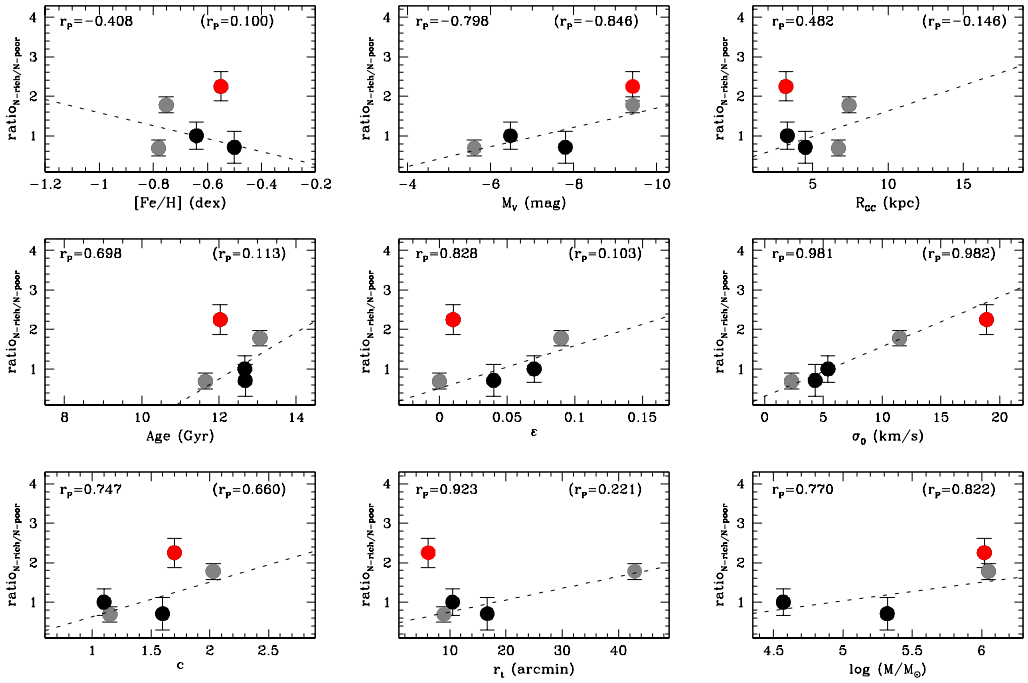

Figure 5.11: Run of the ratio = $n_{(N-rich)}/n_{(N-poor)}$ for NGC 5927 and NGC 6352 (black circles). The red circle represents NGC 6388. Grey circles show the $n_{(N-rich)}/n_{(N-poor)}$ value for 47 Tuc and M 71 from Briley and Cohen (2001) and Cohen et al. (2002), respectively. Dotted lines mark linear fits to clusters with the exception of NGC 6388 and the Pearson r_P correlation coefficients are reported on left-hand top of each panel. The r_P correlation coefficient derived for all the sample is reported in parenthesis. On the X labels, we plotted (from top to bottom, left to right): mean iron abundance ratio; the integrated V magnitude; Galactocentric radius (R_{GC}); the age in Gyr; the isophotal ellipticity ϵ=1–(b/a); the central radial velocity dispersion; the concentration; the tidal radius; and the logarithm of the total mass in solar units .

conclusions. Clearly, with only four clusters (of the same metallicity) in the sample, little more can be said. Would be very interesting to extend this exercise to a larger number of clusters to allow for a direct comparison with the population ratios drawn from different indicators (i.e., Na-O anticorrelation) and methods (i.e., photometry).

5.7 Discussion & conclusions

We have used low-resolution FORS2 spectra from Pancino et al. (2010) to confirm the presence of a bimodality in the [N/Fe] distributions for stars in three metal rich GCs (with [Fe/H] $\simeq$ –0.5 dex). Pancino et al. (2010) were able to detect a substantial spread, with a hint of bimodality in the strength of the S(3839) band, and in CH(4300), among MS stars in these clusters. Furthermore, these bands are found to anticorrelated and almost certainly have a bimodal distribution. Our comparison with synthetic spectra presented in this Chapter confirms that the band strengths correspond to substantial real variations in the abundances of [C/Fe] and [N/Fe]. Moreover, the behavior of NGC 5927, NGC 6352, and NGC 6388 MS stars in the [C/Fe]-[N/Fe] plane is very similar (see Figure 5.7). First, these MS stars display an intrinsic dispersion in bot C and N abundances that could not be accounted for by mixing effects. N shows a clear spread, while the spread in C is not as strong but still well above the measurement errors. *This finding demonstrates that multiple populations are not confined to metal poor clusters that may have formed in a rather quiet environment and perhaps later accreted and stripped off their progenitor; but also the metal-rich GC family formed in a turbulent, clumpy disk or within the bulge itself hosts multiple generation of stars.* Second, N exhibits a clear bimodality in the case of NGC 5927 and NGC 6352: in the case of NGC 6352 stars, we detected a difference in [N/Fe] between the first and the second generation of stars of $\simeq$ 0.8 dex. Third, the N-rich population also appears to have an internal spread in the nitrogen content and possibly a bimodality in the case of NGC 6352 and NGC 5927.

In order to search for possible drivers for the abundance anomalies we studied the ratio of first-to-second generation stars as a function of various cluster parameters. We considered both structural parameters (including concentration, ellipticity, r_t) and orbital parameters or parameters depending on the location in the Galaxy (R_{GC}, age, M_V, [Fe/H]). Although our sample is made up by only five GCs, which have also similar metallicity, we found weak correlations between r and concentration, luminosity, eccentricity, and present-day mass that broadly agree with past findings (Norris, 1987; Smith and Mateo, 1990; Kayser et al., 2008; Pancino et al., 2010; Smolinski et al., 2011). We find that preferably the more luminous/massive clusters exhibit a large number of N-rich stars. This may be an indication that the CNO processed ejecta could be more efficiently retained by more massive objects. Thus they might keep their gas longer, which favors the buildup of a second generation of enriched stars. Furthermore, we find evidence for an increase of the second-generation stars star fraction with cluster tidal radius (see also Kayser et al., 2008). Since GCs with large tidal radii are mostly found in the weak tidal field of the Galaxy (well outside the bulge and disk potential) they might occupy orbits that avoid bulge/disk shocks.

Nevertheless we point out that our study is limited to a small sample of clusters. For a statistically better supported study a larger cluster sample is necessary.

Table 5.3: Carbon and nitrogen abundances for metal-rich GCs.

ID	A(C)	A(N)	V (mag)	I (mag)	T (K)	log g (dex)
NGC5927-1101	7.07 ± 0.23	7.99 ± 0.26	20.216	18.677	5616 ± 274	4.3
NGC5927-1102	6.18 ± 0.26	8.76 ± 0.32	20.285	18.750	5630 ± 276	4.3
NGC5927-1103	7.09 ± 0.22	6.91 ± 0.35	20.172	18.606	5524 ± 261	4.3
NGC5927-1104	7.07 ± 0.23	7.88 ± 0.25	20.149	18.605	5599 ± 272	4.3
NGC5927-1105	7.20 ± 0.23	6.91 ± 0.35	20.368	18.841	5659 ± 280	4.3
NGC5927-1106	6.78 ± 0.22	8.26 ± 0.25	20.140	18.586	5564 ± 267	4.3
NGC5927-1107	6.89 ± 0.23	8.30 ± 0.25	20.392	18.845	5589 ± 270	4.3
NGC5927-1202	7.40 ± 0.25	7.65 ± 0.27	20.448	18.932	5699 ± 286	4.4
NGC5927-1204	6.93 ± 0.21	6.91 ± 0.35	20.729	19.128	5410 ± 246	4.4
NGC5927-1205	6.62 ± 0.21	8.50 ± 0.25	20.392	18.808	5465 ± 253	4.3
NGC5927-1206	6.79 ± 0.22	8.33 ± 0.25	20.396	18.822	5497 ± 258	4.3
NGC5927-1207	7.28 ± 0.22	6.91 ± 0.35	20.770	19.200	5511 ± 259	4.4
NGC5927-1208	7.14 ± 0.21	6.91 ± 0.35	20.170	18.574	5426 ± 248	4.3
NGC5927-1209	7.15 ± 0.23	6.91 ± 0.35	20.376	18.841	5630 ± 276	4.3
NGC5927-1210	7.08 ± 0.22	7.72 ± 0.32	20.210	18.652	5551 ± 265	4.3
NGC5927-2101	7.04 ± 0.27	8.26 ± 0.29	20.143	18.701	5989 ± 329	4.3
NGC5927-2102	7.62 ± 0.28	6.91 ± 0.35	20.289	18.856	6028 ± 335	4.3
NGC5927-2115	7.58 ± 0.25	6.91 ± 0.35	20.216	18.728	5804 ± 301	4.3
NGC5927-2116	7.55 ± 0.24	6.91 ± 0.35	20.167	18.658	5725 ± 290	4.3
NGC5927-3111	7.10 ± 0.21	6.91 ± 0.35	20.186	18.601	5461 ± 253	4.3
NGC5927-3112	7.19 ± 0.21	6.91 ± 0.35	20.411	18.816	5429 ± 248	4.3
NGC5927-3113	7.28 ± 0.21	7.86 ± 0.23	19.818	18.236	5471 ± 254	4.1
NGC5927-3115	7.25 ± 0.20	6.91 ± 0.35	19.958	18.353	5398 ± 244	4.2
NGC5927-3201	7.31 ± 0.20	6.91 ± 0.35	20.425	18.820	5398 ± 244	4.4
NGC5927-3203	7.41 ± 0.23	6.91 ± 0.35	20.133	18.609	5670 ± 282	4.3
NGC5927-3204	7.08 ± 0.20	6.91 ± 0.35	20.226	18.623	5404 ± 245	4.3
NGC5927-3205	7.38 ± 0.22	6.91 ± 0.35	19.930	18.364	5524 ± 261	4.2
NGC5927-3206	7.10 ± 0.23	6.91 ± 0.35	20.031	18.490	5609 ± 273	4.2
NGC5927-3208	7.28 ± 0.21	7.74 ± 0.23	19.834	18.236	5420 ± 247	4.1
NGC5927-3209	7.49 ± 0.23	7.68 ± 0.26	20.114	18.573	5609 ± 273	4.3
NGC5927-3210	7.08 ± 0.22	6.91 ± 0.35	20.438	18.867	5507 ± 259	4.4
NGC5927-4103	6.75 ± 0.23	8.13 ± 0.27	20.113	18.555	5551 ± 265	4.3
NGC5927-4106	6.93 ± 0.21	6.91 ± 0.35	20.315	18.711	5401 ± 244	4.3
NGC5927-4108	7.12 ± 0.21	6.91 ± 0.35	20.273	18.675	5420 ± 247	4.3
NGC5927-4112	7.09 ± 0.21	6.91 ± 0.35	20.411	18.816	5429 ± 248	4.3
NGC5927-4114	7.43 ± 0.23	7.64 ± 0.27	20.002	18.447	5561 ± 266	4.2
NGC6352-1101	6.96 ± 0.19	8.43 ± 0.23	18.661	17.632	5843 ± 153	4.1
NGC6352-1102	7.21 ± 0.16	6.80 ± 0.30	19.006	17.948	5732 ± 145	4.3
NGC6352-1103	7.29 ± 0.16	6.80 ± 0.30	18.988	17.946	5792 ± 149	4.3
NGC6352-1104	7.25 ± 0.18	7.82 ± 0.25	18.644	17.579	5706 ± 143	4.1
NGC6352-1105	6.99 ± 0.18	7.91 ± 0.25	18.633	17.566	5699 ± 143	4.1
NGC6352-1106	7.36 ± 0.17	6.80 ± 0.30	19.153	18.115	5808 ± 150	4.3
NGC6352-1107	7.24 ± 0.17	6.80 ± 0.30	18.550	17.491	5728 ± 145	4.1
NGC6352-1108	6.78 ± 0.19	8.30 ± 0.26	18.882	17.798	5638 ± 138	4.2
NGC6352-1109	6.68 ± 0.19	8.38 ± 0.27	18.682	17.592	5616 ± 137	4.1
NGC6352-1111	6.90 ± 0.18	8.14 ± 0.24	18.931	17.882	5766 ± 147	4.2
NGC6352-1113	7.17 ± 0.18	8.02 ± 0.24	19.081	18.038	5789 ± 149	4.3
NGC6352-1114	6.37 ± 0.20	8.54 ± 0.25	19.147	18.086	5721 ± 144	4.3
NGC6352-1115	6.75 ± 0.18	8.50 ± 0.23	18.522	17.484	5808 ± 150	4.1
NGC6352-1116	7.27 ± 0.16	6.80 ± 0.30	18.623	17.603	5879 ± 156	4.1
NGC6352-1201	7.34 ± 0.16	6.80 ± 0.30	18.603	17.554	5766 ± 147	4.1
NGC6352-1202	7.15 ± 0.20	7.94 ± 0.24	18.792	17.750	5792 ± 149	4.2
NGC6352-1203	7.36 ± 0.16	6.80 ± 0.30	18.664	17.619	5781 ± 149	4.1
NGC6352-1204	7.33 ± 0.16	6.80 ± 0.30	18.785	17.740	5781 ± 149	4.2

Table 5.3: Carbon and nitrogen abundances for metal-rich GCs (continued).

ID	A(C)	A(N)	V (mag)	I (mag)	T (K)	log g (dex)
NGC6352-1208	7.51 ± 0.16	6.80 ± 0.30	18.560	17.539	5875 ± 155	4.1
NGC6352-1210	7.18 ± 0.20	7.90 ± 0.24	18.904	17.857	5773 ± 148	4.2
NGC6352-1211	7.45 ± 0.17	6.80 ± 0.30	18.519	17.487	5831 ± 152	4.1
NGC6352-1212	7.12 ± 0.19	8.08 ± 0.23	18.843	17.830	5907 ± 158	4.2
NGC6352-1213	7.35 ± 0.17	6.80 ± 0.30	18.595	17.562	5827 ± 152	4.1
NGC6352-1214	7.39 ± 0.17	6.80 ± 0.30	18.941	17.915	5855 ± 154	4.2
NGC6388-1103	7.64 ± 0.24	7.31 ± 0.27	20.530	19.170	5981 ± 262	4.2
NGC6388-1104	7.45 ± 0.24	8.12 ± 0.26	20.831	19.469	5973 ± 261	4.3
NGC6388-1106	7.44 ± 0.23	7.85 ± 0.26	20.610	19.254	5998 ± 264	4.2
NGC6388-1108	7.26 ± 0.24	7.65 ± 0.27	20.994	19.619	5919 ± 254	4.3
NGC6388-1109	6.93 ± 0.23	8.45 ± 0.26	20.815	19.446	5944 ± 257	4.3
NGC6388-1112	6.80 ± 0.23	8.60 ± 0.26	20.555	19.172	5887 ± 251	4.2
NGC6388-1113	7.41 ± 0.23	7.00 ± 0.35	20.689	19.267	5736 ± 233	4.2
NGC6388-1202	7.12 ± 0.23	7.00 ± 0.35	20.558	19.133	5725 ± 231	4.2
NGC6388-1203	6.97 ± 0.23	8.10 ± 0.25	21.189	19.790	5823 ± 243	4.4
NGC6388-1206	7.37 ± 0.23	7.00 ± 0.35	20.716	19.299	5755 ± 235	4.2
NGC6388-1207	6.91 ± 0.25	8.72 ± 0.28	20.642	19.276	5956 ± 259	4.2
NGC6388-2103	7.73 ± 0.24	7.00 ± 0.99	20.530	19.170	5981 ± 262	4.2
NGC6388-2105	7.43 ± 0.24	7.53 ± 0.28	20.592	19.232	5981 ± 262	4.2

CHAPTER

6 Conclusions and discussion

The knowledge about how GCs formed and evolved has advanced at a incredible rate over the last 10 years, but there are still several points regarding this *self-pollution* scenario that remain to be properly understood (see Sect. 1.8 for a description). Accurate multi-band photometry and multi-object spectroscopy are providing a huge amount of data, making the observational scenario far more complex than once envisioned: interpretation of all these data in a working scenario for the origin and early stages of cluster life appears anything but simple. As a matter of fact, understanding the chemical enrichment histories of all clusters, from the least to the most complex, represents one of the major challenges in modern astronomy.

It is not easy to put all the result of three years research in a coherent picture, as the field is moving very quickly in the last years. In this last chapter I try to summarize the observational evidence I added to the multi population scenario, the questions addressed, and the conclusion reached. The second part of the chapter is devoted to a review of ongoing and future research developments.

6.1 Summary of Thesis Results and Implications

I can summarize the main results of this dissertation as follows.

1. In Chapter 2 we present radial distributions for the first-to-second generation number ratio for seven GCs in the SDSS. Lardo et al. (2011) more than doubles the number of clusters for which such studies exist. This clearly indicates that second generation stars are *always* more concentrated toward the cluster center with respect to first generation stars. We enlarge and discuss the implications of this result in Sect. 6.2.1.

2. In Chapter 3 we add critical pieces of evidence to the puzzling NGC 1851 observational scenario (Lardo et al., 2012a). This cluster belongs to the group of massive clusters[1], which

[1] Such as ω Centauri (Pancino et al., 2000b; Bedin et al., 2004), M 54 (Siegel et al., 2007), M 22 (Marino et al., 2009, 2011, 2012b), Terzan 5 (Ferraro et al., 2009; Origlia et al., 2011).

are distinguished from the normal GCs. The discrete distributions of RGBs and SGBs observed in the CMDs of these GCs, together with spectroscopic variations in heavy element abundances, indicate that they have experienced a much more troubled star-formation history. These GCs are generally thought to be the relics of more massive primeval dwarf galaxies that were disrupted by and merged with the Galaxy (Lee et al., 1999; Bekki and Freeman, 2003; Carretta et al., 2010d; Bekki and Yong, 2011), and therefore, have important implications on the hierarchical merging paradigm of galaxy formation.

3. In Chapter 4 we present new spectroscopic and photometric findings on the peculiar nature of M 2. Coupling our results with other recent studies (Piotto et al., 2012), we argue that also M 2 could belong to the class of *peculiar* clusters (see Sect. 6.3). The apparent similarity of M 2 to NGC 1851 andM 22 calls for a deeper and complete spectroscopic characterization of stars in this anomalous RGB we discovered (see Sect. 4.5): only accurate measurements of metal abundances for a representative sample of stars will shed light on the origin of this poorly studied cluster.

4. In Chapter 5 we report a spectroscopic study of three metal-rich ([Fe/H] $\simeq$ –0.5 dex) clusters; namely, NGC 5927, NGC 6352, and NGC 6388. When the S/N of our spectra was good enough, we could detect clear [C/Fe] and [N/Fe] anticorrelations, which were always clearly bimodal. The interest related to the presence of a bimodal distribution – rather than a continuous spread – is clear in the light of the latest theories of self-enrichment for GC: if we find a clear bimodality in the data, this supports the idea of two discrete star formation episodes. This result also suggests that the contradiction between GCs discrete photometric properties and continuous spectroscopic ones could be only apparent (see Chapter 5 for a critical discussion).

6.2 Global Results

Our work contributed to make significant progress mainly in two areas: the structural properties and radial distribution of multiple populations and the discrete vs continuos nature of the stellar properties in the different generation of stars.

6.2.1 Spatial distribution of multiple populations

In Chapter 2 we have used wide-field u, g, r SDSS photometry of 9 GCs to search for the spread in UV color along the RGB indicative of multiple populations. We detected a statistically significant UV spread in 7 of the considered clusters and found that in all of these cluster second generation stars are more centrally concentrated than first generation ones. This leads us to conclude that this difference in the radial distribution of different gene ration of stars may be a general property shared by most/all GCs.

At the time at which this result was obtained, only a handful of studies reported the evidence that second generation stars are more concentrated toward the cluster center with respect

to their first generation counterparts (Pancino et al., 2003; Sollima et al., 2007; Kravtsov et al., 2010b,a; Carretta et al., 2009c; Milone et al., 2009b; Zoccali et al., 2009; Bellini et al., 2009). There was also some controversy concerning NGC 1851 (Milone et al., 2009b), but whit our study we more than doubled the number of the GCs for which this effects is reported and dispelled any remaining doubt.

Our result fully confirms the theoretical predictions by D'Ercole et al. (2008). Their hydrodynamical, N-body simulations showed that AGB ejecta form a cooling flow and rapidly collect in the innermost regions of the cluster, forming a concentrated second generation stellar subsystem (see also Bekki, 2011).

Aditionally, we provided the radial profiles of the second-to-first generation number ratio (N_{SG}/N_{FG}). The shape of this observed quantity is a useful basis to test theoretical scenarios, when compared with specific models reproducing the present-day status of the considered clusters. In a recent paper Vesperini et al. (2013) studied the structural evolution of multiple population clusters. They focused on the spatial mixing of the first and second populations, and their relative spatial distribution. After the early loss of first generation stars (after $\simeq$ 1–2 Gyr in D'Ercole et al., 2008 simulations), a multiple-population cluster starts its long-term evolution driven by two-body relaxation with a similar number of first and second generation stars, but with the second population still concentrated in the inner regions.

As shown in Fig. 7 in Vesperini et al. (2013), the system starts with the SG population more concentrated toward the center; then, as the cluster evolves, the first and second generation stars mix. This mixing occurs more efficiently in the cluster innermost regions, where the local two-body relaxation time scale is shorter, resulting in a flat portion in the N_{SG}/N_{FG} profile in the cluster center. The inner portion of the profiles progressively extends toward the outer regions until it reaches the cluster outskirts (i.e., complete mixing). As a result, during a large fraction of cluster evolution, the first and second generation stars are not completely mixed and N_{SG}/N_{FG} varies with the distance from the cluster center. The N_{SG}/N_{FG} radial profile is characterized by an approximately flat N_{SG}/N_{FG} inner region followed by a declining outer portion corresponding to regions increasingly dominated by first generation stars. In the outer regions, the N_{SG}/N_{FG} profile is characterized again by an approximately flat portion followed, in some cases, by a weak final rise in the profile in the cluster outermost regions. Vesperini et al. (2013) simulations indicate that some memory of the initial second population segregation predicted by D'Ercole et al. (2008) should still be preserved and observable in many clusters today, depending on the relaxation times of each cluster. As a matter of fact, the overall shape of the N_{SG}/N_{FG} radial profile we observed (see also Bellini et al., 2009 and Milone et al., 2012c) is entirely compatible to what obtained by Vesperini et al. (2013). This is expected by theoretical models, as all our clusters have values of the $t/t_{rh}(t)$ such that the presence of a radial gradient in the N_{SG}/N_{FG} profile is predicted to be observable (Vesperini et al., 2013).

While our data presented in Chapter 2 do not in general probe these innermost regions (see Fig. 2.6), i.e., indicating the need of complementary HST observations for the central crowded regions, they demonstrated it to be a fundamental starting point to test theoretical predictions.

Systematic and uniform investigation of the photometric properties of a large number of GCs will be one of the basic observational constraints for testing theoretical scenarios (and, hopefully, models) of the multiple populations.

6.2.2 Photometric discreteness vs. spectroscopic continuity

One of the most interesting open issues in the multiple population context is the continuous versus discrete nature of the multiple stellar generations in GCs.

For the most massive clusters, the clearly separated, multiple MSs indicate that within each sequence the matter is homogeneous, both in He and in Fe. That is, He enrichment of the ICM and star formation for the second (and third) stellar generation took place through distinct episodes. However, this is not reflected by the observed Na-O anticorrelations, where first generation and second generation appear to be distributed continuously. A few studies (e.g., Marino et al., 2008 for M 4, Carretta et al., 2012a for NGC 6752, Carretta et al., 2012b for 47 Tuc) seem to indicate a separation between the two stellar generations, but the evidence of multimodality from high resolution spectra is still sparse.

On the contrary, bimodality of the stellar surface abundance of CN is almost universal among clusters having metallicities [Fe/H] $\geqslant$ –1.6 (see the excellent review by Martell, 2011). Because of the large effect of NH and CN molecules (i.e., both proxies for the nitrogen abundance) on the UV filters, first and second generation stars, with different nitrogen abundances, are clearly separated along the RGB in U-based CMD; i.e., Han et al. (2009a); Roh et al. (2011); Kravtsov et al. (2010a); Lee et al. (2009b); Carretta et al. (2011a); Milone et al. (2010, 2012c); Marino et al. (2008, 2012b); see also Sect. 1.2.4. CN bimodality could also be found all the way down to the MS for metal-rich GCs, for which the double-metal molecule CN could be observed also at low S/N (see Fig. 6.1).

All these findings together suggests that maybe the errors associated with the [Na/O] and [O/Fe] abundances derived so far are not sufficiently small for reveal underlying discreteness.

In the case of M 2 (see Chapter 4), we were able to separate between first and second subpopulations and found that N-poor and N-rich stars are clearly separated into two parallel sequences in the broader RGB seen in the $V, U-V$ diagram. Also, the extent of the C-N anticorrelation for second generation stars is greater than the errors associated with abundance measurements. This possibly suggests the presence of a third group of stars; unfortunately, because of uncertainties on abundance measurements and low statistics, we cannot provide conclusive evidence.

For metal-rich ([Fe/H] $\simeq$ –0.5 dex) clusters presented in Chapter 5, the situation is clearer. At these metallicities, in fact, the CH and CN bands are so strong that it is quite easy to reveal their variations also at low S/N for faint unevolved stars. As described in Chapter 5, we obtained [C/Fe] and [N/Fe] abundances of a relatively large number of faint MS stars in three metal-rich clusters: namely NGC 5927, NGC 6352, and NGC 6388. Interestingly, we obtained a bimodal distribution in the C-N plane for two out of three clusters in our sample[2]. This is even more surprising when considering that we are dealing with low resolution spectra in the blue part of the

[2]The lack of detection of bimodality for NGC 6388 is probably due to the low S/N ratio of its spectra.

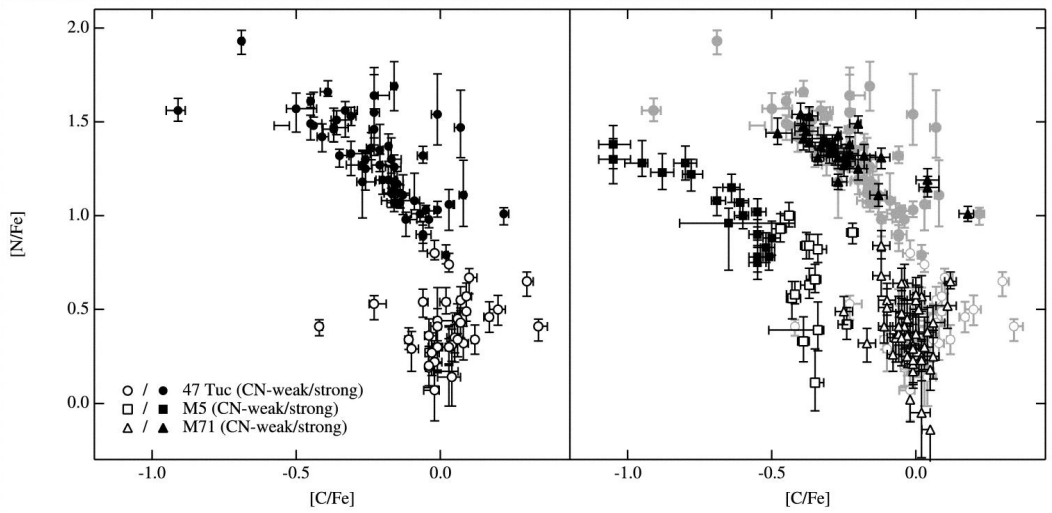

Figure 6.1: *Left*: C and N abundances of 47 Tuc MS stars are shown (from Briley et al., 2004), where a clear bimodality can be seen.*Right*: The distribution of C and N among a similar sample of M 71 and M 5 stars (from Briley and Cohen, 2001 and Cohen et al., 2002) is also plotted. The general pattern is the same between all three clusters, and M 71 and 47 Tuc (two clusters of similar metallicity) appear to be essentially indistinguishable. In the case of the more metal-poor M 5, the C depletions are more extreme, yet the N enhancements are not.

visible spectrum of faint stars. The distribution of first and second generation stars in the C-N anticorrelation closely resembles the case of involved stars in 47 Tuc and M 71 (see Fig. 6.1), where a strong bimodality in the nitrogen content is apparent, with second generation also showing a clear internal C-N anticorrelation.

If this is the case, the implication seems to be that the scenario of cluster formation must include multiple bursts where the second population formed. In each, the interplay between matter processed by polluters of different mass (decreasing with time) and pristine material does combine to give the observed chemical pattern in each group. Not much more can be said using only C and N abundances, ideally one would need a complete set of key element abundances in a significant number of stars and clusters to fully characterize each individual group.

We have now analyzed five Galactic GCs covering a large range in metallicity: NGC 1851 (Chapter 3), M 2 (Chapter 4), NGC 5927, NGC 6352, and NGC 6388 (see Chapter 5). In the case of NGC 1851, NGC 5927, NGC 6352, and NGC 6388, we have large samples of unevolved stars. Only a few determinations of carbon and nitrogen abundances for SGB, TO, and MS stars exist in literature (namely, M 71, M 5, M 13, M 15, and 47 Tuc; see Cohen et al., 2005 and references therein). With our work we double the number of clusters for which viable [C/Fe] and [N/Fe] abundances exist for the low luminosity range.

So far, a clear bimodality in the C and N distribution (see Fig. 6.1) was only found in the case of M 71 Briley and Cohen, 2001 and 47 Tuc (see Cannon et al., 1998 and Briley et al., 2004 for references therein to many earlier studies). In Chapter 5 we demonstrated that also in the case of NGC 6352 and NGC 5927 the MS stars the first generation and second generation are

confined into discrete clumps, enlarging once again the size of the sample for which bimodality is observed.

The existence of a clear separation between populations, possibly bringing into agreement photometry, low- and high-resolution spectroscopy (of all the involved chemical species) would be of immense value, helping us not only to solve the long standing puzzle of who-is-who, but also to resolve all conflicts on the population ratio (see Sect. 5.6.1), a strong constraint on our ability to understand and model the formation and evolution of multiple populations in globular clusters and GC system connection with the Galaxy halo. According to models (see also Sect. 6.2.1), almost all of the stars that manage to escape the clusters at early times are first generation stars (D'Ercole et al., 2008)[3], as the cluster evolution continues into the phase dominated by two-body relaxation, the two populations mix and the fractional escape rates of the first and second generation stars due to evaporation tend to equalize, stabilizing the second generation fraction (Vesperini et al., 2010). Two recent spectroscopic studies have found that the vast majority of halo stars studied have abundances typical of first generation stars in clusters; only about 1.5% – 2.5% of the stars are Na-rich (Carretta et al., 2010c) and CN-strong (Martell et al., 2011), and hence classifiable as second generation stars. Vesperini et al. (2010) confirmed this values and found that the fraction of mass of the Galactic stellar halo in second-generation stars is always small, < 4%-6% for a Kroupa et al. (1993) IMF and < 7%-9% for a Kroupa (2001) IMF. This implies that a large fraction of the Galactic stellar halo (from 20% to about 40%) must be composed of stars originally formed in globular clusters (Vesperini et al., 2010).

6.3 The zoo of Galactic globular clusters

From the discussion to the subject of multiple stellar populations presented in this dissertation and the large literature published on this topic in the last years (and reviewed in Chapter 1), it appears clear that all clusters are different and the main properties of stellar generations (i.e., the first-to-second generation number ratio, their radial trends, extension and shape of the C-N, Na-O anticorrelation, CMD morphologies) differ from cluster to cluster.

Appears, at the moment, difficult to fit all the observational evidence and modeling into a unique scenario. Marino et al. (2011) proposed a a schematic classification, according to the degree of complexity GCs display:

– **normal GCs**, those GCs that show only chemical inhomogeneities in the light element abundances. Nearly all globular cluster have these characteristics[4] and the presence of the Na-O anticorrelation has been suggested as the operative definition of *bona fide* GC (Carretta et al., 2009c). Multiple RGBs can be recognized in their CMDs if proper filters are used.

[3] The fact that first generation stars were much more numerous at the time of cluster formation can also account for the polluting material needed to explain the following stellar generation.

[4] With the possible exceptions of Pal 12, Terzan 7 and IC 4499 (Walker et al., 2011).

– **peculiar GCs**. To this class belong clusters such as M 22 and NGC 1851. Beyond the *classic* C-N, Na-O anticorrelations, these GCs display small metallicity spreads and bimodal heavy element distribution. Additionally, each *s*-process group has its own C-N, Na-O anticorrelation; suggesting that their nucleosynthetic history must be more complicated than for *normal* GCs. Their CMDs appear also complex, with split at also the level of RGB and SGB.

– ω **Centauri**, the more extreme GC, with a huge spread in iron, multiple Na-O anticorrelations, large variation in *s*-process elements with metallicity, and multiple sequences along the entire CMD. Also the massive cluster M 54 displays many similarities with ω Cen [5]. Even more so than those, G 1 could be a kind of transition step between globular clusters and dwarf elliptical galaxies, in being the remaining core of a dwarf galaxy whose envelope would have been severely pruned by tidal shocking due to the bulge and disk of its host galaxy, M 31 (Meylan et al., 2001).

Although high-resolution spectroscopy is the best way to derive abundances, it needs also an enormous amount of observing time. Throughout these pages, we tried to convince the reader that low resolution spectroscopy, aimed to derived C and N abundances can be reasonably regarded as a useful complement to high-resolution observations. Whenever possible, it is worth coupling C and N abundances to U-based photometry, in order to maximize the information on multiple stellar generations. We demonstrated the effectiveness of such approach both in the cases of NGC 1851 and M 2 (see Chapters 3 and 4 for more details).

For NGC 1851, our analysis added new pieces of evidence for the observational scenario (we refer the reader to Chapter 3 for a summary of the previous photometry and spectroscopic findings and for a wider discussion on the peculiarity of this cluster). As for the other clusters belonging to the second group, NGC 1851 could be the link between normal GCs and more massive objects like ω Centauri and even dwarf galaxies.

Recently, Joo and Lee (2012) investigated the star formation histories of these peculiar GCs, by constructing synthetic CMDs for M 22, and NGC 1851. They found that the age differences between the metal-rich and metal-poor subpopulations, as defined by the split SGB, is relatively small ($\simeq$0.3 Gyr, see also Marino et al., 2012b) and metal-rich subpopulations with redder RGBs are also enhanced in helium abundance. The formation time scale of stellar populations in these GCs is therefore expected to be fairly short, i.e., less than 1 Gyr. Hence we can imagine this possible scenario for these two peculiar clusters:

(1) initially, a first generation of metal-poor (bright SGB/blue RGB) stars formed from gas having normal helium and light element abundances,

(2) the remaining gas is then polluted by the winds from FRMSs, which enhance helium and alter the abundance profile of light elements.

[5] As suggested by Carretta et al. (2010b), also M 54 may has formed in a very similar way to ω *Cen*: these two objects (the most massive GCs of the Milky Way) may represent just two subsequent snapshots of the same basic evolution of dwarf galaxies, taken at different times (Carretta et al., 2010b)

(3) The most massive ($\geqslant$8 $M_\odot$) stars then would explode as type II SNe, altering the overall metallicity, including heavy elements and the total CNO content[6].

(4) Further pollution of the gas by the ejecta from intermediate-mass AGB stars ($\simeq$3–7 $M_\odot$) would follow, which enhance helium and change light element abundances.

(5) Finally, formation of the second-generation metal-rich (faint SGB/redder RGB) stars from the gas now enriched in overall metallicity and helium and polluted in light element abundances.

This simple scenario requires that GCs were much more massive in the past, because their present masses are too small to retain the ejecta of SNe explosions (e.g., Baumgardt et al., 2008). This suggests that these GCs were once nuclei of now disrupted dwarf galaxies and then merged and dissolved in the proto-Galaxy, as is widely accepted for ω Cen (e.g., Lee et al., 1999, Bekki, 2011 and references therein).

Finally, our analysis of Chapter 4 possibly suggests that also M 2 may belong to this second group (see also the results on its double SGB presented by Piotto et al., 2012). It is not clear, however, why the additional RGB we discovered is made up only by this tiny fraction of stars. All these findings call for a deeper and complete spectroscopic characterization of stars in this so far neglected cluster.

6.4 Future Prospects

In this concluding Section, we briefly outline possible future work, which would help to clarify or extend the results presented throughout this dissertation.

6.4.1 Search for UV-blue photometry of GCs in public database

Changes in light-element abundance and helium, in addition to those caused by age, overall metallicity and [α/Fe] reflect in a complex collection of photometric shifts and spreads in GC CMDs when suitable filters are used (see Sect. 1.2). A systematic search of archival space and ground-based photometry could be a profitable way to confirm or deny the presence of multiple populations for a large number of GCs. Also, tracing the multiple population phenomenon throughout the different evolutionary phases (MS, SGB, RGB), and different cluster properties (total mass, orbital parameters, structure, metallicity) is important to establish the distribution among stars from different generations (see for example the SUMO project[7]). Wide field ground-based data should be complemented with HST data to cover also the innermost regions (see Sect. 6.2.1).

[6]The enhancement of the total CNO abundance in the metal-rich later generation subpopulations would in fact indicate the contribution by type II SNe (see also Marino et al., 2012b).

[7]`http://www.iac.es/proyecto/sumo/project.html`

6.4.2 Search for GC-like chemical pattern in extra-galactic environments

The chemical inhomogeneities and multiple sequences are not confined to Galactic GCs only, but they were observed in the LMC clusters (Johnson et al., 2006; Mucciarelli et al., 2009; Milone et al., 2009b) and in Fornax clusters (Letarte et al., 2006). On the other hand, Milky Way stars generally do not show anticorrelations (Gratton et al., 2000) and no chemical anomalies were found in Open Clusters (Martell and Smith, 2009; Smiljanic et al., 2009; Bragaglia et al., 2012 but see Geisler et al., 2012 and Carrera, 2012 for the unique case of NGC 6791).

This suggests that the environment at formation is a fundamental key in the understanding of these anomalies. The environment defines in fact the enrichment history of a cluster through dynamical interactions with the ambient medium of the parent galaxy. Evidence that the orbital parameters and present-day total cluster mass have some impact on the extension of anticorrelations (Carretta et al., 2010c) and on the number ratio of the enriched-to-normal stars (Pancino et al., 2010) supports this statement.

Low-resolution spectroscopy aimed to derive C and N abundances could be regarded as the only viable way to detect multiple populations in far away clusters, for which high-resolution spectroscopy for a statistical significant number of stars is out of reach. In extragalactic environments such as Sagittarius, Sculptor, and Sextans dwarf galaxies, observational constraints (i.e., CH and CN band measurements) can be derived with state-of-art ESO facilities. This kind of study will expand our ability to study of the environmental effect on cluster formation and enrichment history, still unknown or under-constrained.

6.4.3 Building the right database

While it is clear that something is going on in almost every well-studied cluster, it is not clear that we understand how that effect depends on the cluster properties. There are indeed very large cluster to cluster differences: some GCs possibly comply with the SSP template paradigm (e.g., IC 4499; see Walker et al., 2011), others have two, or three, or even five distinct sub-populations (see Chapter 1 and Sect. 6.3). Several studies (e.g., Norris, 1987, Smith and Mateo, 1990, Kayser et al., 2008, Carretta et al., 2010c, Pancino et al., 2010) have highlighted the advantage of having data for a set of GCs, with different structural and orbital parameters, to globally study the extension of light element abundance variations with GC parameters.

To this end, it would be of great value to expand the parameter space to study the multiple population phenomenon in a global way. In order to constrain the properties of the stars in the different generations, it is vital to follow their evolution from the MS to the white dwarf cooling sequence in a carefully selected number of clusters spanning a large range in metallicities, considering (old and young) clusters with different degrees of chemical and photometric complexity.

It would be interesting to expand the present research by exploring more GCs, including all the most massive ones as well as a number of those of smaller mass, searching for multiple sequences and performing accurate star counts. Available multiplex high resolution spectrographs would allow for a detailed chemical composition measurement of large samples of GC stars in

various evolutionary phases. A detailed analysis for not only C and N, but also other elements whose potential has not been fully exploited (such as *s*-process elements, F, and Li see also Sect 1.4), is mandatory whenever possible. This chemical tagging would be particularly interesting for stars in clusters which display *s*-process elements variations (e.g., M 22 Marino et al., 2012b; D'Orazi et al., 2012 and NGC 1851 Lardo et al., 2012a; Gratton et al., 2012c) and for stars belonging to anomalous substructures in GC CMDs (e.g., the additional RGB sequence in M 2, see Lardo et al., 2012b and Chapter 4).

Bibliography

K. N. Abazajian, J. K. Adelman-McCarthy, M. A. Agüeros, and et al. The Seventh Data Release of the Sloan Digital Sky Survey. *apjs*, 182:543–558, June 2009.

C. Abia, K. Cunha, S. Cristallo, P. de Laverny, I. Domínguez, K. Eriksson, L. Gialanella, K. Hinkle, G. Imbriani, A. Recio-Blanco, V. V. Smith, O. Straniero, and R. Wahlin. Fluorine Abundances in Galactic Asymptotic Giant Branch Stars. *apjl*, 715:L94–L98, June 2010.

A. Alonso, S. Arribas, and C. Martinez-Roger. The empirical scale of temperatures of the low main sequence (F0V-K5V). *aap*, 313:873–890, September 1996.

A. Alonso, S. Arribas, and C. Martínez-Roger. The effective temperature scale of giant stars (F0-K5). II. Empirical calibration of T_{eff} versus colours and [Fe/H]. *aaps*, 140:261–277, December 1999.

A. Alonso, S. Arribas, and C. Martínez-Roger. Erratum: The effective temperature scale of giant stars (F0-K5). II. Empirical calibration of T_{eff} versus colours and [Fe/H]. *aap*, 376:1039, September 2001.

J. Alonso-García, M. Catelan, P. Amigo, C. Cortés, C. A. Kuehn, F. Grundahl, G. López, R. Salinas, H. A. Smith, P. B. Stetson, A. V. Sweigart, A. A. R. Valcarce, and M. Zoccali. Disentangling multiple stellar populations in globular clusters using the Str\"omgren system. *ArXiv e-prints*, December 2012.

A. Alves-Brito, D. Yong, J. Meléndez, S. Vásquez, and A. I. Karakas. CNO and F abundances in the globular cluster M 22 (NGC 6656). *aap*, 540:A3, April 2012.

D. An, J. A. Johnson, J. L. Clem, B. Yanny, C. M. Rockosi, H. L. Morrison, P. Harding, J. E. Gunn, C. Allende Prieto, T. C. Beers, K. M. Cudworth, I. I. Ivans, Ž. Ivezić, Y. S. Lee, R. H. Lupton, D. Bizyaev, H. Brewington, E. Malanushenko, V. Malanushenko, D. Oravetz, K. Pan, A. Simmons, S. Snedden, S. Watters, and D. G. York. Galactic Globular and Open Clusters in the Sloan Digital Sky Survey. I. Crowded-Field Photometry and Cluster Fiducial Sequences in ugriz. *apjs*, 179:326–354, December 2008.

J. Andersen. Proceedings of the Twenty-third General Assembly. *Transactions of the International Astronomical Union, Series B*, 23, 1999.

J. Anderson, I. R. King, H. B. Richer, G. G. Fahlman, B. M. S. Hansen, J. Hurley, J. S. Kalirai, R. M. Rich, and P. B. Stetson. Deep Advanced Camera for Surveys Imaging in the Globular Cluster NGC 6397: Reduction Methods. *aj*, 135:2114–2128, June 2008.

J. Anderson, G. Piotto, I. R. King, L. R. Bedin, and P. Guhathakurta. Mixed Populations in Globular Clusters: Et Tu, 47 Tuc? *apjl*, 697:L58–L62, May 2009.

G. C. Angelou, R. J. Stancliffe, R. P. Church, J. C. Lattanzio, and G. H. Smith. The Role of Thermohaline Mixing in Intermediate- and Low-metallicity Globular Clusters. *apj*, 749:128, April 2012.

D. Argast, M. Samland, F.-K. Thielemann, and Y.-Z. Qian. Neutron star mergers versus core-collapse supernovae as dominant r-process sites in the early Galaxy. *aap*, 416:997–1011, March 2004.

B. J. Armosky, C. Sneden, G. E. Langer, and R. P. Kraft. Abundance trends among neutron capture elements in giants of globular clusters M5, M3, M13, M92, and M15. *aj*, 108:1364–1374, October 1994.

M. Arnould. The nuclear physics input to astrophysics modelling, and the r- and p-processes: Where do we stand 50 years after B^2FH and Cameron? In C. Charbonnel and J.-P. Zahn, editors, *EAS Publications Series*, volume 32 of *EAS Publications Series*, pages 1–59, November 2008.

K. M. Ashman, C. M. Bird, and S. E. Zepf. Detecting bimodality in astronomical datasets. *aj*, 108:2348–2361, December 1994.

G. Battaglia, E. Tolstoy, A. Helmi, M. J. Irwin, B. Letarte, P. Jablonka, V. Hill, K. A. Venn, M. D. Shetrone, N. Arimoto, F. Primas, A. Kaufer, P. Francois, T. Szeifert, T. Abel, and K. Sadakane. The DART imaging and CaT survey of the Fornax dwarf spheroidal galaxy. *aap*, 459:423–440, November 2006.

H. Baumgardt, P. Kroupa, and G. Parmentier. The influence of residual gas expulsion on the evolution of the Galactic globular cluster system and the origin of the Population II halo. *mnras*, 384:1231–1241, March 2008.

L. R. Bedin, G. Piotto, J. Anderson, S. Cassisi, I. R. King, Y. Momany, and G. Carraro. ω Centauri: The Population Puzzle Goes Deeper. *apjl*, 605:L125–L128, April 2004.

K. Bekki. Secondary star formation within massive star clusters: origin of multiple stellar populations in globular clusters. *mnras*, 412:2241–2259, April 2011.

K. Bekki and K. C. Freeman. Formation of ω Centauri from an ancient nucleated dwarf galaxy in the young Galactic disc. *mnras*, 346:L11–L15, December 2003.

K. Bekki and J. E. Norris. The Origin of the Double Main Sequence in ω Centauri: Helium Enrichment due to Gas Fueling from Its Ancient Host Galaxy? *apjl*, 637:L109–L112, February 2006.

K. Bekki, H. Yahagi, M. Nagashima, and D. A. Forbes. The origin of globular cluster systems from cosmological simulations. *mnras*, 387:1131–1148, July 2008.

K. Bekki and D. Yong. On the origin of the stellar halo and multiple stellar populations in the globular cluster NGC 1851. *mnras*, page 1858, November 2011.

M. Bellazzini. The surface brightness profile of the remote cluster NGC 2419. *aap*, 473:171–176, October 2007.

M. Bellazzini, R. A. Ibata, S. C. Chapman, A. D. Mackey, L. Monaco, M. J. Irwin, N. F. Martin, G. F. Lewis, and E. Dalessandro. The Nucleus of the Sagittarius Dsph Galaxy and M54: a Window on the Process of Galaxy Nucleation. *aj*, 136:1147–1170, September 2008.

M. Bellazzini, F. F. Pecci, F. R. Ferraro, S. Galleti, M. Catelan, and W. B. Landsman. Age as the Second Parameter in NGC 288/NGC 362? I. Turnoff Ages: A Purely Differential Comparison. *aj*, 122:2569–2586, November 2001.

A. Bellini, L. R. Bedin, G. Piotto, A. P. Milone, A. F. Marino, and S. Villanova. New Hubble Space Telescope WFC3/UVIS Observations Augment the Stellar-population Complexity of ω Centauri. *aj*, 140:631–641, August 2010.

A. Bellini, G. Piotto, L. R. Bedin, I. R. King, J. Anderson, A. P. Milone, and Y. Momany. Radial distribution of the multiple stellar populations in ω Centauri. *aap*, 507:1393–1408, December 2009.

P. A. Bergbusch and D. A. VandenBerg. Models for Old, Metal-poor Stars with Enhanced α-Element Abundances. III. Isochrones and Isochrone Population Functions. *apj*, 556:322–339, July 2001.

M. S. Bessell. UBVRI photometry. II - The Cousins VRI system, its temperature and absolute flux calibration, and relevance for two-dimensional photometry. *pasp*, 91:589–607, October 1979.

E. Bica, C. M. Dutra, J. Soares, and B. Barbuy. New infrared star clusters in the Northern and Equatorial Milky Way with 2MASS. *aap*, 404:223–232, June 2003.

H. E. Bond. A new CH star in the globular cluster omega Centauri. *apjl*, 202:L47–L49, November 1975.

A. Bragaglia, E. Carretta, R. Gratton, V. D'Orazi, S. Cassisi, and S. Lucatello. Helium in first and second-generation stars in globular clusters from spectroscopy of red giants. *aap*, 519:A60, September 2010a.

A. Bragaglia, E. Carretta, R. G. Gratton, S. Lucatello, A. Milone, G. Piotto, V. D'Orazi, S. Cassisi, C. Sneden, and L. R. Bedin. X-shooter Observations of Main-sequence Stars in the Globular Cluster NGC 2808: First Chemical Tagging of a He-normal and a He-rich Dwarf. *apjl*, 720:L41–L45, September 2010b.

A. Bragaglia, R. G. Gratton, E. Carretta, V. D'Orazi, C. Sneden, and S. Lucatello. Searching for multiple stellar populations in the massive, old open cluster Berkeley 39. *aap*, 548:A122, December 2012.

M. M. Briley and J. G. Cohen. Calibration of the CH and CN Variations Among Main-Sequence Stars in M71 and in M13. *aj*, 122:242–247, July 2001.

M. M. Briley, D. Harbeck, G. H. Smith, and E. K. Grebel. On the Carbon and Nitrogen Abundances of 47 Tucanae's Main-Sequence Stars. *aj*, 127:1588–1593, March 2004.

M. M. Briley, G. H. Smith, R. A. Bell, J. B. Oke, and J. E. Hesser. CN and CH variations on the M5 subgiant branch. *apj*, 387:612–621, March 1992.

J. A. Brown and G. Wallerstein. High resolution CCD spectra of stars in globular clusters. VIII - The self-enrichment history of Omega Centauri. *aj*, 106:133–141, July 1993.

D. L. Burris, C. A. Pilachowski, T. E. Armandroff, C. Sneden, J. J. Cowan, and H. Roe. Neutron-Capture Elements in the Early Galaxy: Insights from a Large Sample of Metal-poor Giants. *apj*, 544:302–319, November 2000.

M. Busso, R. Gallino, and G. J. Wasserburg. Nucleosynthesis in Asymptotic Giant Branch Stars: Relevance for Galactic Enrichment and Solar System Formation. *araa*, 37:239–309, 1999.

D. Butler, R. J. Dickens, and E. Epps. Studies of RR Lyrae variable stars in the unusual globular cluster Omega Centauri. I - Spectroscopic observations. *apj*, 225:148–164, October 1978.

E. Caffau, H.-G. Ludwig, M. Steffen, B. Freytag, and P. Bonifacio. Solar Chemical Abundances Determined with a CO5BOLD 3D Model Atmosphere. *solphys*, 268:255–269, February 2011.

A. Calamida, G. Bono, P. B. Stetson, L. M. Freyhammer, S. Cassisi, F. Grundahl, A. Pietrinferni, M. Hilker, F. Primas, T. Richtler, M. Romaniello, R. Buonanno, F. Caputo, M. Castellani, C. E. Corsi, I. Ferraro, G. Iannicola, and L. Pulone. Strömgren Photometry of Galactic Globular Clusters. I. New Calibrations of the Metallicity Index. *apj*, 670:400–422, November 2007.

A. G. W. Cameron and W. A. Fowler. Lithium and the s-PROCESS in Red-Giant Stars. *apj*, 164:111, February 1971.

S. W. Campbell, Y. Fenner, A. I. Karakas, J. C. Lattanzio, and B. K. Gibson. Abundance anomalies in NGC 6752. Are AGB stars the culprits? *memsai*, 75:735, 2004.

S. W. Campbell, D. Yong, E. C. Wylie-de Boer, R. J. Stancliffe, J. C. Lattanzio, G. C. Angelou, V. D'Orazi, S. L. Martell, F. Grundahl, and C. Sneden. Cyanogen in NGC 1851 RGB and AGB Stars: Quadrimodal Distributions. *ArXiv e-prints*, November 2012.

R. D. Cannon, B. F. W. Croke, R. A. Bell, J. E. Hesser, and R. A. Stathakis. Carbon and nitrogen abundance variations on the main sequence of 47 Tucanae. *mnras*, 298:601–624, August 1998.

R. D. Cannon and R. S. Stobie. Photometry of southern globular clusters I. Bright stars in omega Centauri. *mnras*, 162:207, 1973.

R. Canterna, T. Ferrall, and W. E. Harris. Abundance indicators from vidicon spectra in six globular clusters. *apj*, 258:612–627, July 1982.

J. A. Carballo-Bello, M. Gieles, A. Sollima, S. Koposov, D. Martínez-Delgado, and J. Peñarrubia. Outer density profiles of 19 Galactic globular clusters from deep and wide-field imaging. *mnras*, 419:14–28, January 2012.

D. F. Carbon, W. Romanishin, G. E. Langer, D. Butler, E. Kemper, C. F. Trefzger, R. P. Kraft, and N. B. Suntzeff. Carbon and nitrogen abundances in giant stars of the metal-poor globular cluster M92. *apjs*, 49:207–258, June 1982.

R. Carrera. Analysis of the CN and CH Molecular Band Strengths in Stars of the Open Cluster NGC 6791. *apj*, 758:110, October 2012.

E. Carretta, A. Bragaglia, V. D'Orazi, S. Lucatello, and R. Gratton. On the radial distribution of stars of different stellar generations in the globular cluster NGC 3201. *ArXiv e-prints*, June 2010a.

E. Carretta, A. Bragaglia, R. Gratton, V. D'Orazi, and S. Lucatello. Intrinsic iron spread and a new metallicity scale for globular clusters. *aap*, 508:695–706, December 2009a.

E. Carretta, A. Bragaglia, R. Gratton, V. D'Orazi D'Orazi, and S. Lucatello. A Strömgren view of the multiple populations in globular clusters. *aap*, 535:A121, November 2011a.

E. Carretta, A. Bragaglia, R. Gratton, and S. Lucatello. Na-O anticorrelation and HB. VIII. Proton-capture elements and metallicities in 17 globular clusters from UVES spectra. *aap*, 505:139–155, October 2009b.

E. Carretta, A. Bragaglia, R. G. Gratton, F. Leone, A. Recio-Blanco, and S. Lucatello. Na-O anticorrelation and HB. I. The Na-O anticorrelation in NGC 2808. *aap*, 450:523–533, May 2006.

E. Carretta, A. Bragaglia, R. G. Gratton, S. Lucatello, M. Bellazzini, G. Catanzaro, F. Leone, Y. Momany, G. Piotto, and V. D'Orazi. Detailed abundances of a large sample of giant stars in M 54 and in the Sagittarius nucleus. *aap*, 520:A95+, September 2010b.

E. Carretta, A. Bragaglia, R. G. Gratton, S. Lucatello, G. Catanzaro, F. Leone, M. Bellazzini, R. Claudi, V. D'Orazi, Y. Momany, S. Ortolani, E. Pancino, G. Piotto, A. Recio-Blanco, and E. Sabbi. Na-O anticorrelation and HB. VII. The chemical composition of first and second-generation stars in 15 globular clusters from GIRAFFE spectra. *aap*, 505:117–138, October 2009c.

E. Carretta, A. Bragaglia, R. G. Gratton, S. Lucatello, and V. D'Orazi. Chemical Tagging of Three Distinct Populations of Red Giants in the Globular Cluster NGC 6752. *apjl*, 750:L14, May 2012a.

E. Carretta, A. Bragaglia, R. G. Gratton, Y. Momany, A. Recio-Blanco, S. Cassisi, P. François, G. James, S. Lucatello, and S. Moehler. Na-O anticorrelation and horizontal branches. VI. The chemical composition of the peculiar bulge globular cluster NGC 6388. *aap*, 464:967–981, March 2007.

E. Carretta, A. Bragaglia, R. G. Gratton, A. Recio-Blanco, S. Lucatello, V. D'Orazi, and S. Cassisi. Properties of stellar generations in globular clusters and relations with global parameters. *aap*, 516:A55+, June 2010c.

E. Carretta, R. Gratton, A. Bragaglia, V. D'Orazi, and S. Lucatello. An aluminium tool for multiple stellar generations in the globular clusters 47 Tuc and M 4. *ArXiv e-prints*, December 2012b.

E. Carretta and R. G. Gratton. Abundances for globular cluster giants. I. Homogeneous metallicities for 24 clusters. *aaps*, 121:95–112, January 1997.

E. Carretta, R. G. Gratton, A. Bragaglia, P. Bonifacio, and L. Pasquini. Abundance analysis of turn-off and early subgiant stars in the globular cluster 47 Tuc (NGC 104). *aap*, 416:925–940, March 2004.

E. Carretta, R. G. Gratton, S. Lucatello, A. Bragaglia, and P. Bonifacio. Abundances of C, N, O in slightly evolved stars in the globular clusters NGC 6397, NGC 6752 and 47 Tuc. *aap*, 433:597–611, April 2005.

E. Carretta, R. G. Gratton, S. Lucatello, A. Bragaglia, G. Catanzaro, F. Leone, Y. Momany, V. D'Orazi, S. Cassisi, F. D'Antona, and S. Ortolani. Abundances for a Large Sample of Red Giants in NGC 1851: Hints for a Merger of Two Clusters? *apjl*, 722:L1–L6, October 2010d.

E. Carretta, S. Lucatello, R. G. Gratton, A. Bragaglia, and V. D'Orazi. Multiple stellar populations in the globular cluster NGC 1851. *aap*, 533:A69, September 2011b.

S. Cassisi, M. Salaris, J. Anderson, G. Piotto, A. Pietrinferni, A. Milone, A. Bellini, and L. R. Bedin. Hot Horizontal Branch Stars in ω Centauri: Clues about their Origin from the Cluster Color Magnitude Diagram. *apj*, 702:1530–1535, September 2009.

S. Cassisi, M. Salaris, A. Pietrinferni, G. Piotto, A. P. Milone, L. R. Bedin, and J. Anderson. The Double Subgiant Branch of NGC 1851: The Role of the CNO Abundance. *apjl*, 672:L115–L118, January 2008.

F. Castelli and S. Hubrig. A spectroscopic atlas of the HgMn star HD 175640 (B9 V) $\lambda\lambda$ 3040-10 000 Å. *aap*, 425:263–270, October 2004.

F. Castelli and R. L. Kurucz. New Grids of ATLAS9 Model Atmospheres. In N. Piskunov, W. W. Weiss, and D. F. Gray, editors, *Modelling of Stellar Atmospheres*, volume 210 of *IAU Symposium*, page 20P, 2003.

C. Charbonnel. A Consistent Explanation for 12C/ 13C, 7Li and 3He Anomalies in Red Giant Stars. *apjl*, 453: L41, November 1995.

C. Charbonnel and J. D. Do Nascimento, Jr. How many low-mass stars do destroy (3) He? *aap*, 336:915–919, August 1998.

L. Ciotti. Stellar systems following the R exp 1/m luminosity law. *aap*, 249:99–106, September 1991.

J. G. Cohen. Abundances in globular cluster red giants. V - The metal-rich globular clusters. *apj*, 270:654–665, July 1983.

J. G. Cohen. The Spectra of Main-Sequence Stars in Galactic Globular Clusters. I. CH and CN Bands in M13. *aj*, 117:2428–2433, May 1999a.

J. G. Cohen. The Spectra of Main-Sequence Stars in Galactic Globular Clusters. II. CH and CN Bands in M71. *aj*, 117:2434–2439, May 1999b.

J. G. Cohen, M. M. Briley, and P. B. Stetson. Carbon and Nitrogen Abundances in Stars at the Base of the Red Giant Branch in M5. *aj*, 123:2525–2540, May 2002.

J. G. Cohen, M. M. Briley, and P. B. Stetson. C and N Abundances in Stars at the Base of the Red Giant Branch in M15. *aj*, 130:1177–1193, September 2005.

J. G. Cohen, W. Huang, and E. N. Kirby. The Peculiar Chemical Inventory of NGC 2419: An Extreme Outer Halo "Globular Cluster". *apj*, 740:60, October 2011.

J. G. Cohen and E. N. Kirby. The Bizarre Chemical Inventory of NGC 2419, An Extreme Outer Halo Globular Cluster. *apj*, 760:86, November 2012.

J. G. Cohen and J. Meléndez. Abundances in a Large Sample of Stars in M3 and M13. *aj*, 129:303–329, January 2005.

J. E. Colucci, R. A. Bernstein, S. Cameron, A. McWilliam, and J. G. Cohen. M31 Globular Cluster Abundances from High-Resolution, Integrated-Light Spectroscopy. *apj*, 704:385–414, October 2009.

C. Conroy and D. N. Spergel. On the Formation of Multiple Stellar Populations in Globular Clusters. *apj*, 726:36, January 2011.

P. Cote, D. A. Hanes, D. E. McLaughlin, T. J. Bridges, J. E. Hesser, and G. L. H. Harris. Discovery of a Probable CH Star in the Globular Cluster M14 and Implications for the Evolution of Binaries in Clusters. *apjl*, 476: L15, February 1997.

P. L. Cottrell and G. S. Da Costa. Correlated cyanogen and sodium anomalies in the globular clusters 47 TUC and NGC 6752. *apjl*, 245:L79–L82, April 1981.

J. J. Cowan and F.-K. Thielemann. R-Process Nucleosynthesis in Supernovae. *Physics Today*, 57(10):100000–53, October 2004.

K. Cunha, V. V. Smith, D. L. Lambert, and K. H. Hinkle. Fluorine Abundances in the Large Magellanic Cloud and ω Centauri: Evidence for Neutrino Nucleosynthesis? *aj*, 126:1305–1311, September 2003.

G. S. Da Costa, E. V. Held, I. Saviane, and M. Gullieuszik. M22: An [Fe/H] Abundance Range Revealed. *apj*, 705:1481–1491, November 2009.

G. S. Da Costa and A. F. Marino. Nucleosynthesis in the Stellar Systems ω Centauri and M22. *pasa*, 28:28–37, January 2011.

E. Dalessandro, G. Beccari, B. Lanzoni, F. R. Ferraro, R. Schiavon, and R. T. Rood. Multiwavelength Photometry in the Globular Cluster M2. *apjs*, 182:509–518, June 2009.

F. D'Antona, M. Bellazzini, V. Caloi, F. F. Pecci, S. Galleti, and R. T. Rood. A Helium Spread among the Main-Sequence Stars in NGC 2808. *apj*, 631:868–878, October 2005.

F. D'Antona and V. Caloi. The Early Evolution of Globular Clusters: The Case of NGC 2808. *apj*, 611:871–880, August 2004.

F. D'Antona and V. Caloi. The fraction of second generation stars in globular clusters from the analysis of the horizontal branch. *mnras*, 390:693–705, October 2008.

F. D'Antona, V. Caloi, J. Montalbán, P. Ventura, and R. Gratton. Helium variation due to self-pollution among Globular Cluster stars. Consequences on the horizontal branch morphology. *aap*, 395:69–75, November 2002.

F. D'Antona, V. Caloi, and P. Ventura. The evolutionary status of the blue hook stars in ω Centauri. *mnras*, 405:2295–2301, July 2010.

F. D'Antona, A. D'Ercole, A. F. Marino, A. P. Milone, P. Ventura, and E. Vesperini. The Oxygen versus Sodium (Anti)Correlation(S) in ω Cen. *apj*, 736:5, July 2011.

F. Dantona, R. Gratton, and A. Chieffi. CNO self-pollution in globular clusters - A model and its possible observational tests. *memsai*, 54:173–198, 1983.

F. D'Antona, P. B. Stetson, P. Ventura, A. P. Milone, G. Piotto, and V. Caloi. The influence of the C+N+O abundances on the determination of the relative ages of globular clusters: the case of NGC1851 and NGC6121 (M4). *mnras*, 399:L151–L155, October 2009.

F. D'Antona and P. Ventura. A model for globular cluster extreme anomalies. *mnras*, 379:1431–1441, August 2007.

B. Davies, D. F. Figer, R.-P. Kudritzki, J. MacKenty, F. Najarro, and A. Herrero. A Massive Cluster of Red Supergiants at the Base of the Scutum-Crux Arm. *apj*, 671:781–801, December 2007.

B. Davies, D. F. Figer, C. J. Law, R.-P. Kudritzki, F. Najarro, A. Herrero, and J. W. MacKenty. The Cool Supergiant Population of the Massive Young Star Cluster RSGC1. *apj*, 676:1016–1028, April 2008.

S. E. de Mink, N. Langer, R. G. Izzard, H. Sana, and A. de Koter. The rotation rates of massive stars: the role of binary interaction through tides, mass transfer and mergers. *ArXiv e-prints*, November 2012.

S. E. de Mink, O. R. Pols, N. Langer, and R. G. Izzard. Massive binaries as the source of abundance anomalies in globular clusters. *aap*, 507:L1–L4, November 2009.

T. Decressin, H. Baumgardt, C. Charbonnel, and P. Kroupa. Evolution of two stellar populations in globular clusters. II. Effects of primordial gas expulsion. *aap*, 516:A73, June 2010.

T. Decressin, H. Baumgardt, and P. Kroupa. The evolution of two stellar populations in globular clusters. I. The dynamical mixing timescale. *aap*, 492:101–109, December 2008.

T. Decressin, C. Charbonnel, and G. Meynet. Origin of the abundance patterns in Galactic globular clusters: constraints on dynamical and chemical properties of globular clusters. *aap*, 475:859–873, December 2007a.

T. Decressin, C. Charbonnel, L. Siess, A. Palacios, G. Meynet, and C. Georgy. CNO enrichment by rotating AGB stars in globular clusters. *aap*, 505:727–733, October 2009.

T. Decressin, G. Meynet, C. Charbonnel, N. Prantzos, and S. Ekström. Fast rotating massive stars and the origin of the abundance patterns in galactic globular clusters. *aap*, 464:1029–1044, March 2007b.

P. A. Denisenkov and S. N. Denisenkova. Possible Explanation of the Correlation Between Nitrogen and Sodium Over Abundances for Red Giants in Globular Clusters. *Astronomicheskij Tsirkulyar*, 1538:11–+, June 1989.

P. A. Denissenkov and D. A. VandenBerg. Canonical Extra Mixing in Low-Mass Red Giants. *apj*, 593:509–523, August 2003.

A. D'Ercole, F. D'Antona, R. Carini, E. Vesperini, and P. Ventura. The role of super-asymptotic giant branch ejecta in the abundance patterns of multiple populations in globular clusters. *mnras*, 423:1521–1533, June 2012.

A. D'Ercole, F. D'Antona, P. Ventura, E. Vesperini, and S. L. W. McMillan. Abundance patterns of multiple populations in globular clusters: a chemical evolution model based on yields from AGB ejecta. *mnras*, 407:854–869, September 2010.

A. D'Ercole, F. D'Antona, and E. Vesperini. Formation of multiple populations in globular clusters: constraints on the dilution by pristine gas. *mnras*, 415:1304–1309, August 2011.

A. D'Ercole, E. Vesperini, F. D'Antona, S. L. W. McMillan, and S. Recchi. Formation and dynamical evolution of multiple stellar generations in globular clusters. *mnras*, 391:825–843, December 2008.

A. Di Cecco, G. Bono, P. B. Stetson, A. Pietrinferni, R. Becucci, S. Cassisi, S. Degl'Innocenti, G. Iannicola, P. G. Prada Moroni, R. Buonanno, A. Calamida, F. Caputo, M. Castellani, C. E. Corsi, I. Ferraro, M. Dall'Ora, M. Monelli, M. Nonino, A. M. Piersimoni, L. Pulone, M. Romaniello, M. Salaris, A. R. Walker, and M. Zoccali. On the $\Delta V^{bump}{}_{HB}$ Parameter in Globular Clusters. *apj*, 712:527–535, March 2010.

M. di Criscienzo, F. D'Antona, A. P. Milone, P. Ventura, V. Caloi, R. Carini, A. D'Ercole, E. Vesperini, and G. Piotto. NGC 2419: a large and extreme second generation in a currently undisturbed cluster. *mnras*, 414:3381–3393, July 2011.

R. J. Dickens. A second CH star in Omega Centauri and the C^{12}/C^{13} ratio. *mnras*, 159:7P–10P, 1972.

R. J. Dickens and R. A. Bell. Enhanced abundances of nitrogen and s-process elements in red giant stars in omega Centauri. *apj*, 207:506–517, July 1976.

V. D'Orazi, S. Lucatello, R. Gratton, A. Bragaglia, E. Carretta, Z. Shen, and S. Zaggia. Lithium and Proton-capture Elements in Globular Cluster Dwarfs: The Case of 47 TUC. *apjl*, 713:L1–L5, April 2010.

V. D'Orazi, S. Lucatello, M. Lugaro, R. G. Gratton, G. Angelou, A. Bragaglia, E. Carretta, A. Alves-Brito, I. I. Ivans, T. Masseron, and A. Mucciarelli. Fluorine variations in the globular cluster NGC 6656 (M22): implications for internal enrichment timescales. *ArXiv e-prints*, October 2012.

V. D'Orazi and A. F. Marino. Lithium Abundances in Red Giants of M4: Evidence for Asymptotic Giant Branch Star Pollution in Globular Clusters? *apjl*, 716:L166–L169, June 2010.

A. Dotter, B. Chaboyer, J. W. Ferguson, H.-c. Lee, G. Worthey, D. Jevremović, and E. Baron. Stellar Population Models and Individual Element Abundances. I. Sensitivity of Stellar Evolution Models. *apj*, 666:403–412, September 2007.

A. Dotter, B. Chaboyer, D. Jevremović, V. Kostov, E. Baron, and J. W. Ferguson. The Dartmouth Stellar Evolution Database. *apjs*, 178:89–101, September 2008.

A. K. Dupree, J. Strader, and G. H. Smith. Direct Evidence for an Enhancement of Helium in Giant Stars in Omega Centauri. *apj*, 728:155, February 2011.

S. Feltzing, F. Primas, and R. A. Johnson. Stellar abundances and ages for metal-rich Milky Way globular clusters. Stellar parameters and elemental abundances for 9 HB stars in NGC 6352. *aap*, 493:913–930, January 2009.

Y. Fenner, S. Campbell, A. I. Karakas, J. C. Lattanzio, and B. K. Gibson. Modelling self-pollution of globular clusters from asymptotic giant branch stars. *mnras*, 353:789–795, September 2004.

F. R. Ferraro, E. Dalessandro, A. Mucciarelli, G. Beccari, R. M. Rich, L. Origlia, B. Lanzoni, R. T. Rood, E. Valenti, M. Bellazzini, S. M. Ransom, and G. Cocozza. The cluster Terzan 5 as a remnant of a primordial building block of the Galactic bulge. *nat*, 462:483–486, November 2009.

F. R. Ferraro, A. Sollima, E. Pancino, M. Bellazzini, O. Straniero, L. Origlia, and A. M. Cool. The Discovery of an Anomalous Subgiant Branch in the Color-Magnitude Diagram of ω Centauri. *apjl*, 603:L81–L84, March 2004.

P. Francois. Chemical composition of globular cluster stars. *aap*, 247:56–63, July 1991.

K. C. Freeman and A. W. Rodgers. The Chemical Inhomogeneity of Omega Centauri. *apjl*, 201:L71, October 1975.

U. Frischknecht, R. Hirschi, and F.-K. Thielemann. Non-standard s-process in low metallicity massive rotating stars. *aap*, 538:L2, February 2012.

D. Geisler, S. Villanova, G. Carraro, C. Pilachowski, J. Cummings, C. I. Johnson, and F. Bresolin. The Unique Na:O Abundance Distribution in NGC 6791: The First Open(?) Cluster with Multiple Populations. *apjl*, 756:L40, September 2012.

L. Girardi, E. K. Grebel, M. Odenkirchen, and C. Chiosi. Theoretical isochrones in several photometric systems. II. The Sloan Digital Sky Survey ugriz system. *aap*, 422:205–215, July 2004.

L. Girardi, M. A. T. Groenewegen, E. Hatziminaoglou, and L. da Costa. Star counts in the Galaxy. Simulating from very deep to very shallow photometric surveys with the TRILEGAL code. *aap*, 436:895–915, June 2005.

O. Y. Gnedin, H. Zhao, J. E. Pringle, S. M. Fall, M. Livio, and G. Meylan. The Unique History of the Globular Cluster ω Centauri. *apjl*, 568:L23–L26, March 2002.

R. Gratton, C. Sneden, and E. Carretta. Abundance Variations Within Globular Clusters. *araa*, 42:385–440, September 2004.

R. G. Gratton, P. Bonifacio, A. Bragaglia, E. Carretta, V. Castellani, M. Centurion, A. Chieffi, R. Claudi, G. Clementini, F. D'Antona, S. Desidera, P. François, F. Grundahl, S. Lucatello, P. Molaro, L. Pasquini, C. Sneden, F. Spite, and O. Straniero. The O-Na and Mg-Al anticorrelations in turn-off and early subgiants in globular clusters. *aap*, 369:87–98, April 2001.

R. G. Gratton and E. Carretta. Diluting the material forming the second generation stars in globular clusters: the contribution by unevolved stars. *aap*, 521:A54, October 2010a.

R. G. Gratton and E. Carretta. Diluting the material forming the second generation stars in globular clusters: the contribution by unevolved stars. *aap*, 521:A54, October 2010b.

R. G. Gratton, E. Carretta, and A. Bragaglia. Multiple populations in globular clusters. Lessons learned from the Milky Way globular clusters. *aapr*, 20:50, February 2012a.

R. G. Gratton, E. Carretta, A. Bragaglia, S. Lucatello, and V. D'Orazi. The second and third parameters of the horizontal branch in globular clusters. *aap*, 517:A81, July 2010.

R. G. Gratton, S. Lucatello, E. Carretta, A. Bragaglia, V. D'Orazi, Y. Al Momany, A. Sollima, M. Salaris, and S. Cassisi. The Na-O anticorrelation in horizontal branch stars. II. NGC 1851. *aap*, 539:A19, March 2012b.

R. G. Gratton, C. Sneden, E. Carretta, and A. Bragaglia. Mixing along the red giant branch in metal-poor field stars. *aap*, 354:169–187, February 2000.

R. G. Gratton, S. Villanova, S. Lucatello, A. Sollima, D. Geisler, E. Carretta, S. Cassisi, and A. Bragaglia. Spectroscopic analysis of the two subgiant branches of the globular cluster NGC 1851. *aap*, 544:A12, August 2012c.

F. Grundahl and M. I. Andersen. Strömgren CCD Photometry of Globular Clusters. In M. Spite, editor, *Galaxy Evolution: Connecting the Distant Universe with the Local Fossil Record*, page 197, 1999.

F. Grundahl and M. Briley. Star-to-star nitrogen abundances in globular cluster stars. *Nuclear Physics A*, 688:414–416, May 2001.

F. Grundahl, M. Catelan, W. B. Landsman, P. B. Stetson, and M. I. Andersen. Hot Horizontal-Branch Stars: The Ubiquitous Nature of the "Jump" in Strömgren u, Low Gravities, and the Role of Radiative Levitation of Metals. *apj*, 524:242–261, October 1999.

F. Grundahl, P. E. Nissen, M. Briley, and S. Feltzing. Strömgren photometry and abundance variations in globular cluster giants - the case of NGC 6752. In T. Lejeune & J. Fernandes, editor, *Observed HR Diagrams and Stellar Evolution*, volume 274 of *Astronomical Society of the Pacific Conference Series*, pages 228–+, 2002.

F. Grundahl, D. A. Vandenberg, and M. I. Andersen. Stroemgren Photometry of Globular Clusters: The Distance and Age of M13, Evidence for Two Populations of Horizontal-Branch Stars. *apjl*, 500:L179, June 1998.

S.-I. Han, Y.-W. Lee, S.-J. Joo, S. T. Sohn, S.-J. Yoon, H.-S. Kim, and J.-W. Lee. The Presence of Two Distinct Red Giant Branches in the Globular Cluster NGC 1851. *apjl*, 707:L190–L194, December 2009a.

S.-I. Han, Y.-W. Lee, S.-J. Joo, S. T. Sohn, S.-J. Yoon, H.-S. Kim, and J.-W. Lee. The Presence of Two Distinct Red Giant Branches in the Globular Cluster NGC 1851. *apjl*, 707:L190–L194, December 2009b.

D. Harbeck, G. H. Smith, and E. K. Grebel. CN Abundance Variations on the Main Sequence of 47 Tucanae. *aj*, 125:197–207, January 2003.

G. A. Harding. A CH star in omega Centauri. *The Observatory*, 82:205–207, October 1962.

W. E. Harris. A Catalog of Parameters for Globular Clusters in the Milky Way. *aj*, 112:1487–+, October 1996.

J. A. Hartigan and P. M. Hartigan. The dip test of unimodality. *The Annals of Statistics*, 13(1):pp. 70–84, 1985. ISSN 00905364. URL `http://www.jstor.org/stable/2241144`.

A. Helmi. The stellar halo of the Galaxy. *aapr*, 15:145–188, June 2008.

J. E. Hesser, R. A. Bell, G. L. H. Harris, and R. D. Cannon. Strong CN stars in the globular cluster NGC 1851. *aj*, 87:1470–1477, November 1982.

I. Iben, Jr. Stellar Evolution. II. The Evolution of a 3 M_{sun} Star from the Main Sequence Through Core Helium Burning. *apj*, 142:1447, November 1965.

I. Iben, Jr. Low-Mass Red Giants. *apj*, 154:581, November 1968.

C. Iliadis. *Nuclear Physics of Stars*. Wiley-VCH Verlag, 2007.

I. I. Ivans, R. P. Kraft, C. Sneden, G. H. Smith, R. M. Rich, and M. Shetrone. New Analyses of Star-to-Star Abundance Variations among Bright Giants in the Mildly Metal-poor Globular Cluster M5. *aj*, 122:1438–1463, September 2001.

I. I. Ivans, C. Sneden, R. P. Kraft, N. B. Suntzeff, V. V. Smith, G. E. Langer, and J. P. Fulbright. Star-to-Star Abundance Variations among Bright Giants in the Mildly Metal-poor Globular Cluster M4. *aj*, 118:1273–1300, September 1999.

H. R. Jacobson, E. D. Friel, and C. A. Pilachowski. Abundances of Red Giants in Old Open Clusters. III. NGC 7142. *aj*, 135:2341–2349, June 2008.

G. James, P. François, P. Bonifacio, E. Carretta, R. G. Gratton, and F. Spite. Heavy elements and chemical enrichment in globular clusters. *aap*, 427:825–838, December 2004.

C. I. Johnson and C. A. Pilachowski. Chemical Abundances for 855 Giants in the Globular Cluster Omega Centauri (NGC 5139). *apj*, 722:1373–1410, October 2010.

J. A. Johnson, I. I. Ivans, and P. B. Stetson. Chemical Compositions of Red Giant Stars in Old Large Magellanic Cloud Globular Clusters. *apj*, 640:801–822, April 2006.

S.-J. Joo and Y.-W. Lee. Star Formation Histories of Globular Clusters with Multiple Populations. I. \omega\ Cen, M22, and NGC 1851. *ArXiv e-prints*, November 2012.

A. Jorissen, V. V. Smith, and D. L. Lambert. Fluorine in red giant stars - Evidence for nucleosynthesis. *aap*, 261:164–187, July 1992.

J. S. Kalirai, D. Saul Davis, H. B. Richer, P. Bergeron, M. Catelan, B. M. S. Hansen, and R. M. Rich. The Masses of Population II White Dwarfs. *apj*, 705:408–425, November 2009.

A. Karakas and J. C. Lattanzio. Stellar Models and Yields of Asymptotic Giant Branch Stars. *pasa*, 24:103–117, October 2007.

A. I. Karakas. Nucleosynthesis of Low and Intermediate-mass Stars. In A. Goswami and B. E. Reddy, editors, *Principles and Perspectives in Cosmochemistry*, page 107, 2010a.

A. I. Karakas. Updated stellar yields from asymptotic giant branch models. *mnras*, 403:1413–1425, April 2010b.

A. I. Karakas, Y. Fenner, A. Sills, S. W. Campbell, and J. C. Lattanzio. The Chemical Evolution of Helium in Globular Clusters: Implications for the Self-Pollution Scenario. *apj*, 652:1240–1245, December 2006.

A. Kayser, M. Hilker, E. K. Grebel, and P. G. Willemsen. Comparing CN and CH line strengths in a homogeneous spectroscopic sample of 8 Galactic globular clusters. *aap*, 486:437–452, August 2008.

I. R. King, L. R. Bedin, S. Cassisi, A. P. Milone, A. Bellini, G. Piotto, J. Anderson, A. Pietrinferni, and D. Cordier. Hubble Space Telescope Observations of an Outer Field in Omega Centauri: A Definitive Helium Abundance. *aj*, 144:5, July 2012.

R. P. Kraft. Abundance differences among globular-cluster giants: Primordial versus evolutionary scenarios. *pasp*, 106:553–565, June 1994.

R. P. Kraft, C. Sneden, G. E. Langer, and C. F. Prosser. Oxygen abundances in halo giants. II - Giants in the globular clusters M13 and M3 and the intermediately metal-poor halo field. *aj*, 104:645–668, August 1992.

R. P. Kraft, C. Sneden, G. H. Smith, M. D. Shetrone, G. E. Langer, and C. A. Pilachowski. Proton Capture Chains in Globular Cluster Stars.II.Oxygen, Sodium, Magnesium, and Aluminum Abundances in M13 Giants Brighter Than the Horizontal Branch. *aj*, 113:279, January 1997.

V. Kravtsov, G. Alcaíno, G. Marconi, and F. Alvarado. Evidence of the inhomogeneity of the stellar population in the differentially reddened globular cluster NGC 3201. *aap*, 512:L6, March 2010a.

V. Kravtsov, G. Alcaíno, G. Marconi, and F. Alvarado. Wide-field multi-color photometry of the Galactic globular cluster NGC 1261. *aap*, 516:A23, June 2010b.

P. Kroupa. On the variation of the initial mass function. *mnras*, 322:231–246, April 2001.

P. Kroupa, C. A. Tout, and G. Gilmore. The distribution of low-mass stars in the Galactic disc. *mnras*, 262: 545–587, June 1993.

J. M. D. Kruijssen and S. F. Portegies Zwart. On the Interpretation of the Globular Cluster Luminosity Function. *apjl*, 698:L158–L162, June 2009.

R. Kurucz. Opacities for Stellar Atmospheres: [-1.0a],[-1.5a],[-2.0a] +.4 alpha. *Opacities for Stellar Atmospheres: [-1.0a],[-1.5a],[-2.0a] +.4 alpha. Kurucz CD-ROM No. 10. Cambridge, Mass.: Smithsonian Astrophysical Observatory, 1993.*, 10, 1993.

R. L. Kurucz. ATLAS12, SYNTHE, ATLAS9, WIDTH9, et cetera. *Memorie della Societa Astronomica Italiana Supplementi*, 8:14, 2005.

G. E. Langer. Bimodal cyanogen distributions in moderately metal-poor globular clusters. II - Evidence for 'mixing' and 'saturation'. *pasp*, 97:382–392, May 1985.

G. E. Langer, R. Hoffman, and C. Sneden. Sodium-oxygen abundance anticorrelations and deep-mixing scenarios for globular-cluster giants. *pasp*, 105:301–307, March 1993.

C. Lardo, M. Bellazzini, E. Pancino, E. Carretta, A. Bragaglia, and E. Dalessandro. Mining SDSS in search of multiple populations in globular clusters. *aap*, 525:A114+, January 2011.

C. Lardo, A. P. Milone, A. F. Marino, A. Mucciarelli, E. Pancino, M. Zoccali, M. Rejkuba, R. Carrera, and O. Gonzalez. C and N abundances of main sequence and subgiant branch stars in NGC 1851. *aap*, 541: A141, May 2012a.

C. Lardo, E. Pancino, A. Mucciarelli, and A. P. Milone. Carbon and nitrogen abundances of stellar populations in the globular cluster M 2. *aap*, 548:A107, December 2012b.

S. S. Larsen, J. Strader, and J. P. Brodie. Constraints on mass loss and self-enrichment scenarios for the globular clusters of the Fornax dSph. *aap*, 544:L14, August 2012.

J.-W. Lee and B. W. Carney. BV Photometry of RR Lyrae Variables in the Globular Cluster M2 (NGC 7089). *aj*, 117:2868–2881, June 1999.

J.-W. Lee, Y.-W. Kang, J. Lee, and Y.-W. Lee. Enrichment by supernovae in globular clusters with multiple populations. *nat*, 462:480–482, November 2009a.

J.-W. Lee, J. Lee, Y.-W. Kang, Y.-W. Lee, S.-I. Han, S.-J. Joo, S.-C. Rey, and D. Yong. Chemical Inhomogeneity in Red Giant Branch Stars and RR lyrae variables in NGC 1851: Two Subpopulations in Red Giant Branch. *apjl*, 695:L78–L82, April 2009b.

S. G. Lee. CN and CH Band Strengths of Bright Giants in the Globular Cluster M15. *Journal of Korean Astronomical Society*, 33:137–142, December 2000.

Y.-W. Lee, J.-M. Joo, Y.-J. Sohn, S.-C. Rey, H.-C. Lee, and A. R. Walker. Multiple stellar populations in the globular cluster ω Centauri as tracers of a merger event. *nat*, 402:55–57, November 1999.

Y.-W. Lee, S.-J. Joo, S.-I. Han, C. Chung, C. H. Ree, Y.-J. Sohn, Y.-C. Kim, S.-J. Yoon, S. K. Yi, and P. Demarque. Super-Helium-rich Populations and the Origin of Extreme Horizontal-Branch Stars in Globular Clusters. *apjl*, 621:L57–L60, March 2005.

B. Letarte, V. Hill, P. Jablonka, E. Tolstoy, P. François, and G. Meylan. VLT/UVES spectroscopy of individual stars in three globular clusters in the Fornax dwarf spheroidal galaxy. *aap*, 453:547–554, July 2006.

K. Lind, C. Charbonnel, T. Decressin, F. Primas, F. Grundahl, and M. Asplund. Tracing the evolution of NGC 6397 through the chemical composition of its stellar populations. *aap*, 527:A148, March 2011.

M. Lugaro, A. I. Karakas, R. J. Stancliffe, and C. Rijs. The s-process in Asymptotic Giant Branch Stars of Low Metallicity and the Composition of Carbon-enhanced Metal-poor Stars. *apj*, 747:2, March 2012.

M. Lugaro, C. Ugalde, A. I. Karakas, J. Görres, M. Wiescher, J. C. Lattanzio, and R. C. Cannon. Reaction Rate Uncertainties and the Production of ^{19}F in Asymptotic Giant Branch Stars. *apj*, 615:934–946, November 2004.

T. J. Maccarone and D. R. Zurek. Novae from isolated white dwarfs as a source of helium for second-generation stars in globular clusters. *mnras*, 423:2–6, June 2012.

A. D. Mackey and G. F. Gilmore. Comparing the properties of local globular cluster systems: implications for the formation of the Galactic halo. *mnras*, 355:504–534, December 2004.

G. Mandushev, A. Staneva, and N. Spasova. Dynamical masses for Galactic globular clusters. *aap*, 252: 94–99, December 1991.

A. Marcolini, A. D'Ercole, F. Brighenti, and S. Recchi. Star formation feedback and metal enrichment by Types Ia and II supernovae in dwarf spheroidal galaxies: the case of Draco. *mnras*, 371:643–658, September 2006.

A. Marín-Franch, A. Aparicio, G. Piotto, A. Rosenberg, B. Chaboyer, A. Sarajedini, M. Siegel, J. Anderson, L. R. Bedin, A. Dotter, M. Hempel, I. King, S. Majewski, A. P. Milone, N. Paust, and I. N. Reid. The ACS Survey of Galactic Globular Clusters. VII. Relative Ages. *apj*, 694:1498–1516, April 2009.

A. F. Marino, A. P. Milone, G. Piotto, S. Cassisi, F. D'Antona, J. Anderson, A. Aparicio, L. R. Bedin, A. Renzini, and S. Villanova. The C+N+O Abundance of ω Centauri Giant Stars: Implications for the Chemical-enrichment Scenario and the Relative Ages of Different Stellar Populations. *apj*, 746:14, February 2012a.

A. F. Marino, A. P. Milone, G. Piotto, S. Villanova, L. R. Bedin, A. Bellini, and A. Renzini. A double stellar generation in the globular cluster NGC 6656 (M 22). Two stellar groups with different iron and s-process element abundances. *aap*, 505:1099–1113, October 2009.

A. F. Marino, A. P. Milone, C. Sneden, M. Bergemann, R. P. Kraft, G. Wallerstein, S. Cassisi, A. Aparicio, M. Asplund, R. L. Bedin, M. Hilker, K. Lind, Y. Momany, G. Piotto, I. U. Roederer, P. B. Stetson, and M. Zoccali. The double sub-giant branch of NGC 6656 (M 22): a chemical characterization. *aap*, 541:A15, May 2012b.

A. F. Marino, C. Sneden, R. P. Kraft, G. Wallerstein, J. E. Norris, G. da Costa, A. P. Milone, I. I. Ivans, G. Gonzalez, J. P. Fulbright, M. Hilker, G. Piotto, M. Zoccali, and P. B. Stetson. The two metallicity groups of the globular cluster M 22: a chemical perspective. *aap*, 532:A8+, August 2011.

A. F. Marino, S. Villanova, G. Piotto, A. P. Milone, Y. Momany, L. R. Bedin, and A. M. Medling. Spectroscopic and photometric evidence of two stellar populations in the Galactic globular cluster NGC 6121 (M 4). *aap*, 490:625–640, November 2008.

S. L. Martell. Light-element abundance variations in globular clusters. *Astronomische Nachrichten*, 332: 467, June 2011.

S. L. Martell and G. H. Smith. CN Variations in High-Metallicity Globular and Open Clusters. *pasp*, 121: 577–584, June 2009.

S. L. Martell, G. H. Smith, and M. M. Briley. CN Bimodality at Low Metallicity: The Globular Cluster M53. *pasp*, 120:7–15, January 2008.

S. L. Martell, J. P. Smolinski, T. C. Beers, and E. K. Grebel. Building the Galactic halo from globular clusters: evidence from chemically unusual red giants. *aap*, 534:A136, October 2011.

R. D. McClure. The binary nature of the CH stars. *apjl*, 280:L31–L34, May 1984.

R. D. McClure and J. E. Hesser. Strengths of spectral features of giant stars in outlying halo clusters. *apj*, 246:136–144, May 1981.

R. D. McClure and J. Norris. A CH star in the globular cluster M22, and the nature of CH and CN anomalies. *apjl*, 217:L101–L104, October 1977.

D. E. McLaughlin and R. P. van der Marel. Resolved Massive Star Clusters in the Milky Way and Its Satellites: Brightness Profiles and a Catalog of Fundamental Parameters. *apjs*, 161:304–360, December 2005.

G. Meylan, A. Sarajedini, P. Jablonka, S. G. Djorgovski, T. Bridges, and R. M. Rich. Mayall II=G1 in M31: Giant Globular Cluster or Core of a Dwarf Elliptical Galaxy? *aj*, 122:830–841, August 2001.

G. Meynet and M. Arnould. Synthesis of ^{19}F in Wolf-Rayet stars. *aap*, 355:176–180, March 2000.

A. P. Milone, L. R. Bedin, G. Piotto, and J. Anderson. Multiple stellar populations in Magellanic Cloud clusters. I. An ordinary feature for intermediate age globulars in the LMC? *aap*, 497:755–771, April 2009a.

A. P. Milone, L. R. Bedin, G. Piotto, J. Anderson, I. R. King, A. Sarajedini, A. Dotter, B. Chaboyer, A. Marín-Franch, S. Majewski, A. Aparicio, M. Hempel, N. E. Q. Paust, I. N. Reid, A. Rosenberg, and M. Siegel. The ACS Survey of Galactic Globular Clusters. III. The Double Subgiant Branch of NGC 1851. *apj*, 673: 241–250, January 2008.

A. P. Milone, A. F. Marino, S. Cassisi, G. Piotto, L. R. Bedin, J. Anderson, F. Allard, A. Aparicio, A. Bellini, R. Buonanno, M. Monelli, and A. Pietrinferni. The Infrared Eye of the Wide-Field Camera 3 on the Hubble Space Telescope Reveals Multiple Main Sequences of Very Low Mass Stars in NGC 2808. *apjl*, 754:L34, August 2012a.

A. P. Milone, A. F. Marino, G. Piotto, L. R. Bedin, J. Anderson, A. Aparicio, S. Cassisi, and R. M. Rich. A Double Main Sequence in the Globular Cluster NGC 6397. *apj*, 745:27, January 2012b.

A. P. Milone, G. Piotto, L. R. Bedin, I. R. King, J. Anderson, A. F. Marino, A. Bellini, R. Gratton, A. Renzini, P. B. Stetson, S. Cassisi, A. Aparicio, A. Bragaglia, E. Carretta, F. D'Antona, M. Di Criscienzo, S. Lucatello, M. Monelli, and A. Pietrinferni. Multiple Stellar Populations in 47 Tucanae. *apj*, 744:58, January 2012c.

A. P. Milone, G. Piotto, I. R. King, L. R. Bedin, J. Anderson, A. F. Marino, Y. Momany, L. Malavolta, and S. Villanova. Multiple Stellar Populations in the Galactic Globular Cluster NGC 6752. *apj*, 709:1183–1194, February 2010.

A. P. Milone, P. B. Stetson, G. Piotto, L. R. Bedin, J. Anderson, S. Cassisi, and M. Salaris. The radial distribution of the two stellar populations in NGC 1851. *aap*, 503:755–764, September 2009b.

L. Monaco, M. Bellazzini, F. R. Ferraro, and E. Pancino. The central density cusp of the Sagittarius dwarf spheroidal galaxy. *mnras*, 356:1396–1402, February 2005.

L. Monaco, S. Villanova, P. Bonifacio, E. Caffau, D. Geisler, G. Marconi, Y. Momany, and H.-G. Ludwig. Lithium and sodium in the globular cluster <ASTROBJ>M 4</ASTROBJ>. Detection of a Li-rich dwarf star: preservation or pollution? *aap*, 539:A157, March 2012.

L. Monaco, S. Villanova, C. Moni Bidin, G. Carraro, D. Geisler, P. Bonifacio, O. A. Gonzalez, M. Zoccali, and L. Jilkova. Lithium-rich giants in the Galactic thick disk. *aap*, 529:A90, May 2011.

A. Moretti, G. Piotto, C. Arcidiacono, A. P. Milone, R. Ragazzoni, R. Falomo, J. Farinato, L. R. Bedin, J. Anderson, A. Sarajedini, A. Baruffolo, E. Diolaiti, M. Lombini, R. Brast, R. Donaldson, J. Kolb, E. Marchetti, and S. Tordo. MCAO near-IR photometry of the globular cluster NGC 6388: MAD observations in crowded fields. *aap*, 493:539–546, January 2009.

D. Moro and U. Munari. The Asiago Database on Photometric Systems (ADPS). I. Census parameters for 167 photometric systems. *aaps*, 147:361–628, December 2000.

N. Mowlavi. Nucleosynthesis in low- and intermediate-mass stars: An overview. In *American Institute of Physics Conference Series*, volume 425 of *American Institute of Physics Conference Series*, pages 507–516, February 1998.

A. Mucciarelli, M. Bellazzini, R. Ibata, T. Merle, S. C. Chapman, E. Dalessandro, and A. Sollima. News from the Galactic suburbia: the chemical composition of the remote globular cluster NGC 2419. *mnras*, 426: 2889–2900, November 2012.

A. Mucciarelli, S. Cristallo, E. Brocato, L. Pasquini, O. Straniero, E. Caffau, G. Raimondo, A. Kaufer, I. Musella, V. Ripepi, M. Romaniello, and A. R. Walker. NGC 1866: a milestone for understanding the chemical evolution of stellar populations in the Large Magellanic Cloud. *mnras*, 413:837–851, May 2011.

A. Mucciarelli, L. Origlia, F. R. Ferraro, and E. Pancino. Looking Outside the Galaxy: The Discovery of Chemical Anomalies in Three Old Large Magellanic Cloud Clusters. *apjl*, 695:L134–L139, April 2009.

H. Neckel and D. Labs. The solar radiation between 3300 and 12500 A. *solphys*, 90:205–258, February 1984.

J. Norris. The correlation of cyanogen, calcium and the heavy elements on the giant branch of Omega Centauri. In D. Hanes and B. Madore, editors, *Globular Clusters*, page 113, 1980.

J. Norris. The cyanogen distribution of M4 and the possible connection between horizontal branch morphology and chemical inhomogeneity. *apj*, 248:177–188, August 1981.

J. Norris. The ellipticities of globular clusters and the cyanogen problem. *apjl*, 313:L65–L68, February 1987.

J. Norris, P. L. Cottrell, K. C. Freeman, and G. S. Da Costa. The abundance spread in the giants of NGC 6752. *apj*, 244:205–220, February 1981.

J. Norris and K. C. Freeman. The cyanogen distribution of the giants in 47 Tucanae. *apjl*, 230:L179–L182, June 1979.

J. Norris, K. C. Freeman, and G. S. Da Costa. The anticorrelation of cyanogen and CH on the giant branch of 47 Tucanae. *apj*, 277:615–622, February 1984.

J. E. Norris. The Helium Abundances of ω Centauri. *apjl*, 612:L25–L28, September 2004.

J. E. Norris and G. S. Da Costa. The Giant Branch of omega Centauri. IV. Abundance Patterns Based on Echelle Spectra of 40 Red Giants. *apj*, 447:680, July 1995.

E. W. Olszewski, A. Saha, P. Knezek, A. Subramaniam, T. de Boer, and P. Seitzer. A 500 Parsec Halo Surrounding the Galactic Globular NGC 1851. *aj*, 138:1570–1576, December 2009.

L. Origlia, R. M. Rich, F. R. Ferraro, B. Lanzoni, M. Bellazzini, E. Dalessandro, A. Mucciarelli, E. Valenti, and G. Beccari. Spectroscopy Unveils the Complex Nature of Terzan 5. *apjl*, 726:L20, January 2011.

W. Osborn. Two new CN-strong globular cluster stars. *The Observatory*, 91:223–224, December 1971.

A. Palacios, M. Arnould, and G. Meynet. The thermonuclear production of ^{19}F by Wolf-Rayet stars revisited. *aap*, 443:243–250, November 2005.

A. Palacios, C. Charbonnel, S. Talon, and L. Siess. Rotational mixing in low-mass stars. II. Self-consistent models of Pop II RGB stars. *aap*, 453:261–278, July 2006.

E. Pancino, F. R. Ferraro, M. Bellazzini, G. Piotto, and M. Zoccali. New Evidence for the Complex Structure of the Red Giant Branch in ω Centauri. *apjl*, 534:L83–L87, May 2000a.

E. Pancino, F. R. Ferraro, M. Bellazzini, G. Piotto, and M. Zoccali. New Evidence for the Complex Structure of the Red Giant Branch in ω Centauri. *apjl*, 534:L83–L87, May 2000b.

E. Pancino, A. Galfo, F. R. Ferraro, and M. Bellazzini. The Rotation of Subpopulations in ω Centauri. *apjl*, 661:L155–L158, June 2007.

E. Pancino, A. Mucciarelli, L. Sbordone, M. Bellazzini, L. Pasquini, L. Monaco, and F. R. Ferraro. The subgiant branch of ω Centauri seen through high-resolution spectroscopy. I. The first stellar generation in ω Cen? *aap*, 527:A18, March 2011a.

E. Pancino, A. Mucciarelli, L. Sbordone, M. Bellazzini, L. Pasquini, L. Monaco, and F. R. Ferraro. The subgiant branch of ω Centauri seen through high-resolution spectroscopy. I. The first stellar generation in ω Cen? *aap*, 527:A18, March 2011b.

E. Pancino, M. Rejkuba, M. Zoccali, and R. Carrera. Low-resolution spectroscopy of main sequence stars belonging to 12 Galactic globular clusters. I. CH and CN band strength variations. *aap*, 524:A44, December 2010.

E. Pancino, A. Seleznev, F. R. Ferraro, M. Bellazzini, and G. Piotto. The multiple stellar population in ω Centauri: spatial distribution and structural properties. *mnras*, 345:683–690, October 2003.

L. Pasquini, P. Bonifacio, P. Molaro, P. Francois, F. Spite, R. G. Gratton, E. Carretta, and B. Wolff. Li in NGC 6752 and the formation of globular clusters. *aap*, 441:549–553, October 2005.

L. Pasquini, P. Mauas, H. U. Käufl, and C. Cacciari. Measuring helium abundance difference in giants of NGC 2808. *aap*, 531:A35, July 2011.

S. E. Persson, J. G. Cohen, K. Matthews, J. A. Frogel, and M. Aaronson. The spread in CO absorption and effective temperature among the giants in omega Centauri. *apj*, 235:452–469, January 1980.

A. Pietrinferni, S. Cassisi, M. Salaris, and F. Castelli. A Large Stellar Evolution Database for Population Synthesis Studies. II. Stellar Models and Isochrones for an α-enhanced Metal Distribution. *apj*, 642:797–812, May 2006.

A. Pietrinferni, S. Cassisi, M. Salaris, S. Percival, and J. W. Ferguson. A Large Stellar Evolution Database for Population Synthesis Studies. V. Stellar Models and Isochrones with CNONa Abundance Anticorrelations. *apj*, 697:275–282, May 2009.

C. A. Pilachowski and C. Sneden. The Carbon Isotope Ratio in Giants in the Globular Cluster M3. In *Bulletin of the American Astronomical Society*, volume 33 of *Bulletin of the American Astronomical Society*, page 1513, December 2001.

C. A. Pilachowski, C. Sneden, and R. P. Kraft. Sodium Abundances in Field Metal-Poor Stars. *aj*, 111:1689, April 1996.

G. Piotto. Observations of multiple populations in star clusters. In E. E. Mamajek, D. R. Soderblom, & R. F. G. Wyse, editor, *IAU Symposium*, volume 258 of *IAU Symposium*, pages 233–244, June 2009.

G. Piotto, L. R. Bedin, J. Anderson, I. R. King, S. Cassisi, A. P. Milone, S. Villanova, A. Pietrinferni, and A. Renzini. A Triple Main Sequence in the Globular Cluster NGC 2808. *apjl*, 661:L53–L56, May 2007.

G. Piotto, A. P. Milone, J. Anderson, L. R. Bedin, A. Bellini, S. Cassisi, A. F. Marino, A. Aparicio, and V. Nascimbeni. Hubble Space Telescope Reveals Multiple Sub-giant Branch in Eight Globular Clusters. *apj*, 760:39, November 2012.

G. Piotto, S. Villanova, L. R. Bedin, R. Gratton, S. Cassisi, Y. Momany, A. Recio-Blanco, S. Lucatello, J. Anderson, I. R. King, A. Pietrinferni, and G. Carraro. Metallicities on the Double Main Sequence of ω Centauri Imply Large Helium Enhancement. *apj*, 621:777–784, March 2005.

S. F. Portegies Zwart, S. L. W. McMillan, and M. Gieles. Young Massive Star Clusters. *araa*, 48:431–493, September 2010.

N. Prantzos and C. Charbonnel. On the self-enrichment scenario of galactic globular clusters: constraints on the IMF. *aap*, 458:135–149, October 2006.

N. Prantzos, C. Charbonnel, and C. Iliadis. Light nuclei in galactic globular clusters: constraints on the self-enrichment scenario from nucleosynthesis. *aap*, 470:179–190, July 2007.

B. J. Pritzl, M. Buttermore, A. Saha, E. D. Skillman, K. A. Venn, H. L. Morrison, and E. W. Olszewski. Using RR Lyrae Stars to Proble the M33 Halo. In *American Astronomical Society Meeting Abstracts*, volume 38 of *Bulletin of the American Astronomical Society*, page 941, December 2006.

C. Pryor and G. Meylan. Velocity Dispersions for Galactic Globular Clusters. In S. G. Djorgovski and G. Meylan, editors, *Structure and Dynamics of Globular Clusters*, volume 50 of *Astronomical Society of the Pacific Conference Series*, page 357, January 1993.

L. Pulone, G. De Marchi, S. Covino, and F. Paresce. HST observations of the metal rich globular clusters NGC 6496 and NGC 6352. *aap*, 399:121–131, February 2003.

M. L. Pumo, F. D'Antona, and P. Ventura. Self-Enrichment in Globular Clusters: Is There a Role for the Super-Asymptotic Giant Branch Stars? *apjl*, 672:L25–L28, January 2008.

G. Raimondo, V. Castellani, S. Cassisi, E. Brocato, and G. Piotto. On the Observational Properties of He-burning Stars: Some Clues on the Tilt of the Horizontal Branch in Metal-rich Clusters. *apj*, 569:975–983, April 2002.

S. V. Ramírez and J. G. Cohen. Abundances in Stars from the Red Giant Branch Tip to Near the Main-Sequence Turnoff in M71. III. Abundance Ratios. *aj*, 123:3277–3297, June 2002.

S. V. Ramírez and J. G. Cohen. Abundances in Stars from the Red Giant Branch Tip to near the Main-Sequence Turnoff in M5. *aj*, 125:224–245, January 2003.

A. Renzini. Origin of multiple stellar populations in globular clusters and their helium enrichment. *mnras*, 391:354–362, November 2008.

A. Renzini and A. Buzzoni. Global properties of stellar populations and the spectral evolution of galaxies. In C. Chiosi and A. Renzini, editors, *Spectral Evolution of Galaxies*, volume 122 of *Astrophysics and Space Science Library*, pages 195–231, 1986.

A. Renzini and M. Voli. Advanced evolutionary stages of intermediate-mass stars. I - Evolution of surface compositions. *aap*, 94:175–193, January 1981.

R. M. Rich, C. Sosin, S. G. Djorgovski, G. Piotto, I. R. King, A. Renzini, E. S. Phinney, B. Dorman, J. Liebert, and G. Meylan. Discovery of Extended Blue Horizontal Branches in Two Metal-rich Globular Clusters. *apjl*, 484:L25, July 1997.

V. Ripepi, G. Clementini, M. Di Criscienzo, C. Greco, M. Dall'Ora, L. Federici, L. Di Fabrizio, I. Musella, M. Marconi, L. Baldacci, and M. Maio. On the Remote Galactic Globular Cluster NGC 2419. *apjl*, 667: L61–L64, September 2007.

I. U. Roederer, A. F. Marino, and C. Sneden. Characterizing the Heavy Elements in Globular Cluster M22 and an Empirical s-process Abundance Distribution Derived from the Two Stellar Groups. *apj*, 742:37, November 2011.

D.-G. Roh, Y.-W. Lee, S.-J. Joo, S.-I. Han, Y.-J. Sohn, and J.-W. Lee. Two Distinct Red Giant Branches in the Globular Cluster NGC 288. *apjl*, 733:L45, June 2011.

M. Salaris, S. Cassisi, and A. Pietrinferni. The Horizontal Branch of NGC 1851: Constraints on the Cluster Subpopulations. *apjl*, 678:L25–L28, May 2008.

M. Salaris, S. Cassisi, and A. Weiss. Red Giant Branch Stars: The Theoretical Framework. *pasp*, 114:375–402, April 2002.

M. Salaris, A. Serenelli, A. Weiss, and M. Miller Bertolami. Semi-empirical White Dwarf Initial-Final Mass Relationships: A Thorough Analysis of Systematic Uncertainties Due to Stellar Evolution Models. *apj*, 692:1013–1032, February 2009.

M. Salaris, A. Weiss, J. W. Ferguson, and D. J. Fusilier. On the Primordial Scenario for Abundance Variations within Globular Clusters: The Isochrone Test. *apj*, 645:1131–1137, July 2006.

A. Sarajedini, L. R. Bedin, B. Chaboyer, A. Dotter, M. Siegel, J. Anderson, A. Aparicio, I. King, S. Majewski, A. Marín-Franch, G. Piotto, I. N. Reid, and A. Rosenberg. The ACS Survey of Galactic Globular Clusters. I. Overview and Clusters without Previous Hubble Space Telescope Photometry. *aj*, 133:1658–1672, April 2007.

I. Saviane, G. S. da Costa, E. V. Held, V. Sommariva, M. Gullieuszik, B. Barbuy, and S. Ortolani. Homogeneous metallicities and radial velocities for Galactic globular clusters. First CaT metallicities for twenty clusters. *aap*, 540:A27, April 2012.

L. Sbordone, M. Salaris, A. Weiss, and S. Cassisi. Photometric signatures of multiple stellar populations in Galactic globular clusters. *aap*, 534:A9, October 2011.

D. Schaerer and C. Charbonnel. A new perspective on globular clusters, their initial mass function and their contribution to the stellar halo and the cosmic reionization. *mnras*, 413:2297–2304, May 2011.

G. Schaller, D. Schaerer, G. Meynet, and A. Maeder. New grids of stellar models from 0.8 to 120 solar masses at Z = 0.020 and Z = 0.001. *aaps*, 96:269–331, December 1992.

M. Sharina, B. Aringer, E. Davoust, A. Y. Kniazev, and C. J. Donzelli. A CH star in the globular cluster NGC 6426. *mnras*, page L503, August 2012.

Z.-X. Shen, P. Bonifacio, L. Pasquini, and S. Zaggia. Li - O anti-correlation in NGC 6752: evidence for Li-enriched polluting gas. *aap*, 524:L2, December 2010.

M. D. Shetrone, C. Sneden, and C. A. Pilachowski. Carbon isotope ratios and lithium abundances in old disk giants. *pasp*, 105:337–349, April 1993.

M. H. Siegel, A. Dotter, S. R. Majewski, A. Sarajedini, B. Chaboyer, D. L. Nidever, J. Anderson, A. Marín-Franch, A. Rosenberg, L. R. Bedin, A. Aparicio, I. King, G. Piotto, and I. N. Reid. The ACS Survey of Galactic Globular Clusters: M54 and Young Populations in the Sagittarius Dwarf Spheroidal Galaxy. *apjl*, 667:L57–L60, September 2007.

L. Siess. Evolution of massive AGB stars. III. the thermally pulsing super-AGB phase. *aap*, 512:A10, March 2010.

A. Sills and E. Glebbeek. Multiple populations in globular clusters: the possible contributions of stellar collisions. *mnras*, 407:277–284, September 2010.

E. D. Skillman. The Metal-Poor IMF, Stellar Evolution, and Star Formation Histories. In L. K. Hunt, S. C. Madden, and R. Schneider, editors, *IAU Symposium*, volume 255 of *IAU Symposium*, pages 285–296, December 2008.

M. F. Skrutskie, R. M. Cutri, R. Stiening, M. D. Weinberg, S. Schneider, J. M. Carpenter, C. Beichman, R. Capps, T. Chester, J. Elias, J. Huchra, J. Liebert, C. Lonsdale, D. G. Monet, S. Price, P. Seitzer, T. Jarrett, J. D. Kirkpatrick, J. E. Gizis, E. Howard, T. Evans, J. Fowler, L. Fullmer, R. Hurt, R. Light, E. L. Kopan, K. A. Marsh, H. L. McCallon, R. Tam, S. Van Dyk, and S. Wheelock. The Two Micron All Sky Survey (2MASS). *aj*, 131:1163–1183, February 2006.

R. Smiljanic, R. Gauderon, P. North, B. Barbuy, C. Charbonnel, and N. Mowlavi. CNONa and $^{12}C/^{13}C$ in giant stars of 10 open clusters. *aap*, 502:267–282, July 2009.

G. H. Smith. CN Abundance Inhomogeneities in the Globular Cluster M3: Results Based on Merged Data Sets from the Literature. *pasp*, 114:1097–1107, October 2002.

G. H. Smith and R. P. Kraft. On the Possibility of Nova Enrichment of Globular Clusters. *pasp*, 108:344, April 1996.

G. H. Smith and S. L. Martell. Comparing Deep Mixing in Globular Cluster and Halo Field Giants: Carbon Abundance Data from the Literature. *pasp*, 115:1211–1219, October 2003.

G. H. Smith and M. Mateo. CN and CH variations among giants in the globular cluster M2. *apj*, 353:533–542, April 1990.

G. H. Smith and J. Norris. The cyanogen distributions in NGC 3201, M55, and M71. *apj*, 254:149–161, March 1982.

G. H. Smith and J. Norris. The Cyanogen distribution of the red giants in M5. *apj*, 264:215–222, January 1983.

G. H. Smith and J. Norris. Spectroscopy of clump giants in NGC 2158. *aj*, 89:263–266, February 1984.

G. H. Smith and J. E. Norris. CN variations among asymptotic giant branch and horizontal branch stars in the intermediate metallicity globular clusters M5, M4, and NGC 6752. *aj*, 105:173–183, January 1993.

G. H. Smith, M. D. Shetrone, R. A. Bell, C. W. Churchill, and M. M. Briley. CNO Abundances of Bright Giants in the Globular Clusters M3 and M13. *aj*, 112:1511, October 1996.

G. H. Smith and G. D. Wirth. The behavior of magnesium and sodium lines among giants within bimodal-CN globular clusters. *pasp*, 103:1158–1175, November 1991.

V. V. Smith, K. Cunha, I. I. Ivans, J. C. Lattanzio, S. Campbell, and K. H. Hinkle. Fluorine Abundance Variations in Red Giants of the Globular Cluster M4 and Early-Cluster Chemical Pollution. *apj*, 633:392–397, November 2005.

V. V. Smith, N. B. Suntzeff, K. Cunha, R. Gallino, M. Busso, D. L. Lambert, and O. Straniero. The Chemical Evolution of the Globular Cluster ω Centauri (NGC 5139). *aj*, 119:1239–1258, March 2000.

J. P. Smolinski, S. L. Martell, T. C. Beers, and Y. S. Lee. A Survey of CN and CH Variations in Galactic Globular Clusters from Sloan Digital Sky Survey Spectroscopy. *aj*, 142:126, October 2011.

C. Sneden. The nitrogen abundance of the very metal-poor star HD 122563. *apj*, 184:839–849, September 1973.

C. Sneden and J. J. Cowan. Genesis of the Heaviest Elements in the Milky Way Galaxy. *Science*, 299:70–75, January 2003.

C. Sneden, J. J. Cowan, and R. Gallino. Neutron-Capture Elements in the Early Galaxy. *araa*, 46:241–288, September 2008.

C. Sneden, R. P. Kraft, C. F. Prosser, and G. E. Langer. Oxygen abundances in halo giants. I - Giants in the very metal-poor globular clusters M92 and M15 and the metal-poor halo field. *aj*, 102:2001–2021, December 1991.

C. Sneden, R. P. Kraft, C. F. Prosser, and G. E. Langer. Oxygen abundances in halo giants. III - Giants in the mildly metal-poor globular cluster M5. *aj*, 104:2121–2140, December 1992.

C. Sneden, R. P. Kraft, M. D. Shetrone, G. H. Smith, G. E. Langer, and C. F. Prosser. Star-To-Star Abundance Variations Among Bright Giants in the Metal-Poor Globular Cluster M15. *aj*, 114:1964–+, November 1997.

A. Sollima, F. R. Ferraro, M. Bellazzini, L. Origlia, O. Straniero, and E. Pancino. Deep FORS1 Observations of the Double Main Sequence of ω Centauri. *apj*, 654:915–922, January 2007.

A. Sollima, R. G. Gratton, J. A. Carballo-Bello, D. Martínez-Delgado, E. Carretta, A. Bragaglia, S. Lucatello, and J. Peñarrubia. Spectroscopic hint of a cold stream in the direction of the globular cluster NGC 1851. *mnras*, 426:1137–1143, October 2012.

A. Sollima, E. Pancino, F. R. Ferraro, M. Bellazzini, O. Straniero, and L. Pasquini. Metallicities, Relative Ages, and Kinematics of Stellar Populations in ω Centauri. *apj*, 634:332–343, November 2005.

C. B. Stephenson. A possible new and very remote galactic cluster. *aj*, 99:1867, June 1990.

P. B. Stetson. DAOPHOT - A computer program for crowded-field stellar photometry. *pasp*, 99:191–222, March 1987.

P. B. Stetson. The center of the core-cusp globular cluster M15: CFHT and HST Observations, ALLFRAME reductions. *pasp*, 106:250–280, March 1994.

P. B. Stetson. Homogeneous Photometry for Star Clusters and Resolved Galaxies. II. Photometric Standard Stars. *pasp*, 112:925–931, July 2000.

T. Suda, Y. Katsuta, S. Yamada, T. Suwa, C. Ishizuka, Y. Komiya, K. Sorai, M. Aikawa, and M. Y. Fujimoto. Stellar Abundances for the Galactic Archeology (SAGA) Database — Compilation of the Characteristics of Known Extremely Metal-Poor Stars. *pasj*, 60:1159–, October 2008.

N. B. Suntzeff. Carbon and nitrogen abundances in the giant stars of the globular clusters M3 and M13. *apjs*, 47:1–32, September 1981.

N. B. Suntzeff and V. V. Smith. Carbon isotopic abundances in giant stars in the CN-bimodal globular clusters NGC 6752 and M4. *apj*, 381:160–172, November 1991.

R. Surman, G. C. McLaughlin, M. Ruffert, H.-T. Janka, and W. R. Hix. r-Process Nucleosynthesis in Hot Accretion Disk Flows from Black Hole-Neutron Star Mergers. *apjl*, 679:L117–L120, June 2008.

L.-S. The, M. F. El Eid, and B. S. Meyer. s-Process Nucleosynthesis in Advanced Burning Phases of Massive Stars. *apj*, 655:1058–1078, February 2007.

A. Thoul, A. Jorissen, S. Goriely, E. Jehin, P. Magain, A. Noels, and G. Parmentier. Accretion of gas by globular cluster stars. *aap*, 383:491–501, February 2002.

R. H. D. Townsend, S. P. Owocki, and I. D. Howarth. Be-star rotation: how close to critical? *mnras*, 350: 189–195, May 2004.

C. Travaglio, R. Gallino, E. Arnone, J. Cowan, F. Jordan, and C. Sneden. Galactic Evolution of Sr, Y, And Zr: A Multiplicity of Nucleosynthetic Processes. *apj*, 601:864–884, February 2004.

A. A. R. Valcarce and M. Catelan. Formation of multiple populations in globular clusters: another possible scenario. *aap*, 533:A120, September 2011.

S. van den Bergh. Mergers of Globular Clusters. *apjl*, 471:L31, November 1996.

P. G. van Dokkum. Cosmic-Ray Rejection by Laplacian Edge Detection. *pasp*, 113:1420–1427, November 2001.

D. Vanbeveren, N. Mennekens, and J. P. De Greve. The effect of intermediate-mass close binaries on the chemical evolution of globular clusters. *aap*, 543:A4, July 2012.

D. A. VandenBerg, P. A. Bergbusch, A. Dotter, J. W. Ferguson, G. Michaud, J. Richer, and C. R. Proffitt. Models for Metal-poor Stars with Enhanced Abundances of C, N, O, Ne, Na, Mg, Si, S, Ca, and Ti, in Turn, at Constant Helium and Iron Abundances. *apj*, 755:15, August 2012.

A. D. Vanture and G. Wallerstein. An abundance analysis of a globular-cluster CH star - M22 III-106. *pasp*, 104:888–893, October 1992.

P. Ventura, V. Caloi, F. D'Antona, J. Ferguson, A. Milone, and G. P. Piotto. The C+N+O abundances and the splitting of the subgiant branch in the globular cluster NGC 1851. *mnras*, 399:934–943, October 2009.

P. Ventura, R. Carini, and F. D'Antona. A deep insight into the Mg-Al-Si nucleosynthesis in massive asymptotic giant branch and super-asymptotic giant branch stars. *mnras*, 415:3865–3871, August 2011.

P. Ventura and F. D'Antona. Toward a Working Model for the Abundance Variations in Stars within Globular Clusters. *apjl*, 635:L149–L152, December 2005.

P. Ventura and F. D'Antona. Self-enrichment by asymptotic giant branch stars in globular clusters: comparison between intermediate and high metallicities. *mnras*, 385:2034–2040, April 2008a.

P. Ventura and F. D'Antona. The self-enrichment scenario in intermediate metallicity globular clusters. *aap*, 479:805–816, March 2008b.

P. Ventura and F. D'Antona. Massive AGB models of low metallicity: the implications for the self-enrichment scenario in metal-poor globular clusters. *aap*, 499:835–846, June 2009.

P. Ventura and F. D'Antona. Hot bottom burning in the envelope of super asymptotic giant branch stars. *mnras*, 410:2760–2766, February 2011.

P. Ventura, F. D'Antona, M. Di Criscienzo, R. Carini, A. D'Ercole, and E. vesperini. Super-AGB-AGB Evolution and the Chemical Inventory in NGC 2419. *apjl*, 761:L30, December 2012.

P. Ventura, F. D'Antona, and I. Mazzitelli. Yields from low metallicity, intermediate mass AGB stars:. Their role for the CNO and lithium abundances in Globular Cluster stars. *aap*, 393:215–223, October 2002.

P. Ventura, F. D'Antona, I. Mazzitelli, and R. Gratton. Predictions for Self-Pollution in Globular Cluster Stars. *apjl*, 550:L65–L69, March 2001.

E. Vesperini, S. L. W. McMillan, F. D'Antona, and A. D'Ercole. The Fraction of Globular Cluster Second-generation Stars in the Galactic Halo. *apjl*, 718:L112–L116, August 2010.

E. Vesperini, S. L. W. McMillan, F. D'Antona, and A. D'Ercole. Dynamical evolution and spatial mixing of multiple population globular clusters. *mnras*, page 442, January 2013.

S. Villanova, D. Geisler, and G. Piotto. Detailed Abundances of Red Giants in the Globular Cluster NGC 1851: C+N+O and the Origin of Multiple Populations. *apjl*, 722:L18–L22, October 2010.

S. Villanova, G. Piotto, I. R. King, J. Anderson, L. R. Bedin, R. G. Gratton, S. Cassisi, Y. Momany, A. Bellini, A. M. Cool, A. Recio-Blanco, and A. Renzini. The Multiplicity of the Subgiant Branch of ω Centauri: Evidence for Prolonged Star Formation. *apj*, 663:296–314, July 2007.

K. Vollmann and T. Eversberg. Remarks on statistical errors in equivalent widths. *Astronomische Nachrichten*, 327:862–+, November 2006.

A. R. Walker, A. M. Kunder, G. Andreuzzi, A. di Cecco, P. B. Stetson, M. Monelli, S. Cassisi, G. Bono, R. de Propris, M. Dall'Ora, J. M. Nemec, and M. Zoccali. Constraints on the formation of the globular cluster IC 4499 from multiwavelength photometry. *mnras*, 415:643–654, July 2011.

G. Wallerstein, E. M. Leep, and J. B. Oke. High-resolution CCD spectra of stars in globular clusters. III - M4, M13, and M22. *aj*, 93:1137–1143, May 1987.

M. Wiescher, J. Görres, E. Uberseder, G. Imbriani, and M. Pignatari. The Cold and Hot CNO Cycles. *Annual Review of Nuclear and Particle Science*, 60:381–404, November 2010.

S. E. Woosley, D. H. Hartmann, R. D. Hoffman, and W. C. Haxton. The nu-process. *apj*, 356:272–301, June 1990.

D. Yong and F. Grundahl. An Abundance Analysis of Bright Giants in the Globular Cluster NGC 1851. *apjl*, 672:L29–L32, January 2008.

D. Yong, F. Grundahl, F. D'Antona, A. I. Karakas, J. C. Lattanzio, and J. E. Norris. A Large C+N+O Abundance Spread in Giant Stars of the Globular Cluster NGC 1851. *apjl*, 695:L62–L66, April 2009.

D. Yong, F. Grundahl, J. A. Johnson, and M. Asplund. Nitrogen Abundances in Giant Stars of the Globular Cluster NGC 6752. *apj*, 684:1159–1169, September 2008a.

D. Yong, J. Meléndez, K. Cunha, A. I. Karakas, J. E. Norris, and V. V. Smith. Chemical Abundances in Giants Stars of the Tidally Disrupted Globular Cluster NGC 6712 from High-resolution Infrared Spectroscopy. *apj*, 689:1020–1030, December 2008b.

R. Zinn. The metal abundance range in the Ursa Minor dwarf galaxy. *apj*, 251:52–60, December 1981.

R. Zinn and M. J. West. The globular cluster system of the galaxy. III - Measurements of radial velocity and metallicity for 60 clusters and a compilation of metallicities for 121 clusters. *apjs*, 55:45–66, May 1984.

M. Zoccali, E. Pancino, M. Catelan, M. Hempel, M. Rejkuba, and R. Carrera. The Radial Extent of the Double Subgiant Branch in NGC 1851. *apjl*, 697:L22–L27, May 2009.